The Pennsylvania State University

The Graduate School

College of Engineering

MODELING RADIOMETRIC AND POLARIZED LIGHT SCATTERING FROM EXOPLANET OCEANS AND ATMOSPHERES

A Dissertation in

Electrical Engineering

by

Michael E. Zugger

Submitted in Partial Fulfillment
of the Requirements
for the Degree of

Doctor of Philosophy

May 2011

The dissertation of Michael E. Zugger was reviewed and approved* by the following:

C. Russell Philbrick
Professor Emeritus, Penn State Dept. of Electrical Engineering
Professor, North Carolina State University Dept. of Physics
Dissertation Co-Advisor and Co-Chair of Committee

Timothy J. Kane
Professor of Electrical Engineering
Dissertation Co-Advisor and Co-Chair of Committee

James F. Kasting
Distinguished Professor of Geosciences

Karl M. Reichard
Assistant Professor of Acoustics

Charles L. Croskey
Professor Emeritus, Electrical Engineering

Thomas N. Jackson
Robert E. Kirby Chair Professor of Electrical Engineering

W. Kenneth Jenkins
Professor of Electrical Engineering
Head of the Department of Electrical Engineering

*Signatures are on file in the Graduate School

Abstract

Of all substances, water appears to be the most vital to the appearance and sustenance of life as we know it. Proposed space-based observatories such as NASA's Terrestrial Planet Finder – Coronograph (TPF-C) may make it possible in the near future to detect the presence of oceans on nearby extrasolar planets (exoplanets) by studying the polarization of visible, infrared, or ultraviolet radiation reflected from the planet. In this dissertation, we model and analyze light scattering properties of various notional exoplanets, including brightness and polarization state versus wavelength and position in the orbit (orbital longitude, OL) in order to predict the potential observability of distant oceans. Our initial working hypotheses are:

1. With simulations we can anticipate terrestrial planet signatures in light scattered from distant star systems;
2. Future instruments will gather sufficient information on terrestrial exoplanets to draw useful conclusions about the planet surfaces and atmospheres;
3. TPF-C will have a baseline wavelength range of 500 – 1000 nm, and will have some capability to observe in spectral sub-bands;
4. Polarized and unpolarized orbital light curves, possibly combined with broad-band spectral information, will provide enough information to discriminate between terrestrial-class planets with and without large oceans;
5. Observation of polarized light curves of exoplanet systems may provide other useful information about the systems beyond that from unpolarized brightness curves.

We find that total flux light curves from Lambertian and Rayleigh scattering dominated planets peak at full phase, OL = 180°, whereas ocean planets with thin atmospheres exhibit peak flux in the crescent phase near OL = 30°. The polarized results for ocean planets show that clouds, wind-driven waves, aerosols, absorption, and Rayleigh scattering in the atmosphere and within the water column, dilute the polarization fraction and shift it away from the OL = 74° predicted by Fresnel theory. On planets for which Rayleigh scattering dominates, the polarization peaks near an orbital longitude of 90°, but clouds and Lambertian surfaces dilute and shift this peak to smaller OL, and a shifted Rayleigh peak might be mistaken for a water signature unless data from multiple wavelength bands are available.

When observing over the baselined TPF-C wavelength range (500–1000 nm), Rayleigh scattering alone from an atmosphere as thick as Earth's is enough to shift the polarization peak to an orbital longitude of 83^{o}, closer to the Rayleigh peak at 90^{o} than to the Fresnel peak at 74^{o}. Ocean radiance in this wavelength band caused by scattering within the water column also dilutes the polarization peak, limiting the polarization fraction to a maximum of slightly over 0.9. Water aerosols shift the peak to even higher OLs and add a rainbow peak near OL = 140°. Clouds also have a strong effect in masking the ocean surface polarization, and water clouds can exhibit the rainbow peak as with water aerosols. The high albedo and multiple scattering of Earth water clouds tends to dilute any liquid polarization signature, and other clouds such as Earth's ice clouds and the sulfuric acid clouds of Venus can produce many different types of signatures depending on composition and particle size and shape. Wind over an ocean surface causes waves and sea foam, both of which tend to dilute the water polarization signal. The magnitude and polarization of exozodiacal light (exo-zodi) is another large unknown, because we have only

limited measurements of zodiacal light in our own Solar System, and instrumentation is not yet sensitive enough to measure exo-zodi in mature exoplanet systems. Exo-zodi is expected to be polarized, so will likely contribute an additional competing "noise" polarization peak.

In addition to end-member planets dominated by Lambertian or Rayleigh scattering, we simulate variations of "water Earths"; these are planets similar to Earth but completely covered by oceans, disturbed only by light winds. For these models, we also include US 1962 Standard Atmosphere absorption, and maritime aerosols using the standard 5 km low visibility and 23 km high visibility aerosols, and some other much higher visibilities for comparison. The polarization fraction for cases with Earth-like aerosols peaks at only about 0.15 at OL = 100° for the 5 km case, and at less than 0.35 at OL = 95° for the 23 km case. With more and more transparent aerosols, the polarization peak for water Earth cases approaches that of a Rayleigh-only atmosphere over an ocean surface.

Our model supports the idea that Rayleigh effects are mitigated by observing at longer wavelengths, taking advantage of the dependence of Rayleigh scattering on the inverse fourth power of wavelength. For example, our simulations show that the polarization fraction for an ocean surface hidden by a Rayleigh-only atmosphere can be increased by using only the longer wavelength portion of the TPF waveband, from 900-1000 nm. However, this would result in a loss of much of the available signal, and it would do nothing to reduce the dilution of the polarization signal by other factors. In particular, the aerosols included in our higher fidelity water Earth model dominate scattering for visibility of 23 km, which represents a clear day on Earth. Still, if multiple wavebands are available on TPF-C, as baselined, then comparing the results of different wavebands from an exoplanet observation, with the above in mind, may be useful.

The net effect of clouds, aerosols, absorption, atmospheric and oceanic Rayleigh scattering, waves, and exo-zodi may severely limit the percentage of ocean planets that would display a significant polarization signature, and may also generate a significant number of false positives on dry planets. Attempting to use the orbital position and strength of the polarization peak to determine whether or not an exoplanet surface is water-covered or dry is risky because so many factors can reduce the strength of the polarization peak, or shift it to higher or lower orbital longitudes. The result is an inversion problem which, for many planets, may be ill-posed. All of this suggests that polarization measurements by a TPF-C type telescope may not provide a positive detection of surface liquid water on exoplanets. On the other hand, the strength and placement of the polarization peak in the orbit relative to the cases we model, combined with the magnitude of the total flux and shape of the orbital flux curve, may give strong evidence of exoplanet surface and atmospheric composition for some nearby Earth-like planets, if they exist.

We have also suggested that polarization could be used to help determine whether an object which appears to be near a star is in fact a planet in orbit around the star, or a background object. If the object exhibits polarization perpendicular to the line between object and the star, then the object probably is a planet and the polarization is likely due to Rayleigh scattering in the planet's atmosphere, reflection from a liquid surface, or a combination of the two effects. This method has the advantage that it can be used to show probable association with a single observation. For

some exoplanet observations, this technique could be implemented immediately by ground-based observatories.

This work is novel in including a more complete atmosphere in simulations of exoplanet light scattering than previous models. The resulting simulations of Earth-like and diffuse scattering planets highlight the potential difficulties in detecting exoplanet oceans, which are not as apparent when using simpler models. The work also includes new ideas on using polarization to help determine planetary association, as well as a novel graphical method of showing different planetary polarization types.

Table of Contents

List of Figures x
List of Tables xiii
Acknowledgements xiv
Dedication xvi
1.0 Introduction 1
1.1 Summary 1
1.1.1 Exoplanet observation and modeling 1
1.1.2 The Search for Exoplanet Oceans 1
1.1.3 Spherical geometry of exoplanet scattering 2
1.1.4 Exoplanet atmospheres 2
1.2 Hypotheses 2
1.3 Goals 3
1.4 Outline of Following Chapters 3
2.0 Solar and Extrasolar Planet Background 4
2.1 Exoplanets 4
2.1.1 Short History of Exoplanet Discovery 4
2.1.2 First Direct Detections 5
2.2 The Search for Life Beyond Earth 8
2.2.1 Life Within the Solar System 8
2.2.2 Life Beyond the Solar System 9
2.3 Planet Finder Missions 12
2.3.1 Astrometry 12
2.3.2 Transits 13
2.3.3 Direct Detection of Terrestrial Planets 14
2.3.4 Diffraction and Coronagraphs 16
2.3.5 Biosignatures 17
2.3.6 Water and Extraterrestrial Life 19
3.0 Electromagnetic Scattering Background 21
3.1 Radiometric Quantities and Terms 21
3.1.1 Radiometry versus Photometry 21
3.1.2 Irradiance 22
3.1.3 Radiant Intensity 22
3.1.4 Radiance 23
3.1.5 Radiometry and Planetary Scattering 24
3.1.6 Received Photons 27
3.2 Types of Scattering 27
3.2.1 Scattering by Small Particles (Rayleigh Scattering) 27
3.2.2 The Mie Solution to Scattering by Spherical Particles 28
3.2.3 Reflection modeling 28
3.2.3 Brewster's Angle 31
3.2.4 Stokes Parameters 32
3.3 Atomic and Molecular Absorption and Emission 34
3.3.1 Types of Transitions 34
3.3.2 Vibrational Modes 35

3.3.3 Rotational Modes 37
3.3.4 Line Broadening 37
4.0 Previous Modeling Work 40
4.1 Scattering from Wavy Oceans 40
4.2 Atmospheric Scattering Code 40
4.2.1 Two-Stream Approximation 41
4.2.2 Multi-Stream Approximations 42
4.2.3 Adding-Doubling Method 42
4.2.4 Discrete Dipole Approximation 42
4.2.5 Successive Orders of Scattering 43
4.2.6 Monte Carlo Methods 43
4.3 Previous Models of Scattering from Earth-like Planets 43
5.0 Development of a Planetary Scattering Model 56
5.1 Approach 56
5.1.1 Overview 56
5.1.2 New Model Development 57
5.2 Atmospheric and Surface Model: 6SV Use and Modification 63
5.2.1 Detailed Description of 6SV 63
5.2.2 Physical Background of Atmosphere/Surface/Observer Interaction 66
5.2.3 Modification of 6SV code to produce reflective Stokes parameters 71
5.3 Planetary System Geometry and Polarization 78
5.3.1 Orbital Geometry 78
5.3.2 Orbital Longitude Effects on Polarization 80
6.0 Results 83
6.1 Unpolarized Light Curves and Contrast Ratios 83
6.1.1 Light curve descriptions 84
6.1.2 Viewing considerations 84
6.1.3 Albedo and Contrast Ratios 85
6.1.4 The Terrestrial Planets 87
6.1.5 Summary of Radiometric Results 87
6.2 Polarized Light Curves 88
6.3 Verification and Error Analysis 101
6.3.1 Overview 101
6.3.2 Assumptions 102
6.3.3 Verification Overview 103
6.3.4 Verification of Combined 6SV/Oceans Model Using Absolute Brightness (Radiant Intensity) 104
6.3.5 Verification of 6SV Sea Surface Model 106
6.3.6 Verification of Rayleigh Scattering Model 107
6.3.7 Computational Accuracy 109
6.3.8 Sensitivity Analysis 109
6.4 Discussion 113
6.4.1 Effect of Orbital Inclination 113
6.4.2 Effect of High Winds 113
6.4.3 Wavelength-Dependent Light Curves 114
6.4.4 Rainbow Angle 114

6.4.5 Clouds 114
6.4.6 Exo-Zodiacal Light 115
6.4.7 Using Polarization to Determine Association and Orbital Inclination 115
6.4.8 The Inverse Problem 116
7.0 Summary and Conclusions 118
7.1 Summary of Work 118
7.2 Hypotheses, Goals, and Results 118
7.3 Conclusions 120
7.4 Contributions 122
7.5 Future Research 123
Appendices 124
Appendix A: Milestones 124
Appendix B: Scattering Theory From Maxwell's Equations 125
B.1 Molecular and Particle Scattering 125
B.2 First Principles 127
B.3 Rayleigh Scattering and the Ideal Dipole 130
B.4 Near Field 132
B.5 Far Field 133
B.6 Scattering Cross Section 134
Appendix C: New IDL Code Developed for This Project 136
C.1 Summary and list of new routines 136
C.2 bilut Routine 136
C.3 Routine inputanggen 137
C.4 Oceans Code Modifications and New Routines 137
Appendix D: Rotating Stokes Parameters to the Scattering Reference Plane 140
D.1 Introduction and Definition of Planes 140
D.2 Formula for Rotation of Stokes Parameters Q and U Using Rotation Angle α 140
D.3 Determination of the Stokes Reference Plane Used by 6SV 141
D.3.1 Expected Results from Different Reference Planes 145
D.3.2 6SV Reference Plane Test Results 145
D.4 Derivation of Formula for Stokes Rotation Angle α 146
Appendix E: Compensating for the 6SV Plane-Parallel Atmosphere Approximation Using Altitude 152
E.1 Introduction 152
E.2 Kasten & Young Approximation 152
E.3 Exponential Approximation (my method) 153
Appendix F: Changes to 6SV Code 161
F.1 Modifications to the sunglint subroutine 162
F.2 Modifications to the POLGLIT.f subroutine 163
F.3 Modifications to main.f 164
Appendix G: Additional Verification and Error Analysis 169
G.1 Additional Verification of Oceans Code 169
G.1.1 Total Illuminated Area 169
G.1.2 Solar Constant 169
G.1.3 Three-Dimensional Trigonometry 169
G.2 Additional Verification of 6SV Code: 6SV implementation of Fresnel equations 176

G.3 Additional Verification Using Independently Developed MATLAB Model 178
G.4 Verification of 6SV calm ocean planet results versus 2% reflecting spherical mirror 179
G.5 Graphical depiction of glint spot on an ocean planet..... 182
References..... 183

List of Figures

Figure 1: NASA views of Venus, Earth, and Mars (Venus and Mars from the Hubble Wide Field Planetary Camera, Earth from Apollo 17) 4
Figure 2: Image of HR 8799 star system including three planets (Marois et al. 2008) 6
Figure 3: Size comparison of the HR 8799 star system with the Solar System (Marois et al. 2008) 6
Figure 4: Image of Fomalhaut b in coronograph image (Kalas et al. 2008) 7
Figure 5: Image of Fomalhaut b showing progress around the orbit (Kalas et al. 2008) 7
Figure 6: Carbonate Silicate Cycle (Kasting et al. 1993) 10
Figure 7: Habitable Zone relative to conditions in our Solar System with consideration of CO_2 feedback (Kasting et al. 1993) 11
Figure 8: Artist's conception of the Kepler spacecraft (NASA/Ames) 13
Figure 9: Kepler field of view in the northern hemisphere summer sky (NASA) 14
Figure 10: Contrast ratios for proposed visible (TPF-C) and infrared (TPF-I) NASA planet finder spacecraft (Beichman and Velusamy 1999) 15
Figure 11: Infrared spectra of Venus, Earth, and Mars from Cockell et al. (2009), using spectra from a number of previous papers (Meadows and Crisp 1996; Tinetti et al. 2006; Tinetti et al. 2006; Kaltenegger et al. 2007; Selsis et al. 2007) 18
Figure 12: Galileo visible spectrum of Earth's atmosphere showing oxygen band (Sagan et al. 1993) 18
Figure 13: The "Red Edge" of chlorophyll for land plants (Kiang et al. 2007) 19
Figure 14: Diagram showing polarization of light due to reflection at or near Brewster's angle 31
Figure 15: Hydrogen emission line spectrum showing frequencies and atomic energy levels ... 35
Figure 16: Representation of the vibrational modes of the carbon dioxide molecule 36
Figure 17: Example Lorentz distributions, where x_0 is the mean value, and γ_0 is a measure of the spread 38
Figure 18: Geometry of single scattering from a plane-parallel atmosphere or locally flat surface 41
Figure 19: Disk-averaged diurnal light curve from a distant Earth, from Ford et al. 2001 45
Figure 20: Block diagram depicting the construction of model in McCullough (2006) 46
Figure 21: Calculated polarization fractions for planets composed of a single type of Earth-like terrain, from McCullough 2006. Upper curves: no clouds, lower curves: Earth-like cloud fraction and reflectance. Lower curves with filled circle data points: scaled from Earthshine data 48
Figure 22: Analytical polarization maxima in simplified case 49
Figure 23: Block diagram depicting the construction of the model described in Williams & Gaidos 2008 50
Figure 24: Depiction of Earth at various orbital inclinations and viewing angles, from Williams & Gaidos 2008 51
Figure 25: Total flux, parallel and perpendicular fluxes, and polarization fractions from a) an Earth-like planet and b) a water world, from Williams and Gaidos (2008) 52
Figure 26: Block diagram depicting the complex, high-fidelity SMART model discussed in Tinetti et al. 2006 53
Figure 27: Early version of model architecture using a Linux script to call the lookup table version of 6SV, called 6SVlut 59

Figure 28: Block diagram of final model configuration, showing interaction between modified 6SV, modified Oceans, bilut IDL program, and user 61
Figure 29: Front panel from Oceans v2xx showing the available GUI controls (left bar), as well as the orbital inclination, axis obliquity, and illuminated fraction of the planet 61
Figure 30: Block diagram of 6SV from the 6SV manual, Part I, p 33 (Vermote et al. 2006) 65
Figure 31: Direct solar irradiance on the surface (Vermote et al. 2006) 68
Figure 32: Diffuse solar irradiance on the surface (Vermote et al. 2006) 69
Figure 33: Solar irradiance multiply scattered to the surface from both surface and atmosphere (Vermote et al. 2006) 69
Figure 34: Radiation received at the sensor from the surface due to both direct and diffuse illumination of the surface (Vermote et al. 2006) 70
Figure 35: Radiation received at the sensor due to scattering from the atmosphere (Vermote et al. 2006) 70
Figure 36: Radiation received at the sensor due to scattering from the surface outside the field of view, scattered into the receiving cone from the atmosphere (Vermote et al. 2006) 71
Figure 37: Diagram of the lightcurve routine in Oceans, showing nested loops 79
Figure 38: Input/output diagram for the Oceans lightcurve routine showing the operations performed by *Oceans* for each pixel at each point in the orbit 80
Figure 39: Geometry of the problem; locations of polarization maxima differ when spherical geometry and other factors are included 81
Figure 40: Double rainbow (photo credit: C. R. Philbrick) 82
Figure 41: Normalized total light curves for end-member planets. The peak near OL = 30° is indicative of an ocean surface (although not necessarily water) 83
Figure 42: Polarized light curves (solid) and polarization fraction (dashed) for a planet with a thick Rayleigh scattering atmosphere (τ_R = 0.5) over a dark surface. Equiv Earth wavelength: 369 nm 89
Figure 43: Polarization fraction variation with τ_R over 0.1 Lambertian surface; pure Rayleigh over dark surface shown (dashed) for comparison. Unpolarized light from the surface dilutes polarization. Equivalent Earth wavelengths: 369, 547, 648, 813, 965, 1150 nm (see section 5.2.1.7) 90
Figure 44: Effect of Lambertian cloud fraction on Rayleigh scattering-dominated planet; τ_R = 0.5 (Earth atmosphere at 369 nm), a relatively low average cloud albedo of 0.3 is assumed 91
Figure 45: Polarized light curves and polarization fraction for a calm ocean planet with thin atmosphere, wavelength range 500-1000 nm 92
Figure 46: Effects of wind speed and wavelength on polarization fraction curve and its approach to the Fresnel curve 93
Figure 47: Polarization fraction for ocean planets vs. wind speed (no absorption, no aerosols, no Rayleigh scattering). For the TPF-C wavelength range 500–1000 nm, at wind speeds below 5 m/s, polarization fraction is limited by scattering within the water 94
Figure 48: Comparison of present model results with those of Williams and Gaidos 2008, both with windspeed = 10 m/s. Wavelength range: 500-1000 nm 95
Figure 49: Polarization fraction for ocean planets vs. Rayleigh optical depth in equivalent Earth atmospheres for the TPF waveband 500-1000 nm. Both atmospheric and in-water scattering are significant. Wind is calm, no aerosols or absorption 97
Figure 50: Polarization fraction for ocean planet with varying cloud fraction and cloud albedo, wavelength range 500–1000 nm 98

Figure 51: Water Earth models with varying aerosols, Earth Rayleigh and absorption, 500-1000 nm. Aerosol versions show reduced polarization, rainbow angle peak near OL = 140° 98
Figure 52: Preliminary simulation of observing at longer wavelength NIR windows (1.55 – 1.75 μm and 2.1 – 2.3 μm) on polarization fraction of water Earth 99
Figure 53: Summary of polarization fraction results for various planet types over the TPF waveband (500-1000 nm). Each point represents the peak polarization fraction and corresponding OL of an earlier curve 100
Figure 54: Light curves for Lambertian planet for our model versus analytical solution 106
Figure 55: Reflectance and polarization fraction from modified 6SV model (solid) vs. analytical result from Fresnel equations (dashed) 107
Figure 56: Verification of Rayleigh scattering model using $\tau_R = 0.5$ 108
Figure 57: Verification of Rayleigh scattering with τ_R reduced to 0.1 109
Figure 58: Sensitivity to plane parallel (solid) versus spherical atmosphere using Kasten and Young approximation (dashed) 110
Figure 59: Sensitivity to maximum zenith angle 111
Figure 60: Sensitivity to number of zenith angles used 112
Figure 61: Sensitivity to orbital lightcurve resolution 113
Figure 62: Diagram showing electromagnetic wave and electric field 125
Figure 63: Dipole scattering pattern viewed in *xz* and *xy* planes (generated using MATLAB) . 125
Figure 64: Logarithmic phase function for 0.5 μm wavelength light scattered by a 5% volume concentration of 5 μm water droplets in air; red = parallel polarization, green = perpendicular 126
Figure 65: Scattering diagram for specular reflection case 142
Figure 66: Scattering diagram for case with equal zenith angles and obtuse relative azimuth angle 143
Figure 67: Scattering diagram for case of equal zenith angles and acute relative azimuth angle 144
Figure 68: Scattering diagram for case with star and observer at same zenith angle and relative azimuth approaching zero 145
Figure 69: Comparison of various approximations to the airmass of Earth's spherical atmosphere with zenith angle 153
Figure 70: Geometry of the spherical atmosphere 155
Figure 71: Diagram of the interplay between 6SV subroutines in calculating ocean-leaving radiance and directional reflectance 161
Figure 72: Spherical triangle showing naming convention for angles and segments 171
Figure 73: Coordinate system and definition of angles 172
Figure 74: Relative flux per pixel, produced at and near the glint spot for a water planet, thin atmosphere, no clouds. Planet is located at OL = 74°. a) parallel polarization, b) perpendicular polarization, same scale 182

List of Tables

Table 1: Common Radiometric Units 22
Table 2: Stokes parameters for unit intensity light with common polarizations. 33
Table 3: values of χ and corresponding values of Stokes Q and U 33
Table 4: Summary of Previous Work 55
Table 5: Selected values of planetary phase function 85
Table 6: Contrast ratios for Lambertian and ocean planets with thin atmospheres, planet with a dark surface and Rayleigh scattering atmosphere 87
Table 7: Sea foam and reflectance versus wind speed, after Koepke (1984). 96
Table 8: Verification matrix 103
Table 9: Expanded model and analytical radiant intensities and contrast ratios. 105
Table 10: Verification of rotation in 6SV - sign change in relative azimuth causes sign change in U 141
Table 11: Results of rotation using the derived formula 150
Table 12: Results of using the Tilstra rotation and the negative of the Tilstra rotation. 151
Table 13: OL of Polarization Peaks as Calculated by MATLAB Model (second peak symmetric about 180°). 179

Acknowledgements

Committee Members

To Dr. C. Russell Philbrick, who has guided my research and improved my writing; and who offered me a Research Assistantship in his Lidar Lab, and thereby an opportunity to fulfill my lifelong dream of obtaining the Ph.D.

To Dr. Timothy J. Kane, whose knowledge of optics, remote sensing, and proposal writing have proven invaluable, and whose encouragement and humor have helped keep me going.

To Dr. James F. Kasting, for offering me the best thesis project I could possibly imagine, the opportunity to model light scattering from extrasolar planets, and for helping me figure out how to accomplish it.

To Dr. Karl M. Reichard, who hired me into his Electro-Optics Group when the Swift satellite engineering effort was over, encouraged my pursuit of the Ph.D., and has found interesting projects for me to work on whenever my efforts to bring in work were insufficient.

To Dr. Charles Croskey, for his many astute comments on the manuscript, for helping me investigate potential thesis topics, and for providing sage career advice over the years.

To Dr. Thomas Jackson, who is one of those people who knows something about everything, for encouraging me to always consider the problem broadly.

Funding and Assistance

To Dr. Richard Stern, who provided educational funding from Penn State Applied Research Laboratory to finish this document.

To Dr. Vikki Meadows of the University of Washington and the Virtual Planetary Laboratory, and Dr. Carl Pilcher of the NASA Astrobiology Institute, who funded much of this research.

To Dr. Nick Woolf of the University of Arizona, who provided initial seed funding to get me started on this project.

To Dr. David Burrows of the Penn State Department of Astronomy, who hired me into the department to design x-ray cameras for space, and encouraged my work towards the Ph.D. during my years in his group.

To the Penn State Astrobiology Research Center, for providing knowledge, facilities, and the opportunity to meet and work with experts in astrobiology from across Penn State and around the world.

To Dr. Eric Vermote of the University of Maryland and NASA/Goddard for providing startup information on the 6SV code, and Dr. James Jenkins of Universidad de Chile for helpful discussions on determining planet association using polarization.

To Patrick Broos of the Penn State Astronomy Department, IDL expert, for providing information on IDL commands which were critical to the completion of this work.

The Center for Exoplanets and Habitable Worlds is supported by the Pennsylvania State University, the Eberly College of Science, and the Pennsylvania Space Grant Consortium.

Contracts

This work was performed under the following NASA Contracts: NNA04CC06A, NNX08A018G, and 463006 UNIWASH VPL (supported under solicitation NNH05ZDA001C).
.

Dedication

To my family, who have made it all worthwhile.

1.0 Introduction

1.1 Summary

1.1.1 Exoplanet observation and modeling

Since 1992 (Wolszczan and Frail 1992), astronomers have discovered nearly 500 planets[1] outside our Solar System, known as extrasolar planets, or exoplanets. These discoveries have been made primarily by indirect methods, in particular the radial velocity technique, which measures red and blue shifts of the parent star due to the gravitational pull of the planet. However, space telescopes now under development, specifically designed for planet-finding, will allow astronomers to capture light scattered directly from the exoplanets themselves.

In order to predict what these new instruments might see, and to help determine what observers should look for, we model the visible and near infrared scattering from hypothetical terrestrial-type planets with Lambertian, dark, and water surfaces, and a variety of atmospheres, as well as cases representing a water Earth. Each planet is assumed to be illuminated by a Sun-like star in an Earth-like orbit, seen edge-on from our vantage point, and scattering is modeled from new phase, through crescent and gibbous, to full phase. These cases are then used to determine how these different planet types can be distinguished based on absolute planet/star contrast ratio, orbital variation in contrast ratio, and orbital variation in polarization fraction of the scattered light.

1.1.2 The Search for Exoplanet Oceans

Although the presence of liquid water clearly does not guarantee the presence of life, it is considered to be one of the best indicators of habitability because it requires both a significant atmosphere and moderate surface temperatures, and because liquid water is considered to be necessary for life as we know it.

Note that modeling the scattering from exoplanets is a forward problem, but interpreting the signatures of exoplanets is an inversion problem, so exoplanet researchers need to use inversion techniques and consider how well-posed the problem is. By running models for a variety of cases, we provide a number of representative cases for observers to compare to their results.

[1] http://exoplanet.eu/catalog.php

1.1.3 Spherical geometry of exoplanet scattering

To model any star/planet system viewed from a fixed location, the complex spherical geometry of the incident and scattered radiation, as well as the temporal variability due to planet rotation on its axis and revolution about the parent star must be considered. A model developed by Darren Williams, which he graciously provided as a starting point for this work, included spherical geometry, terrain types, and polarization (Williams and Gaidos 2008). That original model did not include Rayleigh or Mie scattering by the atmosphere, or scattering from within the water column, and had no spectral component.

1.1.4 Exoplanet atmospheres

Large bodies of liquid water cannot be stable on a planet without an atmosphere. Therefore, in addition to modeling scattering from planetary surfaces, a realistic exoplanet scattering model must include the scattering effects of the exoplanet atmosphere. Atmospheric scattering introduces absorption, wavelength-dependent scattering, multiple scattering, and polarization effects, all of which affect the light received from these planets. In order to create realistic exoplanet light curves, we have included a detailed atmospheric scattering model.

We now describe the project hypotheses and goals. Project Milestones are listed in Appendix A.

1.2 Hypotheses

We propose the following hypotheses as a starting point for the research:

1. By using calculations, simulations, and prior measurements, we can anticipate terrestrial planet signatures in light scattered from distant solar systems.
2. Instrumentation coming on line (e.g. TPF-C[2], Darwin, and ground-based instruments) in the future will permit scientists to gather enough information on terrestrial exoplanets to draw useful conclusions about the planet surfaces and atmospheres.
3. TPF-C will have a baseline wavelength range of 500 – 1000 nm, and other instruments may have capabilities extending through the near infrared into the thermal infrared. These instruments will have some capability to observe in broad sub-bands of this range, even though there are not enough photons to discriminate spectral absorption or emission lines.
4. Light curves including polarization, possibly combined with broad-band spectral information, will provide enough information to discriminate between terrestrial-class planets with and without large oceans. Specifically, sufficient information can be gathered to discriminate between planetary scale oceans and diffusely-scattering land surfaces and clouds.

[2] TPF = Terrestrial Planet Finder, a group of proposed NASA missions to find and characterize Earth-sized extrasolar planets. TPF-C = Terrestrial Planet Finder – Coronograph, one of these mission concepts. Darwin is a proposed European Space Agency exoplanet finding mission.

5. Observation of polarized light curves of putative or known exoplanet systems may provide useful information about the systems beyond that from unpolarized brightness curves.

1.3 Goals

1. Describe observable differences that may be expected in end member terrestrial planet types by modeling polarization-dependent and wavelength-dependent scattering over TPF wavelengths 0.5 to 1.0 μm;
2. Provide input to designers of TPF and other planet-finding missions about what could be observed by instruments with various spectral and polarization characteristics, including making recommendations on possible inclusion of polarization measurement instruments, and optimum choice of spectral bands for detection of interesting species;
3. If justified, suggest modifications of TPF which could enhance the capability to meet the science goals;
4. Help motivate funding of TPF and other missions with predictions describing exciting potential results from an affordable mission.

Additional goals for future possible work:

5. Locate relevant data and use it to calibrate or verify portions of the model;
6. Propose to NASA for funding to study existing data from various Earth-observing missions, and perhaps missions to Mars and Venus, to uncover data that could be used to calibrate or verify the new model;
7. Eventually, produce a model capable of predicting signatures of any type of terrestrial planet.

1.4 Outline of Following Chapters

Chapters 2, 3, and 4 contain background material; Chapter 2 provides background on planets, both in our own Solar System, and in distant star systems. Chapter 3 is a review of electromagnetic scattering, and Chapter 4 is a summary of previous work in the field of light scattering from terrestrial planets, both polarized and unpolarized. Chapter 5 discusses the development of the model for this project, and Chapter 6 presents the results, discussion, and an overview of model verification. Chapter 7 summarizes the project and lists some ideas for future work. The Appendices include descriptions and listings of IDL and Fortran code developed for the project, and details of code verification.

2.0 Solar and Extrasolar Planet Background

Our Solar System contains a variety of objects, grouped broadly into the Terrestrial Planets (Mercury, Venus, Earth, and Mars), the Asteroids, including the dwarf planet Ceres, the Gas Giants (Jupiter and Saturn), and the Ice Giants (Uranus and Neptune). Beyond these are the Kuiper belt objects, including the recently demoted dwarf planet Pluto and its moon Charon, as well as the third dwarf planet Eris and uncounted comets and other objects; and extending far beyond the Kuiper belt, into the Oort cloud. Orbiting the eight major planets, there are now hundreds of known moons. As the number of known extrasolar planets (exoplanets) climbs beyond 500, the exoplanet community is focusing more on attempting to find terrestrial planets around nearby stars – the rocky, solid-surfaced planets with Earth-like masses and orbits – which are expected to have the best chance of harboring life. Figure 1 shows views of three very different terrestrial planets in our own solar system.

Figure 1: NASA views of Venus, Earth, and Mars (Venus and Mars from the Hubble Wide Field Planetary Camera, Earth from Apollo 17)

2.1 Exoplanets

2.1.1 Short History of Exoplanet Discovery

The first exoplanets were discovered by Alex Wolszczan (now at Penn State) in 1991 (Wolszczan and Frail 1992) while seeking to explain small changes they measured in the period of the pulsar PSR B1257+12. The authors found that the period variations were caused by orbiting planets. The first exoplanets around a main-sequence star were discovered by astronomers at the Geneva Observatory (Mayor and Queloz 1995) using the radial velocity method. Nearly all of the ~500 exoplanets discovered since then have been found using the same radial velocity method, in which multiple spectroscopic observations of the parent star are used to measure Doppler shifts (shifts in wavelength toward the red or blue) on the order of meters per second. Wobble of the parent star along the line of sight, toward and away from the observer, caused by orbiting planets, can be measured using this method, and planet parameters

such as orbital period and minimum mass are extracted. The team of Marcy, Butler, and Fischer discovered more exoplanets by the radial velocity method than any other researchers (see, e.g., (Marcy et al. 2005)). Since the inclination of the plane of orbit of the system is typically not known, the absolute mass of the orbiting planet cannot be measured by this method alone.

Another method of indirect detection, which can be used on nearby stars, uses high-precision astrometry to measure the wobble of the parent star in the plane of the sky. The astrometry method requires that the star be close enough compared to the amount of wobble that the star moves a measurable angle on the sky. Astrometry is insensitive to motion in the line of sight, whereas the Doppler method is insensitive to motion in the plane of the sky.

A third method measures drops in stellar brightness as a planet transits the parent star. Unlike the radial velocity and astrometry methods, the transit method provides some information on relative size of the planet. The transit method is limited to a relatively small number of planetary systems where we view the system directly edge-on. In 1999, the first extrasolar planet transit was observed (Henry et al. 2000). This planet was already known from the radial velocity method; in 2002 the first planet was discovered using the transit method (Udalski et al. 2002). Once current candidate planets are confirmed, the Kepler mission[3] is expected to more than double the exoplanet count using the transit method.

Other methods of indirect detection have been proposed and used; these include anomalies in gravitational microlensing by a star with planets, detection of anomalies in infrared radiation from circumstellar disks, and variability in minima of eclipsing binary stars as a planet orbits them. See Perryman (2000) for a more complete description of the different methods of exoplanet detection.

2.1.2 First Direct Detections

In November 2008, two groups announced in Science Express that they had directly imaged the first confirmed extrasolar planets in two different star systems.

1) Christian Marois of the Herzberg Institute for Astrophysics, in Victoria, B.C. (Canada) led a team of Canadian, US, and UK astronomers using the Keck 10 m and Gemini 8 m telescopes on Mauna Kea (Hawaii) to image three planets circling HR 8799[4], as shown in Figure 2 (Marois et al. 2008). This 5th magnitude A-type star is 130 light-years from Earth, and lies just inside the square of Pegasus, on the side of the constellation near Andromeda. The three planets are in orbits of approximately 24, 38, and 68 AU radius, have masses between 5 and 13 Jupiter masses, and are believed to have orbital periods of roughly 100, 190, and 450 years, respectively (see Figure 3). The team observed the new planets in the near infrared range 1.1 to 4.2 μm using the NIRC2 (Keck) and NIRI (Gemini) instruments.

[3] http://kepler.nasa.gov/

[4] HD = Henry Draper. The brighter stars have multiple names from various catalogues. Vega, for example, is also known as α-Lyrae because it is the brightest star in Lyra, as HR 7001 in the Harvard Revised catalogue, as HD 172167 in the Henry Draper catalogue, as BD+38° 3238 in the Bonn Survey, as SAO 067174 in the Smithsonian Astrophysical Observatory catalogue, as HIC 91262 in the Hipparcos Catalog, and as P3X1874 in the Cartouche.

2) Paul Kalas of the University of California, Berkeley, led a North American team using the Hubble Space Telescope along with the Keck 10 m and Gemini to image a planet (primarily at 0.6 and 0.8 μm) circling Fomalhaut in the Southern Hemisphere constellation Piscis Austrinus (Kalas et al. 2008). Fomalhaut is another A-type star which is 25 light-years from Earth, and the newly discovered planet is a three-Jupiter-mass object which orbits about 119 AU from the parent star, see Figures 4 and 5. An October 2008 preprint (Lafrenière et al. 2008) suggested that an eight-Jupiter mass exoplanet at 330 AU may have been imaged, but the authors admit that further observations will be necessary to confirm that the planet moves with the star. By comparison, Uranus is only 30 AU from the Sun.

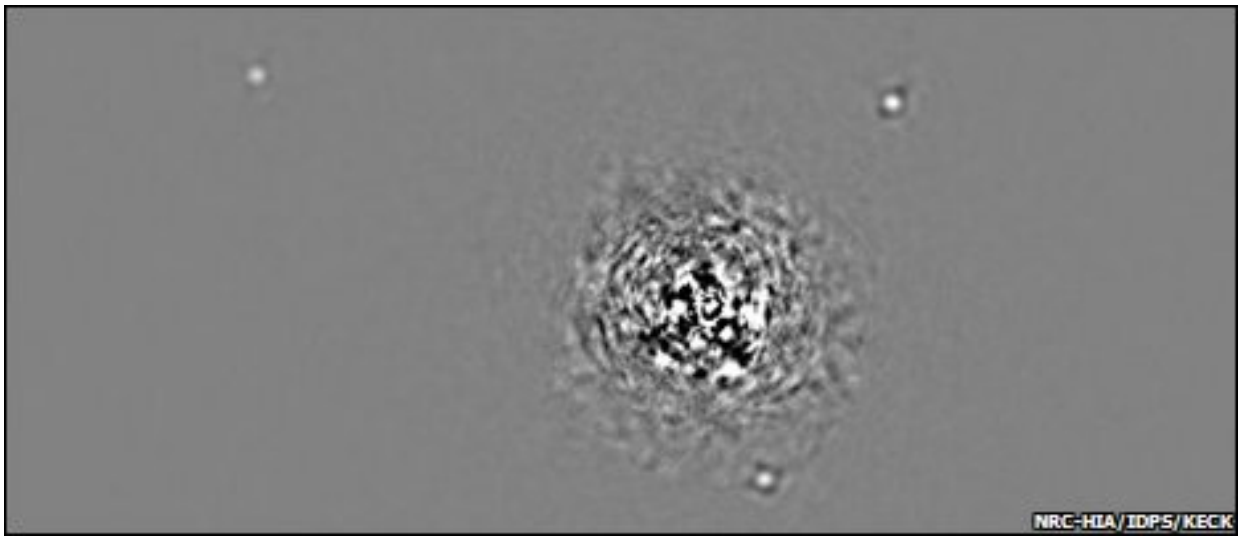

Figure 2: Image of HR 8799 star system including three planets (Marois et al. 2008)

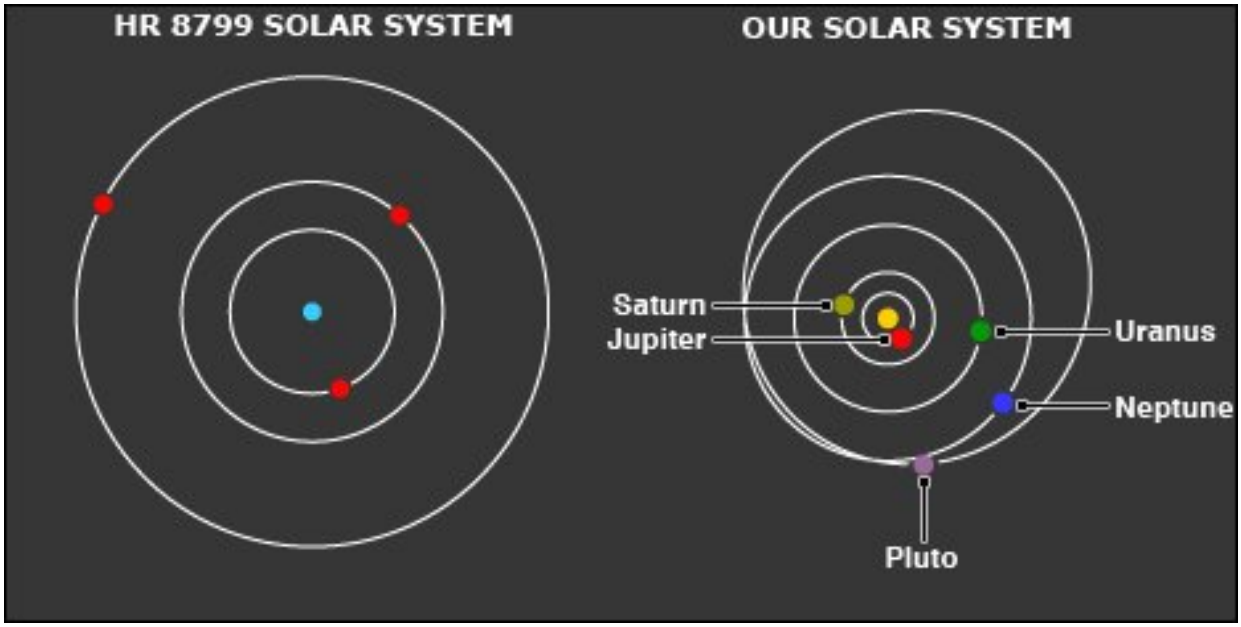

Figure 3: Size comparison of the HR 8799 star system with the Solar System (Marois et al. 2008)

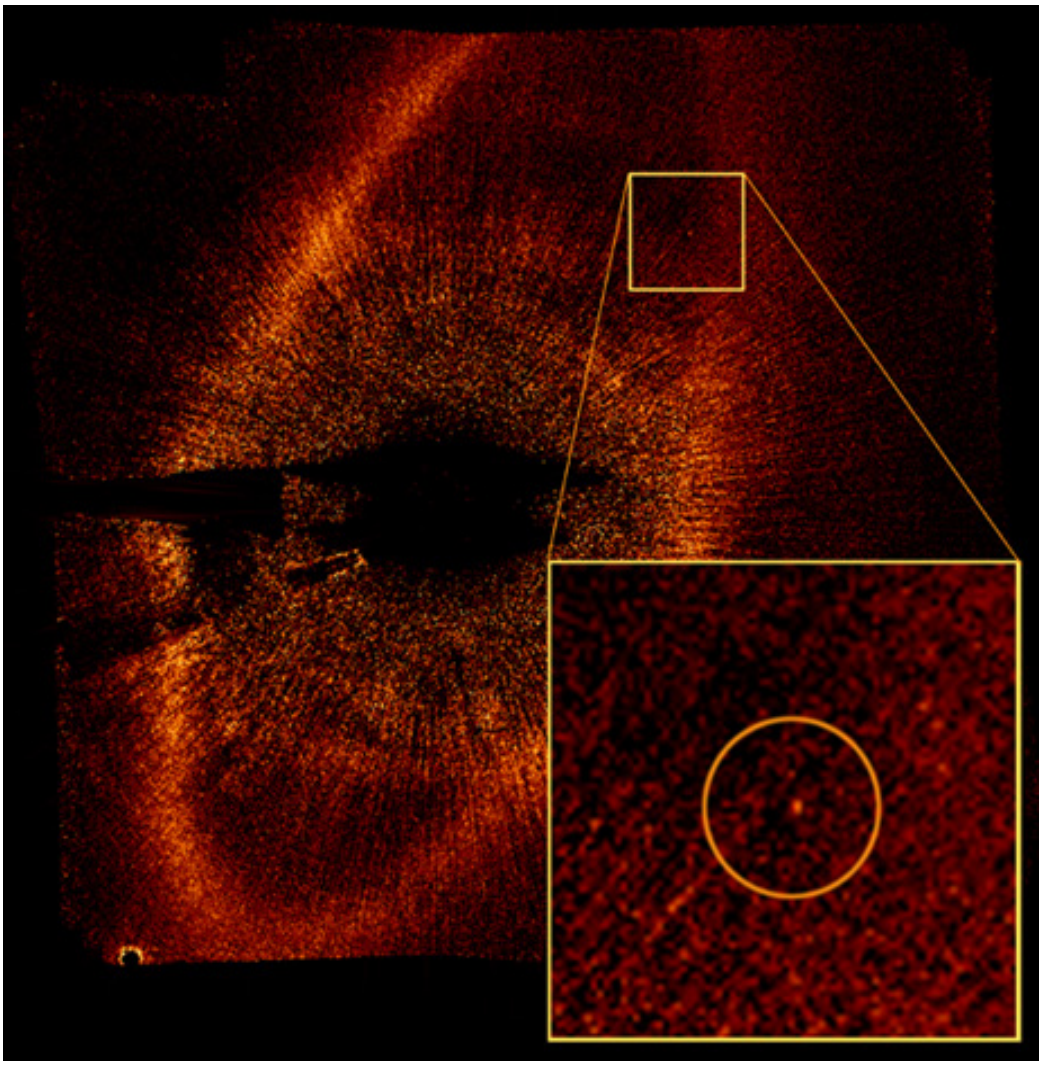

Figure 4: Image of Fomalhaut b in coronograph image (Kalas et al. 2008)

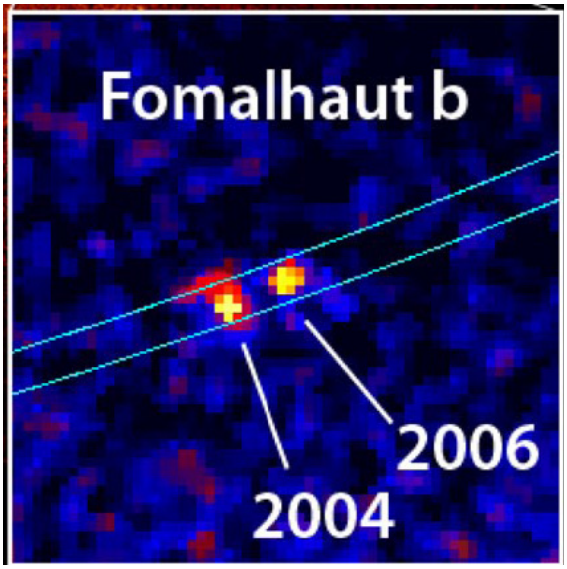

Figure 5: Image of Fomalhaut b showing progress around the orbit (Kalas et al. 2008)

The imaging of planets many light-years from the Earth from both the ground and space is a spectacular achievement -- but what of Earths? These planets are all multiple Jupiters in size, and Jupiter is roughly 300 times the mass of Earth. Although it is conceivable that continuing advancements in adaptive optics may someday allow us to almost completely cancel out the effects of Earth's atmosphere, it seems likely that only a larger space observatory with a better coronograph will have the capability to image Earth-like planets in the presence of Sun-like stars. Also, it will be difficult or impossible to look for biomarker gases through Earth's atmosphere.

2.2 The Search for Life Beyond Earth

The modern search for life within the Solar System concentrates primarily on possible subsurface life on Mars and Europa, along with the chance for chemically exotic life based on liquid or aerosol hydrocarbons on Titan or in the clouds of the gas giants. Portions of this section are based on a presentation by James Kasting (Kasting 2009).

2.2.1 Life Within the Solar System

When looking for life "nearby," astrobiologists try to minimize a priori assumptions about the nature of the life that may be found, and explore all possibilities of evidence for life. Within the Solar System, we can collect much more information, up to and including bringing samples back to Earth, so we may be able to identify life in our planetary neighborhood that is vastly different from that on our home planet.

On Mars, the large number of water-based deposits found by the rovers Spirit and Opportunity, and by several Mars orbiters, shows that liquid water has existed for periods of Mars history. Although the low surface temperature and pressure on modern-day Mars prohibit pools of liquid water from being stable at the surface, Mars is heated from within by radioactive decay (as is Earth), so at some point a kilometer or two below the surface, liquid water pools may exist. The Viking missions from 1976-77 attempted to incubate Martian soil and look for metabolic by-products. Although initial results showed some sort of activity, only a handful of researchers cling to the hope that Viking discovered life in the Martian subsoil. The conventional wisdom is that the activity seen by Viking was actually soil chemistry. However, recent work by several groups, including Mumma et al. (2009), suggest that methane is being produced by biological activity in the Martian soil. These claims are based on parts-per-billion level detections of methane on Mars using Earth-based instruments, with large local variability and a hypothesis of short lifetime of methane in the Martian atmosphere; so far the scientific community is generally skeptical, but if true, this would represent the first detection of extraterrestrial life. On the other hand, we know that Earth and Mars have swapped asteroids, so detection of life on Mars would not necessarily indicate a second origin of life.

The Galileo space probe measurements of the magnetic field in the vicinity of Europa on multiple flybys proved that Europa's magnetic field direction depends on, and tends to oppose, that of Jupiter, which requires that a conductor exists on or below the surface of Europa. Based

on composition, theories of formation, and observations of the surface of Europa, it appears that the only likely candidate for this conductor is a liquid water ocean (or water-ammonia mixture) under the surface ice. Observations and theory are currently unable to estimate the thickness of the ice, however, so NASA would like to send two probes to Europa – the first to determine if the ice is thin enough to be able to get through (less than a kilometer or two), and given a thin-ice result, a second probe to land on the surface and melt its way through the ice into the ocean beneath to explore the Europan ocean. Other ideas for more exotic life, perhaps based on liquid hydrocarbons instead of water, include microbes in the organic haze of Titan, and floating organisms in the clouds of Jupiter or Saturn.

2.2.2 Life Beyond the Solar System

As we search for evidence of other life in the galaxy, and likely homes for life, smaller, rocky planets at a comfortable distance from the parent star - Earth-like planets - remain difficult to find. Also, in contrast with searching for life in the Solar System, when we search farther away we face more constraints and must limit our search. Of course, we cannot sample exoplanet soils or send probes through ice caps. Additionally, we are constrained to sample the entire planet as a single pixel, and we will be limited to very broadband spectroscopy because of the scarcity of photons. As a result of these and other limitations, the search for life beyond our Solar System must, as a practical matter, concentrate on finding Earth-like planets, until such time as we develop the technology to travel to other star systems.

Habitable Planets. The concept of a Habitable Zone (HZ) around a star[5] was first discussed by Harlow Shapley, who called it the "liquid water belt" (Shapley 1953). The concept is based on the ideas that

1) for a planet to be habitable, it must have a surface temperature suitable for the presence of liquid water, and
2) this will, barring exceptional heating from within, require the planet to reside in an orbit at the correct distance from a star – too close and the oceans will boil off, too far and the oceans will freeze.

The concept was further developed by Michael Hart (1978), who used a simple climate model to explore the size of the HZ. Hart also suggested the idea of a Continuously Habitable Zone (CHZ), which is a subset of the HZ based on stellar evolution. As normal stars (that is, stars on the Main Sequence of the HR diagram) progress through stellar evolution, the conversion of hydrogen to helium in the core causes the density of the core to increase, requiring the rate of fusion to increase over time in order to maintain hydrostatic balance. As a result, Main Sequence stars become progressively hotter and brighter over time. The power output from the Sun has increased about 30% since its birth about 4.6 billion years ago. For our purposes, the impact is that the HZ of a star migrates slowly outward over time, so that the range of orbits in which a planet such as Earth would remain continuously habitable over the life of the planet to date is considerably smaller than the HZ at any given time. Hart concluded from his model that Earth is in a very rare orbit, and that the CHZ for Earth to date is only from 0.95 to 1.01 AU. His model

[5] The concept of a habitable portion of a galaxy, a "Galactic Habitable Zone," has also been suggested.

also predicted that other types of stars would have even smaller HZs, and his conclusion was that Earth may be the only habitable planet in the galaxy.

Hart's model did not properly include climate-stabilizing feedback mechanisms that we now know are present in the Earth system. Work by Walker, Hays, and Kasting (1981) and later Berner and colleagues (1983) emphasized the importance of the carbonate-silicate cycle in habitability (see Figure 6). This cycle, which is based on the Earth's tectonic and volcanic activity, provides a negative feedback mechanism to stabilize our climate. Referring to the figure, carbon dioxide produced by volcanoes enters the atmosphere over time, and is removed by rainwater which dissolves it to form carbonic acid. This weak acid rain falls on land surfaces and dissolves calcium silicates and other alkaline rocks, carrying carbonate ions into the ocean. Living organisms in the ocean extract calcium carbonate to form shells, some of which reach the bottom of the deep ocean when the organisms die. Due to seafloor spreading and subduction, some of these carbonates are recycled into the Earth's mantle to be released later as carbon dioxide.

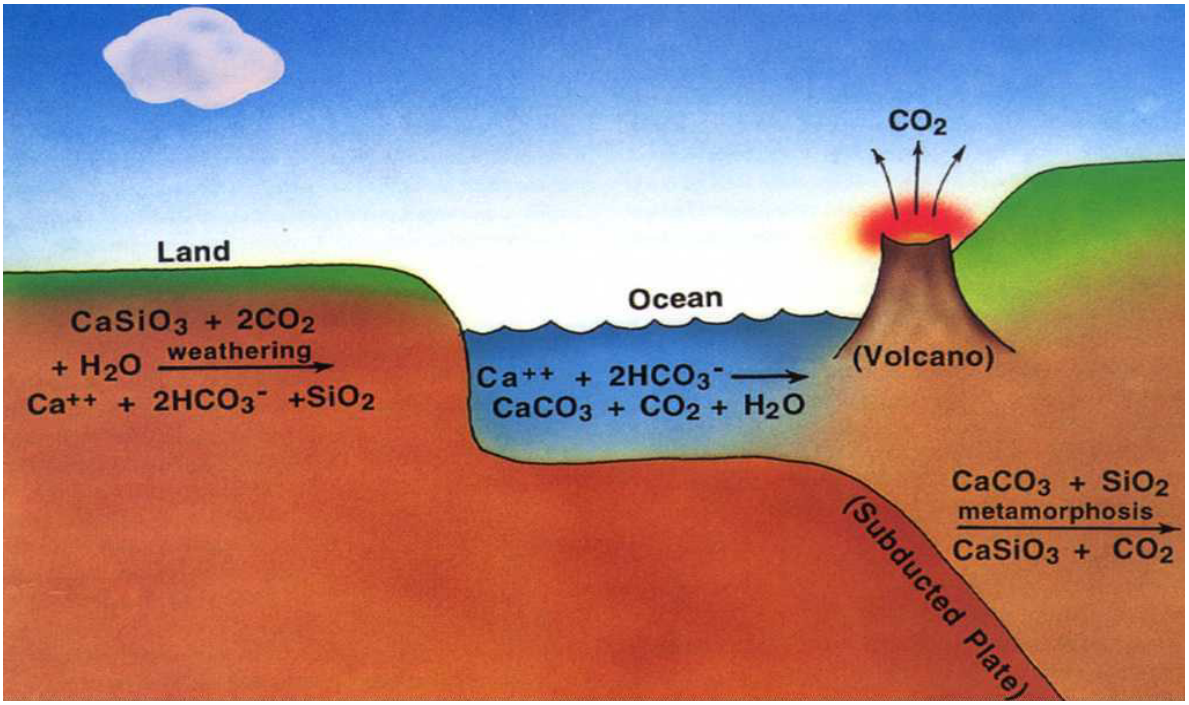

Figure 6: Carbonate Silicate Cycle (Kasting et al. 1993)

An increase in surface temperature causes negative feedback due to both increased chemical weathering rates and increased evaporation, which in turn causes increased rainfall and again more weathering. Likewise, in the case of a snowball Earth or other large glaciation event (Harland 1964; Sumner et al. 1987; Hoffman and Schrag 2002), evaporation, rainfall, and surface weathering are all reduced, but volcanic activity continues unabated (the Earth's interior will continue to produce volcanic gases without regard to a 1 km coating of ice on the surface), and the resulting buildup of carbon dioxide causes a greenhouse effect which eventually becomes large enough to melt the glaciers. Without the carbonate-silicate cycle, previous workers had concluded that the positive feedback of high-albedo glaciers advancing to lower

latitudes, causing further cooling, would lead to a runaway glaciation from which the Earth (or other terrestrial planet) could never escape.

James Kasting and colleagues (1993) used a 1D climate model to show that the carbonate-silicate cycle expands the habitable zone out to at least 1.37 AU, and the continuously habitable zone to 1.15 AU over the history of the Solar System to date; the limit occurs where the formation of carbon dioxide clouds increase planetary albedo and cancel the greenhouse effect. Figure 7 shows the HZ of the Sun soon after it formed (Zero Age Main Sequence) with the addition of climate feedback and other newer data (Kasting et al. 1993).

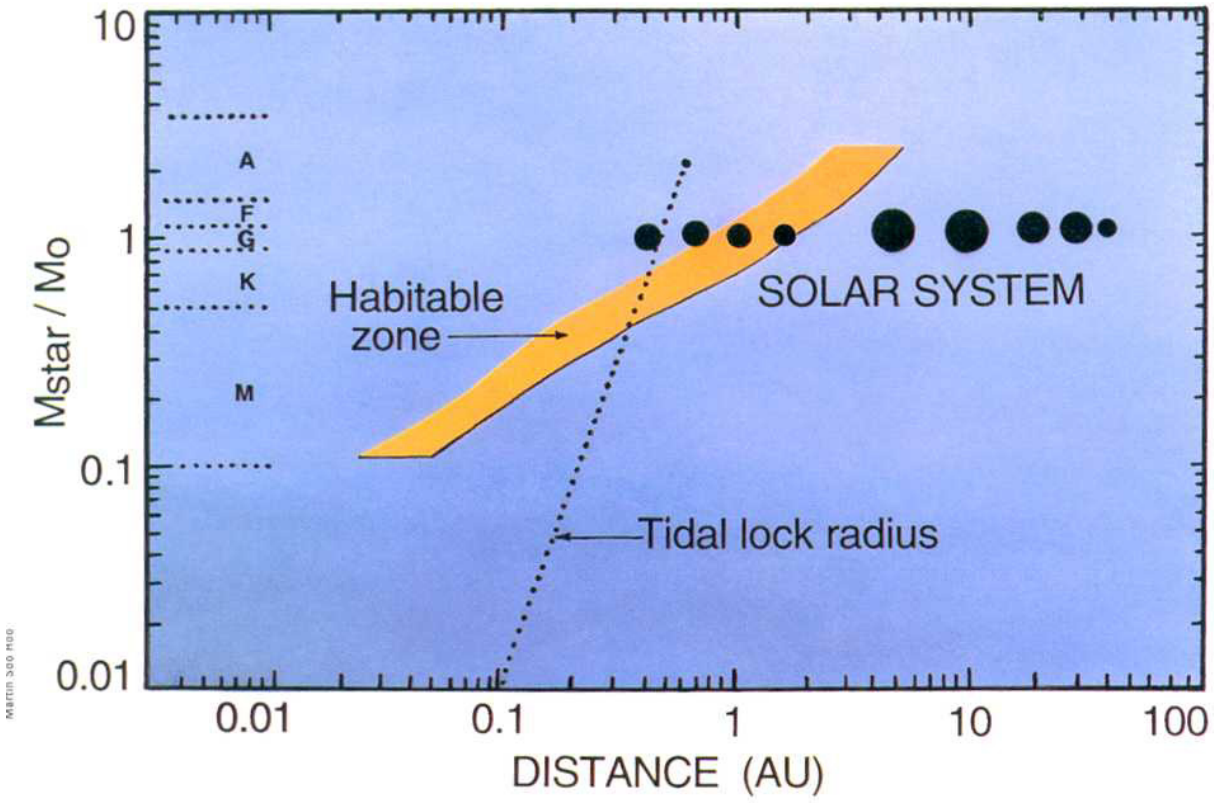

Figure 7: Habitable Zone relative to conditions in our Solar System with consideration of CO_2 feedback (Kasting et al. 1993)

Note that models show that for other star types, HZs may have problems; for hotter O, B, A, and F stars, the ultraviolet flux may be high enough to sterilize planets in the HZ, and these stars have shorter lifetimes on the main sequence; for cooler K and M stars, the HZ is close enough to the star that any planet would become tidally locked. Tidal locking includes both the case where the orbiting body always shows the same face to the star, as the Moon does to Earth, but also includes cases where the orbiting body rotates in a 3:2 or other resonance and so does not always show the same face. For example, Mercury rotates three times on its axis for each revolution around the Sun, so it is tidally locked but does not always show the same face to the Sun. This could cause any liquid water to boil off the hot side and freeze out on the dark side. With sufficient heat transport, however, such a planet might be habitable. Terrestrial planets around

M stars are also easier to find, because the planet exerts enough pull on the smaller M star to make the Doppler method of detection practical.

Further work by Kasting and collaborators has pointed to methane (Pavlov et al. 2000) and nitrogen oxide (Roberson et al., in preparation) as other possible greenhouse gases with a significant effect on the HZ. Somehow, liquid water seems to have been stable on the surface of Mars early in its history (based in part on the finding of iron "blueberries" by the rovers (Squyres et al. 2004), and climate modelers are having difficulty finding a way to make this happen in the face of a significantly dimmer Sun.

In addition to the discovery that Mars probably had a habitable, wet climate and even oceans for roughly 200 Myr, recent modeling efforts have suggested that water planets may be fairly common in the galaxy. In particular, work by Raymond along with Penn State collaborators Sigurdsson and Mandell (2006) showed that giant planets migrating inward in a system may stimulate the formation of water Earths both within and outside of the giant planet orbits. They predict that more than 1/3 of the giant planet systems known at the time may contain Earth-like planets in the HZ with low eccentricities. The presence of two planets with large oceans in our own Solar System, and models showing there may be many water planets even in systems very different than our own, lends support to the idea of searching for global oceans on nearby exoplanets.

2.3 Planet Finder Missions

The Doppler/Radial Velocity method of planet finding has found nearly all of the 500+ extrasolar planets found to date, but the technique is limited by the fact that Earth-mass planets produce very little wobble in the parent star, thus exhibit only a small Doppler shift. In order to find Earth-like planets, both NASA and ESA have plans to develop space-based observatories based on three other techniques: astrometry, transits, and direct observation.

2.3.1 Astrometry

Astrometry is locating the position of a star on the apparent dome of the sky to high-precision. First practiced by observatories such as the Royal Observatory in Greenwich, England (the origin of GMT), for use in generating navigation tables to determine longitude, astrometry in this case means measuring stellar positions and motion to the accuracy of detecting side-to-side wobble of the star. Astrometry avoids some of the inherent limitations of the Doppler radial velocity method, such as seismic and fluid movements in the star which are effectively noise in determining wobble. Also, astrometry allows determination of the plane of the orbit, so the masses reported are actual masses, rather than minimum masses $m \sin i$ reported by the radial velocity method. The Space Interferometry Mission, SIM, which has been postponed after completion of part of its development, would use this type of detection. SIM would obtain resolution of 0.6 micro-arcseconds, which is sufficient to detect Earth-like or slightly larger planets (Unwin 2009). SIM was not selected by the 2010 Decadal Survey committee, but a SIM-like mission called NEAT (Nearby Earth Astrometry Telescope) is being proposed to ESA.

2.3.2 Transits

The Kepler mission[6], launched in March 2009, is a 0.95 m telescope specialized for detecting transiting Earths (see Figure 8). The spacecraft stares at a patch of the Milky Way galaxy in the constellation Cygnus the Swan (see Figure 9), and simultaneously monitors the brightness of about 150,000 stars, watching for transits. The spot is chosen to be away from the enormous clouds of gas and dust in the galactic plane, close enough to the galactic plane to have a high angular density of stars, but sparse enough that the stars can be individually resolved. Kepler does precision photometry, that is, measurement of brightness, and is capable of detecting changes in stellar brightness of 10^{-5} (1 part in 10^5). Earth's diameter is about 1% that of the Sun, so a transit by Earth seen from a distance would result in a brightness drop of 10^{-4}, a factor of 10 above the detectablility threshold of Kepler.

Figure 8: Artist's conception of the Kepler spacecraft (NASA/Ames)

Note that, in order to observe a transit, the observer must be in a position to view a star system edge-on. The chance of being in the correct position to view a transit for any given randomly-oriented system is equal to the radius of the star divided by the radius of the planet's orbit. For the Earth-Sun system, this is

$$R_{Sun}/1 \text{ AU} = 700{,}000 \text{ km}/150{,}000{,}000 \text{ km} = 5 \times 10^{-3} = 0.5\%. \quad (1)$$

for a planet in a circular orbit. So statistically, only one out of every 200 single-planet star systems with Earth-like planets at 1 AU will have the correct orbital inclination to observe a transit from Earth, and such transits will occur about once per Earth year. Hence, in order to get a significant number of "hits", Kepler needs to observe many stars. In fact, this estimate is somewhat optimistic, because probably not every star observed will have an Earth-like planet, and many of the stars in Kepler's field are hotter A-type stars, which means a habitable planet would need to be much farther from the star. This increases the denominator in Equation (1),

[6] http://kepler.nasa.gov/

resulting in the Kepler team predicting 50 Earth-like planets observed in transiting orbits. Three observed transits of a planet are required to confirm that transits are being observed, so two to three years of observations are needed for 1 AU orbits.

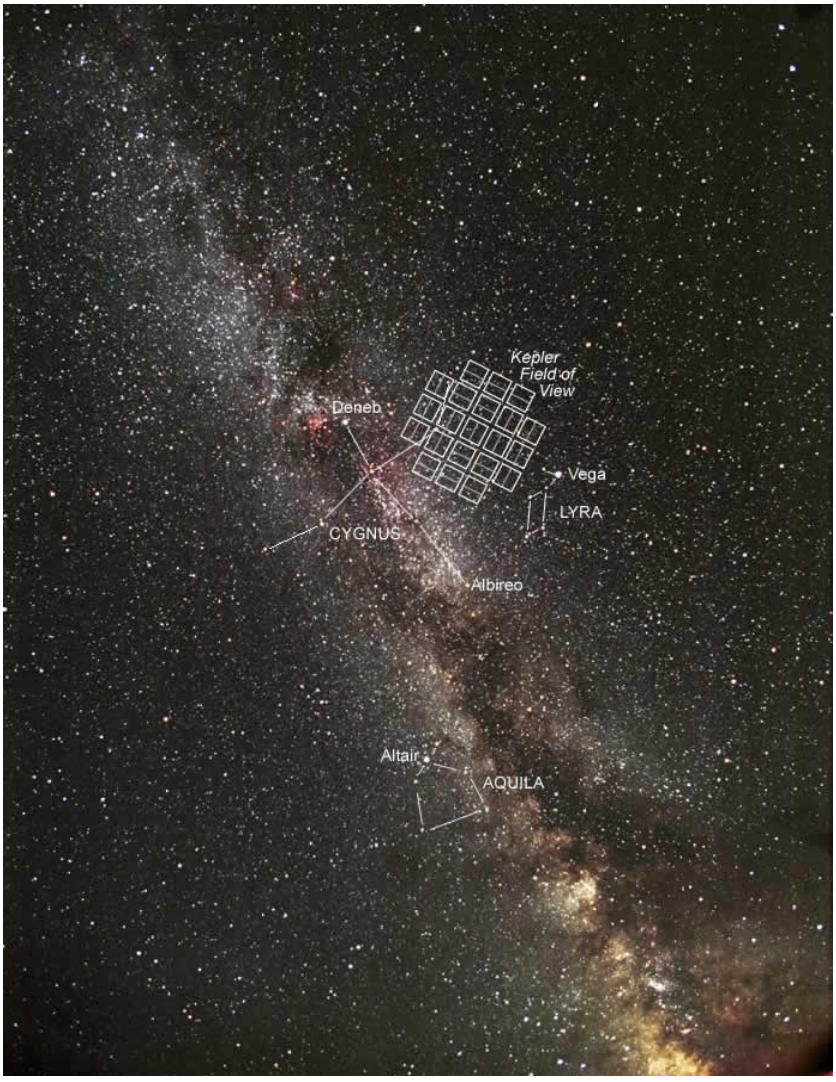

Figure 9: Kepler field of view in the northern hemisphere summer sky (NASA)

2.3.3 Direct Detection of Terrestrial Planets

NASA is considering development of a space-based observatory, called the Terrestrial Planet Finder (TPF), specifically designed to find habitable planets around other stars using direct detection. Figure 10 shows the magnitude of the signal-to-noise problem. The light curve versus wavelength for the Sun and Earth are shown together on logarithmic axes (Beichman and Velusamy 1999). The sunlit Earth reflects the Sun's insolation, attenuated by a factor of about 10^{10}, giving a planet/star contrast ratio of about 10^{-10}. In the thermal infra-red the Earth's black-body radiation peaks, and the Sun's starts to drop off, so in this waveband the contrast ratio is

"only" about 10^{-7}. Contrast ratios are significantly affected by planet surface type, atmosphere, and clouds, as well as stellar properties, but in general the contrast ratio for potentially habitable planets is more favorable in the infrared.

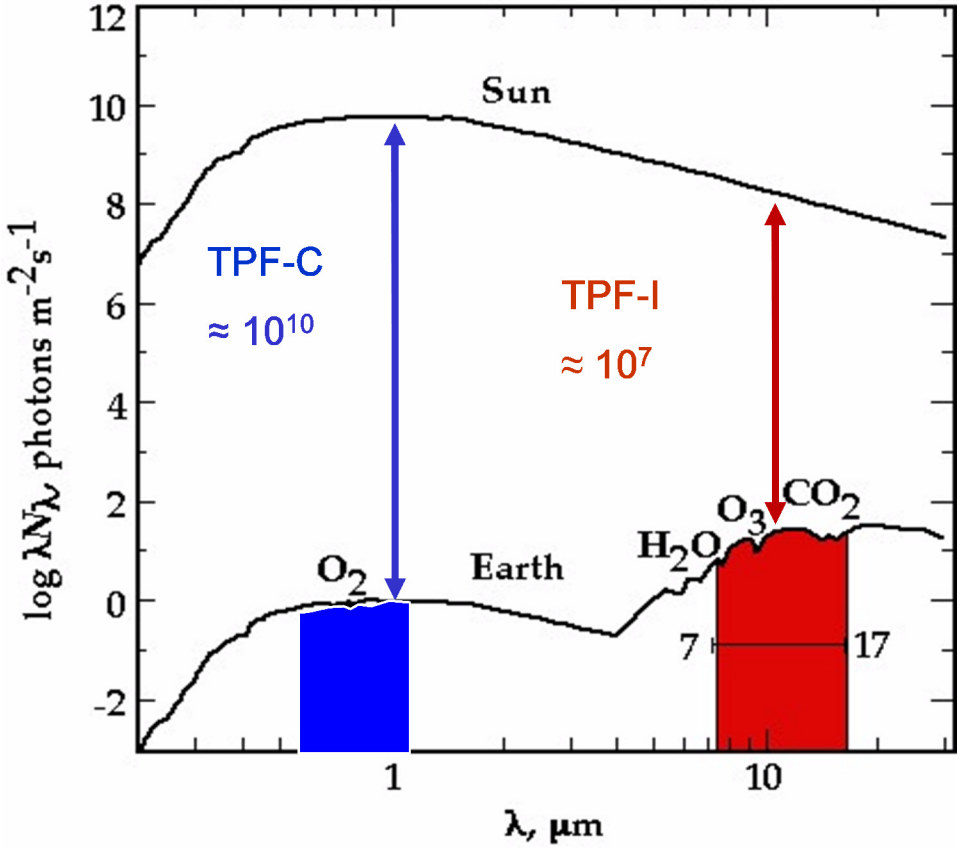

Figure 10: Contrast ratios for proposed visible (TPF-C) and infrared (TPF-I) NASA planet finder spacecraft (Beichman and Velusamy 1999)

The above argument is an important consideration in the conceptual design of the TPF. Two designs under consideration are a visible/near-IR coronagraph, TPF-C (Traub et al. 2006), and a thermal-infrared interferometer, TPF-I (Lawson et al. 2006). Based on contrast ratio, the TPF-I concept appears superior, however the interferometer would require four spacecraft with IR telescopes flying in nearly perfect formation, feeding a fifth combiner spacecraft, also flying in nearly perfect formation. The cost of such a spacecraft fleet would be staggering.

A recently proposed modification of TPF-C is the Occulter, a roughly 50 m diameter disk which will fly in formation with TPF-C, at a distance of 50,000 to 70,000 km (Cash 2006; Cash et al. 2007). The Occulter will be positioned to block the light of the parent star, while allowing light from the planet to reach the telescope. The combination of the two proposed spacecraft is now called TPF-O. Here, two spacecraft need to fly in formation, but not to quite the same tolerance, and one of the spacecraft is simply a moveable light stop. Note that precisely positioning the occulter for each new star will take a significant amount of time and propellant, so it has been suggested that SIM should be launched first in order to determine the best targets for TPF. However, as previously mentioned, SIM is unlikely to be launched.

The European Space Agency (ESA) has also considered an infrared interferometer mission similar to TPF-I, called Darwin[7] (Kaltenegger and Fridlund 2005), however this mission also seems unlikely to receive further funding. A pathfinder mission for Darwin called PEGASE (a French acronym) is currently on hold (Ollivier et al. 2006).

These upcoming NASA and ESA missions will provide both a quantitative and qualitative advance in exoplanet discovery. The qualitative change these observatories will bring is that they will permit the first direct detection of light scattered by terrestrial exoplanets, instead of detection of changes in the spectrum, position, or brightness of the parent star. (The Marois and Kalas teams have directly imaged exoplanets from Hubble and the ground, but these are multiple-Jupiter mass giants, not terrestrial planets.) In preparation for these missions, and as a necessary part of the design effort, the planetary astronomy community has begun the task of modeling the returns from exoplanets we can expect to detect with TPF and Darwin.

2.3.4 Diffraction and Coronagraphs

When a plane wave passes through an aperture, diffraction is observed on the other side. Light from a distant star enters the telescope objective as approximately a plane wave, and forms an image consisting of a central disk (Airy disk) surrounded by diffraction rings. This diffraction pattern limits the resolution of the telescope. When attempting to image extrasolar planets around much brighter stars, the problem is much worse – the disk and diffraction rings from the star, 10^7 to 10^{10} times as bright as the planet (as we saw in Figure 10) obliterate the image of the tiny, faint terrestrial planet. There are two potential optical solutions: 1) use a coronagraph, which is an optical element within the telescope, or 2) use an occulter, an optical element external to the telescope. In either case, the optical element is designed to block the star's light and minimize the diffractive interference described above. A small community of coronograph designers continues to perfect coronograph designs. See, for example, the work by Marc Kuchner and colleagues (Kuchner and Spergel 2003). As another example, a researcher with the Subaru Telescope (Guyon 2003) has proposed a technique he calls phase-induced amplitude apodization (PIAA) which should produce a contrast ratio of greater than 10^9 with a distance less than $2\lambda/D$ from the optical axis. The alternative design, an external occulter such as that mentioned earlier, would be much more expensive, but also more effective, because the star's light is intercepted and blocked before it enters the telescope. With the coronograph, the blocked light is already inside the telescope, and the inevitable scattering (even from flat black surfaces) limits the maximum contrast ratio.

[7]For more information on these missions, see http://en.wikipedia.org/wiki/Extrasolar_planet

2.3.5 Biosignatures

Astrobiologists have suggested a number of things to look for in extrasolar planets as clues to the possible presence of life. If it is possible to take low-resolution spectra of terrestrial exoplanet atmospheres with TPF, here are a couple of things we could look for:

1. James Lovelock (Lovelock 1972; Lovelock and Margulis 1974) pointed out that methane and molecular oxygen are out of thermodynamic equilibrium by 20 orders of magnitude in the Earth's atmosphere, as a result of photosynthesis producing oxygen, and methanogenic bacteria and other life producing methane. It seems extremely unlikely that a planet would have a similar situation in its atmosphere without the presence of life on that planet, so the presence of large amounts of oxygen and significant methane in a terrestrial planet spectrum might be considered a biomarker. The 1990 flyby of Earth by the Galileo spacecraft demonstrated the practicality of detecting oxygen and atmospheric methane far out of equilibrium (Sagan et al. 1993). Figure 11 shows the thermal infrared spectra of Venus, Earth, and Mars; the carbon dioxide bands are similar, but the Earth's spectrum includes water vapor absorption bands as well as a deep ozone absorption feature. (Kasting et al. (1993) discusses the impact of carbon dioxide levels on the outer edge of the habitable zone, including the upper limit where carbon dioxide clouds begin to form and start to cool the planet.) Figure 12 shows the visible spectrum of Earth, including the oxygen band at 760 nm labeled "b-X" but also sometimes referred to as the oxygen A-band. The presence of significant ozone in an atmosphere requires the presence of significant oxygen at lower levels, making ozone also a potential biomarker near 9.5 μm.

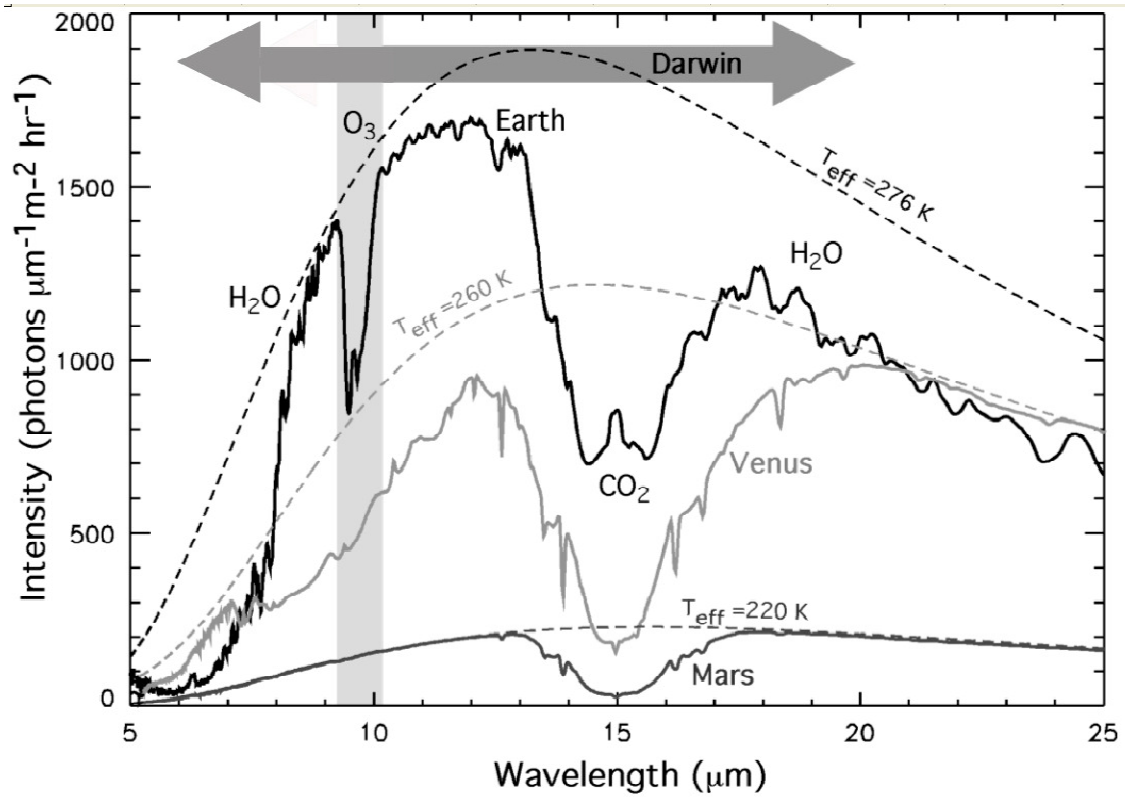

Figure 11: Infrared spectra of Venus, Earth, and Mars from Cockell et al. (2009), using spectra from a number of previous papers (Meadows and Crisp 1996; Tinetti et al. 2006; Tinetti et al. 2006; Kaltenegger et al. 2007; Selsis et al. 2007)

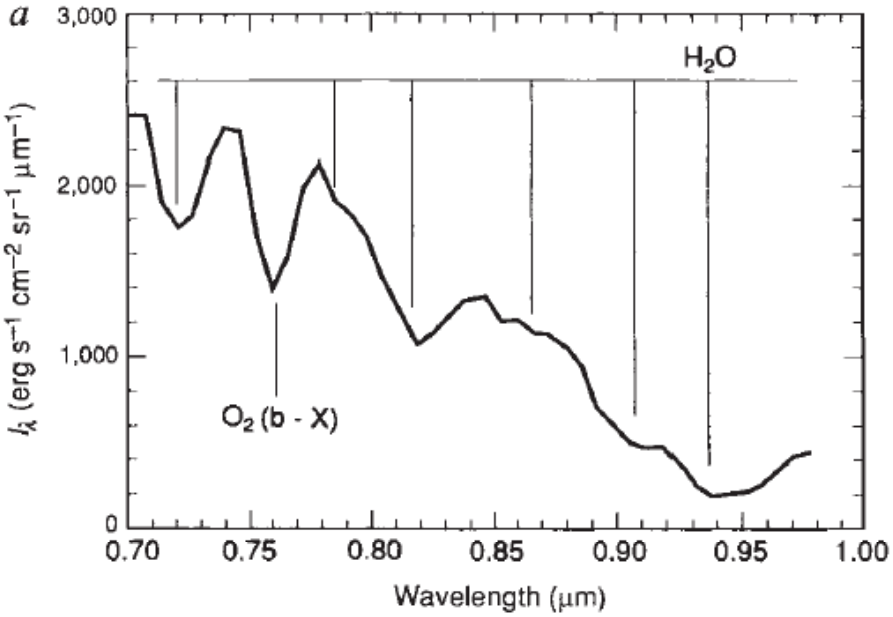

Figure 12: Galileo visible spectrum of Earth's atmosphere showing oxygen band (Sagan et al. 1993)

2. N. Kiang and colleagues (Kiang et al. 2007) pointed out that, because green plants reflect near infrared radiation starting around 700 nm, it might be possible to see the "red edge" of plants on a planet covered with chlorophyll-based plant life (Figure 13). Plants on Earth reflect this band because absorption would cause undesired heating of the plant, and the photons in this range have insufficient energy to be used for photosynthesis. The mechanism is a layer of air bubbles just under the leaf surfaces which are the correct size to reflect the near IR. There may be problems with using this for detecting life, however; on Earth, the red edge is difficult to see in the integrated light from Earth, mostly because reflection from the 70% of the surface that is ocean has little of the red edge effect. Also, there may be many other ways that photosynthetic plants might evolve, some of which might use near IR photons for photosynthesis or simply absorb them to keep warm.

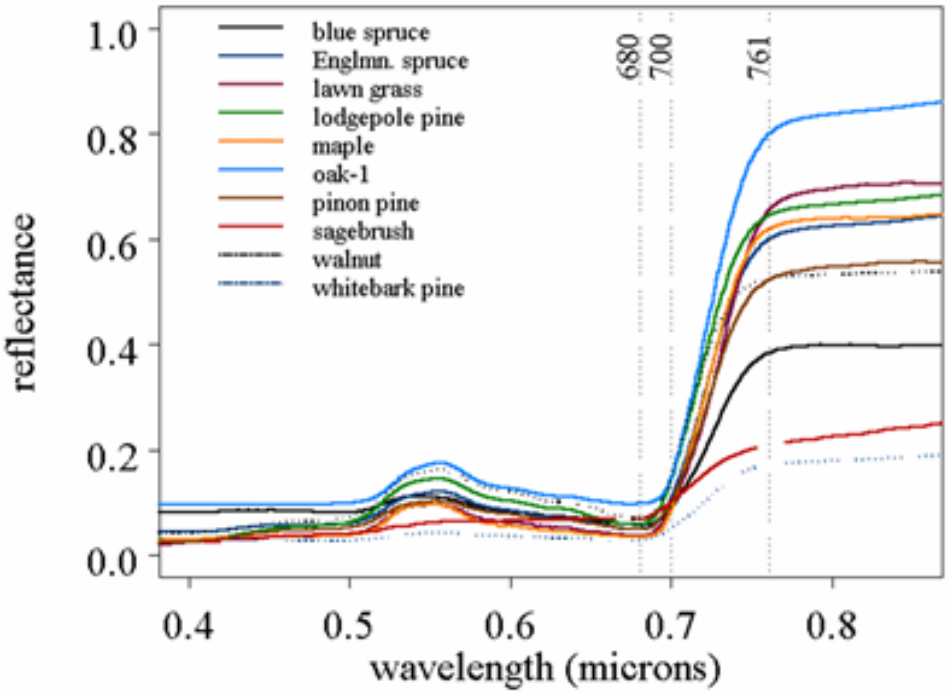

Figure 13: The "Red Edge" of chlorophyll for land plants (Kiang et al. 2007)

2.3.6 Water and Extraterrestrial Life

Liquid water is not a biosignature, and finding it would not prove the presence of life on another planet; however, water is essential to life as we know it, and on Earth there is life in nearly every environment where liquid water is present. The presence of liquid water on a planet does indicate the presence of a significant atmosphere, and fairly moderate temperatures. Note that the presence of other phases of H_2O on a planet says nothing directly about habitability; water vapor has been detected in the atmosphere of Jupiter (Bjoraker et al. 1986) among other planets, and water ice is believed to exist in dark craters on Mercury (Slade et al. 1992) and near the Moon's south pole (Feldman et al. 1998).

Previous work has shown that water vapor is sometimes detectable in exoplanet atmospheres. Water vapor was recently detected in the atmosphere of the giant exoplanet HD 209458b during transit using secondary transit spectroscopy in the thermal infrared (Barman 2007). Furthermore, a recent paper suggests that water droplets could be detected in an exoplanet atmosphere due to polarization at the "rainbow scattering angle," which equates to a phase angle of 40^{o} (Bailey 2007).

Detection of water vapor is a high priority both for the TPF missions and for Darwin. Several water vapor bands are available in the visible/near-IR, and a well-designed TPF-C should be able to observe these on a suitable target planet (Des Marais et al. 2002). Proving that liquid water is present on the planet's surface is more difficult, as a planet's surface temperature cannot be measured directly at these wavelengths. A TPF-I or Darwin interferometer might be able to measure the surface temperature of a target planet if the planet's atmosphere is optically thin in the 8-12 μm "window" region where H_2O and CO_2 absorption is low (Des Marais et al. 2002). However, this last criterion is unlikely to be satisfied on all nearby terrestrial exoplanets; even for those planets where we can measure surface temperature, what we know of biological processes suggests that an arid world with moderate temperatures may never give rise to life (Brack 1993). We must conclude then that of the observable properties of an exoplanet, only the presence of liquid water on a planet gives strong evidence for habitability. Hence, to fulfill its mission of finding habitable planets, rather than just adding to the exoplanet tally, TPF needs a method to determine whether or not liquid water is present on exoplanets. This is the primary motivation for developing our model.

3.0 Electromagnetic Scattering Background

In order to predict polarized light curves for exoplanets, a scattering model must incorporate the known physics of electromagnetic scattering from atmospheric gases, aerosols, and surfaces.

3.1 Radiometric Quantities and Terms

3.1.1 Radiometry versus Photometry

Radiometry is the study and measurement of radiated electromagnetic energy, and is based on the Watt (W). Photometry, by contrast, is the study and measurement of electromagnetic energy in the visible band calibrated to the wavelength-dependent response of the standard human eye; the fundamental unit is the lumen (lm). The standard response curve of the human eye at moderate to high light levels is based on the response of the cones, the color-sensitive receptors in the retina. At low light levels, the rods dominate, and the associated light curve is called the scotopic curve. Photometry is important for determining proper light levels for vehicle headlights, ergonomic workspaces, and other applications where human vision is involved. The present study attempts to predict instrument response to scattered radiation from exoplanets, so we will be concerned with radiometry rather than photometry.

Bohren and Clothiaux point out that field of radiometry is rife with strange units and conflicting definitions:

"The tragedy of radiometry (and photometry) is that an inherently interesting subject – the best scientific instrument we carry with us everywhere is our eyes… - has been made dreadfully boring by wallowing in a mire of terminology and units… Terms are multiplied without end. Units in photometry border on the fantastic (foot-candle, talbot, nit, troland, candela, lux, lumen, stilb, foot-Lambert, nox, skot, and so on *ad nauseam*). Radiometry comes across as the science of terminology, its seeming objective being to multiply distinctions endlessly and thereby coin as many terms as possible… Rather than scrap all the units in photometry they could be recycled as characters in a kind of Lord of the Rings fantasy. Once upon a time, in the land of the Nits, dwelt a king named Troland with his beautiful daughter Candela…" (Bohren and Clothiaux 2006).

To avoid confusion, we briefly review the radiometric and reflection terms we will use in the remainder of this document. Table 1 includes definitions of some common radiometric units; the three units we will use in this thesis are discussed further after the table. Several names have been used for many of these properties; the terms used here are fairly common in the literature.

Table 1: Common Radiometric Units

Symbol	Units	Name and Definition
P, Φ	**W**	**Radiant Flux –** optical power; the basic unit of radiometry.
F	**W m^{-2}**	**Radiant Flux Density (Flux) –** radiant flux incident on or passing through a known surface area. This is usually (although somewhat confusingly) referred to as "flux." This includes all wavelengths in a specified or implied range.
E	**W m^{-2}**	**Irradiance –** radiant flux incident on a known surface area (similar to above).
F_λ	**W m^{-2} nm^{-1}**	**Spectral Flux (Monochromatic Flux) –** radiant flux through a known surface area, per nanometer (micron, etc.) of spectral bandwidth.
I	**W sr^{-1}**	**Radiant Intensity –** radiant flux of a source divided by the solid angle of emission; applies to sources approximating a point source, not extended sources or collimated beams. This quantity is often used in astronomy, and it is the primary unit used in the present work.
I_λ	**W sr^{-1} nm^{-1}**	**Spectral Radiant Intensity –** radiant flux of a source divided by the solid angle of emission, per nanometer of spectral bandwidth.
L	**W-m^{-2}-sr^{-1}**	**Radiance –** radiant flux emitted from a known area of the source and received through a known solid angle. Used for extended light sources.
Q	**J**	**Radiant Energy –** flux (power) integrated over time.
U	**J-cm^{-2}**	**Radiant Energy Density –** radiant energy per area of detector – equal to charge/area or ∫Edt/A.

3.1.2 Irradiance

Irradiance E is defined as the radiant power per unit area falling on a surface in W m^{-2}. The solar constant (average incoming radiant power from the Sun at the Earth's average distance) is approximately E_s = 1365 W m^{-2}.

3.1.3 Radiant Intensity

An optical remote sensing instrument typically measures current from a detector, from which is then calculated the optical power P in watts (W) at the instrument entrance aperture based on instrument characteristics such as the optical losses and detector responsivity over the waveband. For a light from a point source, such as an unresolved star or sub-pixel bright object on the Earth's surface, the natural unit of measurement is radiant intensity I in W sr^{-1}. Conversion from received power P to radiant intensity I requires only the distance to the object and the size of the instrument aperture, which define the solid angle Ω in steradians:

$$I = \frac{P}{\Omega} = P\frac{r^2}{\pi a^2} \tag{2}$$

where

r = distance to the star or other point source

a = radius of the instrument (circular) aperture.

However, for an airborne or satellite instrument observing areas of Earth's surface, a meaningful measurement of the optical power from the surface must also include the extent of the surface area being observed; enter radiance.

3.1.4 Radiance

Radiance L from a surface is defined as power per unit solid angle per unit projected area of the source. For the case of an approximately flat rectangular portion of a planetary surface being observed by an airborne or satellite instrument, with the viewer zenith angle defined as the angle of the instrument line of sight to the surface normal, the "projected area" equals the area times the cosine of the viewer zenith angle. Mathematically, we have

$$L = \frac{d^2\mathrm{P}}{dA\, d\Omega\, \cos(\theta_v)} \tag{3}$$

where

L = measured radiance in W sr^{-1} m^{-2} in the view direction θ_v;
P = total radiant power in Watts (W) reflected or emitted from the surface;
θ_v = viewer zenith angle;
A = area of the source in square meters
Ω = solid angle in steradians (sr)

For approximately constant viewer zenith angle (small enough area A and solid angle Ω), the radiance can be approximated as

$$L = \frac{d^2\mathrm{P}}{dA\, d\Omega\, \cos(\theta_v)} \approx \frac{P}{\mathrm{A}\ \Omega\ \cos(\theta_v)} \tag{4}$$

Spectral radiance is defined similarly but with an added component of μm^{-1} or nm^{-1}. Radiance is conserved in an ideal optical system; only losses due to absorption, scattering, diffraction, etc. diminish it, and only optical amplification and similar energy input processes can increase it. This "conservation of radiance" is also known as constancy of $A\Omega$ product, conservation of etendue, conservation of optical extent, and by several other names.

3.1.5 Radiometry and Planetary Scattering

The most important radiometric quantities for our purposes are flux density F, which is measured in units of W/m^2, and radiant intensity I, which is measured in Watts per steradian (W/sr). The steradian is the SI unit of solid angles;[8] the size of a solid angle Ω, measured from the center of a sphere of radius r, which intercepts a curved area A on the surface of the sphere, is defined as:

$$\Omega \equiv \frac{A}{r^2} \text{ sr.} \tag{5}$$

Equivalently, one steradian is the solid angle subtended by a unit area on the surface of a unit sphere, which corresponds to a cone with a full angle of about 65.5^o. The "unit" here can be any unit of linear distance: 1 cm, 1 m, 1 fathom, or 1 AU. If the unit sphere has a radius of 1 m, then the unit area on the surface is of a 1 sr section of the sphere is 1 m^2. Since the surface area of a sphere is $4\pi r^2$, the area of a unit sphere is 4π, so by definition there are 4π steradians in a sphere. Note that the area A discussed here is the area on the curved surface of the sphere, which makes for some rather messy spherical trig; however, for sufficiently small angles, the area of the curved surface approaches the area of a disk under the curved surface, so

$$\Omega = \frac{A}{r^2} \approx \frac{\pi a^2}{r^2} \quad \text{sr} \tag{6}$$

where r is the radius of the sphere (or distance from the planet to the observer) and a is the radius of the disk (or objective lens / primary mirror of the observing telescope).

Because I is power per solid angle, this quantity is conserved in free space, a property which makes it useful for our purposes. For example, the total radiated power output from the Sun is about $P_{Sun} = 3.85 \times 10^{26}$ W, and the mean radiance is $L_{Sun} = 2.009 \times 10^7$ W·m^{-2}·sr^{-1}. The total solid angle seen by a source which "looks" in all directions is 4π sr, so the radiant intensity of the Sun is

$$I_{Sun} = \frac{3.85 \times 10^{26}}{4\pi} = 3.06 \times 10^{25} \text{ W/sr} \tag{7}$$

Neglecting extinction due to the interstellar medium, this quantity is unchanged by distance, a useful property. The Earth's radius is about 6370 km, and the average Sun-Earth distance is about 150 million km, so the solid angle the Earth intercepts as viewed from the Sun is

$$\Omega \approx \frac{\pi a_{Earth}^2}{r_{1AU}^2} = \frac{\pi (6370)^2}{(150 \times 10^6)^2} = 5.66 \times 10^{-9} \quad \text{sr} \tag{8}$$

[8] The angular measurements radians and steradians are actually unitless, but units are usually attached to them for clarity and to assist in dimensional analysis.

The amount of the Sun's power intercepted by the Earth is then

$$P_{Earth} = \frac{\Omega_{Earth}}{4\pi} P_{Sun} = \frac{5.66\times10^{-9}}{4\pi} 3.85\times10^{6} = 1.73\times10^{17} \text{ W} \quad (9)$$

Dividing by the cross sectional area of the Earth (area of the projected disk) in meters, we obtain the irradiance in W/m^2 of the insolation:

$$E_{Earth} = \frac{P_{Earth}}{\pi(R_{Earth})^2} = \frac{1.73\times10^{17}}{\pi(6370000)^2} = 1360 \text{ W/m}^2. \quad (10)$$

Equivalently, the amount of power striking a one meter square surface placed in the Earth's orbit and facing the Sun would be

$$E_{Earth} = \frac{P_{EarthOrbit}}{1} = \frac{3.06\times10^{25}}{(150\times10^{9})^2} = 1360 \text{ W/m}^2. \quad (11)$$

These values are nearly identical to the commonly quoted value of 1366 W/m^2 for the so-called Solar Constant, S_0, although the Solar input at the top of the Earth's atmosphere varies by nearly 7% on yearly timescales, by about 0.1% on 11-year sunspot cycles, and slowly increases over billion-year timescales (about 40% since the Earth's formation) as the Sun's core becomes more dense. Variations on timescales between these extremes are not well known because of the lack of any known geologic record of Solar intensity, and limited understanding of Solar physics on these timescales.

Because of the conservation of radiant intensity I over distance in free space, we will use this quantity in calculations of scattered power from exoplanets. Following completion of the scattering calculations, we can convert the final radiant intensity into received power at the telescope using:

$$P_{rec} = I \times \Omega \approx I \frac{\pi a^2}{r^2} \quad (12)$$

where r is the distance from the exoplanet (or other light source) to the observer, and a is the effective radius of the telescope primary mirror.

For example, if a 10 cm diameter telescope is trained on the Sun, the power collected by the telescope will be

$$P_{rec} = I_{Sun} \times \Omega_{tel} \approx I_{Sun} \frac{\pi a_{tel}^{\ 2}}{r_{1AU}^{\ 2}} = 3.07\times10^{25} \frac{\pi(0.05)^2}{(150\times10^{9})^2} = 10.7 \text{ W} \quad (13)$$

Or we could obtain the answer as well by multiplying the solar constant in W/m^2 by the area of the telescope aperture:

$$P_{rec} \approx S_0 \times A = 1366 \times \pi (0.05)^2 = 10.7\,\mathrm{W} \tag{14}$$

Now suppose we are observing a star system that is similar to our own Solar system, having a star like the Sun and a planet the size of Earth at a distance of 1 AU (= 150 million km). We will place this system at the standard distance of 10 pc (= 32.6 light years = 3.09 x 10^{17} m) from Earth, and assume it has a constant geometric albedo of 0.2 (also similar to Earth).[9] Then the light received from the star by a 2 m diameter telescope would be

$$P_{rec} = I_{star} \times \Omega_{tel} \approx I_{star} \frac{\pi a_{tel}^{\ 2}}{r_{10\,pc}^{\ 2}} = 3.07 \times 10^{25} \frac{\pi (1)^2}{(3.09 \times 10^{17})^2} = 1.01 \times 10^{-9} \approx 1\,\mathrm{nW} \tag{15}$$

Compared to the Sun/Earth example, the size of the telescope has increased from 0.1 m to 2 m, a factor of 20, while the distance has increased by 10 pc / 1 AU = 2.06 x 10^6; power scales with the square of radius and the inverse square of distance, so the factor is about

$$2 \text{ million} / 20 = (10^5)^2 = 10^{10} \tag{16}$$

which matches our results.

In the visible range, an Earth-like planet will shine only by reflected light from the star, so when the planet is fully illuminated (OL = 180^o in our model), the reflected radiant intensity of the planet I_{planet} is approximately equal to the radiant intensity of the star I_{star} times the fraction of the star's light intercepted by the planet, times the geometric albedo of the planet:

$$I_{planet} = A_{geo} I_{star} \Omega_{planet} \approx A_{geo} I_{star} \frac{\pi a_{planet}^{\ 2}}{r_{1\,AU}^{\ 2}} = 0.2 \times 3.07 \times 10^{25} \frac{\pi (6370000)^2}{(150 \times 10^9)^2} = 3.48 \times 10^{16}\,\mathrm{W/sr} \tag{17}$$

the light received by our telescope can then be calculated as:

$$P_{rec} = I_{planet} \times \Omega_{tel} \approx I_{planet} \frac{\pi a_{tel}^{\ 2}}{r_{10\,pc}^{\ 2}} = 3.48 \times 10^{16} \frac{\pi (1)^2}{(3.09 \times 10^{17})^2} = 1.14 \times 10^{-18} = 1.14\ \mathrm{aW} \tag{18}$$

which is about a factor of 10^{-9} of the received power of 1 nW we calculated for the parent star.

The orbital points of greatest interest are when the planet is at quadrature (phase angle of 90 or 270), when the apparent star/planet separation is at a maximum. As we will discuss later, for a Lambertian planet, the brightness at quadrature is 1/π of that at full phase, so the received power at the telescope in the above example, when the planet is at quadrature, would be 0.363 aW.

[9] Note: the geometric albedo of a planet is the ratio of its actual brightness when illuminated face on (OL = 180 in our model) to the brightness of a 100% reflecting disk of the same diameter with Lambertian scattering characteristic. This contrasts with the Bond albedo, which is the fraction of incoming light scattered back into space without being absorbed. For Earth, approximate albedos are Abond = 0.3, and Ageo = 0.2.

3.1.6 Received Photons

Recalling Einstein's photoelectric equation, we calculate the energy E in a single 500 nm green photon:

$$E_{photon} = h\nu \Rightarrow E_{photon} = \frac{hc}{\lambda} = \frac{6.626\times10^{-34}\times3\times10^{8}}{500\times10^{-9}} = 4.0\times10^{-19} \text{ W s} \quad (19)$$

and then calculate the number of photons per second received from the planet by our telescope:

$$\frac{N_{photons}}{\text{sec}} = \frac{P_{rec}}{E_{photon}} = \frac{1.14\times10^{-18}}{4.0\times10^{-19}} = 2.85 \text{ photons/sec.} \quad (20)$$

3.2 Types of Scattering

Scattering of electromagnetic radiation by matter can be broadly divided into two types, elastic and inelastic. Elastic scattering is scattering in which there is no change (or essentially no change) in the wavelength of radiation, or equivalently, in the energy of the photons. Conversely, in inelastic scattering there is a wavelength shift. Although separating elastic and inelastic scattering is something of a simplification, it is useful in many macroscopic situations. Types of inelastic scattering include Brillioun scattering, Raman scattering, and Compton scattering. In Brillion scattering, a photon interacts with a phonon a (packet of acoustic energy) or other quantized packet of energy, and gains or loses energy from the interaction. Raman scattering occurs when a photon is shifted up or down in frequency by a transfer of energy with an electron in an atom or molecule; Compton scattering is similar to Raman scattering but involves scattered x-rays, which pass enough energy to an electron in an atom that the atom usually emits a lower energy photon in response. For our purposes, we are interested in elastic scattering and absorption; inelastic scattering of Solar-type radiation by an Earth-like planetary atmosphere is a sufficiently small effect that it can be ignored.

3.2.1 Scattering by Small Particles (Rayleigh Scattering)

Small-particle scattering, or Rayleigh scattering, is the process which makes the sky blue. The phenomenon was first explained by the third Lord Rayleigh, John William Strutt (Rayleigh 1871), who later won the 1904 Nobel Prize for Physics for his co-discovery of the element argon.

Rayleigh scattering theory describes the interaction that occurs when electromagnetic radiation impinges on a material in which the particles are smaller than the wavelength of the radiation. Mathematically, this condition is described by:

$$\lambda << 2\pi r \quad (21)$$

where λ is the wavelength of the radiation and r is the radius or characteristic dimension of the particles. Appendix B includes an informal development of Rayleigh scattering theory from Maxwell's equations.

3.2.2 The Mie Solution to Scattering by Spherical Particles

A more general description of scattering which applies to dielectric spherical particles of any size is often attributed to Gustav Mie (1908), although scattering by dielectric spheres was described nearly two decades earlier by Lorenz (1890), partly because the latter published only in Danish. The so-called "Mie theory" is actually a solution to Maxwell's equations (Maxwell 1865); hence some in the field have begun using the terms "Mie solution," "Mie calculation," or Mie scatter calculation." Craig Bohren gives a number of reasons to avoid use of the term "Mie scatterer" (Bohren 1992), so I will avoid using that term.

In any case, Mie and Lorenz independently used Maxwell's equations to derive a wave equation which describes electromagnetic waves in three dimensional space using spherical polar coordinates. After applying the appropriate boundary conditions to the surface of a sphere, a separable partial differential equation (PDE) can be produced. The solution of this PDE is then expressed as an infinite sum of basis functions. Sines and cosines provide the azimuthal (φ) dependence, spherical Bessel functions provide the radial (r) dependence, and associated Legendre polynomials provide the dependence on cos Θ (Petty 2006). Bohren and Huffman (1983) provide guidance on the minimum number of terms of this infinite sum which are needed. Mie showed that the relative sizes of the particle and the incident wavelength determine the pattern of the scattering. Appendix B provides a brief derivation.

3.2.3 Reflection modeling

3.2.3.1 Types of Reflection

Water surface reflectance is a specular (mirror-like) effect, while most rough surfaces are approximately Lambertian.

Lambertian reflection. A Lambertian reflector scatters light in all directions, with the maximum reflected radiation in the direction normal to the surface (straight up), dropping off as the cosine of the view angle to the normal in all directions. A true Lambertian surface is insensitive to the direction of the source, except that geometry dictates that the irradiance ($W\ m^{-2}$) from a point source over a flat surface is reduced by the cosine of the zenith angle. Because a Lambertian surface reflects light in all directions in the upward hemisphere, for a perfectly white Lambertian reflector the outgoing radiance ($W\ m^{-2}\ sr^{-1}$) in the vertical direction is the incoming irradiance divided by π steradians. This result can be verified by assuming conservation of energy, and integrating the Lambertian cosine function for a perfectly white surface over the 2π steradians of the hemisphere of the sky seen from a locally flat surface. In fact, the radiance in all other directions in the upward hemisphere is the same, because the cosine dropoff in the Lambertian function is balanced by the cosine decrease in the projected area.

Neglecting wavelength effects, the human eye responds approximately to radiance, so a Lambertian surface appears equally bright from all angles above the horizon even though the observed (projected) area changes with view angle to the zenith.

Specular reflection. A flat specular surface like a calm water surface is not Lambertian, and instead obeys the commonly known laws of reflection – the angle of incidence equals the angle of reflection, and outgoing light is reflected at an azimuth of 180° from the incoming light ray.

For both specular and Lambertian surfaces, reflectance ρ of a surface over a given wavelength band is defined as a constant factor between 0 and 1 which represents the fraction of the incoming radiant power which leaves the surface directed into the upper hemisphere, without either being absorbed or transmitted. However, the outgoing flux from the specular surface is directed into a smaller angle, so the peak radiant intensity (W sr^{-1}) of the reflection of a specular surface from a point-like source such as the Sun is considerably higher than that from a Lambertian reflection from a surface of the same "reflectance" value ρ. Also, the specular reflection remains high for large zenith angles, while the flux from the Lambertian source drops off as the cosine of zenith angle.

3.2.3.2 Reflectance definitions

Reflectance of an object is the ratio of reflected flux to incoming flux,

$$\rho \equiv \frac{P_{out}}{P_{in}} \tag{22}$$

By conservation of energy, reflectance must lie between zero and unity.

Bond albedo (planetary albedo) is the fraction of the total radiant power input from the parent star which is scattered or reflected back without being absorbed. This measure of reflectance conveys no knowledge of the directionality of the reflection. This is the albedo commonly used in energy balance and greenhouse effect calculations. It is sometimes asserted that specular reflection from water does not contribute to planetary albedo, because it is highly directional. This is inaccurate; in fact, a specularly reflecting sphere covered with a perfect conductor would have a planetary albedo of 1, exactly the same as if the sphere were covered with perfectly white Lambertian paint. The reason specular reflection from water is a secondary contributor to Earth's planetary albedo is that the reflectance of water at normal incidence is only about 2%, while the reflectance of water clouds, although highly dependent on wavelength, cloud composition, and incident angle, is typically much higher.

Geometric albedo is the ratio between the light reflected by a planet and the light that would be reflected by a white Lambertian disk of the same cross-section. For a Lambertian surface, with the planet at full phase (OL=180^o), the ratio of the geometric albedo to Bond albedo is 2/3. Real planets have smaller or larger ratios between geometric and Bond albedo depending on surface type. The Bond albedo of Earth is 0.29 - 0.31, but the geometric albedo is 0.367 (Seidelmann

1992). Mars is closer to being a Lambertian planet, with a Bond albedo of 0.25 and a geometric albedo of 0.15[10].

Bidirectional Reflectance Distribution Function (BRDF) is a function which describes the reflecting properties of a surface from a point-like source (such as the Sun) in any direction to an observer in any direction. The BRDF is therefore a four-dimensional function, depending on the solar zenith angle, viewer zenith angle, and the azimuth angles of both the Sun and the observer. For surfaces which are azimuthally isotropic, this can be reduced to three dimensions: the solar and viewer zenith angles, and the relative azimuth between the Sun and the observer. A wavy ocean surface which is excited by wind from a single direction is generally not azimuthally isotropic; however we will treat it as if it is. BRDF is defined as the ratio of the outgoing radiance of a surface to the incoming irradiance. Given illumination of an azimuthally isotropic surface by the Sun at solar zenith angle θ_s, we have:

$$BRDF\left(\theta_s,\theta_v,\phi_{rel}\right)=\frac{L\left(\theta_s,\theta_v,\phi_{rel}\right)}{E_s\cos\left(\theta_s\right)}=\frac{W\,sr^{-1}\,m^{-2}}{W\,m^{-2}}=sr^{-1} \tag{23}$$

For a Lambertian surface, where BRDF is constant, Girod (2000) tells us that the relationship between BRDF and reflectance is simply:

$$\rho=\pi\times BRDF \tag{24}$$

for this special case.

3.2.3.3 Polarized specular reflection and the Fresnel equations

When light strikes a smooth boundary between transparent media of different indices of refraction at any angle other than normal, the reflected wave is partially linearly polarized. The reflection coefficients for the perpendicular and parallel components are given by the Fresnel equations:

$$R_\perp=\left\{\frac{sin\left[arcsin\left[\frac{n_I}{n_T}sin\left(\theta_I\right)\right]-\theta_I\right]}{sin\left[arcsin\left[\frac{n_I}{n_T}sin\left(\theta_I\right)\right]+\theta_I\right]}\right\}^2 \tag{25}$$

$$R_\parallel=\left\{\frac{\tan\left[\arcsin\left[\frac{n_I}{n_T}\sin\left(\theta_I\right)\right]-\theta_I\right]}{\tan\left[\arcsin\left[\frac{n_I}{n_T}\sin\left(\theta_I\right)\right]+\theta_I\right]}\right\}^2 \tag{26}$$

[10] http://ssd.jpl.nasa.gov/?planet_phys_par

The total reflectance of the boundary to unpolarized light is then the mean of these two:

$$R_{tot} = \frac{R_{\perp} + R_{\parallel}}{2} \tag{27}$$

The difference between the perpendicular and the parallel components, divided by the sum, is called the polarization fraction:

$$PF = \frac{F_{\perp} - F_{\parallel}}{F_{\perp} + F_{\parallel}} \tag{28}$$

.

We will use this parameter to characterize the light scattered from exoplanets.

3.2.3 Brewster's Angle

Any discussion of polarized light reflected by oceans must include Brewster's angle. When light strikes a boundary between two media with different indices of refraction, generally some of it is reflected. At a particular angle which depends upon the two refractive indices n_1 and n_2, none of the light at one polarization is reflected. This angle, called Brewster's angle (θ_B), corresponds to the angle at which the reflected light ray would be at a right angle to the light ray of the light being transmitted into the second medium (Brewster 1815). Figure 14 shows the geometry of reflection and refraction at Brewster's angle.

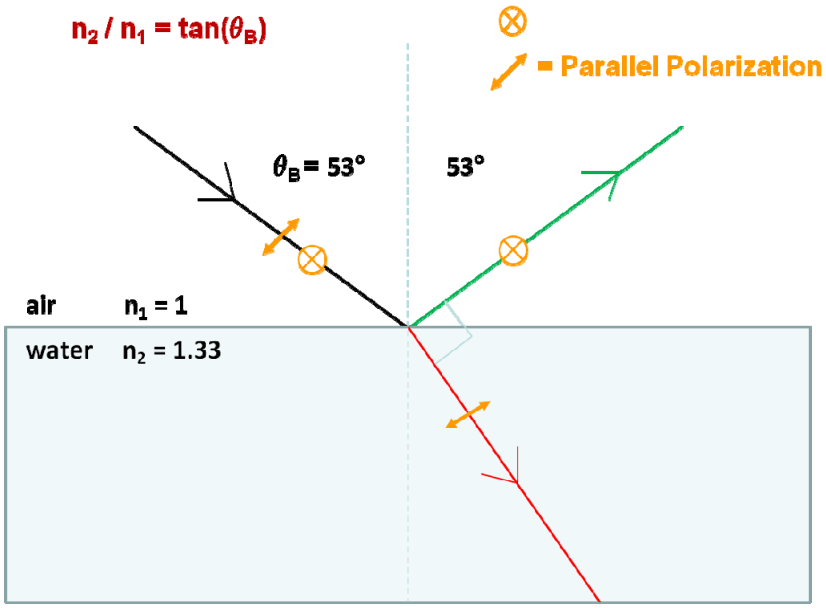

Figure 14: Diagram showing polarization of light due to reflection at or near Brewster's angle

We can derive the Brewster angle using Snell's law:

$$n_1 \sin(\theta_1) = n_2 \sin(\theta_2) \tag{29}$$

and the Brewster angle condition:

$$\theta_B + \theta_{\text{refraction}} = 90^o \tag{30}$$

Substituting into Snell's Law, we can calculate the incident angle $\theta_1 = \theta_B$ at which no light is reflected, where $\theta_2 = 90^o - \theta_B$, so

$$\frac{n_2}{n_1} = \frac{\sin(\theta_1)}{\sin(\theta_2)} = \frac{\sin(\theta_B)}{\sin(90-\theta_B)} = \frac{\sin(\theta_B)}{\cos(\theta_B)} = \tan(\theta_B) \tag{31}$$

Equation (31) is known as Brewster's law. For an air/water interface, $n_1 = 1$ and $n_2 = 1.333$, the Brewster angle is 53.1^o.

3.2.4 Stokes Parameters

For applications such as measuring brightness of a thermal light source or the amount of illumination falling on a surface, it is sufficient to measure intensity I. However, when the polarization state of a radiation field is important, a set of parameters must be specified. The Stokes Parameters (Stokes 1852) are a convenient and useful representation of light of any polarization state. Four quantities define the field:

1) intensity parallel $\parallel$ to the plane of scattering;
2) intensity perpendicular $\perp$ to the plane of scattering;
3) angle χ of the plane of polarization relative to the plane of scattering;
4) phase lag δ between $E_\parallel$ and $E_\perp$

(Chamberlain and Hunten 1987). Then one set of Stokes parameters are:

$$\begin{aligned} I &= I_\parallel + I_\perp \\ Q &= I_\parallel - I_\perp \\ U &= Q \tan 2\chi \\ V &= E_\parallel E_\perp \sin \delta. \end{aligned} \tag{32}$$

These four parameters form a vertical vector, usually represented as **I**. Other choices of elements of the Stokes vector are possible, such as:

$$
\begin{aligned}
&I_{\parallel} \\
&I_{\perp} \\
&U = Q \tan 2\chi \\
&V = E_{\parallel} E_{\perp} \sin \delta
\end{aligned}
\tag{33}
$$

from Goody and Yung (1989).

The dimensions for all Stokes parameters are energy per area per time per wavelength (Mishchenko et al. 2000). For unpolarized light, $I^{\parallel} = I^{\perp}$, so Q, U, and V are all zero. The general state of polarized light is elliptically polarized light. Special cases include linear polarization, in which the phase difference between the two electric components is zero or a multiple of 180°; and circular polarization, in which the two electric components are of equal magnitude and the phase difference between the components is an odd multiple of 90° (Liou 2002). Some examples of Stokes parameters for fields of unit intensity, using the (I, Q, U, V) representation, are shown in Table 2 (Petty 2006).

Table 2: Stokes parameters for unit intensity light with common polarizations.

Stokes Parameter	Horizontal	Vertical	Linear @+45^o	Linear @-45^o	Right Circular	Left Circular	Unpolarized
I	1	1	1	1	1	1	1
Q	1	-1	0	0	0	0	0
U	0	0	1	-1	0	0	0
V	0	0	0	0	1	-1	0

Note that here "horizontal" and "vertical" are used instead of "perpendicular" and "parallel." For this project, we use the values of I and Q generated by 6SV to calculate $I^{\parallel}$ and $I^{\perp}$ as follows:

$$
\begin{aligned}
I_{\parallel} &= (I + Q)/2 \\
I_{\perp} &= (I - Q)/2
\end{aligned}
\tag{34}
$$

and similarly for the parallel and perpendicular reflectances, without the factor of ½.
The angle between the polarization vector and the reference plane is usually designated as χ. Some example values of χ in degrees for 100% linearly polarized light are given in Table 3.

Table 3: values of χ and corresponding values of Stokes Q and U

χ	**polarization**	**Q**	**U**
0	vertical/parallel	+I	0
22.5	22.5	+I/√2	+I/√2
45	45	0	+I
90	horizontal/perp	-I	0
135	135	0	-I

Circular polarization, represented by the V parameter, is essentially zero for land and water surfaces other than vegetation, and is ignored by most atmospheric and surface models, including 6SV. Coulson (1988) points out that, in Earth's atmosphere, circular polarization is either zero (for Rayleigh scattering) or very small (for clouds and aerosols), compared to linear polarization. Measurements of circular polarization by (1971) of other planets in the solar system were in the range 1×10^{-5} to 5×10^{-4}; however, it has been suggested that circular polarization might be used to discover photosynthetic organisms on extrasolar planets (Sparks et al. 2009).

3.3 Atomic and Molecular Absorption and Emission

3.3.1 Types of Transitions

3.3.1.1 Atomic Absorption and Emission

In the lower atmosphere, atoms absorb and emit radiation primarily by transitions of electrons between energy levels. When an electron transitions between energy states, a photon is emitted with energy equal to the difference between the energy states. Recalling that the energy of a photon is equal to Planck's constant times the frequency,

$$h\nu = \Delta E = E_2 - E_1 \tag{35}$$

where E_2 and E_1 are the upper and lower energy states, respectively. The theoretically infinitesimally narrow emission/absorption line of the atom calculated from the above formula is broadened by a number of mechanisms discussed in the following sections.

An atom can also absorb a photon with energy greater than that needed to move the electron out of the potential energy well of the atom; when this happens, the atom is ionized – the electron is freed from the atom – and the excess energy beyond that needed to move the electron out of the potential well is converted to electron kinetic energy. This is the photoelectric effect, the explanation of which led in part to Einstein's receipt of the 1921 Nobel Prize in Physics (Einstein 1905). In this case the energy transfer is expressed in terms of the work function W, which is the minimum energy required to free the electron from the potential well of the atom, and $E_{K\text{-}max}$, the maximum energy left over and available to be converted into kinetic energy of the electron:

$$h\nu = W + E_{K-max} \tag{36}$$

Figure 15 from Clark (2006) shows three series of lines from atomic hydrogen, named after their discoverers, Lyman, Balmer, and Paschen:

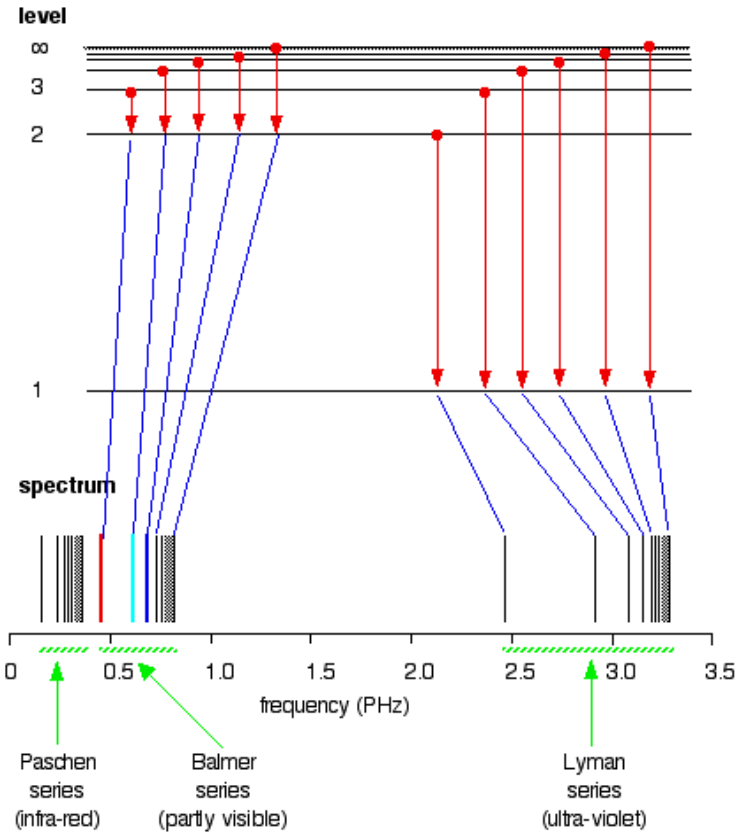

Figure 15: Hydrogen emission line spectrum showing frequencies and atomic energy levels [11]

Electron transitions from higher energy states to the electron ground state (n = 1) produce ultraviolet or x-ray photons. For example, the Lyman-alpha (Ly-α) transition in hydrogen from the n = 2 orbital to the n = 1 orbital, produces a 121.6 nm photon. The same electron transition generalized to all elements is called the Kα transition, and produces higher energy photons for higher atomic number elements. In heavier elements, the transition produces x-rays.

3.3.1.2 Molecular Absorption and Emission

Molecules, being composed of multiple atoms, have additional modes of motion. For this reason, molecular absorption and emission results from three primary mechanisms: 1) electron transitions between energy levels (as in atoms); 2) transitions between vibrational modes; and 3) transitions between rotational modes. Molecules can bend and rotate at the same time, and transitions can occur in which both rotation and vibration change, so rotational-translational energy bands also exist. Transitions between vibrational energy levels (including rotational-translational transitions) are associated with infrared photons, while transitions between rotational energy levels (without vibrational mode changes) produce microwave photons.

3.3.2 Vibrational Modes

[11] http://www.chemguide.co.uk/atoms/properties/tieup4.gif, posted by Jim Clark

In addition to absorbing and emitting energy through transitions of electrons between energy states, molecules can also store energy kinetically in vibrational and rotational modes.

The carbon dioxide (CO_2) molecule demonstrates a number of vibrational modes as shown in Figure 16. The carbon and oxygen atoms in the molecule move much like masses connected by springs. In the asymmetric stretch mode, the two oxygen atoms move left and right in phase with each other, while the central carbon atom moves right and left, in opposing phase. Another way to describe this motion is to say that the carbon atom moves closer to the right oxygen atom, while that oxygen atom approaches the carbon atom (white circles); then, the carbon atom and the left oxygen atom move toward each other, while the right oxygen atom moves away (gray circles). In the bending mode, the two oxygen atoms move up and down in phase while the carbon atom moves down and up, out of phase. In the symmetric stretch mode, the carbon atom remains stationary while the oxygen atoms alternately move toward and away from the central carbon atom. The carbon atom is stationary because the two oxygen atoms are always simultaneously either pulling or pushing on the carbon atom.

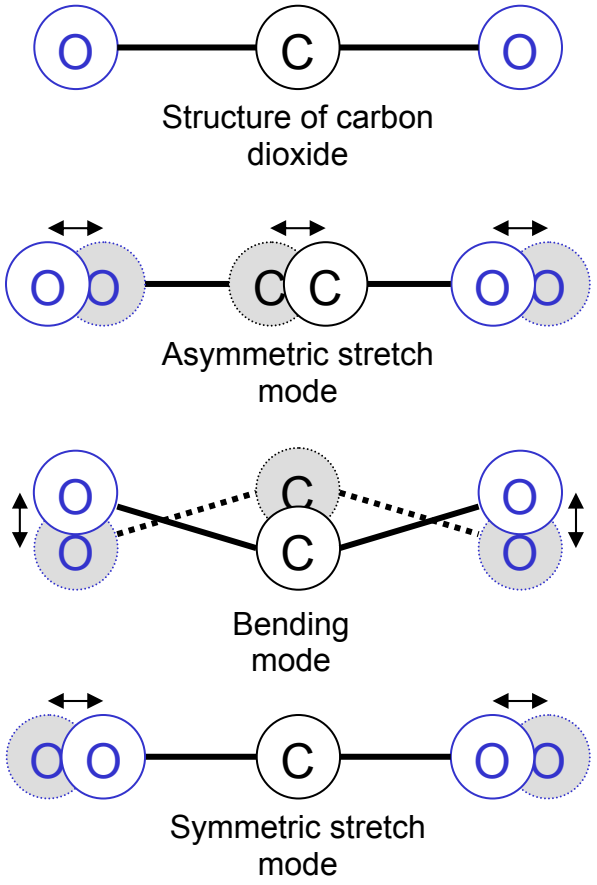

Figure 16: Representation of the vibrational modes of the carbon dioxide molecule[12]

[12] Figure drawn by the author, after figure by Derek Kverno, posted on http://webphysics.davidson.edu/alumni/jimn/Final/Pages/FinalMolecular.htm.

3.3.3 Rotational Modes

The second way that molecules can store kinetic energy is through rotational modes, by rotating around the center of mass. These low-energy transitions absorb and emit photons in the microwave range. In order for a molecule to have rotational modes, it must have a dipole moment; that is, it must be asymmetric such that the center of charge is offset from the center of mass. Single atoms, in which virtually all of the mass of the atom is in the nucleus, have no permanent dipole moment; they can acquire a temporary dipole moment while polarized by an external field.

Molecules may possess electric and/or magnetic dipole moments based on various types of asymmetry. The dipole moment allows an electric (or magnetic) field to exert a torque on the molecule and cause it to rotate, speed up, or slow rotation. As with other energy states of atoms and molecules, these rotational states are quantized.

Carbon monoxide has an electric dipole moment, due to the fact that oxygen is more electronegative than carbon, giving the oxygen end of the molecule a net negative charge, and the carbon end, a net positive charge. Carbon dioxide has no dipole moment, because it is a linear molecule which is symmetric about the central carbon atom. Methane has no permanent dipole moment because the four hydrogen atoms are arranged symmetrically around the carbon atom at the vertices of a tetrahedron. Water has a dipole moment, because the two hydrogen atoms are not directly on opposite sides of the oxygen atom. Diatomic molecules made of a single type of atom such as O_2, N_2, and H_2 have no electric dipole moment when not ionized, however O_2 has a magnetic dipole moment. Note that species with no permanent dipole moment, such as methane, carbon dioxide, and most diatomics, can acquire an electric dipole moment if ionized, and can exhibit oscillating dipole moments during bending vibrational motions that break linear symmetry.

For the study of Earth-like planets, the most important points about rotational modes are the following:

- Single atomic constituents such as Ar, He, O, and N have essentially no moment of inertia, and therefore do not exhibit rotational transitions;
- Molecular nitrogen (N_2) and most other diatomic gases have no dipole moment and therefore no observed rotational transitions;
- Molecular oxygen (O_2) does have a magnetic dipole moment, so it has rotational absorption bands at 60 GHz and 118 GHz;
- Carbon dioxide and methane have no permanent dipole moments

(Petty 2006).

3.3.4 Line Broadening

As mentioned earlier, emission and absorption lines are broadened by a number of mechanisms. The most relevant mechanisms for our purpose are natural, pressure, and Doppler broadening.

3.3.4.1 Natural (Lorentz) Broadening

The most fundamental type of line broadening, natural broadening is a consequence of the Uncertainty Principle. Since the exact energy of a photon cannot be known, absorption and emission bands possess a finite spectral width $\Delta\nu$, where:

$$\Delta\nu = \Delta E / h \tag{37}$$

Equivalently, we can say that natural broadening is due to the uncertainty in the lifetime of an excited state. That is, although the average lifetime of a particular excited state in a species can be measured, the time that a particular excited atom remains in the excited state cannot be predicted. In any case, natural broadening results in a line profile with a Lorentzian distribution (Lorentz 1892), as shown in Figure 17.

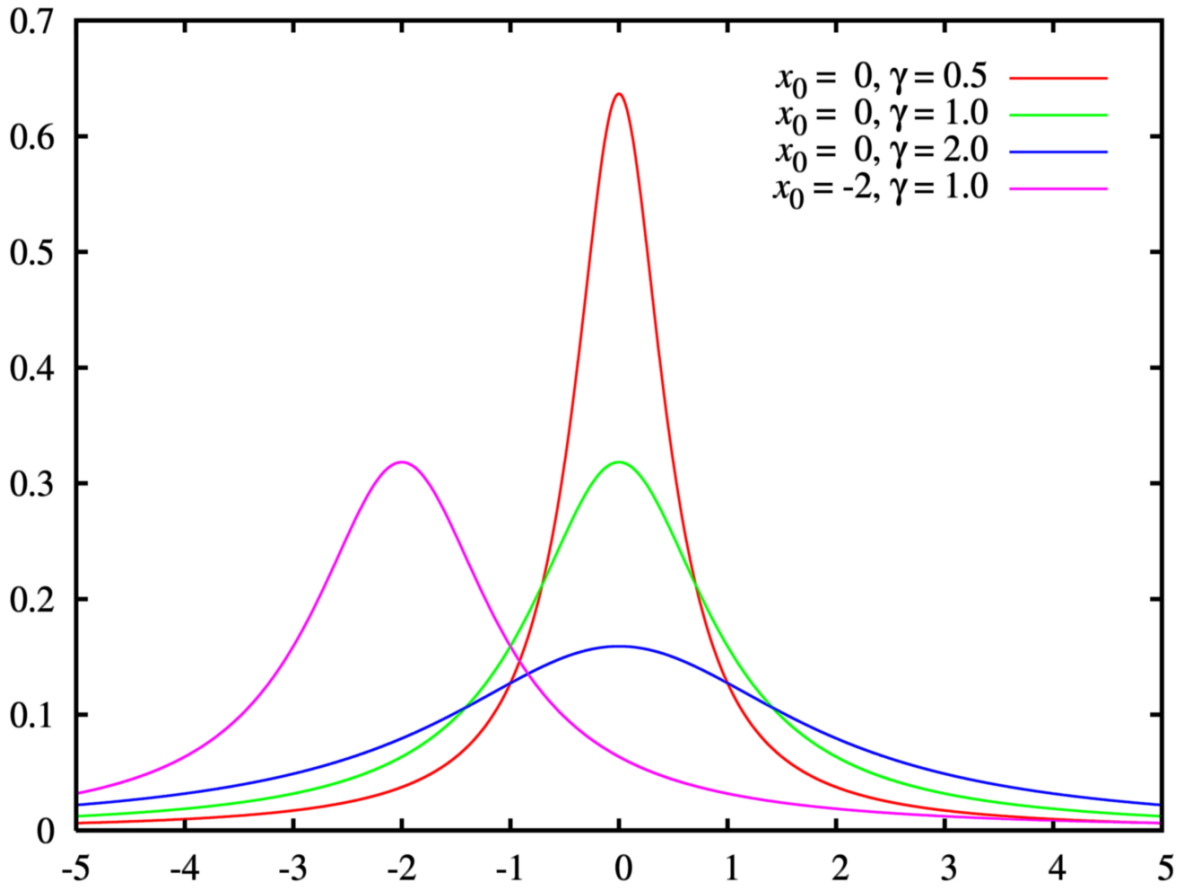

Figure 17: Example Lorentz distributions, where x_0 is the mean value, and γ_0 is a measure of the spread[13]

3.3.4.2 Pressure Broadening

[13] from http://en.wikipedia.org/wiki/Lorentz_distribution, posted by Skbkekas on 2 March 2010, used with permission of the author.

Pressure broadening occurs because collisions between molecules in a pressurized gas cause slight shifts in the energy level spacing of the molecules. No exact theory exists for this complex interaction, but if collisions are numerous enough, as in Earth's lower atmosphere, then the particles reach local thermodynamic equilibrium (LTE), and the pressure broadening can be handled statistically. LTE does not occur under some particular conditions such as those in Earth's ionosphere, where ions experience vastly different effective temperatures than neutral particles due to magnetic field effects. Under LTE conditions pressure broadening can be approximated by a phase-shift model, in which each collision is assumed to cause the oscillator to stop and instantaneously restart with a new phase which is completely unrelated to the original phase. This model results in a prediction that line broadening is directly proportional to pressure, a prediction which has been verified by measurements in Earth's atmosphere. Pressure broadening creates a Gaussian profile.

3.3.4.3 Doppler (Thermal) Broadening

Gas molecules in thermal motion both emit and absorb photons that are variously blue-shifted and red-shifted based on the molecule speed and direction relative to the direction of the photon. In a gas at thermal equilibrium, the velocity distribution of molecules falls into a Maxwell-Boltzmann distribution (Maxwell 1867; Maxwell 1873; Boltzmann 1895) so the Doppler shifts also have that type of distribution.

3.3.4.4 Voigt Line Shape

The Lorenzian shaped broadening produced by natural (lifetime related) broadening convolved with the Gaussian profile produced by Doppler broadening results in the combined profile known as a Voigt line shape (Voigt 1889). The slit used in a spectrometer also produces a Gaussian profile, which is also convolved into the Voigt line shape.

4.0 Previous Modeling Work

This chapter reviews methods of modeling atmospheric scattering, as well as the most relevant prior work on scattering from terrestrial planetary surfaces.

4.1 Scattering from Wavy Oceans

The first quantitative work on scattering from ocean waves was performed by Cox & Munk using aerial photographs of sun glint (Cox and Munk 1954). This now classic work produced an equation for wave slope probability density which is still used today, but their method for converting that probability density into a reflected radiance breaks down near the horizon, where it predicts infinite radiance. Zeisse (1995) pointed out this limitation, and derived an integral equation that removes the singularity but reduces to the algebraic Cox and Munk equation away from the horizon. Zeisse ignored polarization, but Takashima and Masuda (1985) separately calculated the returns from both orthogonal polarizations. Recently a team used the NASA/Goddard wave facility at Wallops Island to attempt to measure scattering from waves in a controlled environment (Ottaviani et al. 2008). This experiment is the first to measure polarization of glint using modern equipment in a controlled environment. The team controlled wave states using a hydraulic ram to create gravity waves and a wind generator to create capillary waves, and even included a subsurface current. The optical apparatus consists of a laser source and a custom-built photopolarimeter which move along a semicircular rail over the tank. The paper primarily discusses the novel method, with results to follow.

4.2 Atmospheric Scattering Code

A review of the literature and internet search reveals a number of atmospheric codes written for various types of modeling over the last few decades. Figure 18 shows the geometry of single scattering from a plane-parallel atmosphere, or a small portion of a planetary surface, and defines the angles of interest. The angle between the incoming radiation from the parent star and the normal to the top of the atmosphere (or planet surface), the stellar (or Solar) zenith angle, is traditionally designated θ_0. The exit angle of the scattered radiation to the normal is denoted θ, and φ is the right-hand azimuthal exit angle of rotation around the normal. It is often measured from the projection of the incoming ray onto the surface, as shown in the diagram; it may also be measured from the extension of that ray, which gives a value of the angle which is equal to $180^o - \varphi$. When this geometry is extended across a spherical or spheroidal planet, the functions which describe the reflectance of the planet across varying values of θ, θ_o, and φ are called Bidirectional Reflectance Distribution Functions (BRDFs).

The following discussion of scattering code methods is based in part on Atmospheric Radiation: Theoretical Basis (Goody and Yung 1989).

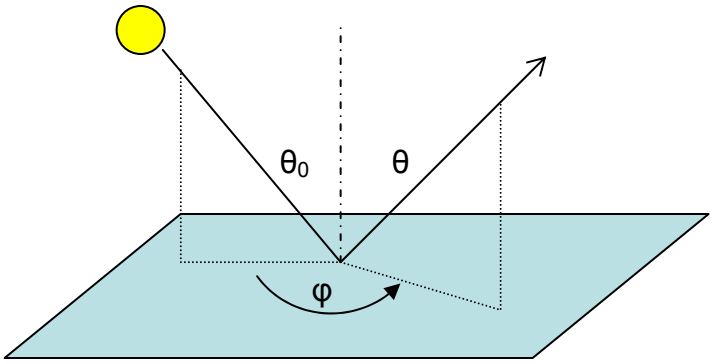

Figure 18: Geometry of single scattering from a plane-parallel atmosphere or locally flat surface

4.2.1 Two-Stream Approximation

Several two-stream models of radiative transfer have been developed for various applications. One of the first was developed by Sagan and Pollack (1967) to study the change in the global albedo due to the presence of an aerosol layer. Yung (1976) developed a two-stream radiative transfer code in FORTRAN that calculates the total integrated radiance incident on a molecule in the atmosphere from all directions due to scattering of the Sun, assuming a plane parallel atmosphere with multiple layers. Because this code was intended to calculate the total radiance to a region from all directions, it is not suitable for calculating the atmospheric scattering seen by an observer at a distant location.

Two-stream models intended to calculate radiation transfer to and from the Earth, in order to study the planetary energy balance, are similar. These models choose a single incoming solar zenith angle, and a single outgoing angle (often the same angle). Such energy balance models calculate outgoing radiation integrated over two separate hemispheres: the radiation scattered up into space, and that scattered down, to strike the Earth. While this is often sufficient for energy balance calculations, it does not provide sufficient angular resolution to calculate light curves from planetary disks.

Perhaps the most well-known atmospheric code, MODTRAN (MODerate resolution atmospheric TRANSmission code) is a two-stream atmospheric modeling code written in FORTRAN that models propagation through the atmosphere of electromagnetic radiation from far infrared to ultraviolet (100 μm to 200 nm). The code is developed and updated by the U.S. Air Force Research Laboratory and distributed by Ontar Corporation. Propagation from an external source (such as the Sun) to the surface can be modeled, as can propagation parallel to the Earth's surface. The resolution of MODTRAN4 is 1 cm^{-1} (improved to 0.1 cm^{-1} in MODTRAN5) so resolution on a fractional basis is much better for shorter wavelengths. MODTRAN includes Rayleigh scattering, molecular absorption bands, and Mie scattering from droplets, making it one of the most powerful and flexible codes available. A version which includes polarization, MODTRAN 4P, does exist, however availability may be a problem, and the code size and complexity (hundreds of thousands of lines) would have made it impractical to modify the code for our project.

4.2.2 Multi-Stream Approximations

The Method of Discrete Ordinates and the Feautrier Method are generalizations of the two-stream approximation in which a number of discrete incoming and outgoing zenith angles are chosen, resulting in a matrix of differential equations. Since these methods assume multiple zenith angles, on the surface they do not immediately appear applicable to our problem. However, note that only the unscattered incoming radiation strikes at the original zenith angle, and in a multiple scattering environment, we must account for radiation traveling at multiple angles θ and φ. The Feautrier Method uses equations analogous to diffusion equations, where electromagnetic flux is analogous to density in diffusion problems. Photons perform a random walk, and are then found to "diffuse" from areas of higher density to those of lower density.

4.2.3 Adding-Doubling Method

The Adding-Doubling Method is a macroscopic approach to radiative transfer which breaks the atmosphere down into layers of optical density τ_i and uses energy conservation along with incident fluxes at boundaries and source distribution within each layer to balance incoming and outgoing radiation at each layer boundary. The first boundary uses a single source at the Solar zenith angle, with an optical depth of zero for space.

PolRadTran RT3 and RT4. The PolRadTran (Polarized Radiative Transfer)[14] codes are Fortran 77-based radiative transfer codes utilizing the adding-doubling method. Both were written by Frank Evans at Colorado State and University of Colorado. The RT3 version models solar or thermal radiation in a medium containing aspheric, randomly oriented particles, and RT4 models thermal radiation in a medium with azimuthally symmetric randomly oriented particles. Because it allows a solar source, RT3 is the code of interest for this project. The newer version of RT3 allows the radiances at any level in the input medium to be output as V and H polarization for a specified number of azimuth angles (typically 16 angles). The code is intended for use in energy balance calculations, and calculates radiation either integrated over the up and down hemispheres, or at specified azimuth angles.

4.2.4 Discrete Dipole Approximation

The Discrete Dipole Approximation (DDA) or Coupled Dipole Approximation (CDA) is a still more general technique to describe light scattering by non-spherical particles. Rather than attempting to solve Maxwell's equations exactly for arbitrary geometries, the method is essentially a finite element approximation in which each polarizable point in an array acquires a dipole moment in response to the external electric field and in coupling to the other points. The method was proposed by Purcell and Pennypacker (1973) and further developed by Draine and Flatau (1994).

[14] PolRadTran codes rt3 and rt4 are available free for download on the web at http://nit.colorado.edu/polrad.html

In addition to the above, other methods are less commonly used because they require more computation to solve radiative transfer equations in plane-parallel atmospheres; on the other hand, they are adaptable to arbitrary geometries.

4.2.5 Successive Orders of Scattering

In the Successive Orders of Scattering (SOS) method, one first calculates the radiation field that results from single scattering of the incident field. The resulting scattered field is then used as the incident field for the second "order" of scattering. The sum of the resultant contributions from all of the orders gives the result. For an infinite sum, this method would be exact; however, for practical calculations one must settle for calculating the sum of a finite series of orders. The more light is absorbed or scattered out of the area of interest, the faster the sum converges toward an acceptable solution and the fewer orders need to be calculated (Petty 2006).

Second Simulation of a Satellite Signal in the Solar Spectrum – Vector (6SV) uses SOS, and provides polarized outputs. [15] Although 6SV was intended to model returns measured by Earth-orbiting satellites viewing a small portion of the Earth's surface, this code was judged to be almost ideal for our purposes, lacking little except for the integration of the three-dimensional BRDFs over a spherical surface. Polarization is calculated using Stokes parameters. The code works throughout the range 350 – 3750 nm, and includes Rayleigh scattering, aerosols, absorption, and a variety of surface types including a wavy ocean. The 6SV code was chosen for this project, and will be discussed in more detail later.

4.2.6 Monte Carlo Methods

Monte Carlo methods calculate the paths of a large number of rays between the source (sun or parent star) and the receiver, and use the results to generate statistical probabilities. Monte Carlo calculations can be accelerated by using time-reversed Monte Carlo techniques, in which the photon starts at the detector and travels back to the source. This reduces the number of photons thrown away because the solid angle looking from the planet to the parent star is much larger than that looking from the planet to the observer (e.g. TPF).

4.3 Previous Models of Scattering from Earth-like Planets

Oakley & Cash (2009) modeled orbital and diurnal light curves of Earth-like exoplanets, but concentrated on planets with Earth-like geography, and did not study polarization. Mallama (2009) generated radiometric light curves for the terrestrial planets, but did not consider other types of planets or model polarization. Williams & Gaidos (2008) demonstrated that large oceans could be detected on exoplanets using the amplitude and shape of polarized and unpolarized orbital light curves. However, that model considered only surface scattering and did not include atmospheric effects. That model also assumed isotropic rather than Lambertian reflectance for diffuse scattering for clouds and rough surfaces. McCullough (2006) also modeled polarization, and included Rayleigh scattering, clouds, and different surfaces, but the work was unfortunately

[15] 6SV code is available free for download on the web at http://6s.ltdri.org/

never published. Neither of the above mentioned polarization papers investigates the significant effects of absorption, aerosol scattering, scattering from within the water column, or varying degrees of ocean waviness, and neither paper compares the polarization signatures of ocean planets and dry planets. Dry planets with Rayleigh polarization signatures diluted by diffuse scattering might produce polarization signatures similar to those from ocean planets, resulting in false positives for the presence of oceans. Stam (2008) modeled Earth-like atmospheres over water surfaces, but she used a simple Fresnel model for oceans which does not include waves, sea foam, or scattering from within the water column, and did not model light curves of different atmospheres over an ocean. We seek here to extend the efforts of these previous workers by simulating polarized and unpolarized orbital lightcurves over a larger variety of atmospheric and ocean parameters.

In anticipation of the revolutionary planet finder missions, a number of recent papers (Ford et al. 2001; Des Marais et al. 2002; Lorenz 2003; McCullough 2006; Williams and Gaidos 2008) have suggested that it may soon be possible to detect oceans on planets around other stars (exoplanets) using specular reflection, or "glint." As the planet moves around its orbit, the phase angle (angle between the parent star, the planet, and the observer on Earth) will change, resulting in changing amplitude of light reflected to the observer due to glint. More importantly, specular reflections cause unequal reflection of the parallel and perpendicular polarization states, with a ratio that varies with the phase angle, and reaches its maximum when the angle of incidence equals the Brewster angle. The Brewster angle is dependent on index of refraction (53.1^{o} for water), so with sufficient theoretical consideration and modeling, it may be possible to unambiguously interpret light curves from some planets as being produced by oceans. Note, however, that the phase angle of maximum polarization ratio for a real planet will be affected by polarization effects due to Rayleigh scattering in the atmosphere, clouds, and other effects; thus, modeling is essential to determine whether it is possible to unambiguously identify the glint from oceans through careful analysis of future light curves.

A number of researchers have published methods and results relevant to scattering of sunlight or starlight from Earth or planets similar to Earth; the following is a review of some of the more relevant papers in the field.

Manalo-Smith et al. (1998) used data from the Earth Radiation Budget Experiment (ERBE) to calibrate analytic expressions for sunlight scattered from Earth. ERBE uses two NOAA satellites and the NASA ERBS (Earth Radiation Budget Satellite) to quantitatively study the flow of energy between the Sun, the Earth, and space. In this paper, which was originally directed towards Earth observing rather than Astrobiology, the authors develop analytic expressions for Bidirectional Reflectance Distribution Functions (BRDFs), also called angular distribution models. The authors' BRDFs are then fit to ERBE operational models.

The Manalo-Smith et al. models include terms for atmospheric Rayleigh scattering and cloud/surface scattering. The fact that the ocean appears dark (outside of the area of Sun glint) allows empirical measurement of atmospheric Rayleigh scattering. The authors compare the analytic functions developed in the paper against observed reflectances in the forward direction; there is excellent correlation, the only exception being in backscatter direction, where the

analytic models are more limb brightened than ERBE observations. Modified versions of the BRDFs developed by Manalo-Smith et al. are used by McCullough (2006).

The Ford et al. (2001) model uses Earth geography to model light curves showing variability due to meteorological changes and rotation period. In Figure 20 (from that paper) the diurnal light curve of a distant planet with Earth geography is modeled. The reflectivity scale on the left side of the figure is normalized to a Lambert disk at a phase angle of 0^o. The diagrams along the bottom of the figure show which portions of the Earth face the observer, and which portions are illuminated by the planet's star (the area which is not cross-hatched). The peak near mid-day (Time = 0.5 – 0.65 day) is due to reflection from the Sahara desert.

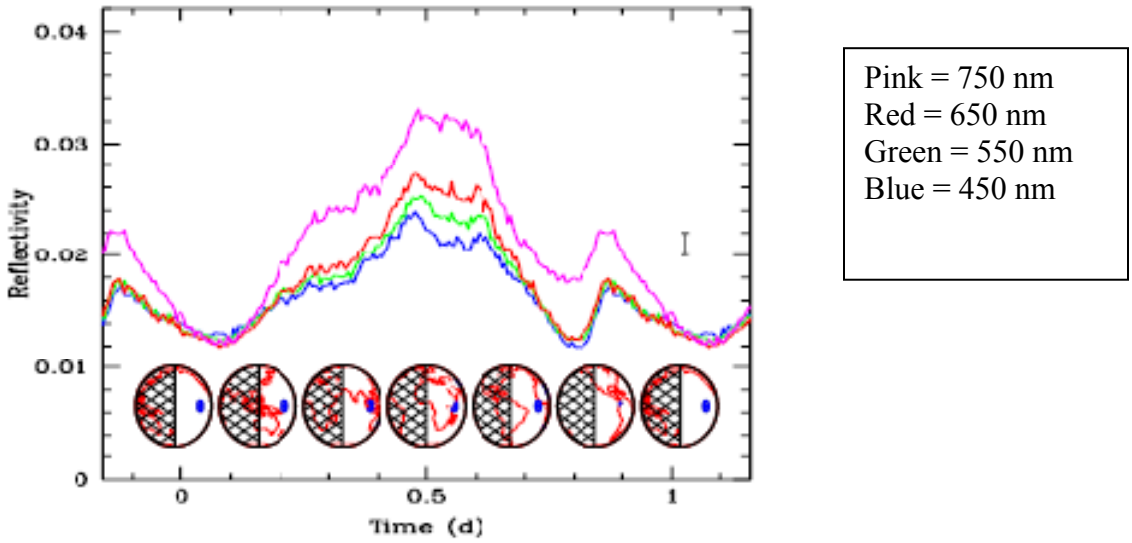

Figure 19: Disk-averaged diurnal light curve from a distant Earth, from Ford et al. 2001

The authors conclude that qualitative changes in surface or climate generate significant changes in the predicted light curves. They also note that for Earth-like planets, we can expect large daily flux variations for planets with partial ice and cloud cover.

The Ford et al.(2001) model predicts that a number of interesting features that should be discernible in light curves obtained by low-precision photometry from TPF or Darwin:

- Meteorological variability;
- Rotation period;

and with less certainty:

- Ocean/land fraction;
- Ice cover;
- Cloud cover;
- Earth-like plant life (red edge).

An interesting but unfortunately unpublished paper by McCullough (2006) reports experiments using painted spheres to simulate planets, and a modeling effort where he builds on the previously mentioned work of Manalo-Smith et al.(1998), Ford et al. (2001), and others.

For the physical model, McCullough built a simplified orrery (model of the Solar System) by painting wooden spheres with acrylic paint. Spheres were painted flat white, flat white with a glossy transparent acrylic overcoat, and flat black with the transparent overcoat – and hung in a darkened room, where they were illuminated only by a small light source. A digital camera in the plane of the sphere's "orbit" was used with a polarizing filter to take quantitative image data of polarization at a number of phase angles. Image subtraction was used to remove any light scattered from the floor, walls, and ceiling of the room. This physical model was used to confirm theoretical predictions. The author concluded that:

1) reflectance increases with angle of incidence;
2) the Brewster angle falls near maximum elongation of a circular orbit;
3) the difference between the polarized reflectances is large for nearly all of the crescent phases, which occur for phase angles greater than or equal to 90^{o}; and
4) at large angles of incidence, the glint becomes elongated rather than circular.

McCullough then developed a theoretical model based on the physical model, as well as on the earlier work of Manalo-Smith et al. (1998), Ford et al. (2001), and others. Unlike previous papers, he combined Rayleigh scattering from the atmosphere and specular reflection from the ocean surface.

Figure 21 is a diagram I constructed to depict McCullough's model, in which he combined cloud cover maps, statistical ocean wave tilt distributions, land surface types, Rayleigh scattering, observing geometries, and phase functions from his orrery (physical model).

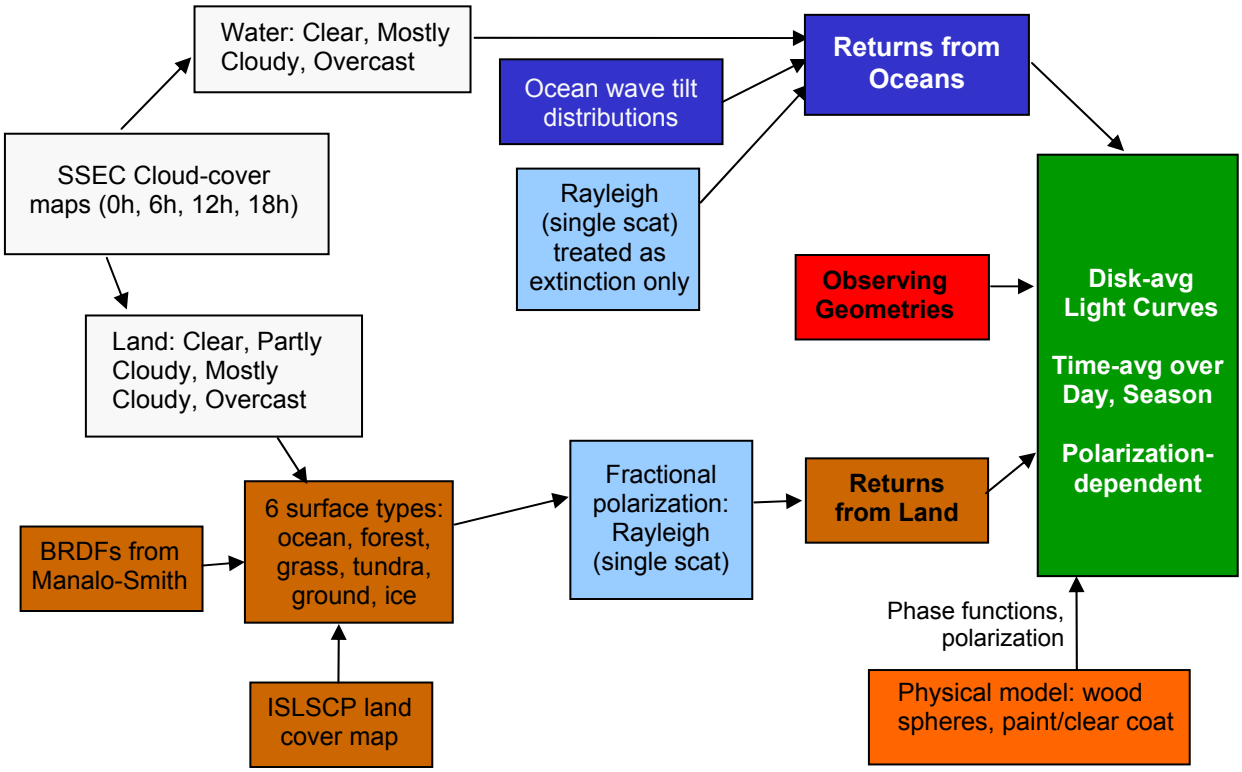

Figure 20: Block diagram depicting the construction of model in McCullough (2006)

One of the primary achievements of McCullough's work is his use of a numerical model of an Earth-like planet to show diurnal modulation of received light from continents and oceans. Using unpolarized satellite observations of Earth, McCullough generated diurnal polarization light curves of planets with a combination of oceans and continents, and phase-dependent light curves for "water world" planets. The light curves in Figure 22 (from McCullough, 2006) show his model predictions for six types of surface conditions (ocean, "land," desert, snow, ocean with only specular returns, and ocean without specular returns). Upper curves for each surface condition assume no clouds, while lower curves assume an Earth-like cloud fraction and reflectance. Lower curves with filled circle data points, in the first and last figures, are scaled from Earthshine data.

McCullough's major conclusions are as follows:

1) The maximum polarization of Earthshine is about 11% at a lunar phase angle[16] of 80^o, which corresponds to a phase angle for Earth of 100^o, based on both the author's model and Dollfus (1957).
2) An Earth-like planet around a Sun-like star at a distance of 10 parsecs, observed with a 10 m telescope, would show a difference in flux between the two polarizations of about 0.14 photon/sec, so integrated over an hour, a signal-to-noise ratio of 20 would be obtainable. If the planet rotates in about 24 hours, this would give a spatial resolution of about 15^o.
3) He also points out that Rayleigh scattering drops off as the fourth power of wavelength, but the specular reflection is essentially wavelength independent in the visible/near infrared range, so operating in the red or near IR would significantly improve the detectability of the specular reflection. (This idea is further investigated in Results, Chapter 6.)
4) The glitter pattern might be used to estimate average wind speed above an ocean, although McCullough admits this seems entirely impractical (but will be referenced if it is ever done…)
5) Sea surface glint increase and decrease as ocean and land alternately rotate into the area of specular reflection, perhaps allowing a simple mapping of continents and oceans. He then speculates on using some combinations of orbital inclination and planetary obliquity to map continents in 2D, and to search for evidence of plate tectonics based on outlines of continents fitting together, such as Africa and South America.

To summarize, McCullough (2006) produced light curves, and diagrams showing areas of diffuse and specular reflection of Earth-like planets for both an Earth day and an Earth year, with land desert, snow, ocean, ocean without specular reflection, and ocean with only specular reflection. Each of these was modeled with an Earth-like atmosphere, with and without clouds

[16] The phase angle is the angle between 0 and 180 degrees formed between the light source, the illuminated body, and the observer. When observing phases of the Moon, the angle is formed by the Sun, the Moon, and the observer on Earth. When observing Earthshine, the angle is formed by the Sun, the Earth, and the Moon; the Moon is treated as the observer, because it "sees" the phase of Earth and reflects the Earthshine back to the human observer on Earth in an approximately Lambertian way.

with an Earth-like covering fraction and reflectance. His model includes atmospheric attenuation as combined absorption and scattering, effective on both the incoming and outgoing light.

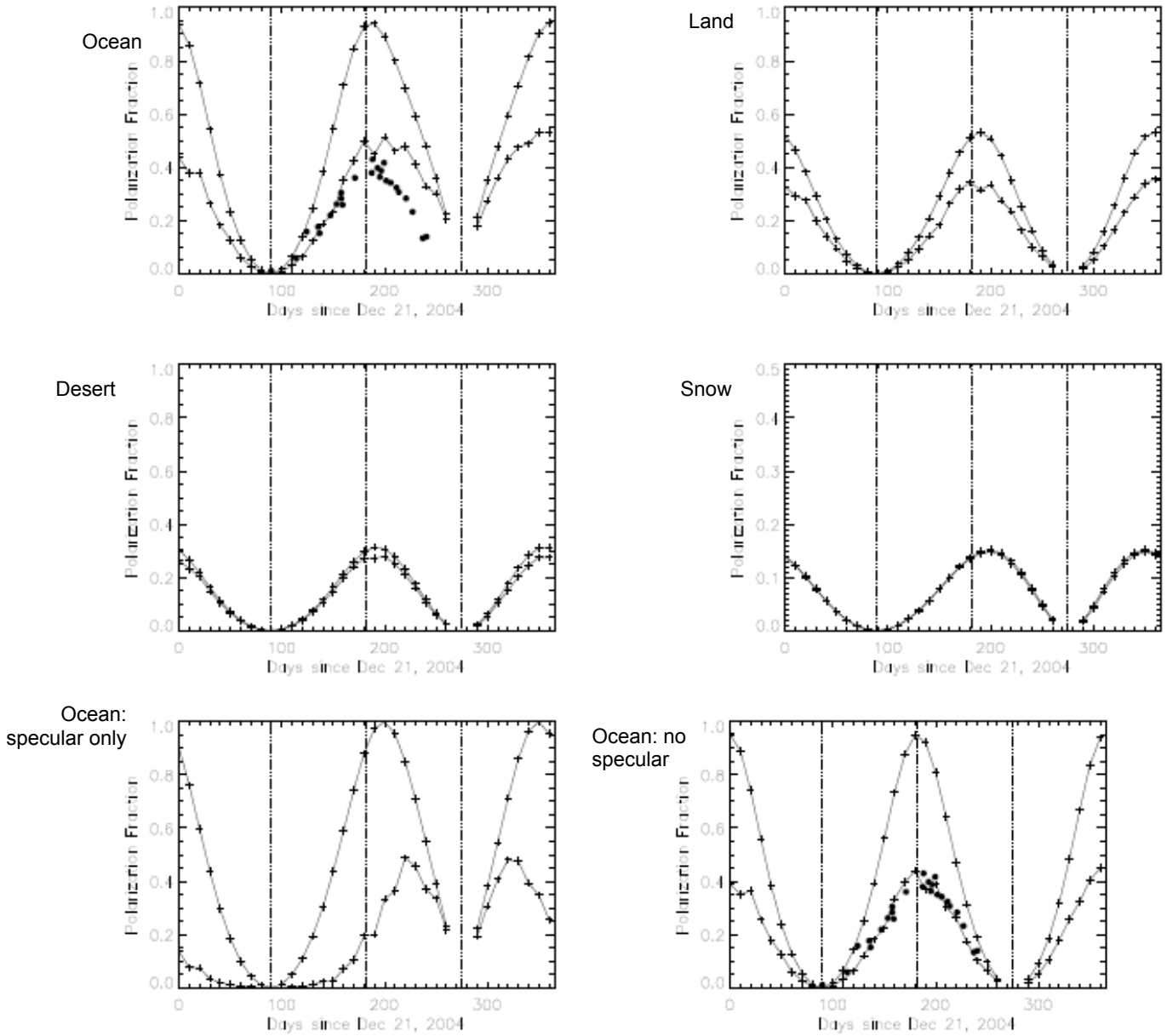

Figure 21: Calculated polarization fractions for planets composed of a single type of Earth-like terrain, from McCullough 2006. Upper curves: no clouds, lower curves: Earth-like cloud fraction and reflectance. Lower curves with filled circle data points: scaled from Earthshine data

However, incoming light scattered onto the ocean is not permitted to reflect back into the line of sight, but is assumed to be lost. Polarization components are discussed and plotted. In addition to neglecting incoming scattered light which is then reflected from the ocean into the line of sight, the model also makes the following simplifications:

- ignores interaction of polarization states of scattered and specularly reflected light;

- ignores multiple scattering (uses single scattering model, where light scattered from the path is immediately lost);
- light reflected from clouds is assumed to be completely unpolarized.

The polarization of the oceanic and atmospheric Rayleigh scattering as shown by "ocean with no specular" (bottom right in Figure 22) peaks when the star, planet, and observer are at right angles, represented by days 182 (June 21) and 0/365 (December 21), but the polarization peaks from specular reflection (bottom left) are closer to new phase/transit (day 274), because the peak of polarization from the specular ocean occurs at twice the Brewster angle of water. Figure 23 shows these planetary phase angles diagrammatically. Our results agree with McCullough's for the thin atmosphere/calm ocean case; we will further consider planetary phase angles and orbital light curves in depth in Chapter 5.3, which also includes a more detailed figure.

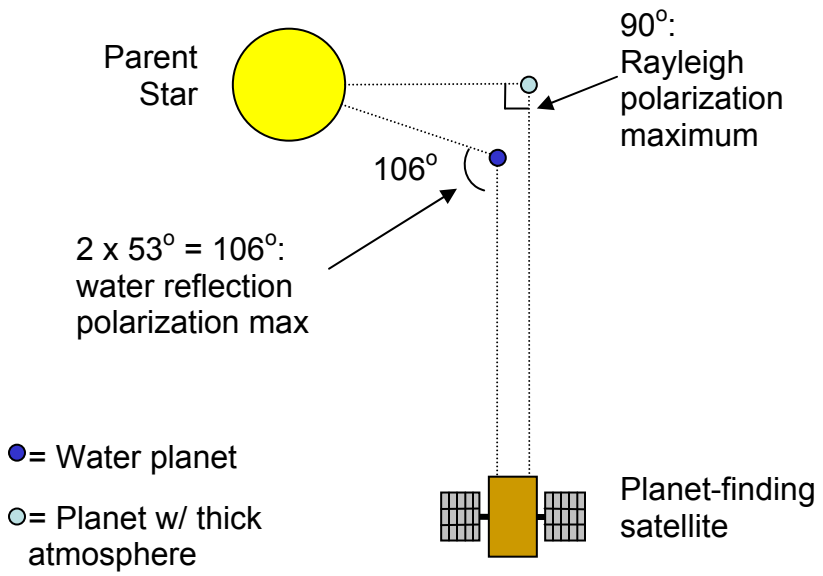

Figure 22: Analytical polarization maxima in simplified case

In Williams & Gaidos (2008), Darren Williams of Penn State Erie/Behrend College has developed an interesting model which produces light curves with polarization for Earth-like planets as well as for theoretical planets with any desired combination of Earth surfaces. I have described this model diagrammatically in Figure 24.

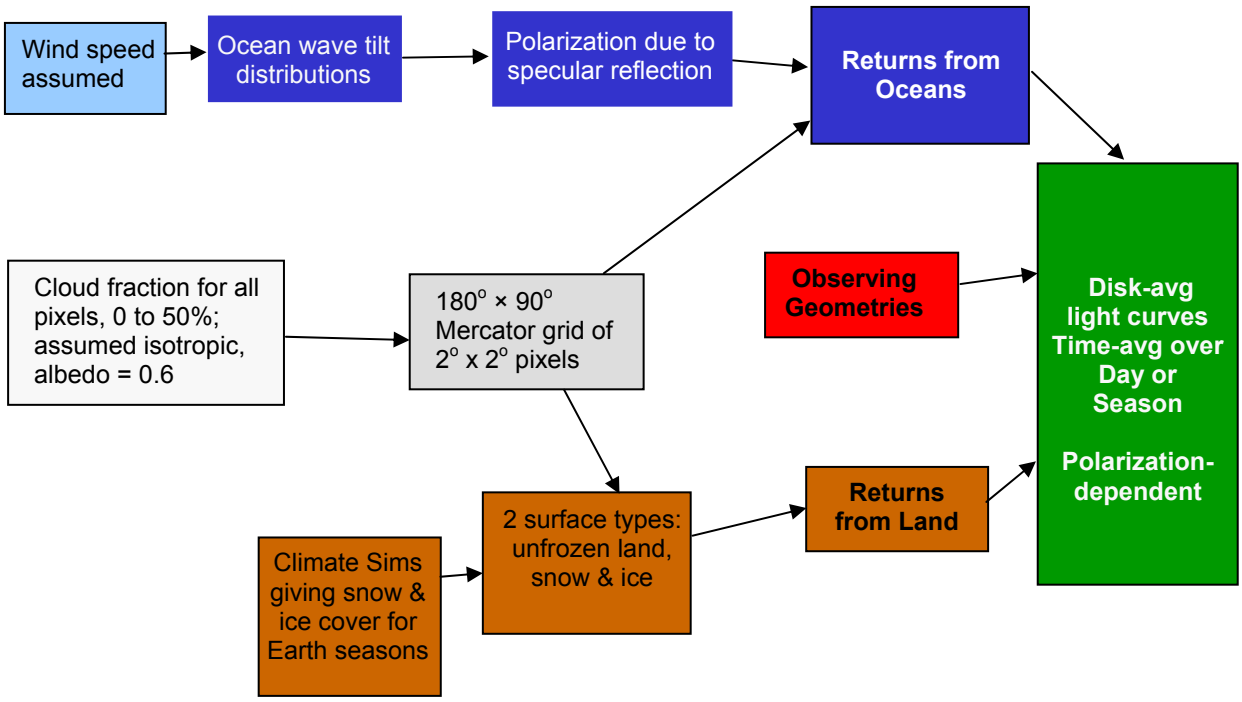

Figure 23: Block diagram depicting the construction of the model described in Williams & Gaidos 2008

The Williams model includes all characteristics of the spherical geometry, including orbital inclination, viewing angle, and Sun (star) angle, as shown in Figure 24. This output from the model shows four different orbital inclinations and phase angles, and provides animations showing the path of the model planet around its star.

The most useful outputs from the Williams model are the disk-averaged light curves, such as those shown in Figure 26. These example light curves show the fluxes and percentage of polarization from an Earth-like planet with Earth geography (left) and an Earth water world (right) for cloudless planets with an orbital inclination of 90^o (fluxes for the water world are multiplied x10 for clarity). The dark line in each figure is the polarization percentage, while the parallel and perpendicular polarization fluxes are plotted on the dotted and dashed curves, and the total fluxes are shown by the thin solid line.

Note that Williams places the left edge of his diagram at $\theta = 0^o$, which in his system corresponds to the point in the orbit when the planet is closest to the observer; this point is also known as inferior conjunction, new phase, or transit. (I follow his convention in this work.) The left edge of the Williams diagram corresponds to the ¾ point in the McCullough diagram.

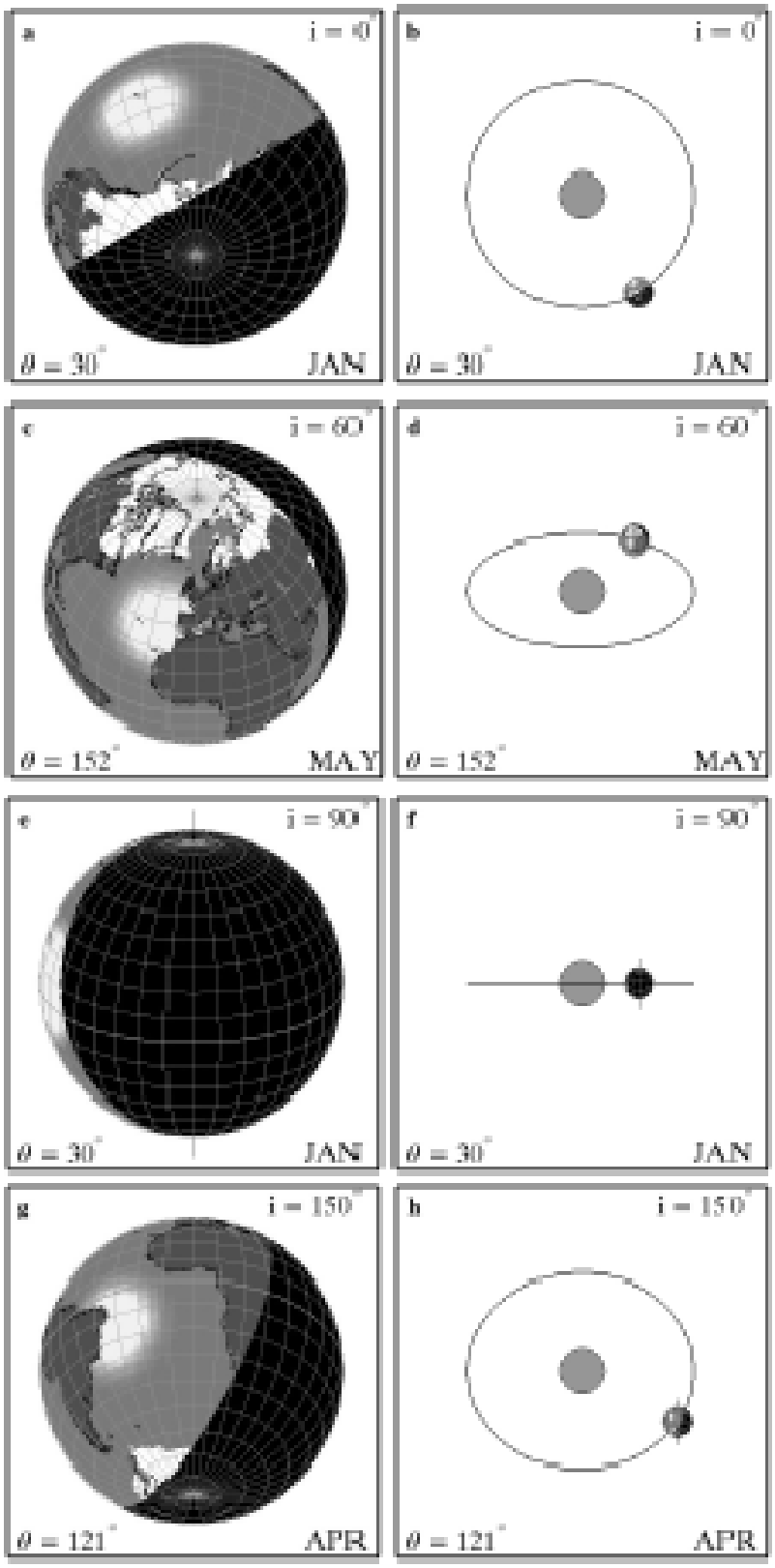

Figure 24: Depiction of Earth at various orbital inclinations and viewing angles, from Williams & Gaidos 2008

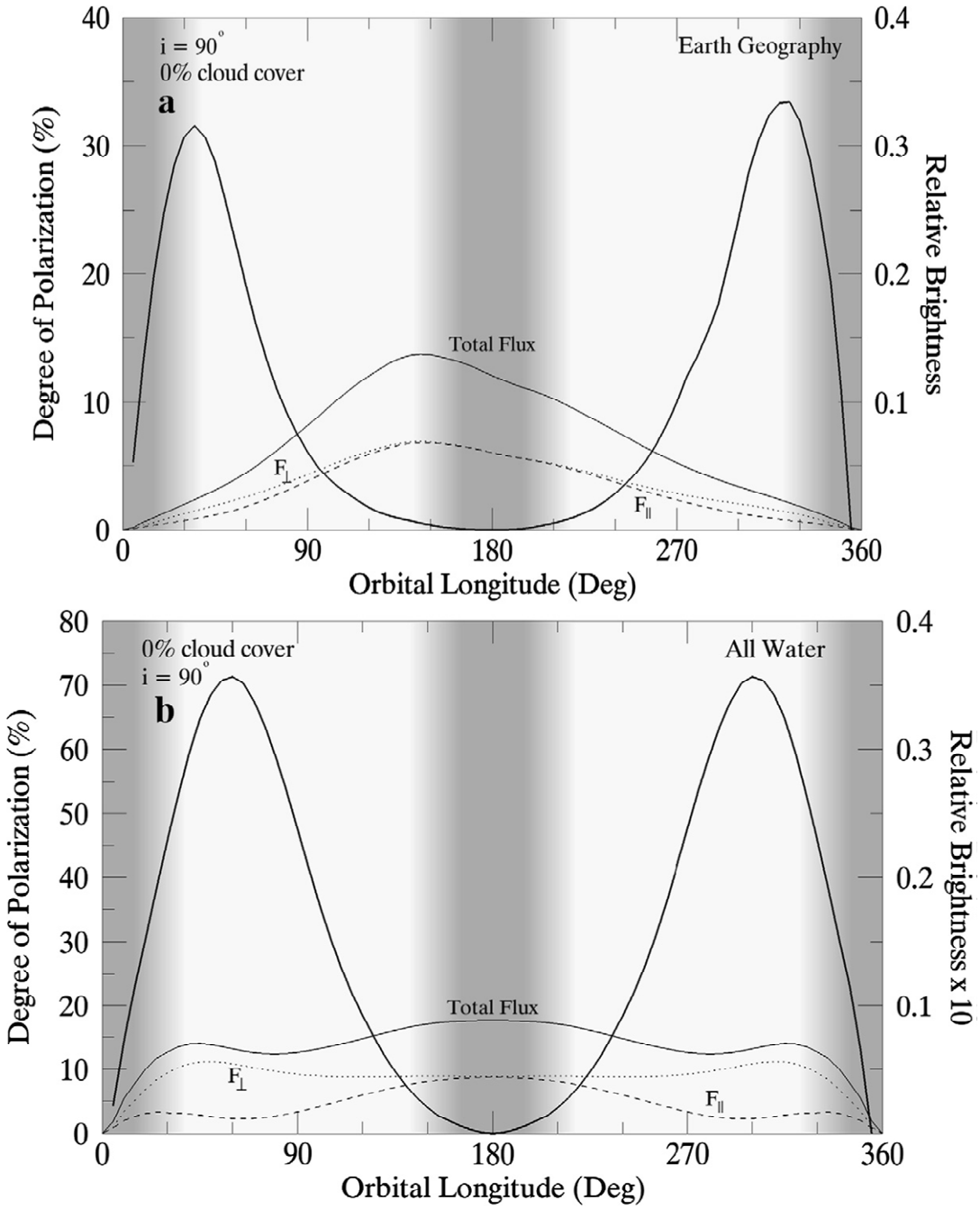

Figure 25: Total flux, parallel and perpendicular fluxes, and polarization fractions from a) an Earth-like planet and b) a water world, from Williams and Gaidos (2008)

In its original form, the Williams model included a number of useful features:

- Spherical geometry of the problem, including orbital inclination, and star/planet/observer angle;
- Effects of ocean glint, including glint area, polarization, and statistics of wave slopes;
- Terrain types: three types each of land surface and ocean surface;

- Cloud fractions - clouds are modeled simply by using a user-defined cloud fraction to replace that percentage of the surface with reflective clouds.

Except for cloud fraction, the model does not include an atmosphere – neither Rayleigh scattering by air molecules nor Mie scattering from aerosols are considered. Clearly, this represents an opportunity to upgrade the model. The model also does not perform any wavelength-dependent computations.

To summarize, Williams and Gaidos (2008) produced polarization-dependent light curves and diagrams showing areas of diffuse and specular reflection, for Earth-like planets at various orbital inclinations, with a variety of surface types including wavy oceans, with no cloud cover and 50% cloud cover. Clouds were modeled as unpolarized reflectors; otherwise, the atmosphere was ignored (no Rayleigh scattering from either the atmosphere or ocean, and no atmospheric absorption or wavelength dependence).

Tinetti, Meadows, Crisp, and colleagues (2006) have developed an impressive model of extrasolar spectra, which includes a solar spectrum, six types of planetary surfaces, realistic observing geometries, clouds, and line-by-line atmospheric gas absorption from HITRAN2000. I have shown some of the characteristics and inputs of the model in Figure 27.

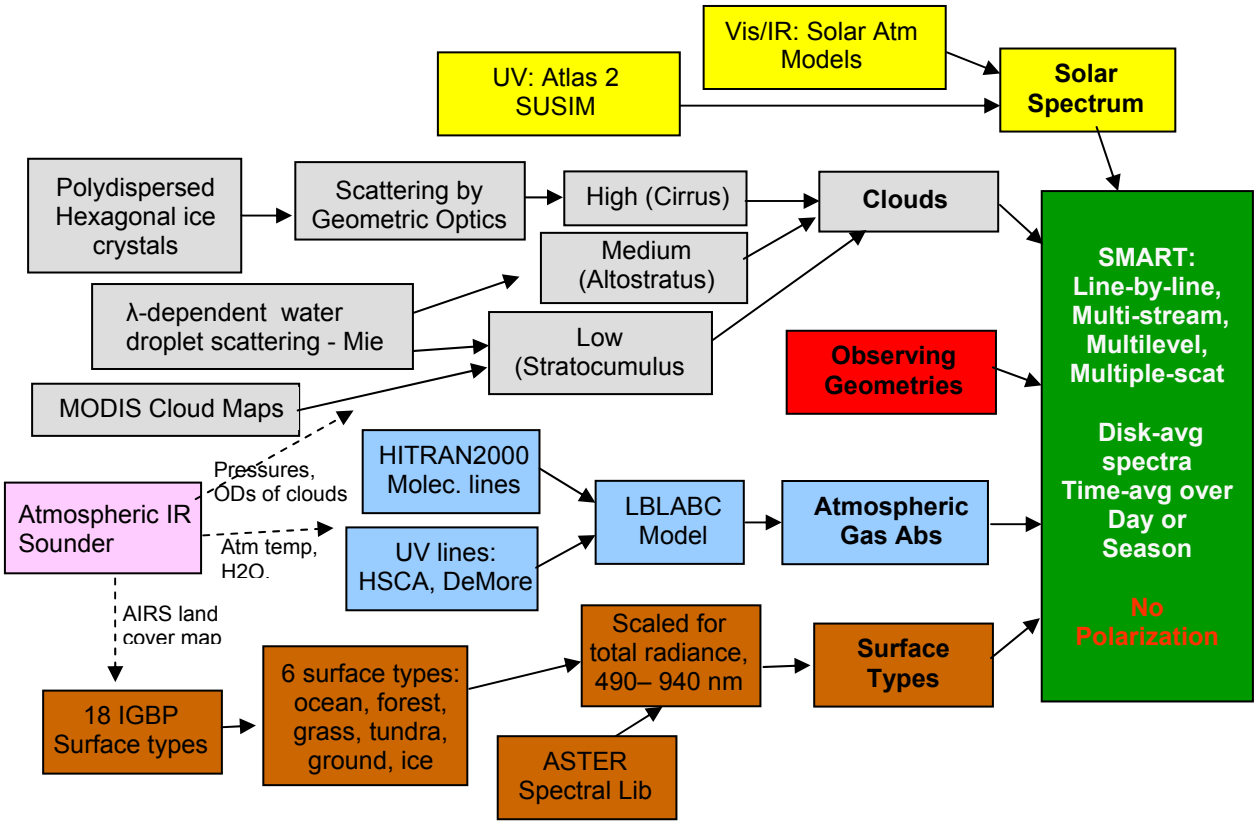

Figure 26: Block diagram depicting the complex, high-fidelity SMART model discussed in Tinetti et al. 2006

Tinetti and co-workers have perfected high-resolution line-by-line spectral transmission, and they have provided spectral calculations for the Kasting atmospheric modeling group for several papers. However, it is important to note that (1) their model does not include polarization, and (2) TPF and other missions for the foreseeable future will measure visible and infrared returns in broad bins, not high resolution spectroscopic lines. There simply will not be enough photons scattered from terrestrial planets many light years away to allow instruments to do high-resolution spectroscopy. It is possible that transits by extrasolar planets might allow testing of spectroscopic models such as this one, although the signal-to-noise ratio of transit spectra is expected to be poor even for space-based telescopes because the instrument has to stare at the star.[17]

Each of the above papers represents a significant contribution to modeling light scattering from extrasolar planets. The work of McCullough (2006) and Williams and Gaidos (2008) in particular have set the stage for the current project. Table 4 summarizes the features of the above papers which are most relevant to the present work.

[17] T. Jackson and J. Kasting, separate personal communications

Table 4: Summary of Previous Work

Model Parameter	Ford 2001	Kotchenova et al. 2006, 2007	Tinetti & Meadows 2006a, b	McCullough 2006	Williams & Gaidos 2008
Clouds	0% & 50%, unpol refl	Not included	High, medium, low (cirrus, altostratus, stratocumulus)	0% & Earth-like, unpol refl	0% & 50%, unpol refl
Rayleigh Scattering, absorption	Ignored – no atmosphere	Absorption from US 1962 atmosphere, Rayleigh multiple scattering	Absorption using HITRAN2000 data base	Single scattering on incoming and outgoing light	Ignored – no atmosphere
Polarization	Not considered	Included in model	Not considered	Discussed and Plotted	Discussed and plotted
Wavelength	Irrelevant – no Rayleigh	0.35 – 4.0 μm	Spectral char of disk-averaged planet from HITRAN2000 data	Assumed flat for single scattering	Irrelevant – no Rayleigh
Orbital Inclination	N/A	Not included, "flat Earth" geometry only	9 solar zenith angles, 4 viewing zenith, 7 viewing azimuth	Edge-on only	Face on and edge-on studied
Terrain	Permanent ice, temp/dirty ice, ocean, forest, brush, desert; 1° x 1° pixels	sand, vegetation, Lambertian, ocean, lakewater, and clear water	Disk-averaged Earth, planets with 1 type of Earth terrain	Desert, "land," snow, ocean, ocean w/o specular, ocean w/ only specular	Unfrozen land, snow & ice, sea foam, water; Earth-like geography, 2° x 2° pixels
Waves	Not considered	Included	Not considered	Distribution of tilts on air/water surface (Zeisse 1995, Takashima 1985)	Gaussian wave probability (Cox & Monk 1954, Vokroughlicky & Farinella 1995)

5.0 Development of a Planetary Scattering Model

Primary Project Goal. Our goal is to describe observable differences between end member hypothetical terrestrial planets seen at a distance, by modeling polarization-dependent and wavelength-dependent scattering from planets over TPF wavelengths 0.5 to 1.0 μm. To meet this goal, we create wavelength-dependent, polarized light curves for Lambertian, Rayleigh-dominated, and ocean planets, as well as planets with scattering from both surfaces and atmospheres, including water Earth, all orbiting a Sun-like star at 1 AU.

5.1 Approach

In Zugger et al. (2010) we used the atmospheric and surface modeling code 6SV, in combination with the planetary modeling code Oceans, to model light scattering from Earth-sized planets orbiting Sun-like stars. To do this, we called 6SV thousands of times to generate lookup tables of polarized reflectance versus solar zenith angle (angle of incidence), viewer zenith angle, and relative azimuth between the Sun (or parent star) and the viewer. We then used Oceans to calculate the total integrated light scattered to an observer from a planet with the surface and atmosphere described in the generated lookup table, and repeated this calculation every 2° around the planet's orbit. For simplicity in modeling Earth-like planets, we have assumed an Earth size planet in a circular orbit around a Sun-like star at the Earth-Sun distance, and we assumed that the plane of the planet's orbit is edge-on to our line of sight.

5.1.1 Overview

The model developed here consists of an atmospheric and surface modeling program (6SV) coupled with a planetary surface and orbital geometry program (Oceans). The 6SV code calculates molecular scattering and absorption, aerosol scattering, and surface effects, including water surfaces with waves, and computes polarization effects in all of these scattering calculations. We have modified 6SV and written an IDL program which calls the modified 6SV and produces a lookup table of calculated scattering in both polarization components for thousands of combinations of stellar zenith angle, viewer zenith angle, and relative azimuth.

The Oceans code was developed originally by Williams, and used to simulate scattering from planets without atmospheres (Williams & Gaidos 2008). We have modified this code to use lookup tables generated by 6SV as inputs. The Oceans code computes the 3-D geometry of extrasolar planet orbits, calculates the light scattered to the observer at both polarizations from each 2° x 2° grid area on the planet, sums all of these contributions over the illuminated surface of the planet at each orbital point, and generates light curves and graphics illustrating orbit parameters, for planets without atmospheres. As modified for this work, the Oceans code also rotates the polarization reference plane from a ground-referenced system used by 6SV to the scattering-plane reference before summation. See Appendix C for details of the modifications to Oceans, and the other new IDL code developed for this project. Appendix D describes the modifications to Oceans to rotate the Stokes parameters, and Appendix E describes the

algorithms and routines added to Oceans which allow partial compensation for the plane-parallel atmosphere approximation.

5.1.2 New Model Development

In order to better understand the reflected signatures of exoplanet oceans, and the instrumentation necessary to see them with TPF, we carry exoplanet modeling beyond prior work as detailed below. Specifically, our goal is to model observable differences between terrestrial planets seen at a distance by modeling polarization-dependent and wavelength-dependent scattering from planets over TPF wavelengths 0.5 to 1.0 μm, possibly extended to 0.3 to 1.7 μm, or 0.2 to 2.0 μm. To meet this goal, we create wavelength-dependent, polarized light curves for hypothetical end-member exoplanets and a water world Earth, all orbiting a Sun-like star at 1 AU.

In order to achieve the above goal, we model the geometry of the planet orbiting the parent star, with an orbit edge-on to our line of sight from Earth; then we model the geometry of the light path, which includes the Solar zenith angle, the viewer zenith angle, and the azimuth angle between the two.

5.1.2.1 Williams' Oceans Model

During the literature search we found Darren Williams' Oceans model, which models all of the above geometry (Williams and Gaidos 2008). The Oceans program also includes a number of surfaces, including oceans with waves, as well as cloud fractions, but does not include any other atmospheric effects[18]. For point in the planet's orbit, and for each 2^o x 2^o element of surface grid, on the planet, the original Oceans code calculated polarized and total scattering from the surface type assigned to the grid element. For the new model, we decided to combine the Oceans geometry model with an atmospheric model.

5.1.2.2 Atmospheric Scattering

Previous exoplanet light scattering models use simplified atmospheres such as a thin, single-scattering molecular atmosphere without molecular absorption or aerosols. In addition to ignoring multiple scattering, thin atmosphere assumptions ignore depolarization of glint reflections by Rayleigh scattering of the outgoing light. For a moderately thick atmosphere, both polarization by Rayleigh scattering and depolarization of reflection-polarized glint can be significant effects. Our model includes multiple scattering, molecular absorption, and aerosol scattering, making it the first complete and realistic model of disk-integrated scattering from a water planet with an Earth-like ocean.

5.1.2.3 Contributions from Oceans and 6SV

[18] I contacted Darren Williams, and he expressed interest in working together on the project, and provided his code and associated files.

We concluded that the best path forward would be to combine the geometry portion of the Oceans code with the atmospheric and surface modeling from the 6SVcode, along with additional software and input files, to create a combined model capable of accurately predicting polarized light curves from extrasolar terrestrial planets.[19] In fact, both Williams' Oceans program and the atmospheric modeling software 6SV include modeling of surfaces. The 6SV code was intended for MODIS simulations, so it does everything from the Solar source, through the atmosphere both ways, and includes polarized radiance due to both the atmosphere (Rayleigh + aerosols) and the surface. We decided to use the 6SV surfaces because (1) it would be more difficult to deconvolve surfaces from 6SV than from Oceans, and (2) the 6SV code is involved in a continuing multi-code validation project with the MODIS instrument.[20]

Note: The 6SV software specifies the Stokes parameters in the coordinate system associated with the direction of propagation of incident light. In order to obtain the Stokes parameters oriented with respect to the TPF coordinate system, we rotate them in Oceans using the transformation matrix (Hansen and Travis 1974; Liou 2002; Tilstra et al. 2003; Kotchenova et al. 2006) as described in Appendix D.

To summarize, the Williams model includes:

1. Spherical geometry of the problem
2. Polarization due to ocean glint
3. Terrain types, cloud fractions

The Williams code does not include:

1. Molecular (Rayleigh) scattering
2. Scattering from aerosols
3. Wavelength dependence
4. Multiple scattering
5. Reflection of downgoing scattered light to add to surface illumination

The 6SV model includes:

1. Atmospheric transmission from Sun to Earth, back up to satellite
2. Atmospheric molecular scattering, aerosol scattering, and molecular absorption
3. Surface reflectances (BRDFs) including irregular surfaces, common Earth surfaces, including water with waves.

The 6SV model lacks these features that we include from the Oceans model:

1. the 3D geometry of the problem,
2. integration over all of the pixels,
3. clouds,
4. 3D plots, and
5. light curves.

[19] I contacted Eric Vermote, who co-developed the polarized version of the 6S radiative transfer code at the Laboratoire d' Optique Atmospherique, the University of Maryland, and NASA/Goddard; he provided the source code, but noted that he was fully subscribed and could only help briefly with getting me started.

[20] http://rtcodes.ltdri.org/Description_of_the_codes_simple.htm

5.1.2.4 Original Model Architecture: Linux bash script calling 6SVlut

As usual, there were several false starts in the development process; the most time consuming of these were

- initial use of a Linux script (written in the "bash" scripting language) to call 6SV, later replaced by the much more capable and intuitive IDL program "bilut;"
- use of the unreleased version of 6SV called "6SVlut;" however, testing showed that 6SVlut reported only unpolarized reflectance.

These are explained briefly below. Figure 27 diagrams the earlier method I used to generate lookup tables using a Linux script and the 6SVlut version.

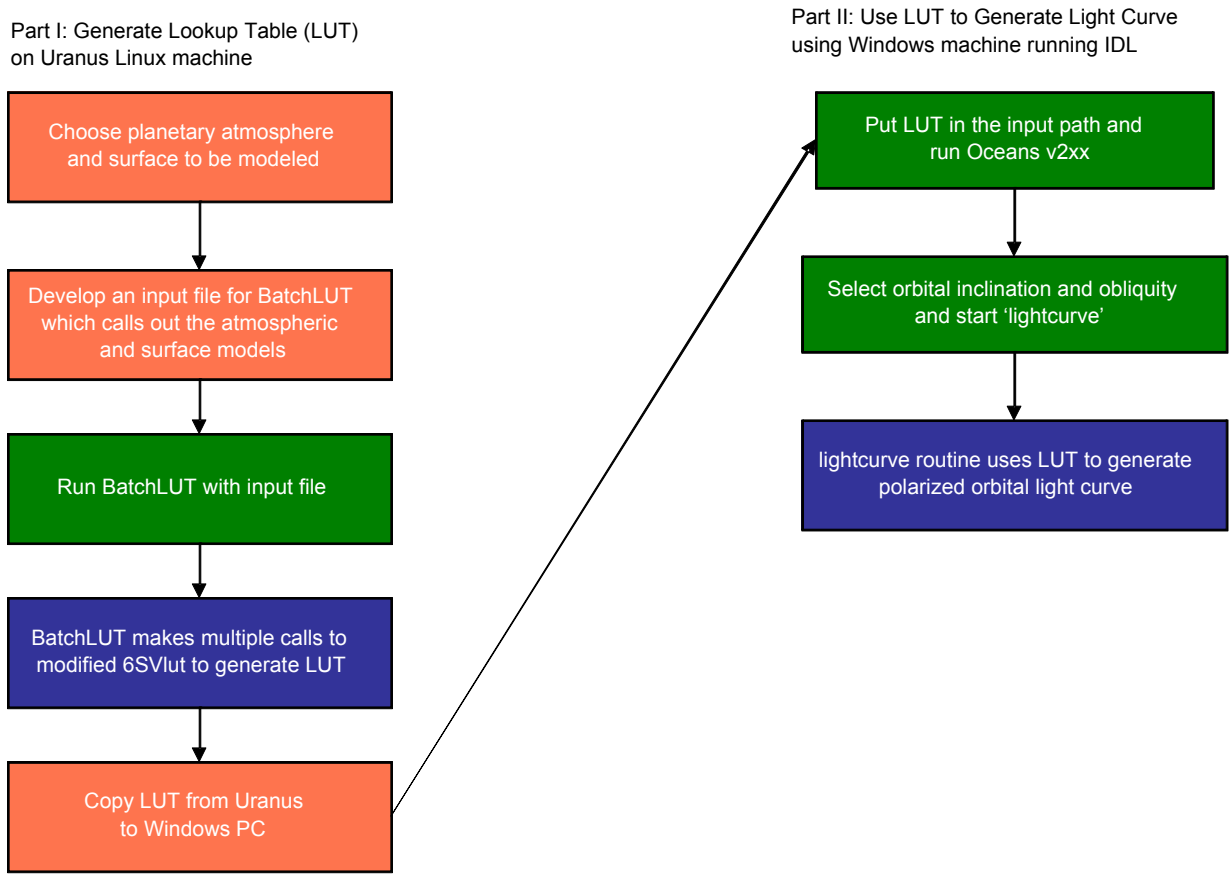

Figure 27: Early version of model architecture using a Linux script to call the lookup table version of 6SV, called 6SVlut

The 6SVlut version calculates lookup tables for MODIS; these tables include a number of quantities calculated for various viewer zenith angles and relative azimuth angles, for a given solar zenith angle. Eric Vermote recommended I use this version, as it saves significant computer time when generating a lookup table by using internally generated values.

Unfortunately, after a significant amount of work, I realized that 6SVlut was not calculating polarized flux or reflectance. I contacted Eric Vermote, and he agreed that polarization was not reported in 6SVlut, although he believed it was calculated at some level in the code. After

spending some time attempting to add polarization to 6SVlut, I eventually abandoned the effort and returned to the standard 6SV. Also, using the bash scripting language proved to be extremely cumbersome and difficult to modify and troubleshoot, so eventually I replaced the bash script with an IDL program.

5.1.2.5 New Model Architecture: IDL program *bilut* calling 6SV

In the combined model (block diagram shown in Figure 28), a lookup table (LUT) is generated using calls to 6SV with various combinations of solar and viewer zenith angles and relative azimuth. The LUT is then used to generate a light curve showing parallel and perpendicular fluxes versus orbital longitude. The LUT is a table of reflectances of the two polarizations, in the Stokes parameters I, Q, and U, which include the summed reflectances of the surface and the atmosphere.

In the second half of the model, the LUT is used to generate a lightcurve text file, which includes parallel, perpendicular, and total fluxes versus orbital longitude (OL). The IDL program that accomplishes this is called Oceans. Oceans divides the planet into a grid, typically 2° latitude x 2° longitude, and divides the orbit up discretely, typically into 2° segments. For each point on the half orbit (symmetry is used to calculated the other half), Oceans calculates the flux reflected per pixel and sums them. For each pixel, the solar zenith angle, viewer zenith angle, and relative azimuth are calculated, and the LUT is consulted. Typically there is no exact match, so the closest matches above and below the input angle combination in each direction are used to form a "cube" of eight neighbors around the input angle combination. The reflectance of the pixel is then calculated by a 3D interpolation between these 8 closest neighbors. The pixel reflectance is then multiplied by the pixel size, which drops off as the cosine of latitude, and by the solar constant, which drops off as the cosine of solar zenith angle.

The Oceans code also displays some graphics showing the orientation of the planet and star, including orbital inclination and the inclination of the planet's axis (Figure 29). The original Oceans code allows the user to rotate the Earth on its axis and move the planet around on its orbit, but the reduced version Darren Williams provided does not include these motion graphics.

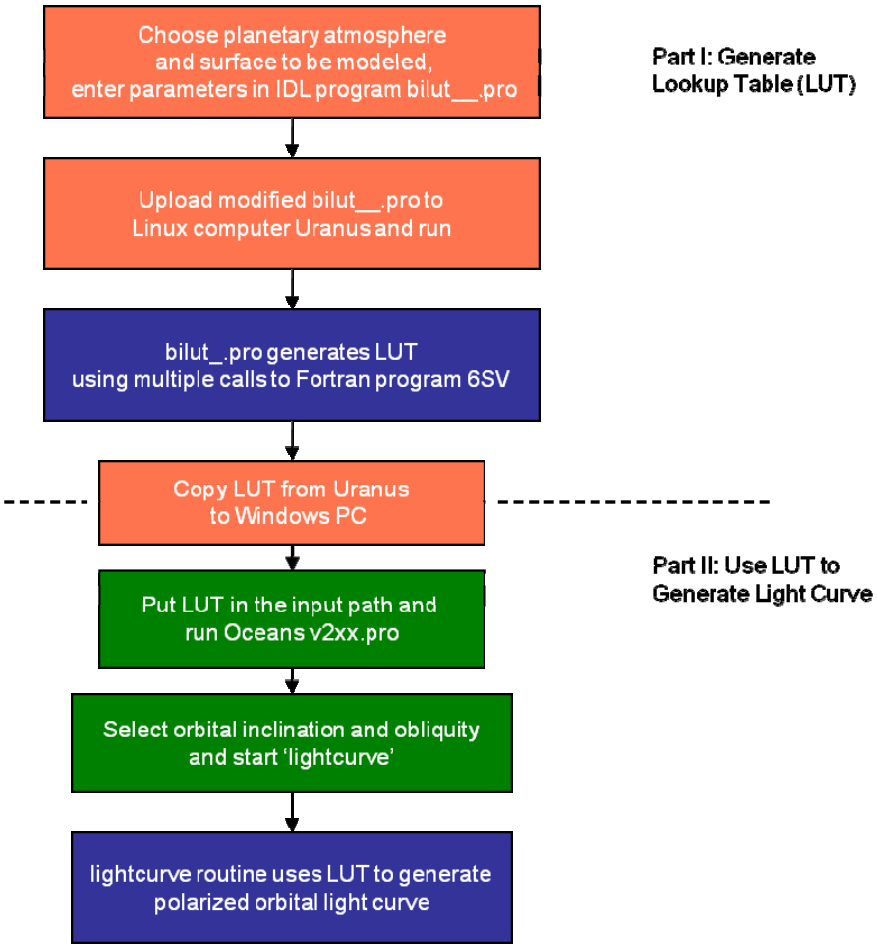

Figure 28: Block diagram of final model configuration, showing interaction between modified 6SV, modified Oceans, bilut IDL program, and user

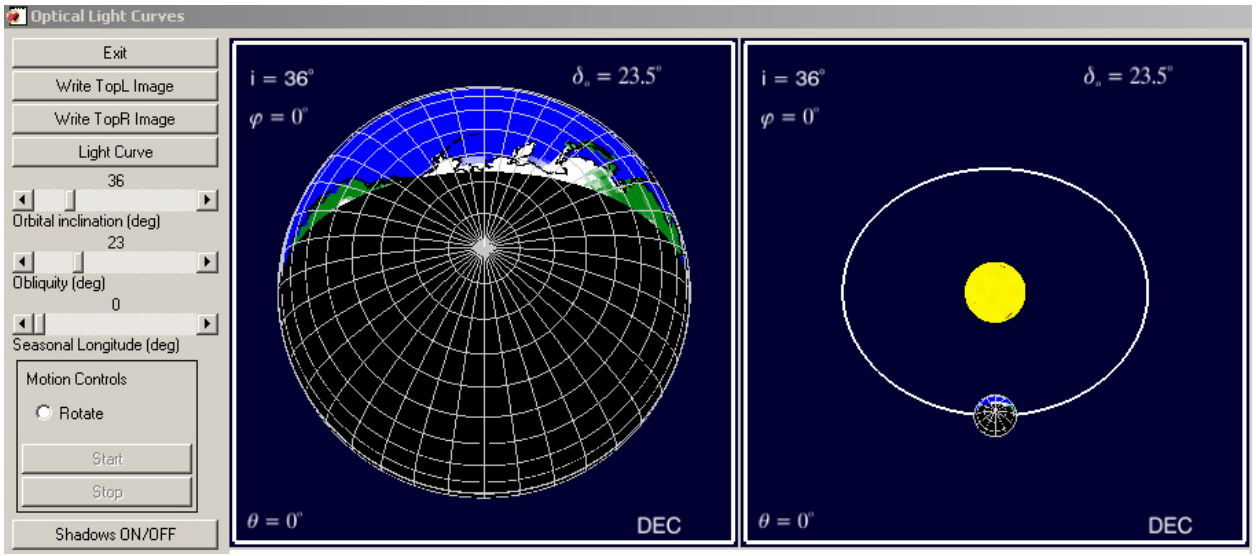

Figure 29: Front panel from Oceans v2xx showing the available GUI controls (left bar), as well as the orbital inclination, axis obliquity, and illuminated fraction of the planet

5.1.2.6 Modifications to 6SV

The 6SV code has been used to calibrate the MODIS instruments on the Earth-observing satellites Aqua and Terra, and it was recently verified against other codes and actual data for some cases (Kotchenova et al. 2006; Kotchenova and Vermote 2007). It has some inherent limitations, however, so we modified it as follows:

1) The code as written reports "apparent reflectance," which assumes a diffuse surface, and for ocean surfaces calculates a reflectance that increases without limit for large zenith angles (see sections 5.2.2 and 5.2.3 for more on this). We modified the code so that it reports reflective Stokes parameters for ocean and diffuse Lambertian surfaces as values between zero and one, with a perfect mirror being assigned the value of unity. For ocean surfaces, we did this by replacing the wave tilt probability formula used in two subroutines of 6SV, and adding appropriate output statements to the main routine;

2) The above change in the ocean surface model also made the model insensitive to wind direction[21], which should be viewed as beneficial, as this will generally be unknown and variable over time and space for an extrasolar planet;

3) We modified the Rayleigh scattering algorithm to allow exact round-number values of optical depth to be used for figures.

We also developed an algorithm to use the Kasten & Young (1989) equation to partially compensate for the difference between the plane-parallel and spherical atmosphere assumptions, but the resulting maximum difference in the integrated light curves was less than 1% (see Verification and Error Analysis, section 6.3).

5.1.2.7 Model Wavelength Ranges

To model hypothetical planets we must of course make some assumptions; with regard to wavelength, we do this in three different ways. The three cases are:

1) Lambertian surfaces, Lambertian clouds, and dark surfaces are assumed to be gray, and thus these results are independent of wavelength given that the albedo modeled corresponds to the albedo of the surface or cloud in the wavelength band of interest;

2) For the water Earth models, we assume an Earth-like Rayleigh scattering atmosphere, molecular absorption, and maritime aerosols, and specify the baseline TPF waveband of 500 – 1000 nm;

3) For other cases, we parameterize Rayleigh scattering by atmospheres of hypothetical planets by showing how the planetary light curve changes with the Rayleigh optical depth τ_R. When we

[21] Sensitivity testing showed that rotation of the wind direction produced a variation of less than 1% in polarization fraction and contrast ratio.

parameterize by τ_R, each curve for a given τ_R can represent a range of combinations of wavelengths and atmospheric densities.

In order to give a sense of scale, the captions for the results figures in Chapter 6.2 include the equivalent wavelength range for an Earth-like Rayleigh scattering atmosphere corresponding to each value of τ_R for cases 2) and 3), and for case 1), states that the curves are wavelength independent.

5.2 Atmospheric and Surface Model: 6SV Use and Modification

5.2.1 Detailed Description of 6SV

The Second Simulation of a Satellite Signal in the Solar Spectrum-Vector (6SV) atmospheric code is a Fortran 77 radiative transfer code using successive orders of scattering. Originally developed by the Laboratoire d'Optique Atmospherique and the European Centre for Medium Range Weather Forecast as 5S, then 6S, a vector version (6SV) was later developed to compute polarization (Kotchenova et al. 2006; Kotchenova and Vermote 2007). The 6SV code simulates molecular scattering and absorption, aerosol scattering, and surface effects, including Lambertian land surfaces, and water surfaces, and computes polarization effects in all of these scattering calculations. The code is used to calculate look-up tables for the MODIS[22] (Moderate Resolution Imaging Spectroradiometer) instruments (Vermote and Kotchenova 2008) aboard the Terra and Aqua[23] Earth-observing satellites, as well as in other applications in remote sensing and modeling of terrestrial light scattering.

The code is included in a continuing validation effort against the MODIS instrument, Coulson's Tables (Coulson et al. 1960), and other radiative transfer codes (Kotchenova et al. 2006; Kotchenova and Vermote 2007)[24].

5.2.1.1 Code Applicability

The 6SV code was designed to model the polarized, wavelength-dependent flux received by a satellite or aircraft above the Earth's surface due to scattering from the atmosphere and the surface. The code models gaseous absorption, molecular and aerosol scattering, and a number of common Earth surfaces over the wavelength range 350 nm to 3.75 μm. Gaseous absorption is modeled for the chief absorbers in Earth's atmosphere, which are water vapor, CO_2, O_2, O_3, CH_4, and N_2O.

5.2.1.2 Modifications

I modified the code to provide the Stokes parameters and to calculate the parallel and perpendicular flux, and also to put the values in columns for easy extraction by the modified

[22] http://modis.gsfc.nasa.gov/
[23] http://terra.nasa.gov/ and http://aqua.nasa.gov/ respectively
[24] For details of this validation effort, see http://rtcodes.ltdri.org/Description_of_the_codes_simple.htm.

Oceans code. Also, I wrote an IDL file which generates input files for 6SV, calls the modified 6SV multiple times with a series of solar zenith angles, concatenates all of these values into a single table, and saves to the LUT directory with a name which includes the wavelength range, the aerosol model, the altitude of the target, and the surface reflectance model. For details on the modifications of 6SV, see Appendix F.

5.2.1.3 Code Format

The 6SV code is written in Fortran 77, the last official version of Fortran that still has column position rules. This means that code statements appear only between columns 7 – 72; the other columns are reserved for control characters. Specifically, a "c" or "*" in column 1 indicates that the row is a comment row; statement labels, which are used by GOTO and other commands, appear in columns 1-5; and a character in column 6 (usually &, +, or sequential natural numbers 1, 2, …) indicates that the line is a continuation from the previous line. Columns 73 – 80 are reserved for sequence numbers, which were originally used to keep Fortran punch cards in order.

5.2.1.4 Code Computation Method

The 6SV code uses the Successive Orders of Scattering (SOS) approximation, as described earlier. The code computes integrals using Gaussian quadrature[25] to approximate the integrals. In this technique, a continuous function f(x) is approximated by a summation of values of a discrete function $f(x_i)$ multiplied by a series of weighting functions w_i:

$$\int_{-1}^{1} f(x)dx \approx \sum_{i=1}^{n} w_i f(x_i) \tag{38}$$

where the points x_i are properly chosen, and the range of integration is taken as -1 to +1 by convention.

5.2.1.5 6SV Structure

The 6SV manual (Vermote et al. 2006) provides a block diagram showing the user inputs and the computations which 6SV performs; this diagram is shown here as Figure 30.

[25] For more information on Gaussian quadrature, see http://en.wikipedia.org/wiki/Gaussian_quadrature

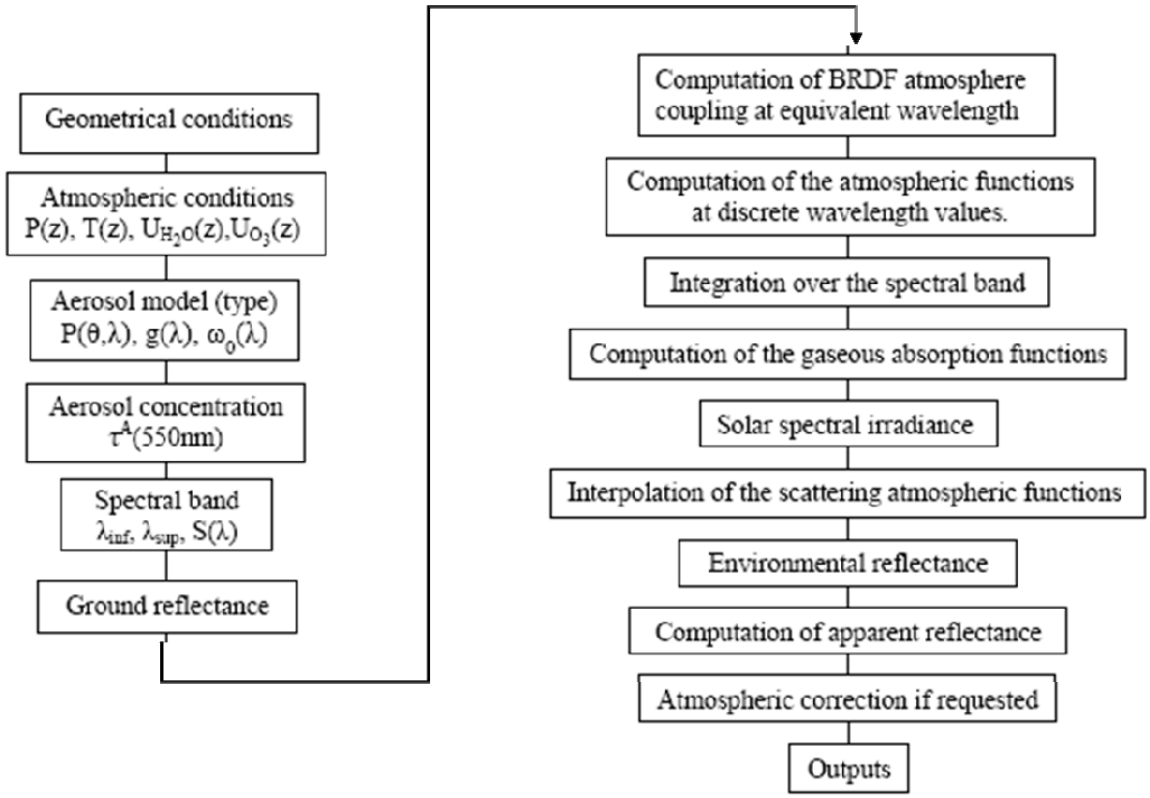

Figure 30: Block diagram of 6SV from the 6SV manual, Part I, p 33 (Vermote et al. 2006)

5.2.1.6 6SV Model Details

The 6SV code approximates the vertical structure of the atmosphere with 30 layers, and solves the radiative transfer equation for each layer. An Earth-like pressure and temperature profile is assumed. The code performs numerical integration using decomposition in Fourier series for the azimuth angle, and using Gaussian quadratures for the zenith angle. The 6SV code uses 48 angles to simulate scattering without aerosols; for aerosol simulations, 83 angles are used, including 0°, 90°, and 180°. Polarization is incorporated by calculating the first three Stokes parameters (I, Q, and U); circular polarization (V) is ignored. The effects of wavelength are included by using 20 node wavelengths between 0.25 and 4.0 μm and interpolating between them. We include absorption in the water Earth models; this is computed by 6SV for O_3, H_2O, O_2, CO_2, CH_4, and N_2O using statistical band models with a resolution of 10 cm^{-1}. Earth-like altitude profiles are used for ozone and water vapor, and the other species are assumed to be well mixed.

We also include the effects of maritime aerosols in the water Earth models. Maritime aerosols are modeled after those found over Earth's oceans, and consist of a mixture of water droplets and crystals of sea salts. The parameters of maritime aerosols are as described in Levoni et al. (1997), and an exponential aerosol profile with a scale height of 2 km is assumed. The size distribution of the aerosols is then calculated by assuming a log-normal distribution, normalized so that the extinction coefficient at 550 nm corresponds to the visibility selected by the user. We

follow U.S. Air Force Research Lab convention (McClatchey et al. 1972) in using 5 km as the standard for poor visibility aerosol (hazy conditions), and 23 km as the standard for good visibility, and add some higher visibility conditions (e.g. 80 km) for comparison. The 6SV code then computes the aerosol scattering using the Lorenz-Mie solution.

5.2.2 Physical Background of Atmosphere/Surface/Observer Interaction

The 6SV code was developed for modeling observations by Earth-observing satellites, so the solar spectrum is built in to the model. Also, we are interested in wavelengths of 1 μm and shorter, and in this wavelength range, solar radiation received at the Earth dwarfs black-body emission from the Earth; the same would be true for the Earth-like planets we model.

The 6SV manual notes that there are a number of things that can happen to a photon between the Sun (or other parent star) and the sensor on a satellite (or planet finder near Earth). The photon can be:

1. Absorbed by the atmosphere, principally by O_3, H_2O, O_2, CO_2, CH_4, and N_2O. The 6SV code uses statistical band models with 10 cm^{-1} resolution to model these species. Ozone and water vapor are given altitude-dependent profiles, while the other species are considered well mixed.
2. Scattered elastically by the atmosphere before reaching the ground. These photons can then continue on and be:
    a. Backscattered to space and lost;
    b. Scattered to the observer;
    c. Scattered by the atmosphere multiple times; or
    d. Scattered to the ground. The photons scattered to the ground can then be:
        i. Reflected from the ground to space and lost;
        ii. Reflected from the ground to the observer;
        iii. Scattered again by the atmosphere; or
        iv. Absorbed by the surface and lost.
3. Reflected from the ground. These photons can then be:
    a. Transmitted to space and lost;
    b. Transmitted to the observer;
    c. Scattered by the atmosphere to the observer;
    d. Scattered multiple times by the atmosphere; or
    e. Scattered by the atmosphere back to the ground.

Clearly, both multiple scattering in the atmosphere (2c and 3d) and the atmospheric scattering/surface reflection "trapping" effect (2d and 3e) can continue without limit, but the 6SV authors note that the effect converges quickly for Earth, and after one or two iterations, can be neglected. In a 92-bar CO_2 atmosphere like that of Venus, the two-iteration assumption might lead to significant errors; however, the thick cloud layer of Venus prevents this from being an issue. It is possible to imagine a planet with little cloud cover, a highly scattering but low absorption atmosphere, and a highly reflective surface, such as snow or white sand, where the trapping effect could dominate; however, a water surface reflects only 2% of visible light at

normal incidence, so atmospheric/surface multiple-reflection trapping is a complication we will ignore for now.

Note that the authors of the 6SV code wrote the code for use by groups using remote sensing to study Earth's surface, so they consider photons scattered to the observer by the atmosphere without interacting with the surface (2b above) to be noise. The code includes a feature called "atmospheric compensation" which attempts to decouple and remove the effect of the atmosphere (atmospheric compensation is disabled for this work). In exoplanet research, photons scattered by the atmosphere tell us something about the atmosphere of the exoplanet, and are polarized at and near a scattering angle of 90^o, so researchers looking for water would consider them noise, but those looking for evidence of an atmosphere would consider them signal.

Another point to note is that photons scattered by the atmosphere back to the ground (2d and 3e) provide additional illumination to the surface, which can result in increased signal, or noise. The authors of 6SV need to be careful in treating these photons, especially in geographic areas where the surface varies (inhomo = 1). In modeling hypothetical distant exoplanets, we deal only with planets which have the same surface type across a 2^o x 2^o pixel (inhomo = 0), so we can neglect these issues.

5.2.2.1 Absorption

The physics of molecular gaseous absorption are discussed in Section 3; here we touch on the treatment of absorption by the 6SV absorption subroutine, ABSTRA. In order to give accurate wavelength-dependent absorption results without excessive computation time, 6SV divides the Solar spectrum into 10 cm^{-1} resolution bands with values from the HITRAN database.

5.2.2.2 Scattering Effects

Here we repeat the 6SV manual's derivation of the fundamental equation, expanding on and clarifying the portions which relate to the task at hand, and skipping the portions that do not impact on our application. The simplest surface of interest is a uniform, Lambertian surface. First, we define the relevant quantities:

Reflectances:
ρ^* = equivalent reflectance
ρ_t = reflectance of the target
ρ_a = reflectance of the atmosphere

Radiances and Fluxes:
L = measured radiance
E_s = Solar flux at the top of the atmosphere

Transmittances and optical thicknesses:
τ = optical thickness of the atmosphere

Angles:
θ_s = Solar Zenith Angle (SZA)
$\mu_s = \cos(\theta_s)$
φ_s = Solar Azimuth (SAz)
θ_v = Viewer Zenith Angle (VZA)
$\mu_v = \cos(\theta_v)$
φ_v = Viewer Azimuth (VAz)
$\Delta\varphi$ = Relative Azimuth (RelAz)

$$\rho^* = \frac{\pi L}{\mu_s E_s} \tag{39}$$

where the angles are as shown earlier in Figure 18.

We now consider the successive orders of scattering of radiation between the Sun, the target surface on the Earth, and the satellite. We start with the largest, the original direct Solar flux, as attenuated by the atmosphere and the cosine of the zenith angle. The flux reaching the target is then:

$$E_{sol}^{dir} = \mu_s E_s \exp(-\tau / \mu_s) \tag{40}$$

as shown in Figure 31.

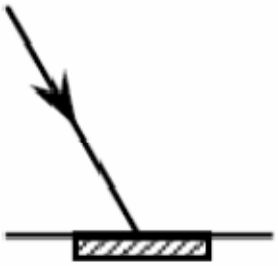

Figure 31: Direct solar irradiance on the surface (Vermote et al. 2006)

Next we define a downward diffuse Solar irradiance, consisting of light scattered by the atmosphere (but not the surface) one or more times, and the associated diffuse atmospheric transmittance factor:

$$t_d(\theta_s) = \frac{E_{sol}^{diff}(\theta_s)}{\mu_s E_s} \tag{41}$$

shown in Figure 32.

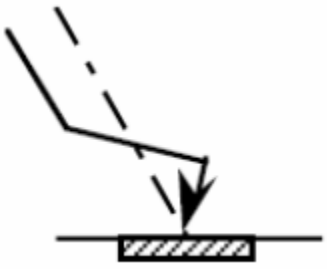

Figure 32: Diffuse solar irradiance on the surface (Vermote et al. 2006)

Let's now define a total transmittance T, which is the total of the direct and diffuse transmittance from the top of the atmosphere to the target surface, and is a function of Solar zenith angle:

$$T(\theta_s) = \exp(-\tau / \mu_s) + t_d(\theta_s) \tag{42}$$

Now we define a second scattered flux, orthogonal to that defined above, which includes all light scattered by both the surface and the atmosphere one or more times, that eventually reaches the target. Taking the spherical albedo of the atmosphere as *S*, and the reflectance of the surface as ρ_t, this term is equal to the total transmittance times the sum of all multiple surface/atmosphere double scattering terms (Figure 33):

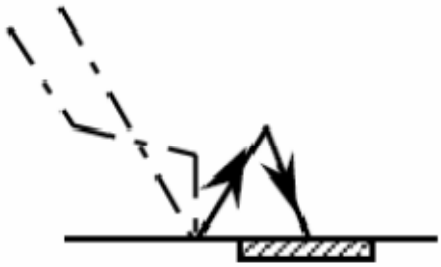

Figure 33: Solar irradiance multiply scattered to the surface from both surface and atmosphere (Vermote et al. 2006)

$$T(\theta_s)\sum(\text{Surface-Atm Scat Terms}) = [\exp(-\tau / \mu_s) + t_d(\theta_s)][\rho_t S + \rho_t^2 S^2 + ...] \tag{43}$$

Recalling the Taylor/Mclaurin series expansion,

$$\begin{aligned} (1-x)^{-1} &= 1 + x + x^2 + x^3 + ... \\ \rho_t S[1 + \rho_t S + \rho_t^2 S^2 + ...] &= \frac{\rho_t S}{1 - \rho_t S} \end{aligned} \tag{44}$$

The total normalized irradiance at the surface is then

$$\frac{T(\theta_s)}{1-\rho_t S} \tag{45}$$

Now that we have defined the terms which relate the incoming Solar irradiance to the irradiance that reaches the target, we now consider the radiance that reaches the satellite sensor. This can be divided into three terms:

(1) The direct plus diffuse Solar radiation reflected by the target surface and transmitted from the surface to the sensor, attenuated on the way out of the atmosphere as shown in Figure 34:

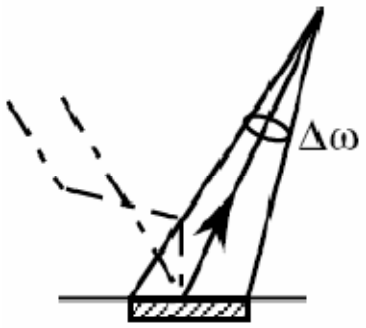

Figure 34: Radiation received at the sensor from the surface due to both direct and diffuse illumination of the surface (Vermote et al. 2006)

(2) The light scattered by the atmosphere to the satellite, expressed as an effective atmospheric reflectance ρ_a, and a function of the Solar and viewer zenith angles, and relative azimuth (Figure 35);

Figure 35: Radiation received at the sensor due to scattering from the atmosphere (Vermote et al. 2006)

(3) Combined direct and indirect solar irradiance scattered from the surrounding surface, then scattered by the atmosphere into the sensor field of view (Figure 36), denoted as $t_d^{'}(\theta_v)$.

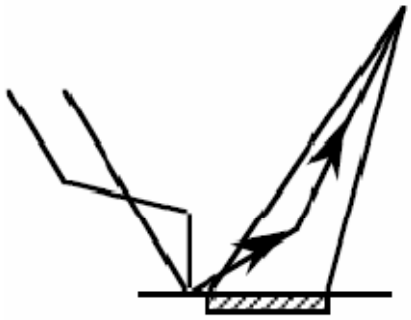

Figure 36: Radiation received at the sensor due to scattering from the surface outside the field of view, scattered into the receiving cone from the atmosphere (Vermote et al. 2006)

Then the apparent reflectance ρ* at the satellite is expressed as the atmospheric radiance plus the product of the total normalized irradiance at the surface and the target reflectance:

$$\rho^*(\theta_s,\theta_v,\varphi_s-\varphi_v)=\rho_a(\theta_s,\theta_v,\varphi_s-\varphi_v)+\frac{T(\theta_s)}{1-\rho_t S}[\rho_t \exp(-\tau/\mu_v)+\rho_t t_d^{'}(\theta_v)] \quad (46)$$

The reciprocity principle tells us that t_d and t'_d are identical, so ρ* can be rewritten as:

$$\rho^*(\theta_s,\theta_v,\varphi_s-\varphi_v)=\rho_a(\theta_s,\theta_v,\varphi_s-\varphi_v)+\frac{\rho_t T(\theta_s)T(\theta_v)}{1-\rho_t S} \quad (47)$$

where the transmittance of the atmosphere to the light leaving the surface is expressed as

$$T(\theta_v)=\exp(-\tau/\mu_s)+t_d(\theta_v) \quad (48)$$

Note that ρ* is called apparent reflectance by the 6SV manual (Part I, p 14), and this term is used to describe refet, which we use as the *I* component of the Stokes parameters of the reflectance.

5.2.3 Modification of 6SV code to produce reflective Stokes parameters

5.2.3.1 6SV Code Limitations

The 6SV atmospheric and surface modeling code is used in a number of remote sensing applications, including calibrating the MODIS instruments on the Aqua and Terra satellites. The code is popular because it includes Rayleigh and aerosol multiple scattering, atmospheric absorption, and polarization effects, models typical Earth surface types, and calculates contributions from interaction between atmospheric and surface scattering. However, the code reports apparent reflectance, which by definition increases without limit with zenith angle for

water surfaces in the direction of specular reflection. Additionally, the code does not provide Stokes parameters, so rotation to another reference plane is not straightforward, and the code requires knowledge of wind direction for ocean surfaces. These characteristics restrict the usefulness of 6SV in this and perhaps some other applications. As part of this project, I modified the code to calculate and output the Stokes-*I*, *Q*, and *U* reflectance parameters, with values between zero and one, for a wavy ocean surface; the Stokes parameters are then easily rotated to any chosen reference plane and converted into the reflectance for the parallel and perpendicular components. The modification also removes the requirement that the modeler stipulate the wind direction above the ocean surface.

The definition of apparent reflectance assumes that light received at the aperture of an Earth-observing satellite instrument is reflected from a Lambertian source. As a result, calculated values of apparent reflectance for an ocean surface far exceed unity in the direction of specular reflection, even at moderate incidence and reflectance angles. For our application in Zugger et al. (2010), we calculated reflectances without normalizing to a Lambertian surface, and also rotated the polarization frame of reference to the scattering plane. To achieve this we modified the *sunglint* and *polglit* subroutines in 6SV to produce the Stokes *I*, *Q*, and *U* parameters and the resulting parallel and perpendicular reflectances which match known analytical results for a calm ocean, and appear to be correct for higher wind speeds. We also eliminated the need to specify the wind direction. We then modified the *main* routine to output these results. These modifications are discussed in more detail in the following sections.

5.2.3.2 Polarized Surface Scattering and 6SV

Apparent reflectance. The 6SV code uses spectral radiance (as defined in section 3.1), with wavelength units of μm^{-1}, and also gives the equation for apparent reflectance ρ^* (also called equivalent reflectance by the 6SV manual) as

$$\rho^* = \frac{L}{E_s \cos(\theta_s)} \tag{49}$$

where

L = measured radiance in W m^{-2} sr^{-1} μm^{-1};
E_s = solar flux at the top of the atmosphere in W m^{-2} μm^{-1}; and
θ_s = solar zenith angle in radians.

Here, a Lambertian surface is implicitly assumed by including a factor of π steradians in the numerator, cancelling the 1/π factor that arises from integrating the Lambertian scattering in all directions (see section 2.1). Using the small solid angle approximation, we calculate the apparent reflectance as:

$$\rho^* \approx \frac{\pi}{E_s \cos(\theta_s)} \times \frac{P_v}{A\,\Omega \cos(\theta_v)} \tag{50}$$

The definition of radiance L (and therefore the definition of ρ^*) includes a factor of $1/\cos(\theta_v)$, because radiance is defined in terms of projected area. Therefore, we can see that as we observe from an angle closer to the grazing angle (θ_v approaches 90°), the outgoing flux P_v must also drop off (at least) as $\cos(\theta_v)$ in order to prevent the calculated apparent reflectance value from increasing without limit. In fact this does occur for a Lambertian source by definition, where the radiance is given by ρ times the incoming irradiance in W m^{-2} times $\cos(\theta_v)$.

However, for a specular surface such as a calm ocean surface, the reflectance approaches 1 at the glint angle, so the apparent reflectance approaches infinity. Like most seeming paradoxes, this is simply a matter of conflicting assumptions. The definition of apparent reflectance assumes a Lambertian surface, from which the radiant intensity in W sr^{-1} drops off as the cosine of the zenith angle; when one is in fact observing reflection from an ocean at moderate or large zenith angles, the calculated apparent reflectance can range into the thousands or higher.

Calculating ocean radiance. From the definitions of the BRDF and apparent reflectance, it is clear that, for a given spectral band and given input and output geometry, BRDF is simply apparent reflectance divided by π. Therefore, we can calculate outputs from 6SV and use them as BRDFs by dividing out the factor of π. Also, we can modify routines used by 6SV to calculate scattering from the wavy ocean surface, as long as the outputs of these routines are $BRDF(\theta_s, \theta_v, \phi_{rel}) \times \pi$, with the factor of π inserted to be consistent with other parameters calculated by 6SV (and divided out later in our version).

Calculating radiance and radiant intensity. For this work we wished to calculate the radiance of the planet at different points in the orbit, and from this the contrast between the planet and the parent star, which is expected to be the primary limiting factor in direct exoplanet imaging. In order to do this we first chose various combinations of surface and atmospheric parameters to represent a variety of hypothetical end-member planet types. For each combination of surface and atmospheric parameters, we used 6SV to generate a table of reflective Stokes parameters for thousands of combinations of stellar zenith angle, viewer zenith angle, and relative azimuth. With this Stokes parameter lookup table as an input, we used a modified version of the Oceans code (Williams and Gaidos 2008) to calculate the radiant intensity I (W sr^{-1}) of the light scattered from the planet. We assumed an Earth-size planet in a circular, edge-on orbit (to our line of sight) 1 AU from a Sun-like star, and calculated the radiance of the planet every 2° around the orbit from new phase (transit) to full phase (secondary transit). To perform this calculation, Oceans divided the planet surface into 2° x 2° patches of latitude and longitude, and used the lookup table to calculate the polarized radiance L (W sr^{-1} m^{-2}) from each surface patch in the direction of the observer; it then multiplied by the area of the surface patch in m^2 to obtain radiant intensity, and summed the radiant intensities from the planet surface to obtain total planet radiant intensity. This value can be compared to the radiant intensity of the Sun to calculate contrast ratio at any point in the orbit.

Recalling the equations for I and L, we can see that, for some small homogeneous patch on a planet of area A that reflects power P into solid angle Ω, the radiant intensity from that patch is

$$I \approx \frac{P}{\Omega} = \frac{P}{\mathrm{A}\,\Omega \cos(\theta_v)} A \cos(\theta_v) \approx LA \cos(\theta_v) \tag{51}$$

where $A\cos(\theta_v)$ is the projected area of the patch. Rearranging the equation for apparent reflectance to calculate radiance, multiplying the calculated radiance of each patch times the area of the patch, and summing over all illuminated patches on the planet, we have the radiant intensity of a planet as observed from a particular direction:

$$I_{planet} = \sum_{\text{lat, long}} \left[L_n A_n \cos(\theta_v) \right] = \frac{1}{\pi} \sum_{\text{lat, long}} \left[\rho^* \mathrm{E_s} \cos(\theta_s) \cos(\theta_v) A_{\text{lat,long}} \right] \tag{52}$$

We calculate the radiance of a latitude/longitude patch of surface on the model planet given the zenith angle of the parent star at the patch, then multiply by the area of the surface patch (assuming an Earth-size planet), and finally sum the radiances of all of the surface patches to obtain the radiant intensity from the entire planet.

5.2.3.3 6SV Code Modification

6SV reflectance outputs for a calm ocean. As mentioned earlier, the 6SV algorithm for calculating light reflection from an ocean surface yields results which may not be useful to some users. Let us consider an example output from 6SV for an ocean surface. To simplify the discussion, assume that atmospheric absorption and aerosols are both disabled, and Rayleigh scattering is also disabled by placing the sensor at satellite altitude, and the target at the maximum altitude of 100 km (essentially above the Rayleigh scattering atmosphere). Also, let us choose the date as the vernal equinox (March 21st) to eliminate any effects of the Earth's axis tilt, and set the level of dissolved organic pigment in the ocean to zero.

Consider the case of the Sun striking a portion of the ocean surface at an angle of 75° to the normal, and a satellite observing that patch of ocean at the specular reflection angle, that is, at an angle of 75° to the normal, and a relative azimuth of 180°. Let us specify a light wind of 1.5 m/s from an azimuth of 45°, and a wavelength range of 1 to 1.1 micron – wavelengths long enough to minimize scattering from within the water column, but short enough to include significant solar radiation and avoid Earth's thermal emission. For this case the (unmodified) 6SV code calculates a direct solar irradiance of 177.4 W m^{-2} μm^{-1}, an apparent radiance of 4695 W m^{-2} sr^{-1} μm^{-1}, and an apparent reflectance of 83.1, which can also be obtained as

$$\rho^* = \frac{L}{\mathrm{E_S} \cos(\theta_s)} = \frac{\pi \times 4694.6}{177.4} = 83.1 \tag{53}$$

from which it is clear that 6SV is using the same definition of apparent reflectance for the specular water reflection as for Lambertian surfaces. For zenith angles of 0°, 6SV calculates an

apparent reflectance of 0.522, and for zenith angles of 80°, 6SV calculates an apparent reflectance of about 300. In practice this would mean that satellite radiance data is converted to an apparent ground radiance based on the assumption of a Lambertian surface, regardless of whether the surface is Lambertian, specular, or other.

For this project we used 6SV to calculate reflectances of grid areas on hypothetical planets, and summed contributions to calculate contrast ratios between these planets and the parent Sun-like star at different points in the orbit. For our application, and probably others, it is more useful to have reflectances defined such that they range between zero and one. Specifically, we would like the reflectance in the near infrared for a calm water surface at normal incidence to be calculated as approximately 0.02, and the reflectance at grazing incidence to be calculated as approaching 1.[26] To accomplish this, the 6SV code was modified by replacing sections of the two subroutines that calculate reflectance from water: subroutine *sunglint* (in OCEATOOLS.f), which computes the unpolarized intensity Stokes *I* parameter, and POLGLIT.f, which computes the Stokes *Q* and *U* polarization parameters. An output statement was then added in *main.f* to print the calculated parameters. We begin by returning to the original source of data about the reflection of sunlight from a wavy ocean.

Modifying 6SV for ocean surface BRDF. The classic paper by Cox and Munk (1954) gives the equation for the probability *p* that a given small piece (facet) of the ocean surface will have the correct x and y tilt to reflect the Sun to the observer as (using our notation):

$$p = \frac{4L\cos^4(\beta)\cos(\theta_v)}{\rho E_s \cos(\theta_s)} \tag{54}$$

where
β = tilt of the ocean facet
θ_v = viewer zenith angle
θ_s = solar zenith angle

As pointed out by Zeiss (Zeisse 1995), Equation (54) can be rearranged to give the reflected radiance from the ocean surface for a given solar input, which is our definition of BRDF:

$$\frac{L}{E_s \cos(\theta_s)} = \frac{\rho}{4\cos^4(\beta)\cos(\theta_v)} p \tag{55}$$

The view angle is known, and the tilt angle can easily be calculated from geometry, so the remaining necessary item is an equation for p in terms of known quantities. Another paper by Cox and Munk published the following year (Cox and Munk 1955) provides the needed equation

[26] If the factor of pi and division by cosine of the viewer zenith angle were the only issues, then for a calm ocean surface at normal solar and viewer zenith angles, 6SVshould calculate an apparent reflectance of approximately 0.02 x pi / cos(0) = 0.0628, not 0.522. This fact along with apparent inconsistencies in the 6SV equations for wavy ocean scattering, as well as a comment in the *polglit* routine to the effect that the algorithm did not work and needed further investigation, led me to believe that there is a coding error in this portion of 6SV 1.1. I have been in contact with Eric Vermote concerning this issue and he is looking into it as of this writing. These concerns motivated the derivation and implementation of new sunglint and polglit routines as described here and in Appendix F.

as Equation 1, which in fact is identical to the equation for a two-dimensional probability density function with zero mean (with the factor of 2 included in σ^2):

$$p(z_x, z_y) = \frac{1}{\pi\sigma^2} \exp\left[\frac{-(z_x{}^2 + z_y{}^2)}{\sigma^2}\right] \tag{56}$$

where
$z_x = \partial z/\partial x$ = facet tilt in the x direction
$z_y = \partial z/\partial y$ = facet tilt in the x direction
σ^2 = empirically determined tilt distribution.

Here, σ^2 is the familiar Gaussian spread parameter; for this equation, it is an empirically determined, wind direction-independent parameterization tilt sigma squared for a given windspeed W, given in Cox and Munk (1955) as Eq. 2:

$$\sigma^2 = 0.003 + 5.12\times10^{-3}W \tag{57}$$

Using a single parameter instead of an upwind and a crosswind parameter causes some loss in accuracy because there is an asymmetry. In Cox and Munk (1954), the authors calculate the standard deviations between the observed values of slope as +/- 0.002 for the upwind and crosswind slopes, and +/- 0.004 for the combined. However, this loss in accuracy only applies if the wind direction is both known and fairly consistent over the time interval and spatial extent of the measurement in question.

From the definitions of z_x and z_y, and using the Cox and Munk definition of α as the angle of ascent of the facet tilt (angle between the Sun azimuth and the azimuth of greatest facet tilt), we have Cox and Munk (1955) Eq. 3:

$$\begin{aligned} z_x &= \sin\alpha\tan\beta \\ z_y &= \cos\alpha\tan\beta \end{aligned} \tag{58}$$

Then the numerator of the exponential for our equation of probability becomes

$$\begin{aligned} -\left(z_x{}^2 + z_y{}^2\right) &= -\sin^2\alpha\tan^2\beta - \cos^2\alpha\tan^2\beta \\ &= -\tan^2\beta = -\frac{\sin^2\beta}{\cos^2\beta} = \frac{\cos^2\beta - 1}{\cos^2\beta} \end{aligned} \tag{59}$$

We now insert this result into our equation for probability of a given wave tilt to obtain

$$p(\beta) = \frac{1}{\pi\sigma^2} \exp\left[\frac{\cos^2\beta - 1}{\sigma^2\cos^2\beta}\right] \tag{60}$$

and then insert this into the equation for BRDF to obtain:

$$\frac{L}{E_s \cos(\theta_s)} = \frac{\rho}{4\pi\sigma^2 \cos^4(\beta)\cos(\theta_v)} \exp\left[\frac{\cos^2\beta - 1}{\sigma^2 \cos^2\beta}\right] \tag{61}$$

which is the equation we use in the modified 6SV, multiplied by π to be consistent with the apparent reflectance calculations performed by 6SV.

Modifications to the 6SV code and subroutines. The main subroutine of 6SV was modified to output the Stokes parameters, and to remove unneeded outputs. The 6SV subroutine *sunglint* in OCEATOOLS.f calculates the unpolarized reflectance *rog*, equivalent to the Stokes-I reflectance parameter, and the subroutine POLGLIT.f calculates the Stokes *Q* reflectance *ropq* and Stokes *U* reflectance *ropu* using *factor* and the rotation factors it calculates. These subroutines were modified to use the equations derived above. Details of the code modifications are given in Appendix F.

Factors of ½ and π. In order to be consistent with the calculations in 6SV for apparent reflectance from atmospheres and other surfaces, we multiply the calculated reflectance of the water by π. We then divide reflection coefficients calculated in 6SV (whether from Lambertian, specular, and/or atmospheric path radiance) by π to cancel this factor out. Likewise, the parallel and perpendicular components of electromagnetic radiation are usually generated from the Stokes parameters as

$$I_{//} = \frac{I+Q}{2}; \quad I_{\perp} = \frac{I-Q}{2} \tag{62}$$

but for reflective Stokes parameters, the factor of one half is often omitted:

$$R_{//} = I + Q; \quad R_{\perp} = I - Q \tag{63}$$

Instead, for unpolarized incident light, the factor of one half is applied to the total incident power to indicate that half of that power is in the parallel, and half in the perpendicular polarization.

Summary of 6SV Modifications. The modifications of the 6SV atmospheric and surface modeling code described above provide the user with reflective Stokes parameters I, Q, and U for the reflectance of atmospheres and of ocean and Lambertian surfaces at given Sun angles and view angles. The modifications also remove the dependence of the code on wind direction. The modifications are verified against analytical results in the Verification section 6.3. For further details on the 6SV code modifications, see Appendix F.

5.3 Planetary System Geometry and Polarization

Here we present the geometry of the problem, the methods the code uses to handle this geometry, and the points in the orbit which, in a simple model, would yield the maximum polarization fractions.

5.3.1 Orbital Geometry

In keeping with our desire to present idealized examples, we consider exoplanets with a single surface type and atmosphere type, in circular, edge-on orbits. Circular orbits are assumed both for simplicity and because such systems are presumed to be more likely to have stable climates suitable for continuously liquid water and life. We also assume that planets have a horizontally homogeneous atmosphere and a single surface type. A planet with a homogeneous surface in an orbit that is face-on to the observer (inclination, $i = 0$) has little variation with orbital phase, and so is not of interest. The effects we seek are maximized for edge-on inclinations ($i = 90$), so this is the case we model. This restriction is not unduly limiting, because half of all extrasolar planets will have orbital inclinations in the range $60 < i < 120$ because of geometrical considerations (Williams and Gaidos 2008). We will also assume an Earth-size planet at 1 AU from a Sun-like star.

5.3.1.1 Orbital Longitude

Orbital longitude (OL) is defined such that OL = 0° at new phase, when the planet passes in front of the parent star as seen from Earth (transit), and full phase (OL = 180°) occurs when the planet passes behind the star and is fully illuminated. When the apparent planet-star separation is at its maximum, orbital longitude is 90° or 270°, and the planet is said to be at quadrature. If the planet (or moon) is close enough to be resolved, as with Mercury and Venus, the planet will be in crescent phase in the "front" portion of the orbit between 270° and 90°, in first or last quarter at 90° and 270°, and in gibbous phase in the "back" portion of the orbit, between 90° and 270°. We take advantage of orbital symmetry to simplify our curves by including only waxing phases (OL 0° to 180°) in our calculated light curves.

5.3.1.2 Oceans and Planetary Geometry

IDL calculates the three-dimensional (3D) geometry involved with the problem, as the spherical planet moves in a circular, edge-on orbit around the parent star. This is accomplished in Oceans using a number of nested loops, as shown in Figure 37. The outermost loop steps the planet around the orbit; for our purposes, this is done in 2° steps around the half-orbit from front (transit) to back (secondary transit). The next loop calculates scattering as the planet rotates. This feature is used for planets with, for example, Earth geography, but has no effect for planets with a single surface and atmosphere type, so for this model it is disabled. The third loop steps through planetary pixels around the equator (longitude), while the fourth loop steps through pixels from pole to pole (latitude).

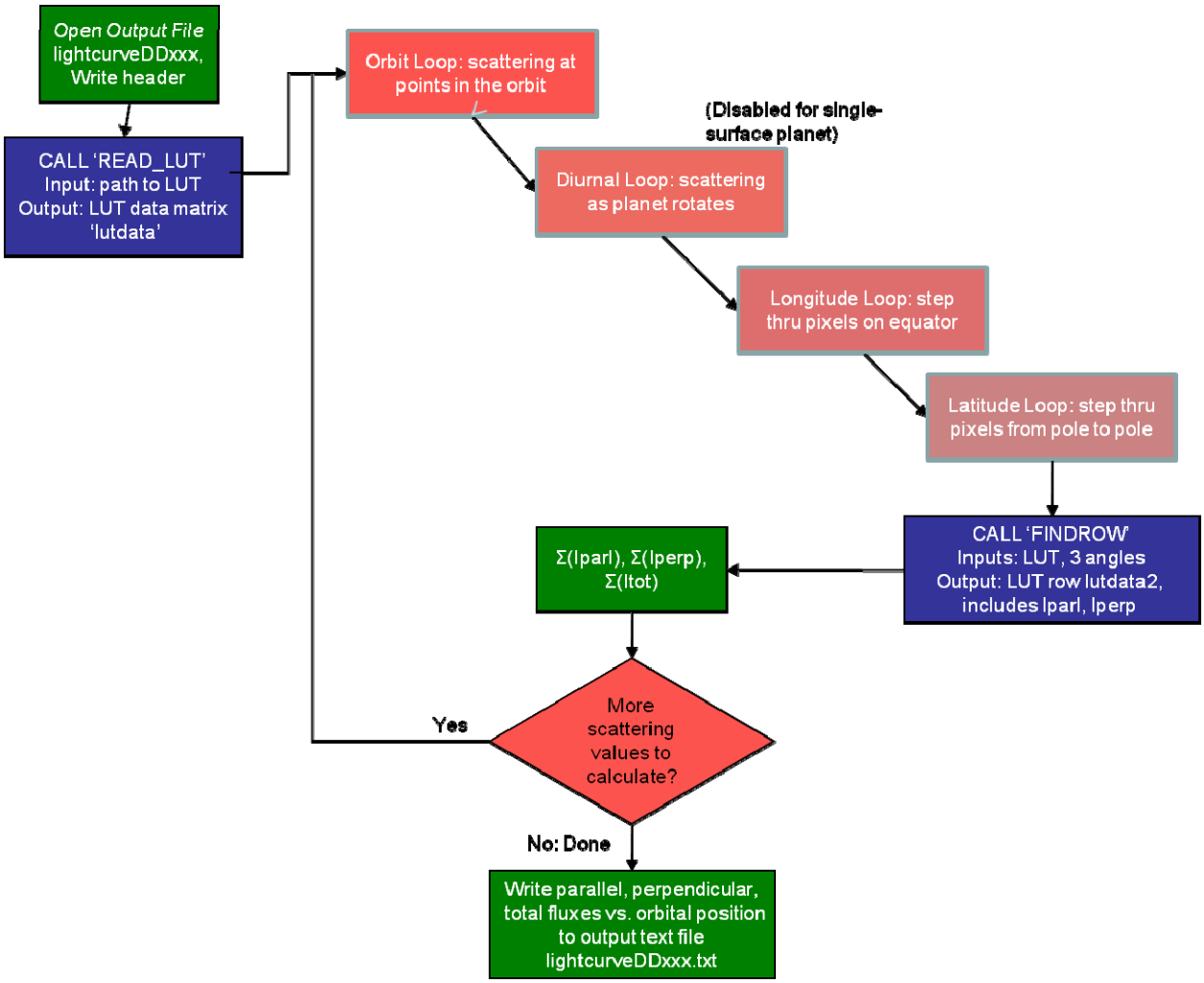

Figure 37: Diagram of the lightcurve routine in Oceans, showing nested loops

Figure 38 shows the *lightcurve* routine from an input/output standpoint. For each pixel, the *lightcurve* routine takes in the apparent latitude and longitude of the parent star and the observer, and calculates the resultant angles – the solar zenith angle, viewer zenith angle, and relative azimuth between the two.

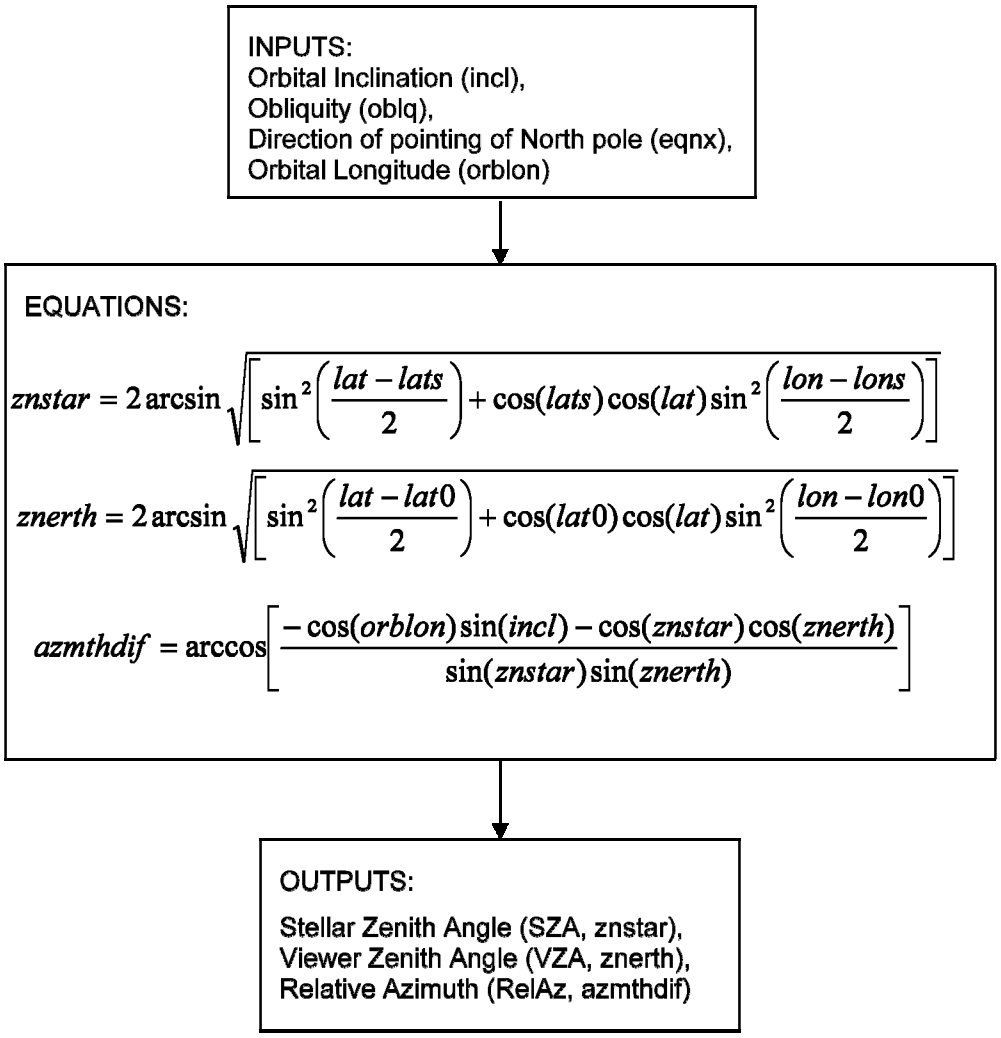

Figure 38: Input/output diagram for the Oceans lightcurve routine showing the operations performed by *Oceans* for each pixel at each point in the orbit

5.3.2 Orbital Longitude Effects on Polarization

The angle of polarization is defined relative to a chosen reference plane. In this case, we use the scattering plane, which is defined by the parent star, the planet, and the observer. For our edge-on geometry, the scattering plane is identical to the orbital plane. In Figure 39, it is also the plane of the paper. Although it appears at first glance that the scattering plane depends on what point on the star a particular light ray originates, and from where on the planet it is scattered, these effects are entirely negligible. One can understand this by noting that the apparent diameter of the Sun as seen from Earth is only about 0.5° (about 6.8 x 10^{-5} sr), and the size of the Earth as seen from the Sun is 1 percent of that, and of course both objects appear very much smaller from the distance of another star system.

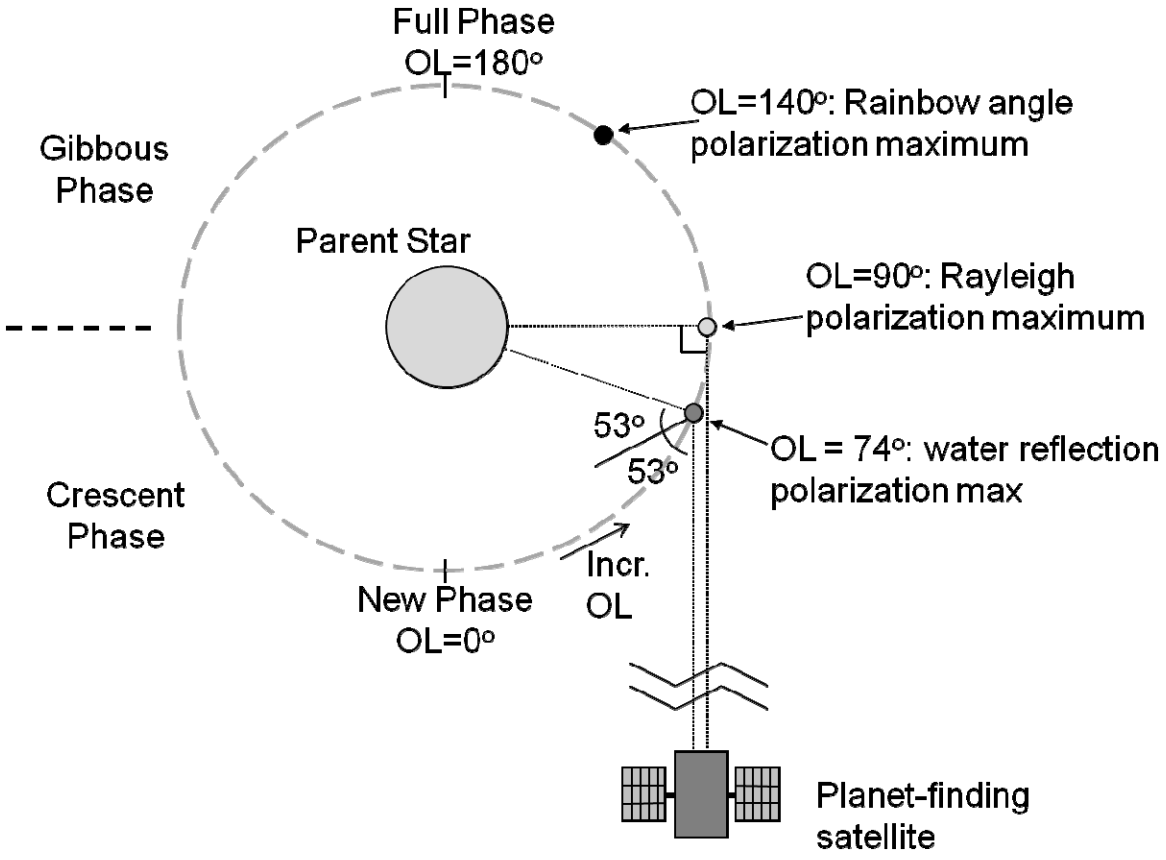

Figure 39: Geometry of the problem; locations of polarization maxima differ when spherical geometry and other factors are included

Three orbital longitudes are of particular interest: OL = 74°, where the peak polarization of a flat water surface occurs, OL = 90°, where the peak polarization of Rayleigh scattering occurs, and OL = 140°, where the rainbow peak for water aerosols occurs. Polarization from Rayleigh scattering peaks when the source, scattering volume, and observer form a 90° scattering angle, a fact which can be verified by observing a clear blue sky at varying angles to the Sun with polarized sunglasses. Physically, the parallel component is unable to propagate to the observer in this geometry because the electric field vector is pointing in the direction of propagation. Therefore, for Rayleigh scattering in a thin atmosphere over a dark planet surface, the polarization fraction approaches 100%. If the atmosphere is thick, multiple scattering occurs, and the polarization fraction decreases. However, Chandrasekhar & Elbert (1954) calculated a number of cases, and found that polarization from a Rayleigh scattering atmosphere can exceed 90% before being limited by multiple scattering. In our case, the polarization fraction can be limited either by multiple scattering, or by dilution from unpolarized or partially polarized light from the planet's surface, or both.

Simplistically, polarization from a flat water surface peaks at OL = 74°, as indicated in Figure 39. Light reflecting off a flat air/water interface at the Brewster angle, which for water is 53.1° to the normal, will also be polarized nearly 100%. Therefore, when the planet is at OL ~180 – (2 x

53°) = 74°, the polarization fraction from a flat water ocean (neglecting sea foam and scattering within the water column) is greatest. It is the parallel component that is not well reflected because it is oriented in the direction of travel. (This description is approximate and based on a simple conceptual model, but provides a useful starting point.) Our model below includes the effects of waves, sea foam, scattering from within the ocean, multiple Rayleigh scattering, clouds, and 3D geometry, and we compare various ocean planets against Lambertian land surfaces under Rayleigh atmospheres.

Returning to Figure 39, we see a third polarization peak at the rainbow angle OL = 140°, as described by Bailey (2007)[27]. This peak results from light interacting with approximately spherical airborne water droplets, as in a rainbow; light striking along the side of a droplet is refracted as it enters the droplet, reflects off of the inside back surface of the droplet, and refracts again as it leaves the droplet on the other side. The resulting angle between the incoming and outgoing light rays is 40°, resulting in a peak near OL = 140°. An example of a double rainbow is shown in Figure 40.

Figure 40: Double rainbow (photo credit: C. R. Philbrick)

[27] Our results may at first appear to disagree with Bailey's and Stam's results, but this is caused by differences in angle conventions. For orbital position, Bailey and Stam use phase angle, which is defined as the angle between the incident and outgoing light rays, so 0° occurs when the planet is on the opposite side of the star, or full phase for edge-on orbits. Orbital longitude (which we use) is defined such that 0° occurs when the planet is on the near side of the star, or in new phase for edge-on orbits. Therefore, for edge-on orbits, phase angle = 180 – OL.

6.0 Results

6.1 Unpolarized Light Curves and Contrast Ratios

First, we consider how total radiometric flux varies with orbital longitude. Figure 41 shows normalized light curves from three end member cases: a planet with a calm ocean under a thin atmosphere, a planet with a Lambertian surface under a thin atmosphere, and a planet with a single-scattering Rayleigh atmosphere over a dark surface. The Lambertian surface is a mathematical approximation of a diffuse scattering surface; it assumes that reflectance drops off with the cosine of the viewing angle, so that it appears equally "bright" from any viewing angle, where "brightness" is measured in watts per steradian per square meter of projected area. The resulting light curves are distinctive, especially the ocean planet light curve; hence, for terrestrial planets similar to the end member cases, unpolarized light curves by themselves could be useful in characterizing a planetary surface. We now discuss each of the three curves, and why their shapes are different.

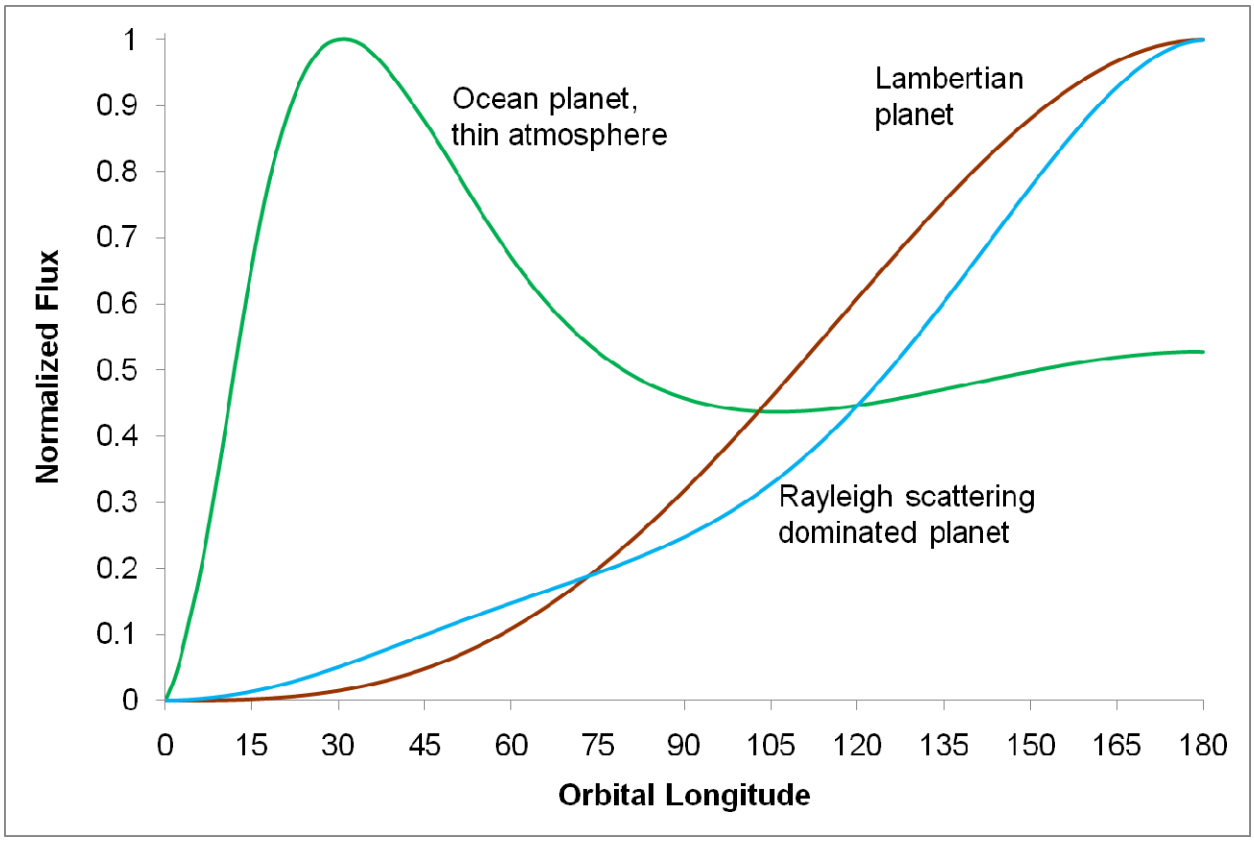

Figure 41: Normalized total light curves for end-member planets. The peak near OL = 30° is indicative of an ocean surface (although not necessarily water)

6.1.1 Light curve descriptions

1) The Lambertian light curve closely matches the analytical result (Russell 1916; Sobolev 1975) and varies smoothly in an S-curve between zero flux and full flux as phase varies from new to full. At quadrature, the flux is $1/\pi \cong 0.32$ of that at full phase. The Lambertian planet is faint at small orbital longitudes because of the small illuminated surface fraction and the cosine weighting of the reflected flux.

2) The ocean light curve shows the opposite behavior: it peaks at small orbital longitudes (near 30^o) when the planet is in crescent phase. This is because reflection from (calm) water is largest (~100%) near grazing incidence, and smallest (~2%) at normal incidence. The calm ocean curve was generated assuming a light wind of 1.5 m/s, which roughens up the surface enough so that nearly every illuminated pixel reflects some light to the observer. At full phase, OL = 180°, the entire face of the planet is illuminated, but with little reflectance. As the planet moves from full phase (OL = 180°) through the gibbous phase toward quadrature (OL = 270°), the illuminated fraction becomes smaller, but the loss is mostly compensated by increased reflectivity. At orbital longitudes below 90^o, the reflectance increases rapidly, much faster than the loss of illuminated surface, as the planet goes into crescent phase. The flux peaks near OL = 30^o, where the incidence and reflection angles for specular (mirror-like) reflection are 75°, and the reflectance has increased tenfold to 20%. At OL < 30^o, the loss in illuminated surface area dominates and the flux falls towards zero.

3) At small orbital longitudes, the normalized Rayleigh flux is higher than the normalized Lambertian flux, because the pathlength available for Rayleigh scattering becomes larger with increasing stellar zenith angles through the atmosphere. Both the normalized Rayleigh and Lambertian planet fluxes grow at high orbital longitudes because more of the observable planet surface is illuminated. The Rayleigh flux curve here assumes an Earth-like atmospheric pressure profile; the shape of the curve would change somewhat with a different atmospheric pressure profile, but should remain distinct from the light curve of an ocean planet with a thin atmosphere and no clouds.

6.1.2 Viewing considerations

Although it appears from Figure 41 that discriminating between three types of surface scattering is straightforward, it may be difficult to do in practice for several reasons. First, the planet can only be viewed[28] when it is at sufficient separation from the star to be outside the inner working angle of the coronagraphic telescope. Exactly when that occurs will vary from one target to the next, but we can conservatively assume that most target planets will be observable only in the OL = 45 - 135^o window. Second, the contrast ratio between the planet and the star must be sufficient to allow observation of the planet. Dark planets may not be observable, even at

[28] Here, when we consider a planet being "viewed," we the mean the planet is directly observed in starlight scattered by the planet's surface and atmosphere to the viewer. As discussed in Chapter 2.3.2, a fraction of planets will be observed when they transit in front of the parent star, but our model does not consider these.

quadrature. And, third, real planets are likely to represent a combination of our three end-member cases, and so the respective light curves must somehow be deconvolved. Here, we discuss the specific issue of contrast ratios.

6.1.3 Albedo and Contrast Ratios

In chapter 2 we discussed Bond albedo, the fraction of electromagnetic energy from the star that the planet scatters back to space in all directions, and geometric albedo, the ratio between the light reflected by a planet and the light that would be reflected by a white Lambertian disk.

The contrast ratio between an exoplanet and its parent star is an important factor in determining the observability of an exoplanet, and thus helps motivate the design of a planet-finding mission like TPF-C. Following earlier work by Russell (1916) and Sobolev (1975) calculated the phase function for a Lambertian planet as:

$$\Phi(\alpha) = \frac{1}{\pi}\left[\sin\alpha + (\pi - \alpha)\cos\alpha\right] \tag{64}$$

Note that α and orbital longitude OL are defined differently; a planet in full phase (fully illuminated) has α = 0, but OL = 180°. The zero point for OL is when the planet is in transit, while the zero point for α is when the planet is on the other side of the star. With this in mind, some values of phase function Φ are shown in Table 5.

Table 5: Selected values of planetary phase function

phase	α	OL	[sin α + (π - α)cos α]/ π	Φ
full	0	180	[sin(0) + (π)cos0]/ π = π/ π	1
quadrature	90, 270	270, 90	[sin(π/2) + (π – π/2)cos(π/2)]/ π = [1+0]/ π	1/ π
new/transit	180	0	[sin(π) + (π- π)cos π]/ π = 0/ π	0

The TPF Science and Technology Study Definition Team Report[29] (Levine et al. 2006) gives the following formula for the planet/star contrast ratio C as a function of orbital longitude/phase angle alpha, which can be derived from Sobolev's phase function:

$$C_{quadrature}(\alpha) = \frac{2}{3} A_{Bond} \left(\frac{r_{planet}}{a} \right)^2 \frac{\sin(\alpha) + (\pi - \alpha)\cos(\alpha)}{\pi} \tag{65}$$

For an Earth-like planet at 1 AU from the star, with the planet at quadrature (α = π/2), the report calculates:

[29] http://planetquest.jpl.nasa.gov/TPF/STDT_Report_Final_Ex2FF86A.pdf

$$C_{quadrature}(\alpha=\frac{\pi}{2})=\frac{2}{3}A_{Bond}\left(\frac{r_{planet}}{a_{1AU}}\right)^2\frac{1}{\pi}=\frac{1}{\pi}A_{geo}\left(\frac{r_{planet}}{a_{1AU}}\right)^2$$
$$=\frac{1}{\pi}\frac{2}{3}0.3\left(\frac{6370}{150\times10^6}\right)^2=1.154\times10^{-10} \quad (66)$$

where

$C_{quadrature}(\alpha=\frac{\pi}{2})=$ planet/star contrast ratio between at greatest apparent separation

$A_{Bond}=$ Bond albedo (an Earth-like 0.3 was assumed)

$A_{geo}=$ Geometric albedo

$r_{planet}=$ radius of the planet, here we take to equal the radius of the Earth

$a_{1AU}=$ distance of the planet from the star, we take to be 1 AU, the Earth-Sun distance

From the definition of *C*, the angular light outputs from the planet and star *I* in W/m^2 are related by:

$$I_{planet}(\alpha)=C(\alpha)I_{star}(\alpha)$$
$$I_{planet}(\frac{\pi}{2})=C(\frac{\pi}{2})I_{star}(\frac{\pi}{2}) \quad (67)$$

so multiplying by the power output of the Sun in watts divided by 4π steradians,

$$I_{planet}(\frac{\pi}{2})=1.15\times10^{-10}\left(\frac{3.85\times10^{26}}{4\pi}\right)=3.52\times10^{15}\ \text{W sr}^{-1} \quad (68)$$

for an Earth-size planet with a Lambertian surface and a geometric albedo of 0.3, at 1 AU from a Sun-like star, at the point of maximum separation in the orbit. From Sobolev (1975), we know that the brightness of a planet at full phase is larger than that at maximum separation by a factor of π. Thus, at full phase, we have:

$$I_{planet}(0)=\pi\times I_{planet}(\frac{\pi}{2})=1.11\times10^{16}\ \text{W sr}^{-1} \quad (69)$$

Table 6 lists three example planets with the corresponding contrast ratios at quadrature and full phase. Each case is based on an Earth-sized planet in a circular, edge-on orbit about a Sun-like star. Contrast ratio is calculated by dividing the radiant intensity from the planet (calculated above for the Lambertian case) by the radiant intensity of the Sun. The first row is the analytical result for a Lambertian planet with a Bond albedo of 0.3 (our model matches this to within 0.2%). The second and third rows give the contrast ratios for planets with a dark surface (Bond

albedo = 0.01) and Rayleigh scattering atmospheres with $\tau_R = 0.05$ and $\tau_R = 0.50$. The fourth row of the table gives the contrast ratios for a water planet with a thin atmosphere and light wind.

A potential diagnostic of an ocean planet is that, at quadrature, the brightness of the ocean planet is only about 9% of the brightness of the Lambertian planet. The ocean planet is also much dimmer than Earth, because Earth's albedo is dominated by clouds, with smaller contributions from Rayleigh scattering and from continental surface scattering. Rows two and three highlight the fact that the brightness of the planet dominated by Rayleigh scattering is not a strong diagnostic, because it can vary widely based on the Rayleigh depth, surface brightness, and amount of absorption on the atmosphere. We will use the above results and others to verify our model results in section 6.3, Verification and Error Analysis.

Table 6: Contrast ratios for Lambertian and ocean planets with thin atmospheres, planet with a dark surface and Rayleigh scattering atmosphere

Surface	Atmos.	τ_R	Earth equiv wavelength	C@90 Rel. to Lamb 0.3	C @ 90	C @ 180
Lambertian, A_{bond} = 0.3	none	0.00	--	1.000	1.154E-10	3.625E-10
Dark ρ = 0.01	Rayleigh only	0.50	369 nm	0.898	1.036E-10	4.187E-10
Dark ρ = 0.01	Rayleigh only	0.05	648 nm	0.168	1.940E-11	7.261E-11
ocean 1.5 m/s TPF wavelengths	none	0.00	500-1000 nm	0.083	9.603E-12	1.137E-11

6.1.4 The Terrestrial Planets

Mallama (2009) derived light curves for Mercury, Venus, and Mars, based on observations compensated for distance, and compared them to light curves based on earthshine from the Moon. All four terrestrial planet light curves decrease nearly monotonically as the planet moves from full phase to new phase, with Venus appearing three to four times as bright as the others. All four curves resemble some combination of our Rayleigh and Lambertian curves, except that Mercury shows a marked increase in brightness near full phase, and Venus shows a small flux increase near OL = 10°. If the brightness and approximate radius of a terrestrial exoplanet is known, a planet which is brighter than expected based on the above modeling may indicate a cloud-covered exo-Venus, or possibly a snow-covered planet.[30]

6.1.5 Summary of Radiometric Results

In summary, the Lambertian, Rayleigh-dominated, and ocean planets have widely differing unpolarized light curves that appear readily distinguishable. However it must be remembered that the ocean planet would be comparatively very dim and that observing at OL ≤ 45° may not

[30] C. R. Philbrick, personal communication, December 2010

be possible for many systems. Additionally, a realistic ocean planet would require a background atmosphere to hold onto its water, and it would almost certainly have clouds. It is nonetheless useful to simulate such idealized planets so that we understand the end-member cases. Also, the decreasing brightness of the water planet in the range OL = 45° to 90° should be a useful diagnostic. Because ambiguities will likely remain in the interpretation of radiometric (unpolarized) exoplanet light curves, we now address these by considering the polarization effects of various end-member planet types.

6.2 Polarized Light Curves

Figure 42 shows polarized and total light curves for a planet with a thick Rayleigh atmosphere (τ = 0.5) over a dark surface (A_{bond} = 0.01). The disk-averaged polarization fraction peaks near quadrature (OL = 90°) because Rayleigh scattering polarizes starlight to the greatest degree when the atmosphere scatters starlight at right angles toward the observer. Planets with other Rayleigh optical depths over dark surfaces would have similar light curves, with the peak polarization fraction limited by dilution from the surface in cases of lower optical depths, and limited by multiple scattering for higher optical depths. A potentially useful measure of the contribution of Rayleigh scattering to the reflected flux is the phase lag between peak polarization and quadrature; planets with thin atmospheres and weak Rayleigh signatures will show polarization peaks at orbital longitudes less than (or sometimes greater than) 90°.

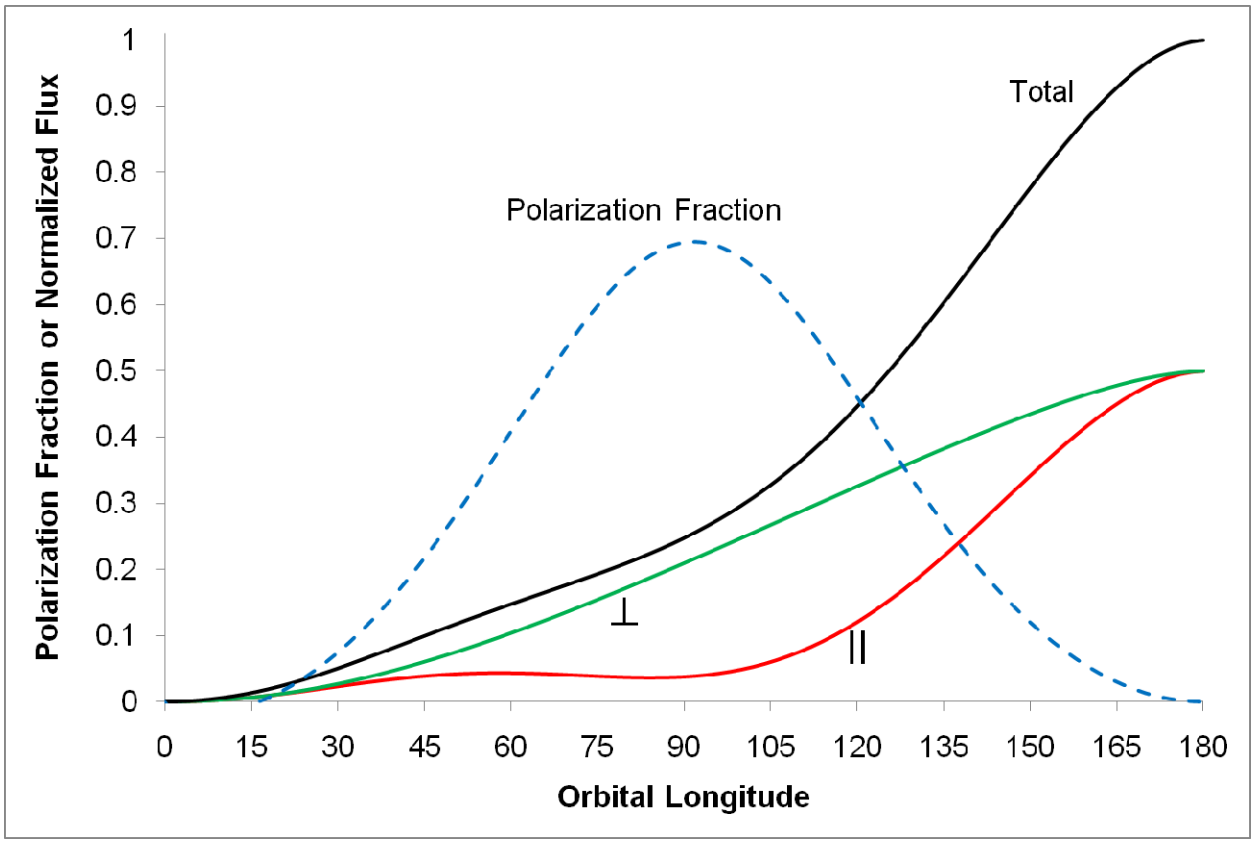

Figure 42: Polarized light curves (solid) and polarization fraction (dashed) for a planet with a thick Rayleigh scattering atmosphere (τ_R = 0.5) over a dark surface. Equiv Earth wavelength: 369 nm

In Figure 43, we compare the light curves for planets with different Rayleigh optical depths. The planet surfaces are uniform Lambertian scatterers with a surface Bond albedo of 0.1, similar to that of Mercury and the Moon. The light curve for a τ = 0.05 Rayleigh atmosphere over a black surface is shown for comparison (dashed curve). Light becomes increasingly polarized by Rayleigh scattering as optical depth increases, and the polarization maximum occurs nearer to quadrature as the atmosphere thickens. The effect is similar to that seen in Figure 4 of Stam (2008), although in that case the atmospheric density was held constant while the surface albedo was varied. The reference case in our figure (dashed), an atmosphere over a dark surface, shows the effect of removing surface backscattering, which otherwise dilutes the polarization fraction.

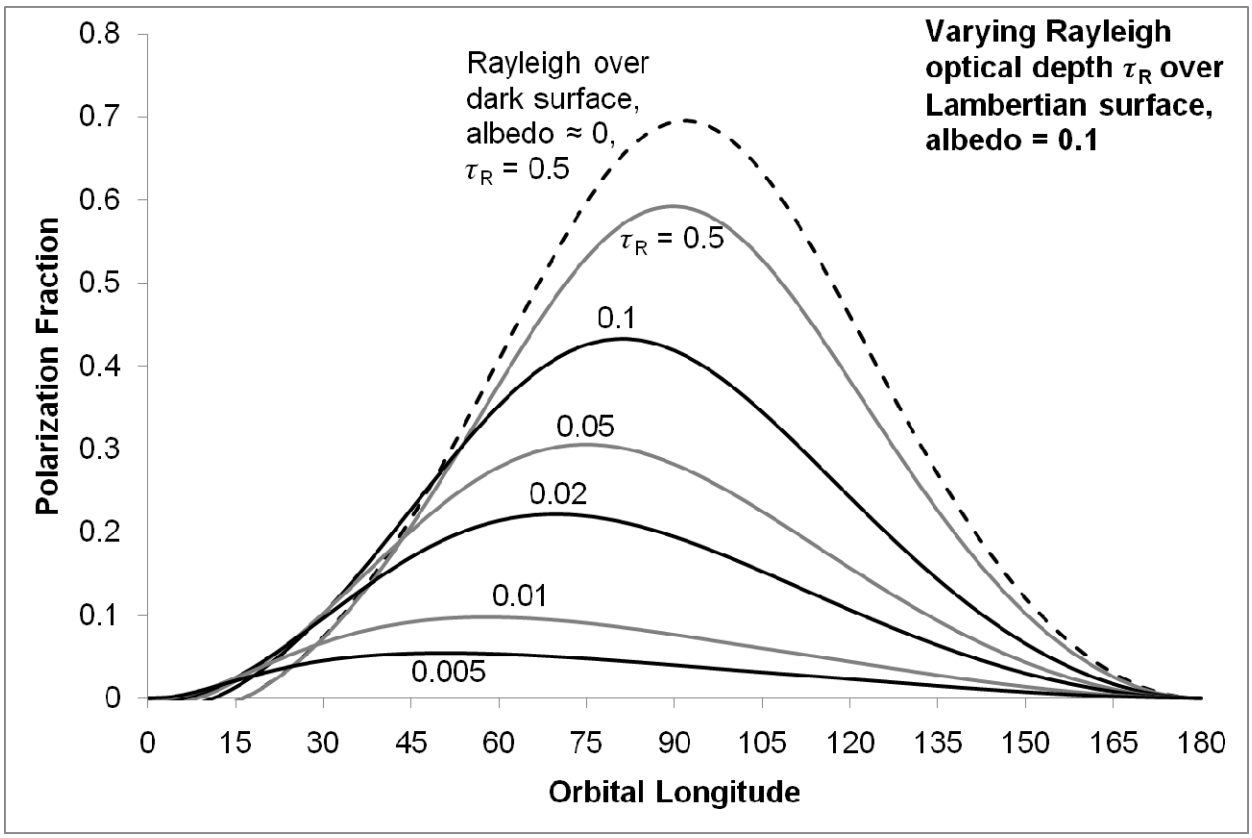

Figure 43: Polarization fraction variation with τ_R over 0.1 Lambertian surface; pure Rayleigh over dark surface shown (dashed) for comparison. Unpolarized light from the surface dilutes polarization. Equivalent Earth wavelengths: 369, 547, 648, 813, 965, 1150 nm (see section 5.2.1.7)

On a real planet with an atmosphere, scattering by clouds is also likely to be important. In Figure 44, we have replaced a fraction of each pixel on the planet with clouds, which are assumed to reflect light without polarizing it, in a Lambertian pattern (see section 6.5 for a brief discussion of this approximation). For simplicity we assume that the atmosphere above the clouds is thin enough to be ignored. We varied both cloud fraction and albedo, and found through comparative analysis (not shown) that the two parameters have nearly identical effect. Lambertian clouds dilute the polarization fraction and shift it towards smaller OL, as would a reflective Lambertian surface. Some clouds composed of liquid water droplets exhibit the rainbow angle effect; a planet with primarily these types of clouds would show a second polarization peak near OL = 140°. This "cloudbow" feature was measured for some Earth clouds by the POLDER instrument during aircraft-based testing (Goloub et al. 1994), and was also predicted for exoplanet water clouds by Bailey (2007) (see section 6.5).

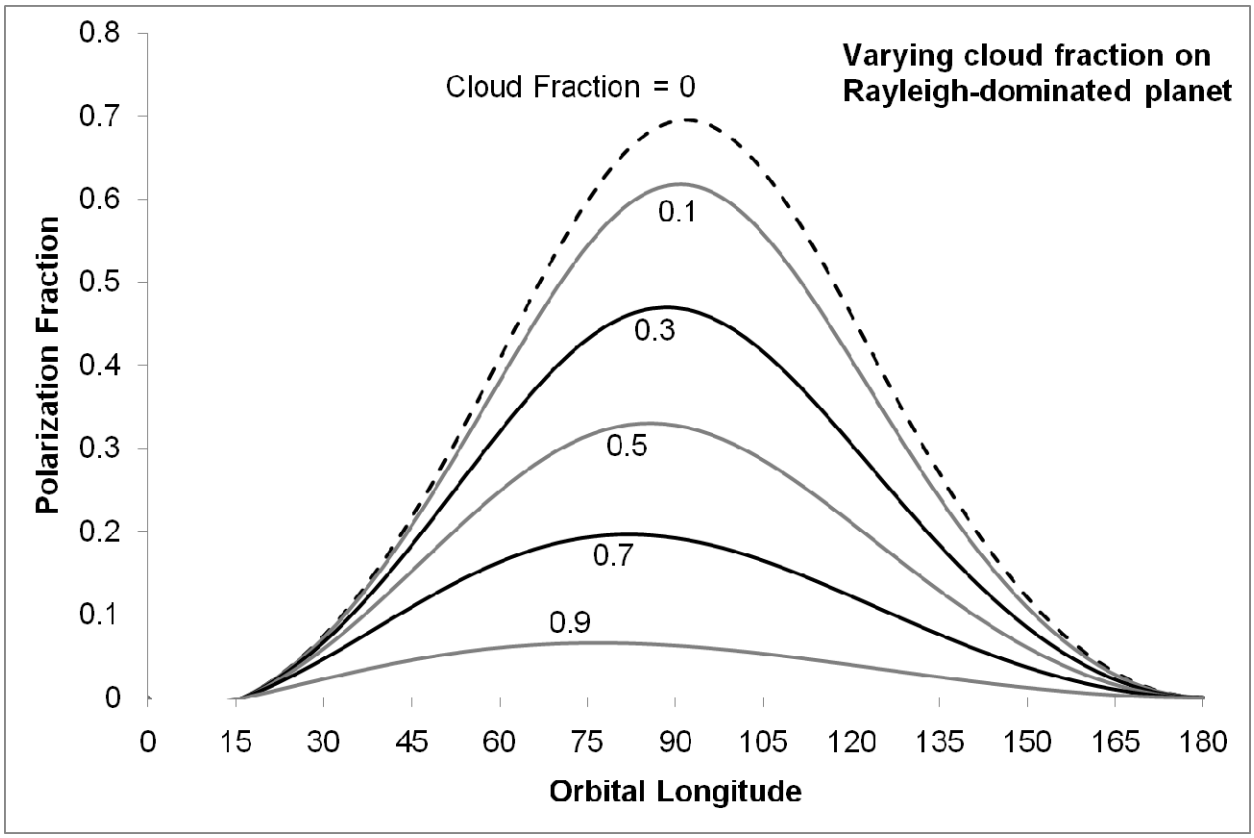

Figure 44: Effect of Lambertian cloud fraction on Rayleigh scattering-dominated planet; $\tau_R = 0.5$ (Earth atmosphere at 369 nm), a relatively low average cloud albedo of 0.3 is assumed

For comparison, the sulfuric acid clouds of Venus give our neighbor planet a more complex (but diluted) polarization fraction, with peaks of about 0.02 near OL = 25° and OL = 165°, and a negative peak of about -0.035 near OL = 60° (Hansen and Hovenier 1974). These weak features would likely be lost in the noise when observing an extrasolar Venus.

Similar calculations were performed for ocean planets with thin atmospheres (Figure 45). As reflection from water-covered surfaces is affected by wind-driven waves and sea foam, the strength of winds is an important modeling parameter. For light winds (1.5 m/s), the polarization fraction approaches the value calculated by Fresnel theory for reflection at a smooth air/water boundary (dashed line). Our model departs slightly from the Fresnel equations because of the effects of sea foam (dependent on wind speed) and Rayleigh scattering (dependent on wavelength) from within the ocean.

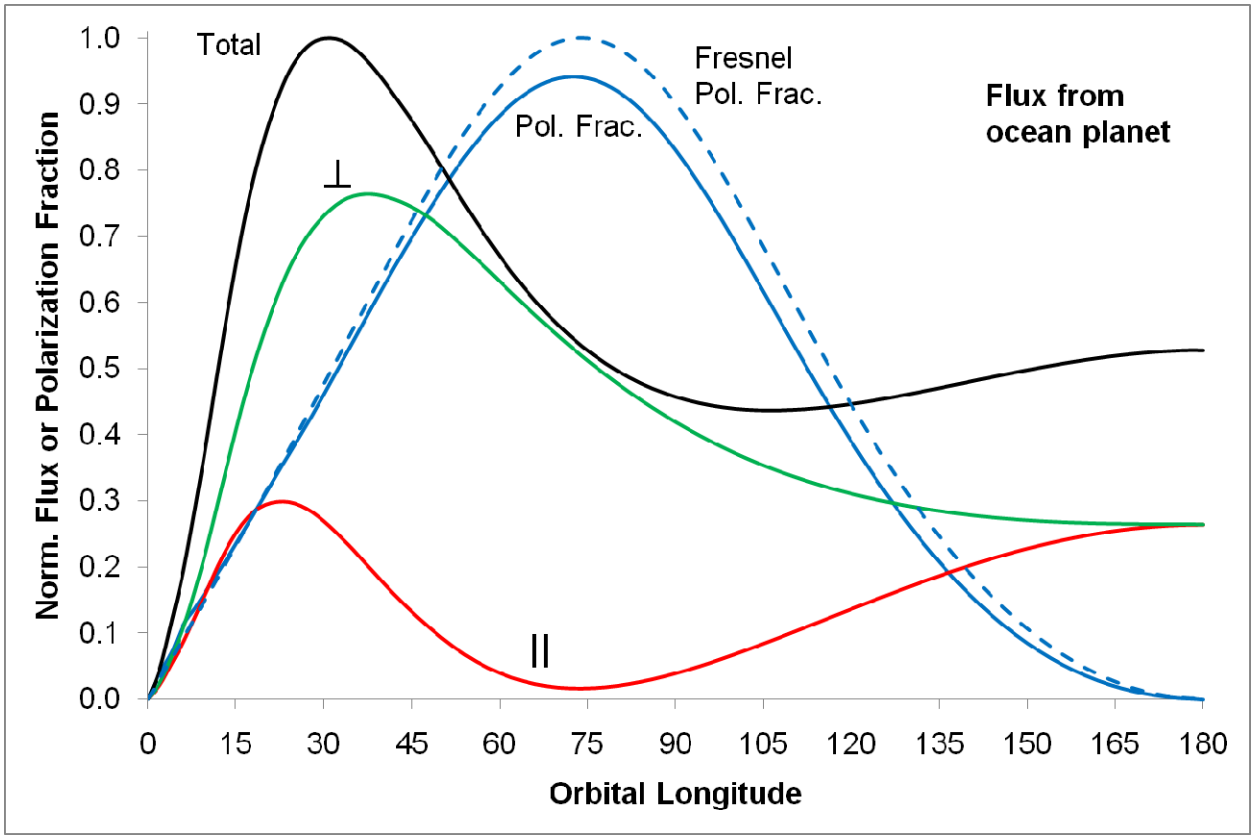

Figure 45: Polarized light curves and polarization fraction for a calm ocean planet with thin atmosphere, wavelength range 500-1000 nm

At wavelengths beyond 900 nm with the wind speed 1.5 m/s or less, the model results approach the Fresnel solution (red dashed line in Figure 46). As wind speed (and waviness) increases, the polarization fraction decreases and the OL of maximum polarization shifts to smaller values[31] (Figure 47). This figure was generated using the TPF waveband 500 – 1000 nm; when the model is run for a wavelength of 1000 nm and a wind speed of 1.0 m/s, the peak polarization is 0.978 at 74° (solid blue line in Figure 47).

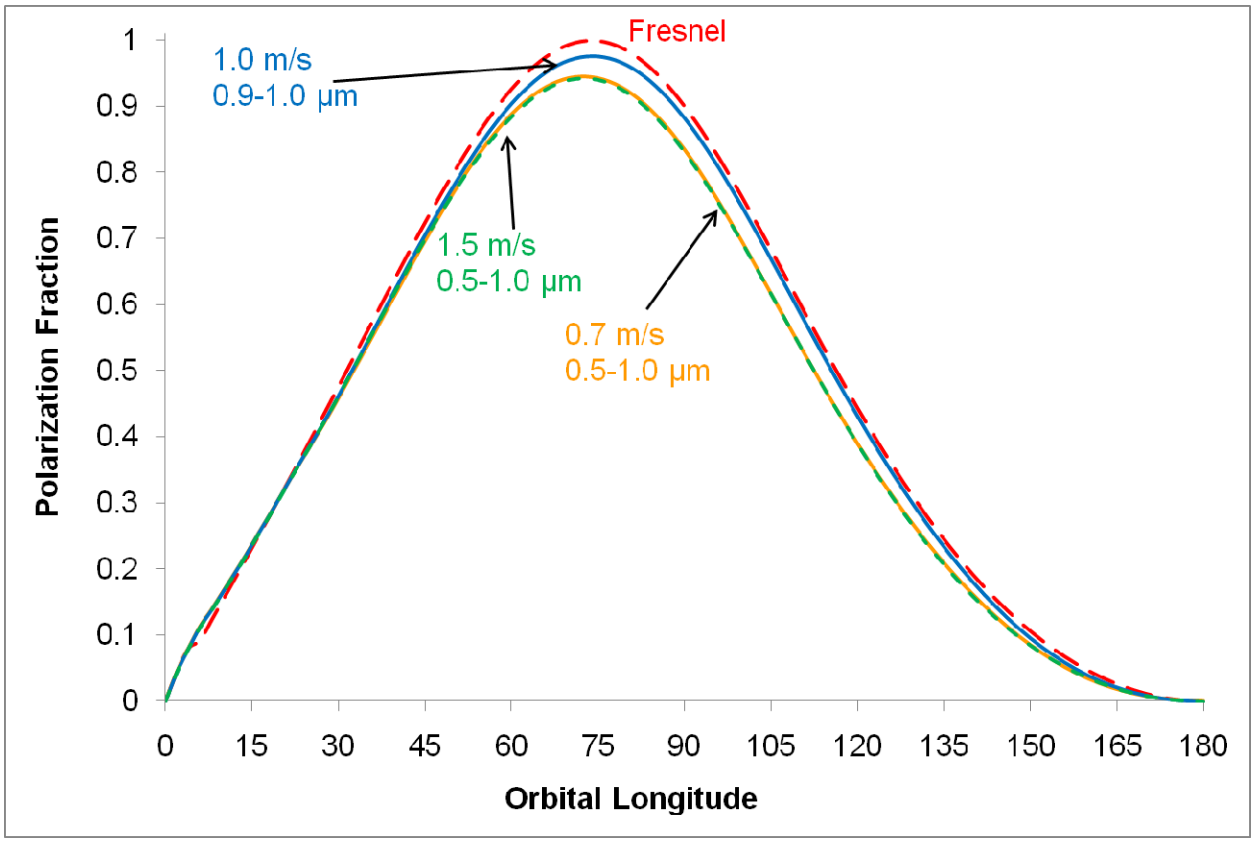

Figure 46: Effects of wind speed and wavelength on polarization fraction curve and its approach to the Fresnel curve

At higher wind speeds (Figure 47), an increasing fraction of the surface is covered with sea foam, which reflects light diffusely in approximately a Lambertian pattern, with little polarization selectivity. Also, the surface becomes more covered with waves and ripples, and acts less and less like a flat air/water interface. In both Figure 46 and Figure 47, waviness is parameterized using algorithms from Cox & Munk (1954) and wind speeds in the range 1-14 m/sec at 1 atm pressure.

In light of the discovery of methane oceans on Titan, it is reasonable to consider whether a liquid water surface could be confused with a surface covered by another liquid. Liquid methane has a refractive index of about 1.286 over the wavelength band of interest, resulting in a Brewster

[31] In order to remove a nonphysical shoulder feature caused by numerical limitations of the model, ocean surface lightcurves from our model were smoothed for OL = 2° to 6°, a portion of the orbit that will not typically be observable.

angle of 52.1°, corresponding to OL = 76°. For a methane ocean planet with thin atmosphere and no clouds, our model yields a peak polarization fraction of 0.902 at OL = 72°, very close to that for water. However, knowledge of the star's luminosity and the planet's orbital parameters should allow astronomers to distinguish between these two different liquids which have boiling points that differ by over 260 K at 1 atm.

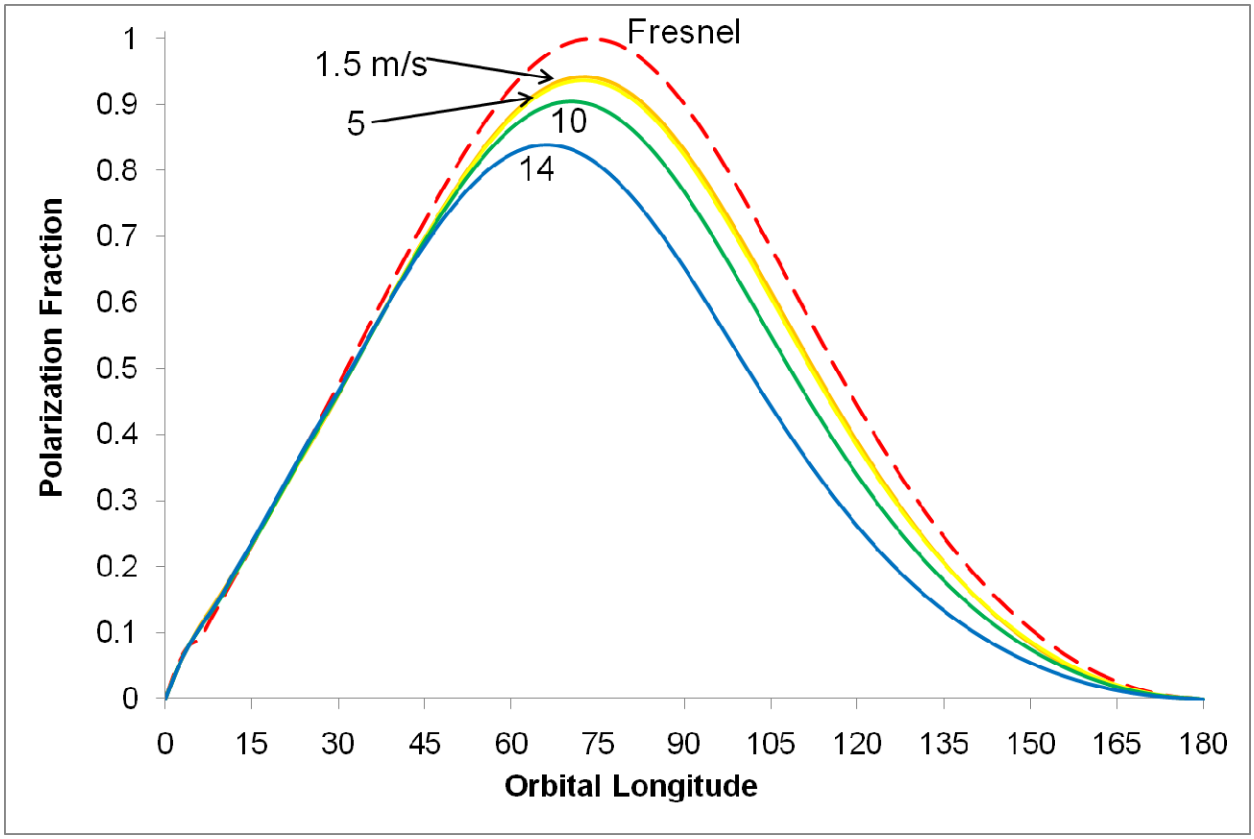

Figure 47: Polarization fraction for ocean planets vs. wind speed (no absorption, no aerosols, no Rayleigh scattering). For the TPF-C wavelength range 500–1000 nm, at wind speeds below 5 m/s, polarization fraction is limited by scattering within the water

In Figure 48, we compare the results of our model for 10 m/s winds (from Figure 47) with the results from Williams & Gaidos (2008). The primary differences between the 2008 ocean model and the current one are that the current model uses a slightly different parameterization of wind-generated sea foam, assumes Lambertian rather than isotropic scattering from sea foam, and includes scattering from within the water column.

The equation used in Oceans for sea foam fraction is

$$f_{foam} = 1.2\times10^{-5}(v_{wind})^{3.3} \tag{70}$$

which is the equation Haltrin (2002) uses for wind speeds up to 9 m/s. For wind speeds of 9 – 14 m/s, Haltrin uses:

$$f_{foam} = 1.2\times10^{-5}\left(v_{wind}\right)^{3.3}\left(0.255v_{wind} - 0.99\right) \tag{71}$$

(but the original Oceans code uses only the first formula). Dr. Williams later agreed that Lambertian scattering is a better approximation for sea foam.[32]

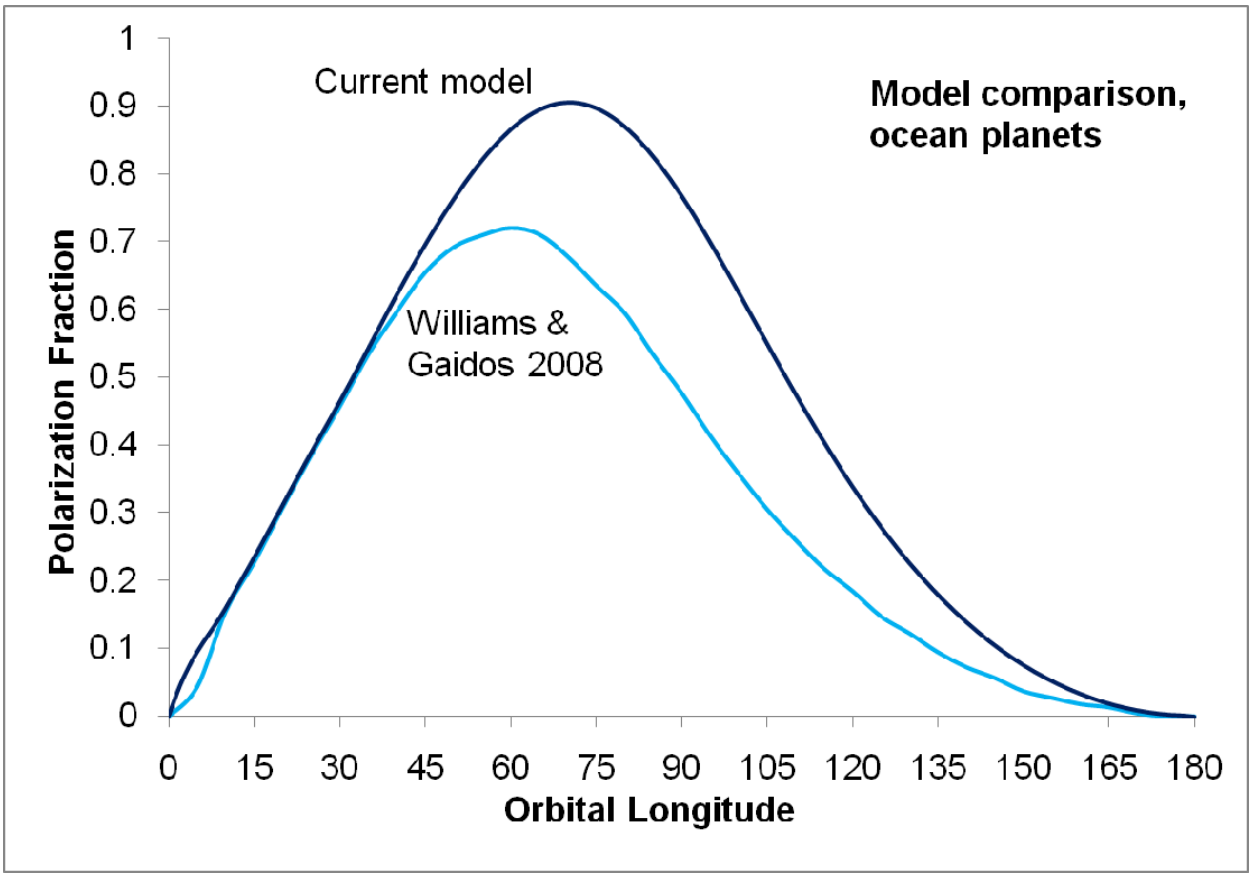

Figure 48: Comparison of present model results with those of Williams and Gaidos 2008, both with windspeed = 10 m/s. Wavelength range: 500-1000 nm

The 6SV code uses equations and data from Koepke (1984) which provide the "effective reflectance" of ocean foam, in which the fraction of sea surface covered by foam is given as (in our notation)

$$f_{foam} = 2.95\times10^{-6}\times wndspd^{3.52} \tag{72}$$

from Monahan & Muircheartaigh (1980), and the reflectance is given by

[32] D. Williams, personal communication, 2009

$$\rho_{f,tot}(\lambda) = f_{foam} \times f_{ef} \times \rho_f(\lambda) \quad (73)$$

where

f_{foam} is as given above;
f_{ef} = wind speed efficiency factor ≈ 0.4
$\rho_f(\lambda)$ ≈ 0.22 for wavelengths from visible to 800 nm, 0.2 at 1000 nm.

The resulting Total Reflectance versus windspeed is given by Koepke (1984); portions of his data are shown in Table 7. The sea foam reflectance data in Koepke (1984) extend up to wind speeds of 25 m/s, but the wave reflectance data for both our modified code and the original 6SV code are limited to a maximum wind speed of 14 m/s based on the original Cox & Munk (1954) data set.

Table 7: Sea foam and reflectance versus wind speed, after Koepke (1984).

Wind Speed *U*, m/sec	**% Area Covered with Foam, *W(U)***	**Efficiency Factor, $f_{ef}(U)$**	**Effective Reflectance, %, $R_{ef}(U)$**	**Total Reflectance due to Foam, %, $R_{f,tot}(U)$**
4	0.0	0.4	22	0.0
6	0.2	0.4	22	0.0
8	0.5	0.4	22	0.1
10	1.0	0.39	21.7	0.2
12	1.9	0.39	21.4	0.4
14	3.2	0.38	21.2	0.7

As expected, a Rayleigh scattering atmosphere over an ocean surface produces a polarization fraction curve which is intermediate between the ocean-only and Rayleigh-only cases (Figure 49). Our model predicts that Rayleigh scattering from an Earth-like atmosphere with a pressure of 1 atm has a peak polarization at an orbital longitude of 83°, closer to the Rayleigh peak at 90° than to the Fresnel peak at 74°. This result is for the nominal TPF-C spectral band of 500-1000 nm. The Fresnel result is shown again for reference.

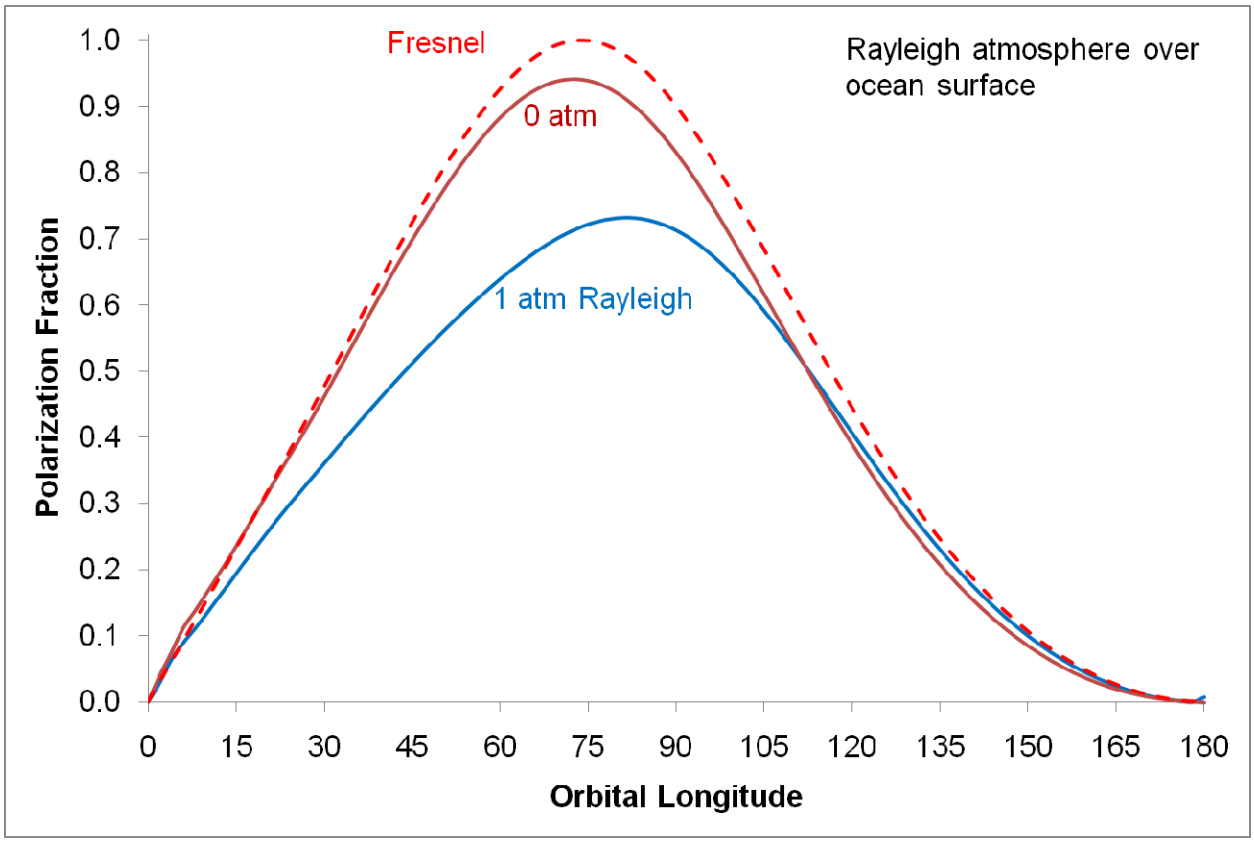

Figure 49: Polarization fraction for ocean planets vs. Rayleigh optical depth in equivalent Earth atmospheres for the TPF waveband 500-1000 nm. Both atmospheric and in-water scattering are significant. Wind is calm, no aerosols or absorption

We consider the effect of clouds on the polarization signature of a calm ocean in Figure 50. The dilution effect of Lambertian clouds depends on the product of cloud fraction and cloud albedo. As with wind speed, increasing cloud fraction or albedo causes the polarization peak to decrease in magnitude and shift to smaller orbital longitudes. Clouds with the rainbow angle effect included should show a second peak near OL = 140°, and the overall peak may be shifted slightly to higher OL.

The polarization fraction curves of three water Earth models (Figure 51) demonstrate the significant effect of maritime aerosols even using a relatively high visibility of 23 km. Without aerosols, the water Earth polarization peak occurs at OL = 83°, as in the 1 atm curve in Figure 49 (the curve in Figure 51 adds absorption). Aerosols dilute the polarization peak, and add a shoulder near OL = 140° caused by the rainbow angle peak (Bailey 2007). This feature also appears in the "cloudy" planet light curves of Stam (2008) Fig. 9 (upper right-hand panel).

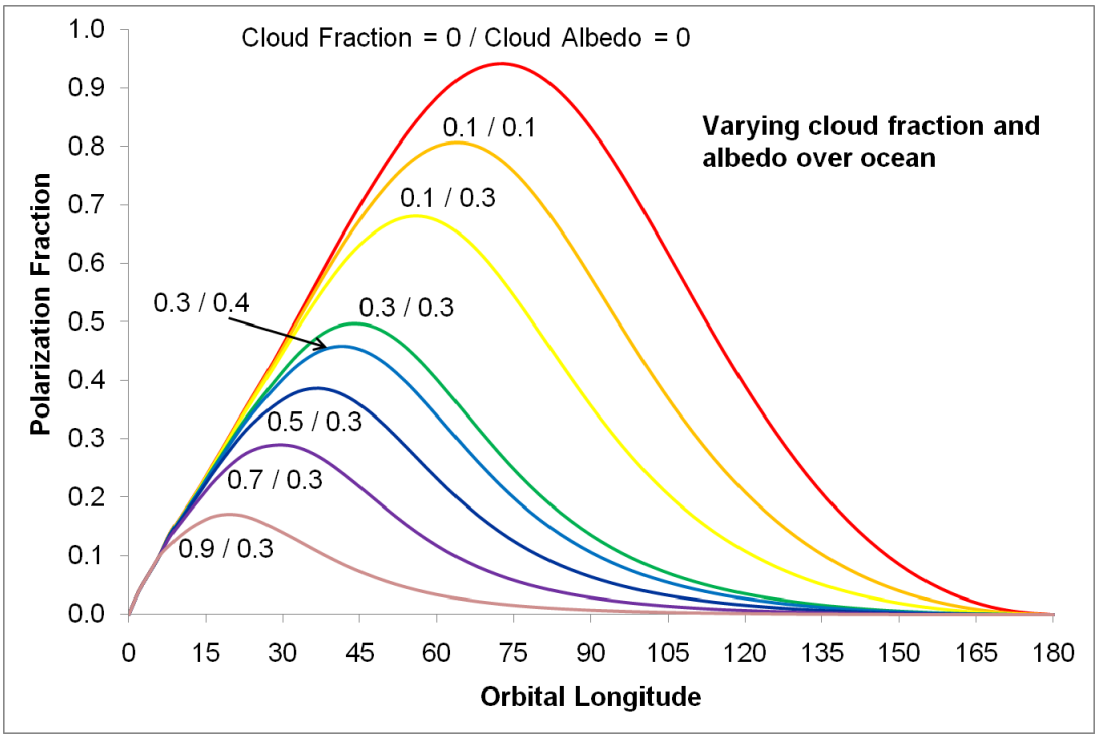

Figure 50: Polarization fraction for ocean planet with varying cloud fraction and cloud albedo, wavelength range 500–1000 nm

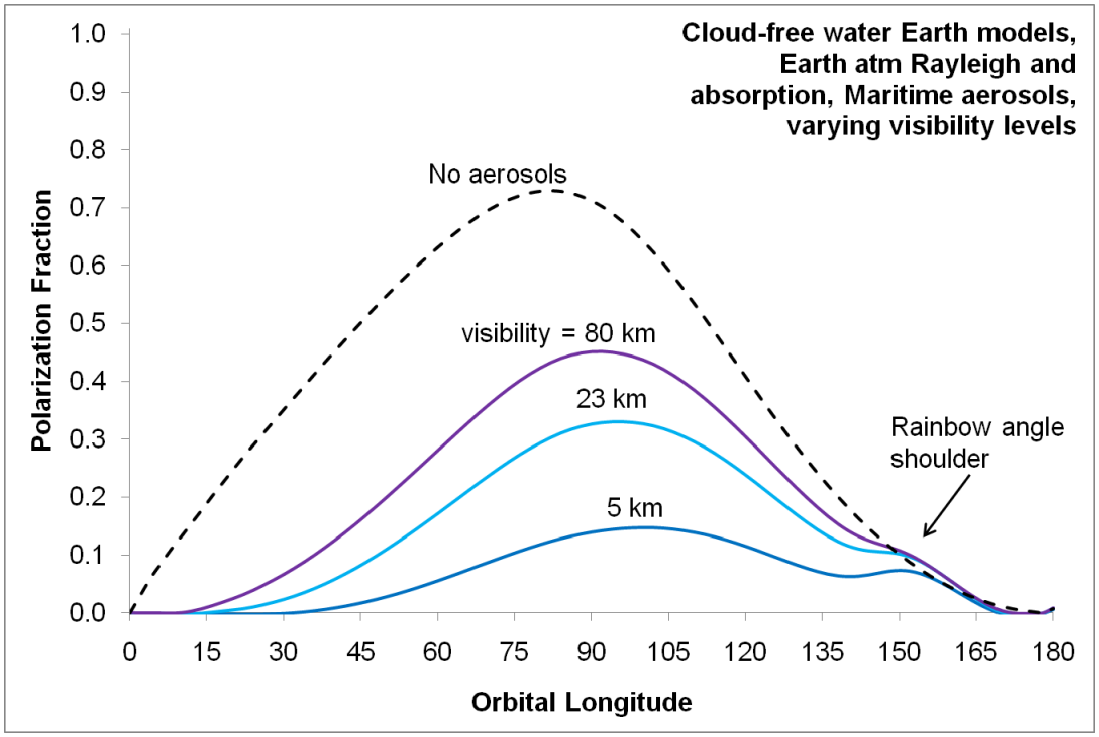

Figure 51: Water Earth models with varying aerosols, Earth Rayleigh and absorption, 500-1000 nm. Aerosol versions show reduced polarization, rainbow angle peak near OL = 140°

Figure 52 shows some preliminary simulations of the effects of longer wavelengths on observing the ocean surface polarization signature. The dark red curves indicate polarization fraction curves from the 1.55 – 1.75 µm window; the violet curve is a simulation from the 2.1 – 2.3 µm window, and the green curve is from the TPF waveband for reference. The longer wavelength portion reduces Rayleigh scattering, but has little effect on the aerosols. However, for very clear conditions such as a visibility of 60 km, the polarization fractions for both NIR windows peak at about 83°. A future paper, in process as of the date of this dissertation, will discuss additional simulations as well as contrast ratio curves in these wavebands. (The visibility distances used in this discussion refer to optical visibilities at 0.55 µm. Scattering by aerosols is calculated by 6SV using Mie calculations of particle distributions fitting these visibilities.)

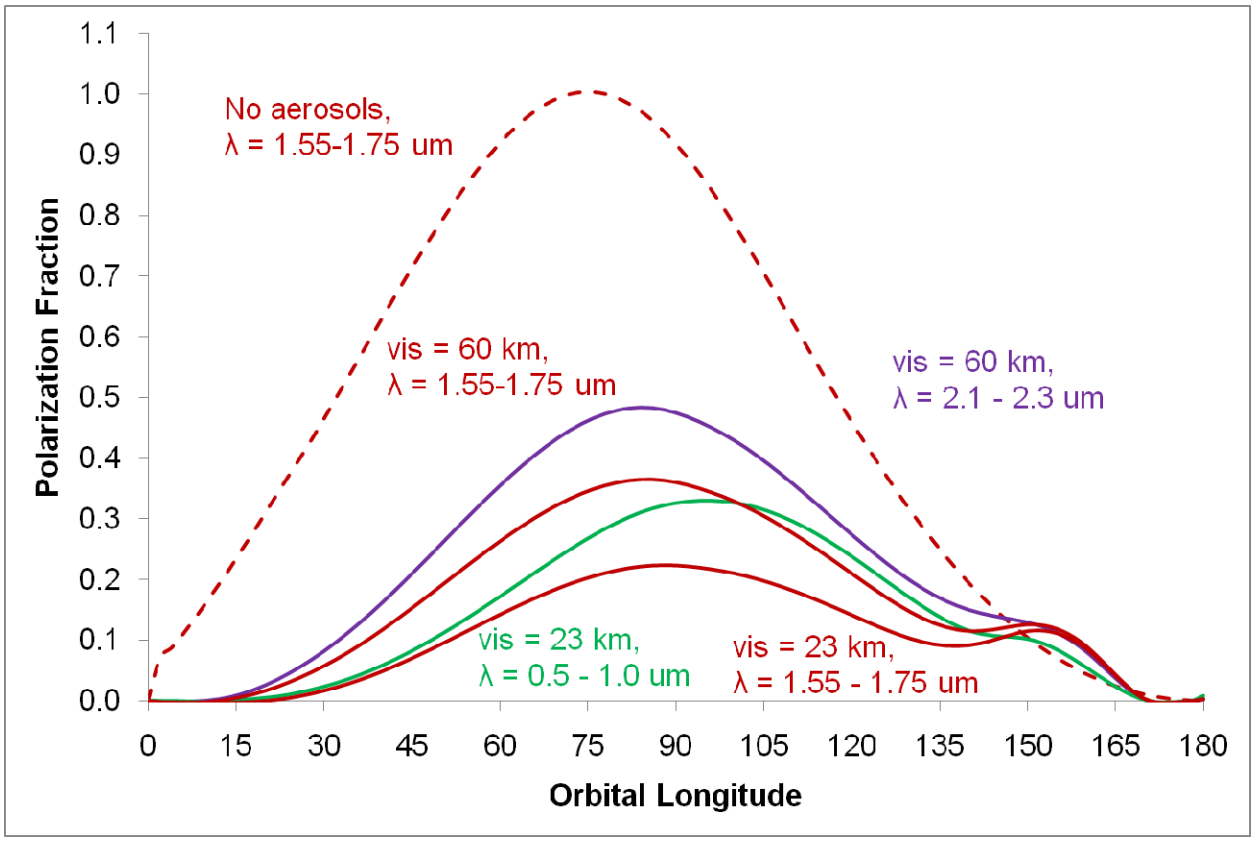

Figure 52: Preliminary simulation of observing at longer wavelength NIR windows (1.55 – 1.75 µm and 2.1 – 2.3 µm) on polarization fraction of water Earth

Figure 53 summarizes our polarized simulation results for the TPF waveband. We graph the point of peak polarization fraction for each model, thereby reducing each model case to a single point on the graph. This allows us to see trends as each parameter is varied. We now discuss these results in more detail.

The ocean planet results cluster around the point in the top center of the graph labeled "Calm ocean, $\tau_R = 0$, no clouds." For wavelengths > 900 nm, this point would fall near the Fresnel peak polarization fraction of 1.0 at OL = 74°; the position we calculate here for the TPF band is

caused primarily by dilution from Rayleigh scattering within the water column. The blue curve trending to the right shows the effects of increasing optical depth of a Rayleigh scattering atmosphere. Also, starting from the "Calm ocean, no clouds" result, the green curve shows that increasing either cloud fraction or cloud albedo reduces the polarization fraction, and moves the peak to lower OL. The violet curve shows the similar effects of increasing wind speed. The Williams and Gaidos 2008 polarization peak for a 10 m/s wind is denoted by a W, and lies below and to the left of the triangle designating the equivalent 10 m/s result for the current model (the reasons for this departure between the models are discussed in the text referring to Figure 48).

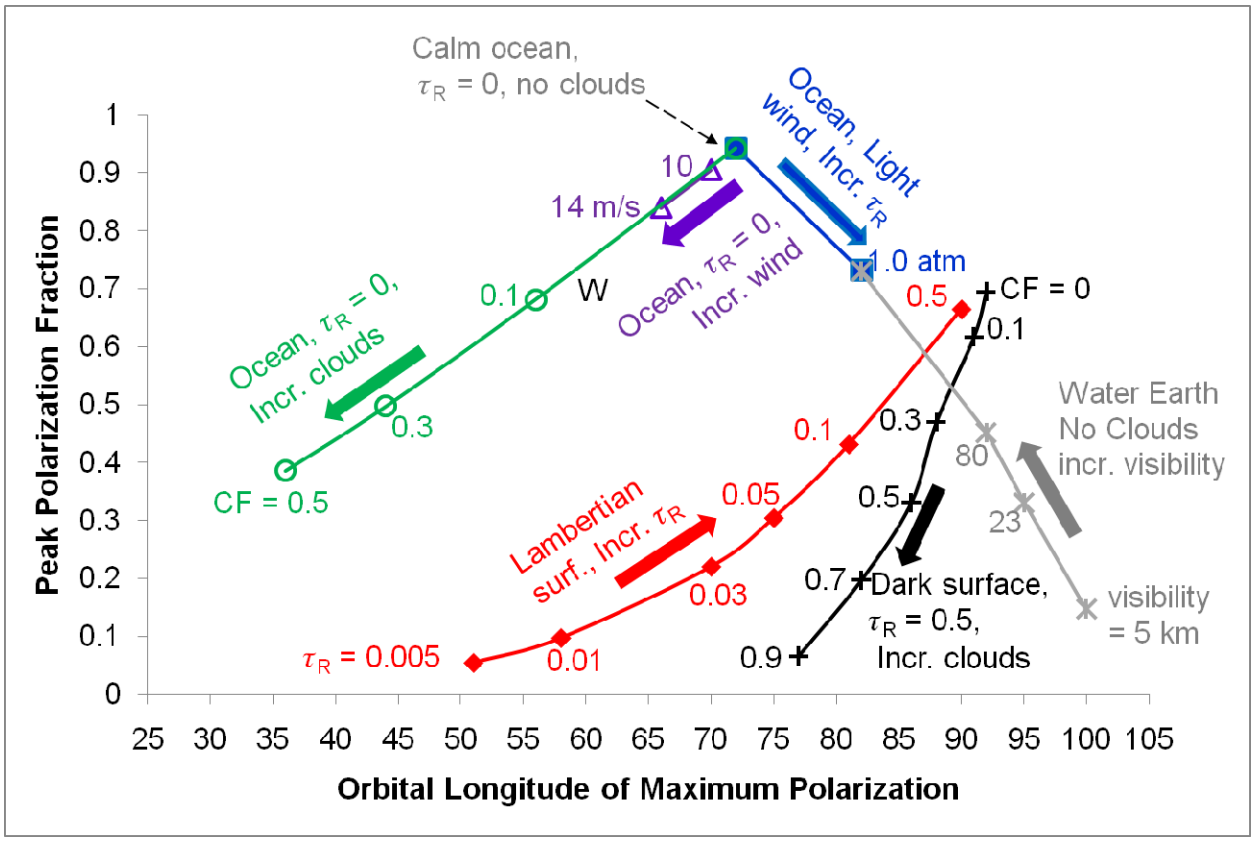

Figure 53: Summary of polarization fraction results for various planet types over the TPF waveband (500-1000 nm). Each point represents the peak polarization fraction and corresponding OL of an earlier curve

The black curve on the right side of Figure 53 shows results for a Rayleigh scattering atmosphere over a dark surface, with constant optical depth and increasing clouds. This curve models a planet dominated by Rayleigh scattering, with varying cloud cover. The polarization fraction drops and the peak moves toward smaller orbital longitude as more of the planet surface is covered by Lambertian clouds, and as the albedo of these clouds increases. The effects of increasing cloud fraction and increasing cloud albedo (not shown) are almost indistinguishable. For this curve, the surface reflectance is held constant at 0.001 (near the lower limit of model stability), and the atmospheric Rayleigh scattering optical depth is held at 0.5; however the shape of this curve is not strongly dependent upon either τ or surface reflectance as long as the Rayleigh scattering dominates and multiple scattering is present.

The red curve in Figure 53 shows polarization fraction from a Lambertian surface with reflectance of 0.10 with varying levels of Rayleigh scattering. The Lambertian surface curve approaches that for a dark surface when the same Rayleigh optical depth of 0.5 is assumed, because this atmosphere is thick enough to dominate the Lambertian surface reflectance of 0.1. As the optical depth is decreased, the peak polarization fraction drops and moves to lower orbital longitudes, as for the other cases.

Variations of "water Earths" are shown in the gray curve on the right side of Figure 53. For these models, we also include US 1962 Standard Atmosphere absorption (COESA 1962), and maritime aerosols with 5 km (low visibility standard), 23 km (high visibility standard), and 80 km visibility, all from 6SV. The surface is an ocean with a light wind speed of 1.5 m/s. The polarization fraction for these cases peaks at about 0.15 at OL = 100° for the 5 km case, and 0.33 at OL = 95° for the 23 km case. With more and more transparent aerosols, the polarization peak for water Earth cases approaches the blue curve representing a Rayleigh-only atmosphere over an ocean surface; when the aerosols are completely removed, the two curves meet.

The polarization fraction for an ocean surface hidden by a Rayleigh-only atmosphere can be increased by using only the longer wavelength portion of the TPF waveband, from 900-1000 nm. However, our more complex water Earth model shows that the polarization curve with 23 km visibility is dominated by aerosols, whether in the TPF band or in the longer wavelength NIR bands centered on 1.6 μm or 2.2 μm.

If we were to use the position of the polarization peak in Figure 53 to determine whether or not an exoplanet is watery or dry, we might say that if the polarization fraction falls near the "Calm ocean" point or the green or blue curves, then the planet has an ocean surface, and if it falls in the lower right near the water Earth cases, it has water aerosols, and therefore has at least some water. Conversely, if the planet's polarization peak falls near the red Lambertian or black dark planet lines, then it is probably dry. Also, the position of the polarization peak should be interpreted in concert with the shape of the unpolarized light curve relative to the end-member cases given in Figure 41, and the overall planet-to-star contrast ratio in comparison to the examples in Table 6. On the other hand, the gray curve shows that the peak polarization for a water Earth planet with thin aerosols can fall on or near the Lambertian and dark planet curves, producing a false negative. As demonstrated by the green and violet curves, clouds and waves shift the peak polarization point down and left on the chart, so a water planet with a combination of aerosols, clouds, and waves could have a peak polarization point falling virtually anywhere on the chart below the triangle formed by the green, blue, and gray curves, including near the Lambertian or dark curves.

6.3 Verification and Error Analysis

6.3.1 Overview

As with any code development, this new combined model must be verified. We first list the assumptions implicit in the model, then verify the code by analysis and by comparison of results

against known analytical results. To verify the model through analysis, we check the model using calculations of total illuminated area and the solar constant, and we verify the 3D trigonometry used in the model through derivation. This material is found in Appendix G. To verify the model against analytical results and other models, we use the following special cases. These compare our model results against those of other models and against analytical results; all except the first are comparisons of calculated radiant intensity *I* (W/sr). The items which are found in Appendix G are labeled (G).

1. Reflectance of a calm, flat air/water boundary versus the Fresnel equations for reflection;
2. Calm ocean-covered planet with a very thin atmosphere (ocean boundary only) versus spherical 2% mirror (G);
3. Planet with a thin atmosphere, and a wind speed of 10 m/s, which should give results very similar to those of the Williams model alone;
4. Planet with gray Lambertian surface versus analytical result;
5. Planet with gray Lambertian clouds versus analytical result;
6. Planet with Rayleigh atmosphere over a dark surface calculated in 6SV versus simplified Rayleigh model from formula inserted into Oceans.

6.3.2 Assumptions

The following assumptions are included in our model of exoplanet scattering:

1. We assume that, since Earth is teeming with life, and elsewhere in the Solar System life is either hidden or absent, Earth-like planets are the most likely to harbor detectable life;
2. We are interested in Earth-like planets, so we assume terrestrial planets exist in our stellar neighborhood (within, say, 10 parsecs/33 light years) orbiting Sun-like stars;
3. For the above reasons, we ignore gas giants, ice giants, and other non-terrestrial type planets;
4. We model broadband scattering, so
    a. coherence effects due to monochromatic sources can be ignored;
    b. spectral absorption curves can be averaged over spectral bands;
5. We assume that aerosols modeled are distributed randomly, not in any systematic way that could lead to any other frequency-selective coherence effects;
6. We model only elastic scattering and absorption, and we assume that nonlinear effects such as Raman scattering and fluorescence can be ignored;
7. We are interested in scattering from distant planets, therefore we can deal strictly with the far-field, so electric and magnetic fields are always perpendicular to the direction of propagation;
8. Because we are dealing with far-field incoherent scattering, we can sum intensities and Stokes parameters across the planetary disk.

Note that Mishchenko et al. (2000) point out that direct forward scattering and direct backward scattering always exhibit some coherence effects, at least for monochromatic light, but for our investigation, neither case is of interest. Direct forward scattering represents a planet in transit across the face of the parent star, and direct backscattering represents a planet passing behind the

parent star (secondary transit); while both cases are of interest for researchers measuring faint intensity changes or doing spectroscopic studies of atmospheres, for our purposes we note that as the planet approaches the star from our point of view, polarization approaches zero, and the instrument we seek to model will lose the ability to effectively block light from the star.

6.3.3 Verification Overview

To the extent possible, we verify the model by comparing results against analytical results. However, analytical results are available only for certain limited cases; also, time and funding limits prohibit testing all features and portions of the pre-existing code.

Table 8: Verification matrix

Model Feature Verified	6SV	Oceans	Method	Ch
Absolute brightness of Lambertian surface	X	X	Integrated radiant intensity *I*, in W sr^{-1} of Lambertian planet vs. Sobolev (1975) analytical	6.3.4
Calm water surface reflectance vs. incidence angle	X		Reflectance for 1000 nm wavelength, thin atmosphere case vs. Fresnel	6.3.5
Rayleigh scattering model	X	X	Compared Rayleigh single scattering graph against model	6.3.6
Computational Accuracy		X	Oceans calculation for Lambertian cloud-covered planet versus analytical value	6.3.7
Error induced by plane parallel approximation	X		Compared results from published plane parallel/spherical atmosphere conversion algorithm and new algorithm against uncompensated results	6.3.8, E
Sensitivity to maximum zenith angle	X		Calculated curves for water Earths using lookup tables with varying max zenith angle	6.3.8
Sensitivity to number of zenith angles used	X		Calculated curves for water Earths using lookup tables with varying number of zenith angles	6.3.8
Sensitivity to orbital lightcurve resolution		X	Calculated curves for water Earths using lookup tables with varying numbers of orbital points and zenith angles	6.3.8
Solar constant		X	Calculated	G.1.2
Surface area algorithm		X	Total Illuminated Area	G.1.1
Oceans 3D trig		X	Three-Dimensional Trigonometry	G.1.3
Water planet	X	X	calm ocean planet results versus 2% reflecting spherical mirror	G.4
Stokes rotation		X	Graphical depiction of glint spot on ocean planet	G.5

6.3.4 Verification of Combined 6SV/Oceans Model Using Absolute Brightness (Radiant Intensity)

Here, we verify the absolute brightness values calculated by our model for Lambertian clouds and surfaces, planets with thick Rayleigh scattering dominated atmospheres, and water planets with thin atmospheres. In the following discussion we refer to Table 9, which is a more detailed account of some of the same model results (and some additional results) shown earlier in

Table 6.

In section 6.1.3, we use the contrast ratio calculated in the TPF report for an Earth-like (but Lambertian) planet orbiting a Sun-like star at 1 AU (the average Earth-Sun distance) to calculate the absolute brightness of a Lambertian planet at quadrature and full phase. We now use these results to verify the Lambertian surface model in 6SV, and the Lambertian cloud model we added to the Oceans code. Row 1 of Table 9 shows the analytical results for radiant intensity, *I*, and contrast ratio, *C*, (discussed previously) for an Earth-sized planet in an Earth-like orbit about a Sun-like star, having a Lambertian reflectance pattern and a Bond albedo of 0.3. Row 2 gives our model result for a cloud-covered planet with Lambertian clouds and the same Bond albedo. Row 3 gives our model result for a planet with no atmosphere and a Lambertian surface with the same Bond albedo. The column labeled "C@90 Rel. to Lamb/TPF" gives the ratio between the model results and the analytical solution, showing that all three agree within two parts in a thousand. The cloud Lambertian result is calculated in Oceans without a lookup table, and the surface Lambertian result uses a lookup table from 6SV including the built-in Lambertian surface option.

Row 4 of Table 9 provides results generated using outputs of a two-stream radiative transfer model with a Rayleigh scattering atmosphere as a lookup table input to Oceans. We compare these results with the output of our model as an order-of-magnitude verification of our results for the Rayleigh atmosphere. For Row 4, we ran the modified Oceans software with the normal 6SV lookup table replaced by results from a two-stream model (Toon et al. 1989; Pavlov et al. 2000), for three incidence angles (vertical, 60°, and 85°). The two-stream model gives Bond albedo for each of these incidence angles, effectively averaging the reflectance into all outgoing angles. Our model sums all contributions from across the planet surface. In light of this difference, the models are in good agreement. Both models assume an atmosphere with a Rayleigh depth τ_R = 0.05.

To verify our water Earth model, we follow McCullough (2006) in comparing the brightness of a water Earth with a spherical convex mirror of the same size. Specifically, we have calculated the radiant intensity (W sr^{-1}) reflected in full phase (OL = 180°) from an ocean-covered world with light surface winds against the calculated radiant intensity from a spherical convex mirror with 2% reflectance at 1 AU from a Sun-like star. The mirror case is shown in green in row 6, and the calm ocean cases are shown in rows 7-9. The column labeled "C@180 Rel 2% mirror" compares the ocean cases with the mirror case. As expected, the ocean case with the lightest winds (1 m/s) and only long wave radiation (1000 μm) has the closest match to the mirror case, because the surface is disturbed the least by the wind, and the Rayleigh scattering from within the water column is minimized.

Table 9: Expanded model and analytical radiant intensities and contrast ratios.

Row #	Surface	Atmos.	τ_R	Earth equiv wavelength	C@90 Rel. to Lamb/ TPF	C @ 90	I @ 90	C @ 180	C@ 180 Rel 2% mir-ror	I @ 180	Com-ments
1	Lambertian, A_{bond} = 0.3	none	0.00	--	1.000	1.154E-10	3.536E+15	3.625E-10		1.111E+16	from Sobolev
2	Lambertian, Cloud A = 0.3	none	0.00	--	0.997	1.150E-10	3.524E+15	3.613E-10		1.107E+16	CF =1, refl = 0.3
3	Surface Lamb., ρ = 0.3	none	0.00	--	0.998	1.152E-10	3.530E+15	3.603E-10		1.104E+16	
4	Dark	Earth Rayl.+ abs.	var	solar spectrum	0.483	5.575E-11	1.708E+15	1.115E-10		3.416E+15	Kasting results
5	Dark ρ = 0.01	Rayleigh 648 nm	0.05	648 nm	0.168	1.940E-11	5.945E+14	7.261E-11		2.224E+15	
6	Spherical mirror, ρ = 0.02	none	0.00					9.074E-12	1.00	2.780E+14	from Tousey
7	ocean 1.5 m/s TPF wavelengths	none	0.00	500 - 1000 nm	0.083	9.603E-12	2.942E+14	1.137E-11	1.25	3.484E+14	
8	ocean 1.0 m/s 900-1000 nm	none	0.00	900 - 1000 nm	0.079	9.060E-12	2.776E+14	9.633E-12	1.06	2.951E+14	
9	ocean 1.0 m/s 1000 nm	none	0.00	1000 nm	0.078	9.043E-12	2.771E+14	9.605E-12	1.06	2.943E+14	

In Figure 54, the contrast ratio versus orbital longitude for a Lambertian planet with a Bond albedo of 0.3 is plotted. The two curves represent the output of two different cases: the black dashed cure is our model output for this case, and the gray solid curve is the analytical result from Russell (1916), Sobolev (1975), and the TPF report. The excellent agreement throughout the orbit serves to verify our model for Lambertian surfaces.

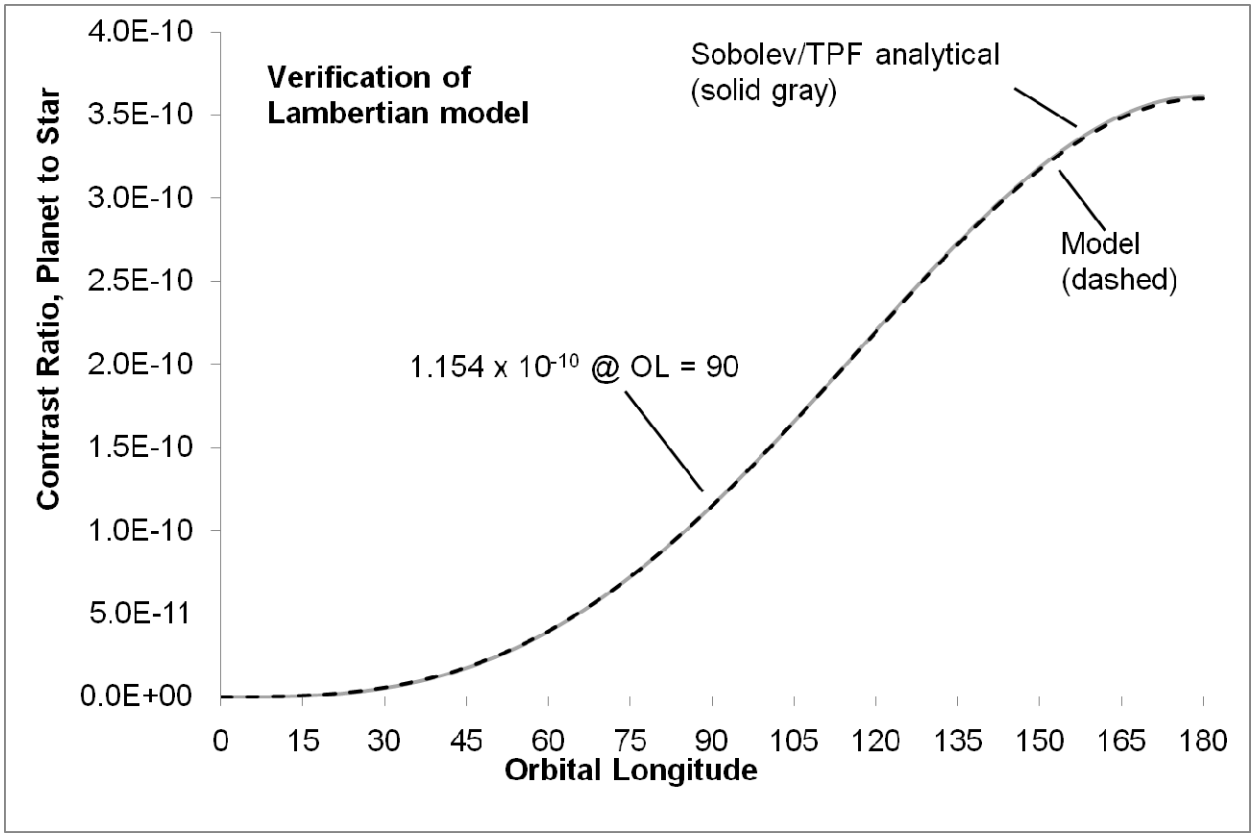

Figure 54: Light curves for Lambertian planet for our model versus analytical solution

6.3.5 Verification of 6SV Sea Surface Model

6.3.5.1 Summary

The implementation of the Fresnel equations in the 6SV ocean surface model was verified by checking the equations in the code. The modifications to 6SV were verified first by comparing runs of the modified 6SV against the analytical results from the Fresnel equations, then by running the combined exoplanet modeling code and comparing those results against analytical results. The model results versus Fresnel equations are shown below, and the remainder can be found in Appendix G.

6.3.5.2 Verification of 6SV calm ocean results versus Fresnel equations

Figure 55 shows the results of running modified 6SV code for a calm ocean surface, for both polarizations and the polarization fraction versus the Fresnel equations. The small difference between the polarization fractions near the Brewster angle is primarily due to dilution by unpolarized light reflected by sea foam and scattered within the water column, both included in the 6SV model but not in the Fresnel equations.

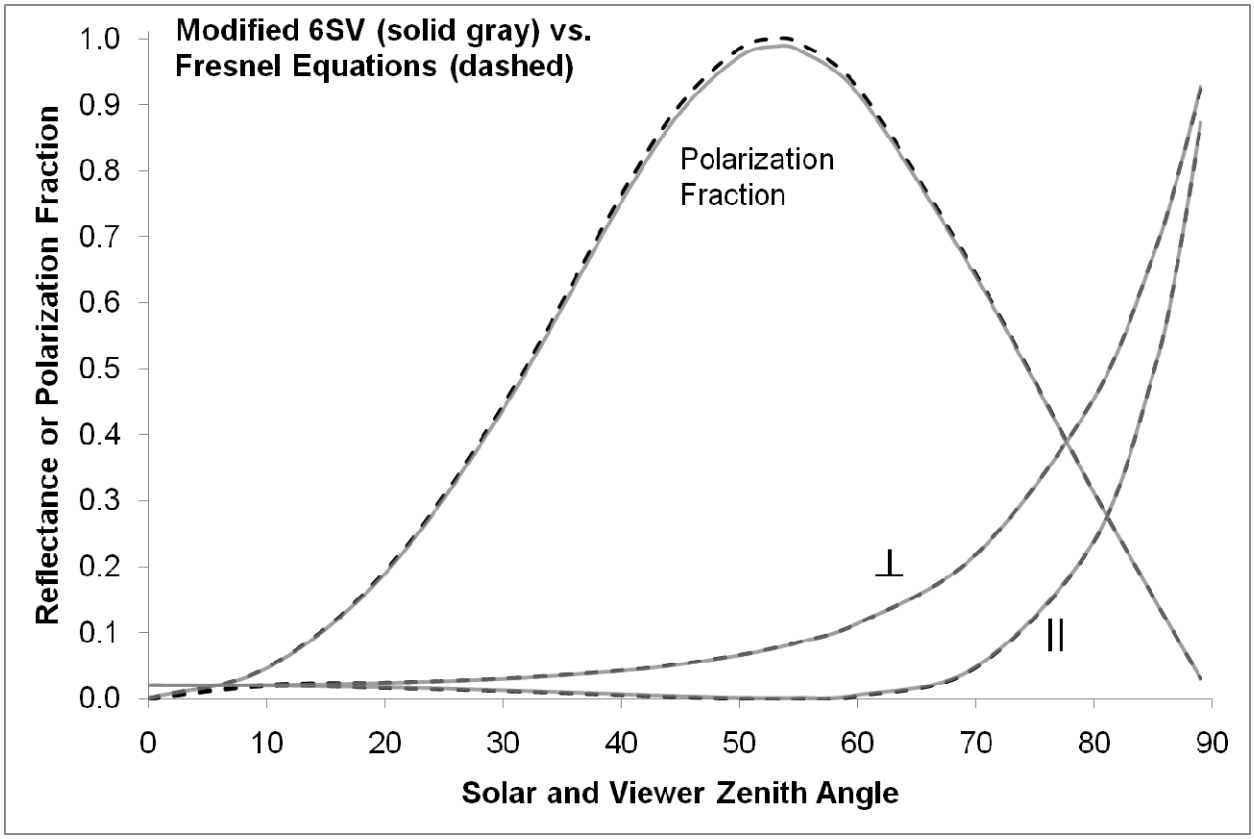

Figure 55: Reflectance and polarization fraction from modified 6SV model (solid) vs. analytical result from Fresnel equations (dashed)

6.3.6 Verification of Rayleigh Scattering Model

Now we replace the 6SV Rayleigh scattering calculation with a simplified analytical calculation of relative Rayleigh single scattering; here the light scattered is proportional to one minus the exponentially decreasing transmission through the Rayleigh atmosphere, the path length increases as 1 over the cosine of the zenith angle, and the parallel polarization scattered in the direction of interest is decreased by the square of the cosine of the scattering angle:

```
pathN = 7
tauR = 0.5
path = pathN/(cos(znstar)+1e-6)
path = min([path,pathN*10.0])
```

```
path = max([path,0.0])

roIparl = (1-exp(-path*tauR))*csca*csca
roIperp = 1-exp(-path*tauR)
```

For Rayleigh scattering coefficient $\tau_R = 0.5$ the shapes of the curves are close, although multiple scattering is evident in the Oceans/6SV curve, as seen in Figure 56, where the minimum in the parallel polarization is diluted by light multiply scattered from the perpendicular to the parallel polarization.

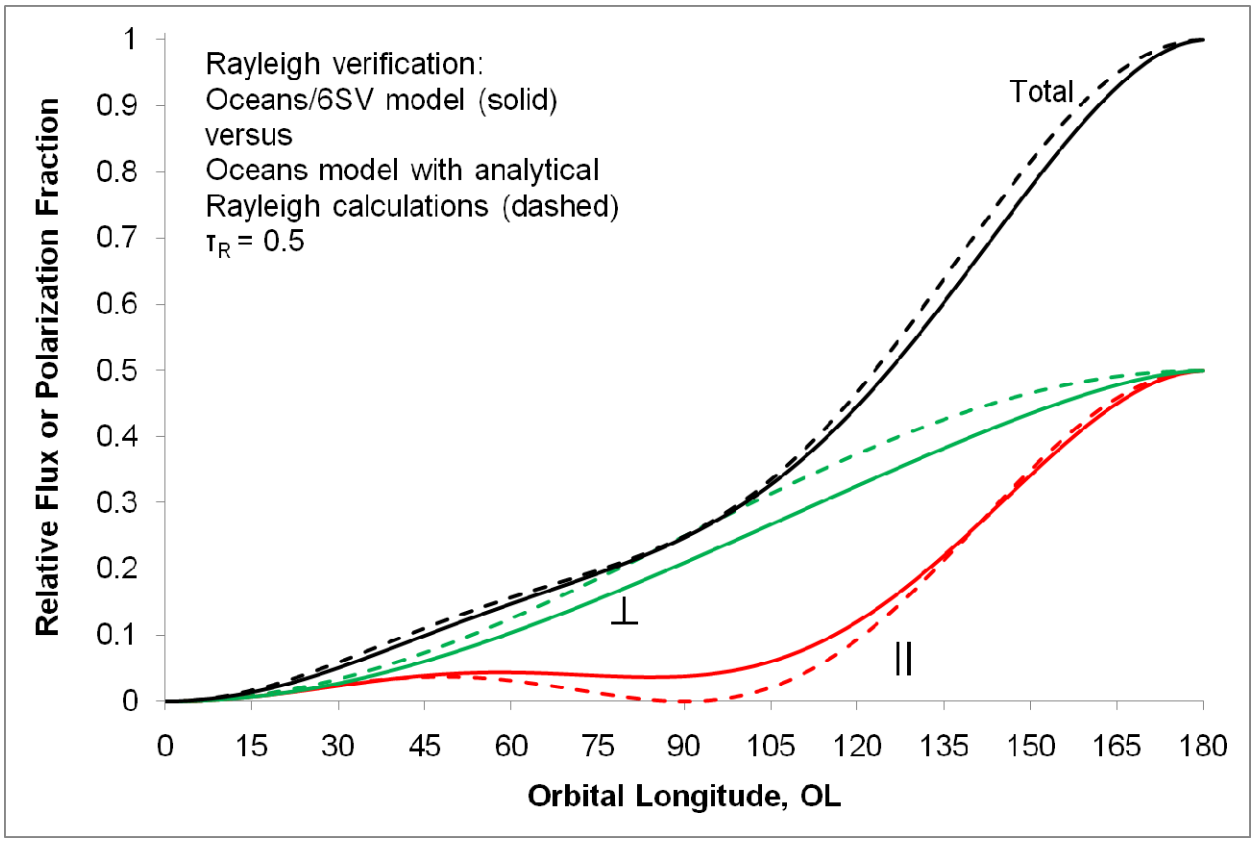

Figure 56: Verification of Rayleigh scattering model using $\tau_R = 0.5$

When we reduce τ_R to 0.10, which should reduce double scattering by approximately a factor of $(0.5)^2/(0.1)^2 = 25$, we obtain Figure 57 below, in which the simplified model and complete model are in better agreement. The value of the normalized parallel reflectance at 90° is 0.018 from the Oceans/6SV model, compared to 0.038 for the $\tau_R = 0.5$ case.

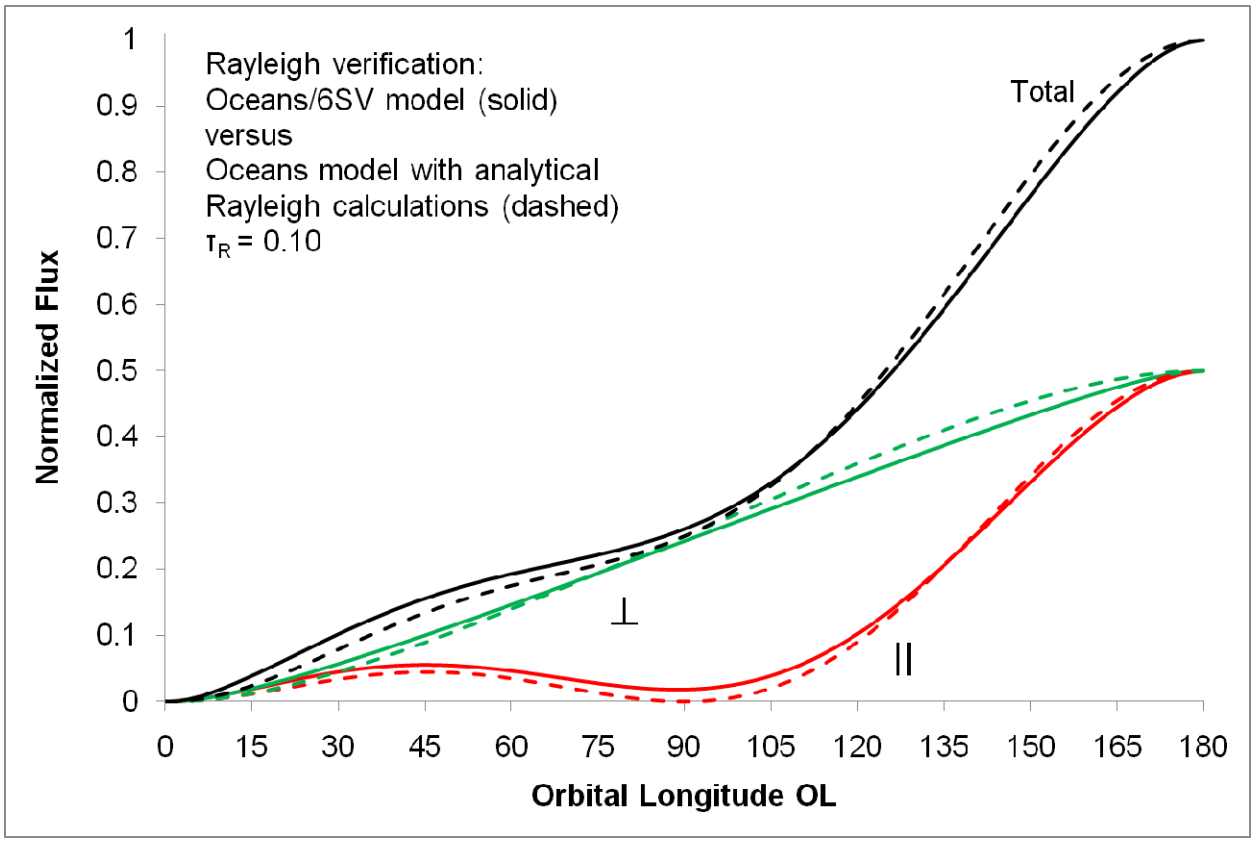

Figure 57: Verification of Rayleigh scattering with τ_R reduced to 0.1

6.3.7 Computational Accuracy

Dividing the planet surface into discrete 2° x 2° pieces introduces some spatial quantization error. We can get an idea of the level of this error by referring to Table 9. The Lambertian cloud calculation removes 6SV from the calculation; the value calculated by Oceans for the cloud-covered planet is 0.998 of the analytical value, so the error in this case from all Oceans calculations is 2 parts per thousand or 0.2%.

6.3.8 Sensitivity Analysis

In order to further verify the model, we need to know if the answers we are obtaining are critically dependent on a particular model parameter. To do this, we determine the effect of the plane-parallel atmosphere approximation, and the sensitivity of the model to the following internal parameters:

1. Maximum zenith angle modeled in the 6SV-generated lookup table;
2. Number of discrete angles used in the lookup table;
3. Number of latitude and longitude points on the quantized planet;
4. Number of points in the planet orbit.

6.3.8.1 Plane parallel versus spherical atmosphere

The 6SV code assumes a plane parallel atmosphere, but of course a planet's atmosphere is approximately spherical. In order to address this, I added the capability to my IDL bilut routine to partially compensate for the plane parallel approximation using either the Kasten and Young approximation or an approximation that I developed based on an exponential atmospheric pressure profile. For a disk-averaged planet, the differences turned out to be negligible, as shown in Figure 58. For details of these algorithms, see Appendix E.

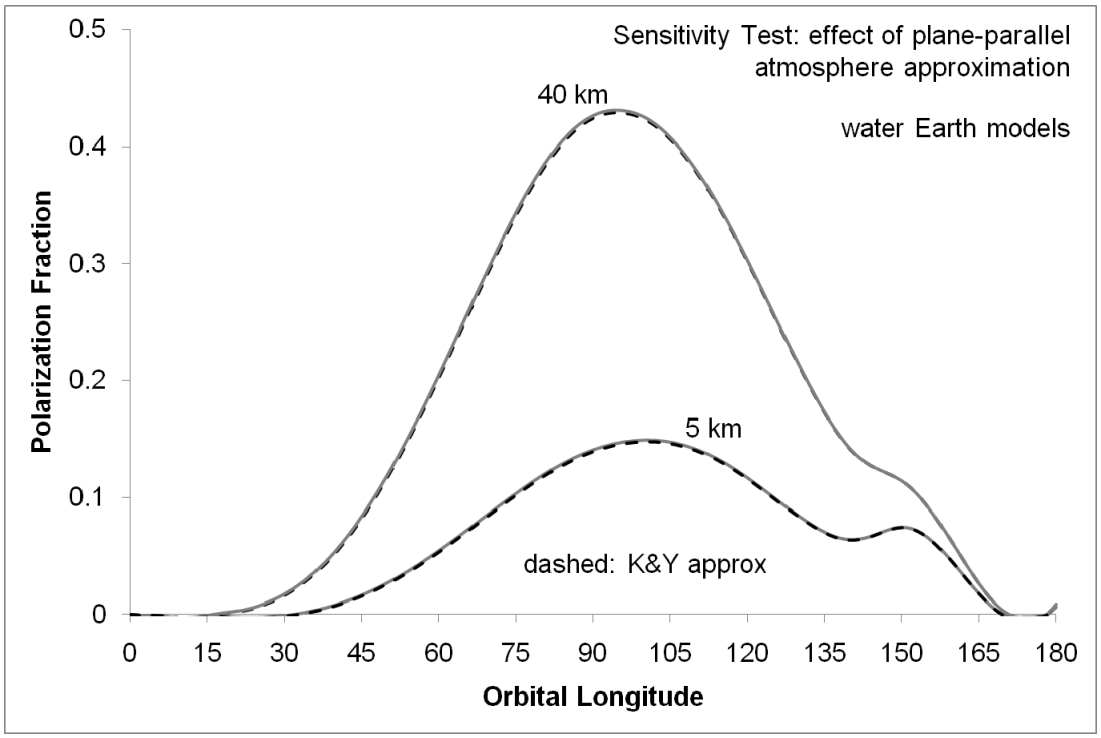

Figure 58: Sensitivity to plane parallel (solid) versus spherical atmosphere using Kasten and Young approximation (dashed)

6.3.8.2 Effect of Maximum Zenith Angle

In order to test the sensitivity of the result to maximum zenith angle, the water Earth model, with an ocean surface, wind speed of 1.5 m/s, Earth-like Rayleigh scattering and absorption, and Maritime aerosols with a visibility of 23 km, was run four times with different maximum incoming and outgoing zenith angles. The wavelength range used was the TPF band, 500 – 1000 nm. The four cases (Figure 59) fall almost on top of each other, and can be separated only by using color combined with different dash styles. The maximum zenith angle of 87° was used for most of the figures in this thesis and in the Astrophysical Journal paper (Zugger et al. 2010).

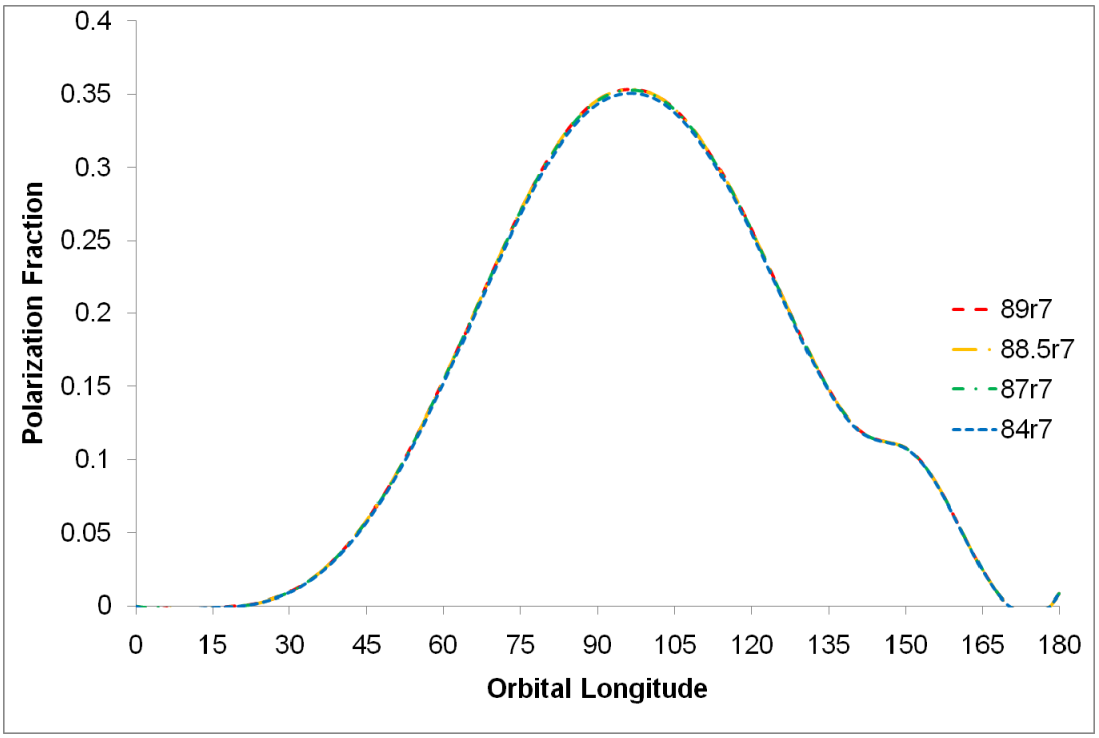

Figure 59: Sensitivity to maximum zenith angle

6.3.8.3 Effect of Number of Angles Generated by 6SV for Lookup Table

The conditions for this sensitivity are the same as those in the above test. Here, we test the effect of the number of angles in the lookup table. For the "d" full set of angles, the incoming and outgoing zenith angles are primarily spaced at 3°, while the zenith angles for the reduced angle set "r7" are primarily spaced at 10°: The relative azimuth angles for the two are identical:

88.5r7:

```
Solar and Viewer Zenith Angles = [0.0, 10.0, 20.0, 30.0, 40.0, 50.0, 53.1,
55.0, 60.0, 70.0, 75.0, 80.0, 84.0, 87.0, 88.5]

Relative Azimuth Angles = [0.0, 10.0, 20.0, 30.0, 40.0, 50.0, 60.0, 70.0, $
  80.0, 90.0, 100.0, 110.0, 120.0, 130.0, 140.0, 150.0, $
  160.0, 165.0, 170.0, 175.0, 177, 178.0, 179.0, 179.5, 180.0]
```

88.5d:

```
Solar and Viewer Zenith Angles = [0.0, 3.0, 6.0, 9.0, 12.1, 15.0, 18.0, 21.0,
24.0, 27.0, 30.0, 33.0, 36.0, 39.0, 42.0, 45.0, $
  48.0, 51.0, 54.1, 57.0, 60.0, 63.0, 66.0, 69.0, 72.0, 75.0, 78.0, 81.0,
84.0, 87.0, 88.5]

Relative Azimuth Angles = [0.0, 10.0, 20.0, 30.0, 40.0, 50.0, 60.0, 70.0, $
  80.0, 90.0, 100.0, 110.0, 120.0, 130.0, 140.0, 150.0, $
  160.0, 165.0, 170.0, 175.0, 177, 178.0, 179.0, 179.5, 180.0]
```

The two different sets of angles listed above were used to generate separate light curves, and these are plotted together in Figure 60.

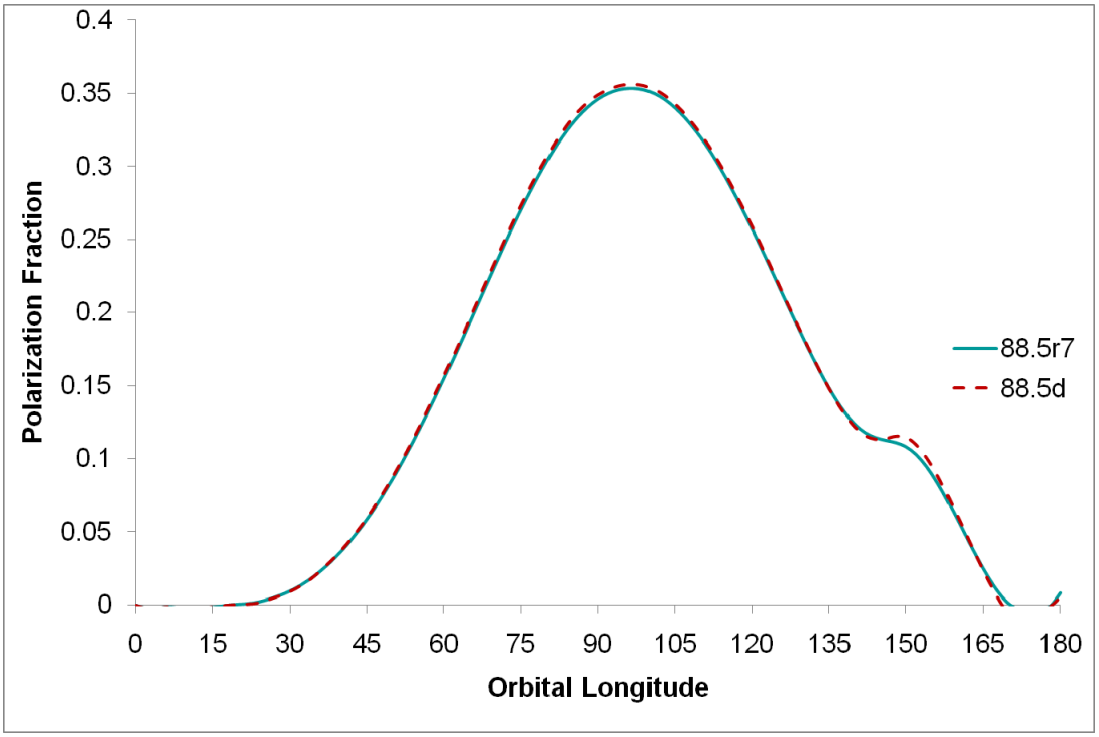

Figure 60: Sensitivity to number of zenith angles used

The only significant effect of the higher angular resolution in the lookup table is that the "cloudbow" feature from the aerosols is slightly enhanced in the curve using the high-resolution set of angles. The penalty in run time for the lookup table is to increase runtime from approximately 12 hours to 5 days (120 hours), or about a factor of ten. In practice, some of the longer runs took much longer because the Linux computer was taken down because of power failures or system maintenance and upgrades, and as a result sometimes needed to be run two or three times before the lookup table was completed.

6.3.8.4 Effect of Resolution of Lightcurve

Here, we start with a high-resolution lookup table, and change the resolution of the Oceans portion of the model to determine the effect on the plot. For the 87d2 curve, we use the standard resolution of 2° in latitude and 2° in longitude on the planet surface, and 2° in orbital longitude. For the 87d1 curve, all of these resolutions are 1°, twice as fine. Figure 61 shows that increasing the resolution to 1° in all these dimensions has negligible effect on the plot. The time to run Oceans increases by approximately a factor of $2^3 = 8$, from 2-4 hours to 16-32 hours.

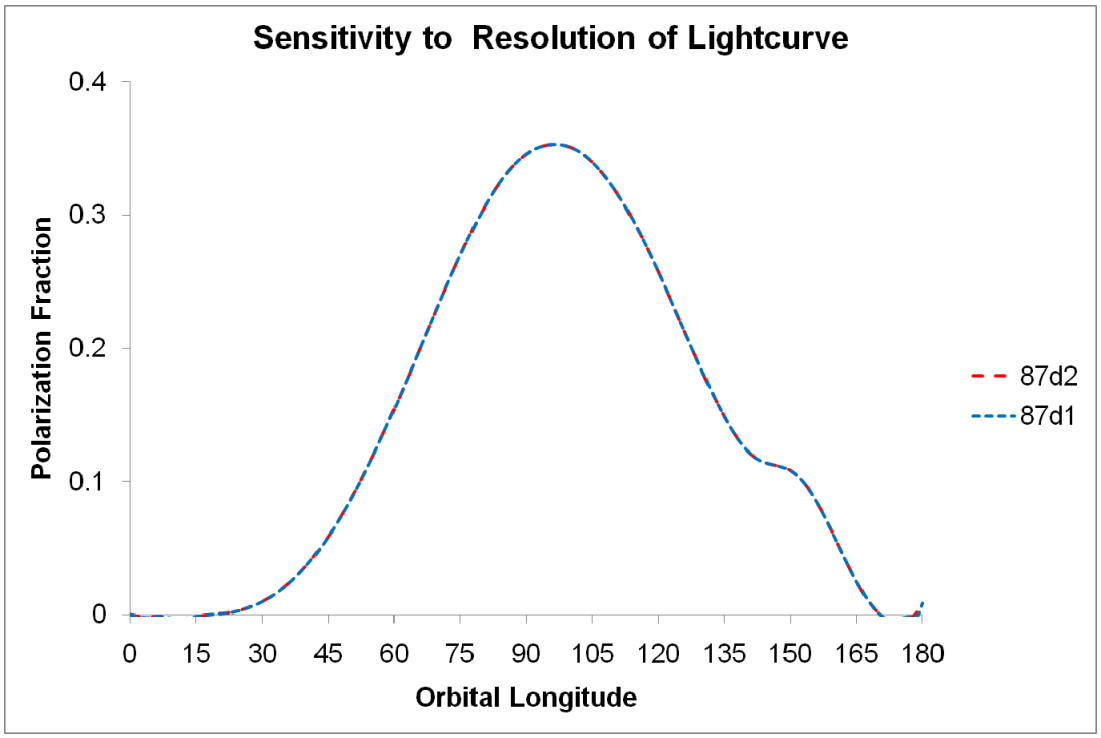

Figure 61: Sensitivity to orbital lightcurve resolution

6.4 Discussion

6.4.1 Effect of Orbital Inclination

As discussed earlier, the results shown here are for a planet with a homogeneous surface in an edge-on orbit (i = 90°). For increasingly face-on orbits, the variation in both total flux and polarization fraction over the planet's orbit is expected to approach zero, as was shown explicitly in Figure 6 of Stam (2008). On the other hand, slightly inclined orbits could increase the fraction of the orbit in which the planet-star distance exceeds the minimum value that can be observed.

6.4.2 Effect of High Winds

Our model is limited to waviness caused by sea-level wind speeds up to approximately 14 m/s, the highest wind speed investigated by Cox & Munk (1954) measured at 12 m above the sea surface. An ocean planet with no land to impede the winds might conceivably have high wind speeds and a foamy, bright Lambertian surface. Alternatively, such a planet could conceivably have sustained winds from the same direction, creating a reflectance pattern that is highly asymmetric in azimuth, resulting in a complicated light curve that may be asymmetric in orbital longitude. This source of confusion might be minimized by observing over all orbital longitudes.

6.4.3 Wavelength-Dependent Light Curves

Using the Deep Impact spacecraft to observe the Earth as if it were an exoplanet, the EPOXI team (Cowan et al. 2009) obtained light curves of Earth over seven 100-nm-wide wavebands between 300-1000 nm. Principal component analysis showed that two "eigencolors" captured 98% of the diurnal color changes caused by Earth's rotation. These eigencolors are essentially spectra of filters which could be used to distinguish between land surfaces and water surfaces. The cutoffs are gradual, but the land filter passes the red and near-infrared wavelengths between about 700 and 1000 nm, while the water filter passes the green, blue, and violet wavelengths below about 550 nm. Using this method the team was able to map the longitudinal variation in land surface area, which peaks when Africa and Europe are being observed and which approaches zero in the mid-Pacific. The technique proved successful despite the confusion generated by 50% cloud cover. This method of detecting land-sea contrasts might also work for an exoplanet, provided that enough photons were available to resolve diurnal variations.

6.4.4 Rainbow Angle

For planets with liquid droplets in the atmosphere, Bailey (2007) shows that at the "rainbow angle," total flux is higher and the polarization fraction can be as high as 0.2. For water droplets, the rainbow angle occurs at about OL = 140°, and for methane droplets, at OL = 131°. His calculations show that the effect is consistent for particle sizes from 10-100 μm at a wavelength of 400 nm, and that it weakens for smaller particles. These results are scalable throughout the TPF-C wavelength band when the ratio of particle size to wavelength is held constant. The Bailey paper predicts this effect for water droplets in clouds, but our model shows that the effect is similar for water aerosols such as the maritime aerosols typically found over Earth's oceans. Bailey's model and the 6SV aerosol model both use Lorenz-Mie scattering, so our result is a confirmation both of Bailey's result and of the 6SV aerosol model.

The effect of the rainbow angle for an ocean planet is to add a third competing polarization peak near OL = 140° to those caused by the water surface (near OL = 74°) and by atmospheric Rayleigh scattering (near OL = 90°). In our cloud-free water Earth model, the rainbow peak from aerosols shifts the total polarization peak to about 99°. We model clouds as simple Lambertian reflectors. If our cloud model included Lorenz-Mie scattering and exhibited a rainbow angle enhancement, clouds would serve not only to dilute the Fresnel water polarization peak, but to further strengthen the competing rainbow polarization peak. Such a cloud model may be developed for future analysis; however, clouds, even considering only those on Earth, are varied and complex (see section 6.4.5).

6.4.5 Clouds

Since seven of the eight solar planets and many of their moons have clouds of some type, we can reasonably expect that most exoplanets with atmospheres may have clouds. Across the solar system the variety of cloud types is impressive: sulfuric acid clouds on Venus, ice clouds on

Mars, ammonia clouds on Jupiter and Saturn, and methane clouds on Neptune and Uranus. Earth clouds alone include a wide variety of water clouds with varying droplet sizes and distributions, as well as ice clouds made of particles ranging from highly symmetric hexagonal crystals to irregular particles. Each type of cloud has different scattering properties, so the parameter space for scattering from cloudy planets is enormous.

As mentioned earlier, some liquid water clouds have share the aerosol property of producing a polarized "cloudbow" near OL = 140°, which in some water-rich planets could reinforce the polarization signal from water aerosols. Ice clouds have different properties; work by Takano and Liou (1989; 1995) found that hexagonal and irregular ice clouds can exhibit a wide range of both local scattering peaks and polarization peaks depending on the particle size and shape distribution.

Rather than attempt to parameterize this range of characteristics of hypothetical exoplanet clouds, we have chosen to model clouds as Lambertian, a common practice in remote sensing of Earth, as pointed out by Acaretta et al. (2004). The Lambertian approximation is reasonable (especially for a broadband unpolarized stellar input) because, depending upon the variety of types of clouds present, the particle size range, and the amount of multiple scattering, the total cloud integrated signal can be nearly Lambertian. We discuss the cloudbow effect as one possible deviation from our model.

6.4.6 Exo-Zodiacal Light

Zodiacal light in our solar system is caused by scattering of sunlight by dust particles concentrated in and near the plane of the ecliptic. First detected around β-Pictoris by Smith and Terrile (1984), exo-zodiacal light (exo-zodi) scattered by similar disks in exoplanet systems is now considered to be a significant concern for future exoplanet investigation, and will generally be partially polarized. Additional data from surveys is needed to determine the characteristics of exo-zodi in order to optimize both future planet finding telescopes and analysis software.

6.4.7 Using Polarization to Determine Association and Orbital Inclination

The presence of significant linear polarization in the light from a candidate planet could be used in showing that the object is indeed in orbit around the parent star, and is not a background object. Regardless of whether the polarization is caused by Rayleigh scattering, a liquid surface, or both, a reduction in the "parallel" polarization component – the component parallel to the plane defined by the parent star, the planet, and the observer – would indicate that the object is probably a planet that is being illuminated by the star it appears to orbit. The inclination of planetary orbits could also be constrained by polarization measurements. To date, polarization from giant exoplanets has been difficult to detect in the combined light of the planet and star (Lucas et al. 2009), but our model predicts significant levels of polarization for many different types of terrestrial planets when the planets can be resolved from the parent star.

6.4.7.1 Polarization and Planet Mass Determination

Planets studied using the radial velocity (Doppler) method are assigned masses of m sin(*i*), where *i* is the unknown angle of inclination of the orbit to the line-of-sight; without further information from transits, dynamical constraints, direct observations of the planet, or other methods, the actual mass can be anywhere between *m* and infinity. If the planet transits the star as seen from Earth, then the orbital inclination and mass can be accurately estimated, however for an Earth-like system this is only four planets out of one thousand. The $1 billion Space Interferometry Mission (SIM) is intended to determine the actual mass of many planets, but it has been delayed due to cost concerns and may be cancelled based on the 2010 Decadal Survey.

Is there another way to measure actual planet masses? Perhaps polarization could assist in determining the inclination of the orbit of planets with surfaces and atmospheres that are approximately horizontally homogeneous. Returning to our simple model, for a planet that has either a Rayleigh scattering atmosphere or a liquid surface, or both, the direction of polarization of the scattered light rotates with the planet. For edge-on orbits, the polarization fraction varies widely as the planet orbits, but the direction of the polarization vector does not; for face-on orbits, the polarization factor is constant but the direction rotates with the planet's orbital motion. A combination of polarization fraction and polarization direction could be used, along with the planet's changing position angle in images, to constrain the orbital inclination angle.

6.4.7.2 Determining Planet/Star Association

A smaller, dimmer object which appears to be near a star can be in orbit around the star, or simply a background object that happens to fall near the star's line of sight as we see it. Typically, multiple observations of the star and putative planet over days, weeks, or even months are necessary to confirm or refute a possible planetary companion. However, association could be tentatively confirmed from a single observation by showing that the polarization vector of light from the object is perpendicular to the line between the star and object. Regardless of whether the polarization is caused by Rayleigh scattering, a liquid surface, or both, a reduction in the "parallel" polarization component – the component parallel to the plane defined by the parent star, the planet, and the observer – would indicate that the object is probably a planet that is being illuminated by the star it appears to orbit. To date, polarization from giant exoplanets has been difficult to detect in the combined light of the planet and star (Lucas et al. 2009), but our model predicts significant levels of polarization for many different types of terrestrial planets when the planets can be resolved from the parent star.

6.4.8 The Inverse Problem

The variety of parameters which dilute, shift, or compete with the Fresnel polarization peak suggests that solving the inverse problem – that is, determining from observations whether or not a planet has a large ocean – could be subject to numerous false positives and false negatives. Likewise, the end-member unpolarized light curves are distinctive, but an ocean surface with clouds, Rayleigh scattering, and aerosols can easily be dominated by any of the three atmospheric effects, or a combination of these and absorption. Still, some nearby ocean planets, if they exist, may have thin atmospheres and light cloud cover; other wet planets may be

dominated by aerosols or water clouds, and detection of these would also be an indicator of potential habitability, whether or not they hide an ocean below.

7.0 Summary and Conclusions

7.1 Summary of Work

We have developed a model for simulating orbital light curves from extrasolar planets which includes atmospheres with Rayleigh scattering, absorption, and aerosols, Lambertian clouds, dark and Lambertian surfaces, and ocean surfaces with varying degrees of roughness, scattering from within the water column, and sea foam. We used this model to generate light curves for various hypothetical exoplanets in edge-on orbits, verified our model against analytical results, and compared our results to those of Williams and Gaidos 2008. We generated unpolarized total flux light curves for three end member cases: a Lambertian planet, a pure ocean planet, and a pure Rayleigh scattering planet with a dark surface. We also generated polarization fraction light curves for planets with various combinations of surfaces, atmospheres, and cloud cover. This work adds to the prior investigations by including clouds, varying wind-driven waves, Rayleigh scattering atmospheres, and Earth-like absorption and aerosol scattering; we also compare results for ocean planets with Rayleigh-scattering dominated planets and planets with diffuse scattering surfaces.

7.2 Hypotheses, Goals, and Results

Our model of light scattering by Earth-like exoplanets confirms prior results that, under ideal conditions, a planet-wide ocean on an exoplanet could be observed with a space-based telescope using brightness and polarization orbital curves. However, we also show that there are numerous planetary factors which can obscure the polarization signature, leading to potential misidentification of ocean planets as dry planets, and vice-versa.

We now recall our Hypotheses and Goals, and discuss our results in terms of these.

Hypotheses:

1. By using calculations, simulations, and prior measurements, we can anticipate terrestrial planet signatures in light scattered from distant solar systems.
2. Instrumentation coming on line (e.g. TPF, Darwin, and ground-based instruments) in the future will permit scientists to gather enough information on terrestrial exoplanets to draw useful conclusions about the planet surfaces and atmospheres.
3. This instrumentation will have a baseline wavelength range of 500 – 1000 nm, but will have some capability to observe in broad sub-bands of this range, even though there are not enough photons to discriminate spectral absorption or emission lines.
4. Light curves including polarization, possibly combined with broad-band spectral information, will provide enough information to discriminate between terrestrial-class planets with and without large oceans. Specifically, sufficient information can be gathered to discriminate between planetary scale oceans and diffusely scattering, Lambertian land surfaces and clouds.

5. Observation of polarized light curves of putative or known exoplanet systems may provide useful information about the systems beyond that from unpolarized brightness curves.

In order to truly confirm hypotheses (1) and (2), we will need data from observations of terrestrial exoplanets, which are not yet available. Still, we have simulated a range of orbital light curves, and verified our model against analytical results, so hypothesis (1) is tentatively confirmed. Hypothesis (3) constitutes assumptions about the wavelength ranges and approximate resolution of future instrumentation which we make in order to choose reasonable parameters for our simulations.

We cannot definitively prove or disprove hypothesis (4), but we did find that the effects of aerosols, Rayleigh scattering in the atmosphere and the water column, waves, sea foam, absorption, and clouds can individually and collectively obscure the polarization signature of the air/water interface. Exo-zodi remains a significant unknown. The model shows that, in some cases, the capability to measure polarization could provide strong confirmation of the existence of an extrasolar ocean; however, we know of only one planet with a water ocean, and the number of similar planets within range, with a large enough ocean, thin enough atmosphere and cloud cover, and favorable orbit could be hundreds or zero. Our results can thus be used to help decide whether or not it would be worthwhile to incorporate a polarization wheel (or polarizing beamsplitter with two detectors). However, we cannot answer the question from this work alone, because there is no significant scientific downside to incorporating polarization capability; the tradeoff to be studied is in cost, complexity, and possibly reliability, which are beyond the scope of this work.

Hypothesis (5) has led us to the interesting result that polarization could be used to establish that an object which appears to be associated with a star is in fact an exoplanet in orbit about that star. This technique could be used to help identify candidate exoplanets in a single observation.

Goals:

1. Describe observable differences that may be expected in end member terrestrial planet types by modeling polarization-dependent and wavelength-dependent scattering over TPF wavelengths 0.5 to 1.0 μm;
2. Provide input to designers of TPF and other planet-finding missions about what could be observed by instruments with various spectral and polarization characteristics, including making recommendations on possible inclusion of polarization measurement instruments, and optimum choice of spectral bands for detection of interesting species;
3. If justified, suggest modifications of TPF which could enhance the capability to meet the science goals;
4. Help motivate funding of TPF and other missions with predictions describing exciting potential results from an affordable mission.

We have met goal (1) by showing how both polarized and unpolarized orbital light curves vary depending on the atmospheres and surfaces of various end-member planets, both over the TPF waveband and at additional wavelength bands in the NIR. We had anticipated that goals (2) and (3) would be met by recommending polarization capability be included on a future TPF mission,

and possibly suggesting ideal wavebands for detecting an ocean. However, with the variety and strength of the factors which can obscure and dilute the ocean surface polarization signature, it is not clear that such a capability is warranted. Scientifically, there is no down-side to including the capability in a filter wheel with two or three polarizers at different angles and an open position for unpolarized observation; on the other hand, any such mechanism incurs additional cost in design, acquisition, and test, and reduces reliability by creating additional potential failure modes. As for wavebands, we find that the ocean polarized and unpolarized signatures will be difficult to detect at any wavelength in the visible and NIR unless an ocean planet exists in our stellar neighborhood with few clouds, fairly calm winds, and extremely thin aerosols, in an orbit with a favorable inclination and dim exozodiacal light. Had our results been more encouraging, we could have more easily met goal (4). Our results on the detectability of exoplanet oceans are primarily negative. However, these results are important, as they could impact future decisions on both inclusion of polarization capability and choice of detector type on a future planet-finding satellite mission.

Additional goals for future possible work:

1. Locate relevant data and use it to calibrate or verify portions of the model;
2. Propose to NASA for funding to perform data mining on various Earth-observing missions, and perhaps missions to Mars and Venus, to uncover data that could be used to calibrate or verify the new model.
3. Eventually, produce a model capable of predicting signatures of any type of terrestrial planet.

7.3 Conclusions

We conclude that while polarization by planetary oceans might be remotely detected on exoplanets with thin atmospheres, a multiplicity of factors can obscure the characteristic polarization peak from a liquid surface. Earlier models with simpler atmospheres suggested that planetary atmospheres might be detectable using polarization; however, the phase angle of maximum polarization ratio for a real planet will be affected by polarization effects due to Rayleigh scattering in the atmosphere, clouds, and other effects, so modeling is essential to determine whether it is possible to unambiguously identify the glint from oceans through careful analysis of future light curves.

When observing over the TPF-C wavelength range (500–1000 nm), Rayleigh scattering only from an atmosphere as thick as Earth's is enough shift the polarization peak to an orbital longitude of 83^{o}, closer to the Rayleigh peak at 90^{o} than to the Fresnel peak at 74^{o}. Ocean radiance in this wavelength band caused by scattering within the water column also dilutes the polarization peak, limiting it to a maximum of slightly over 0.9.

Water aerosols shift the peak to even higher OLs and add a rainbow peak near OL = 140°. Clouds also have a strong effect in masking the ocean surface polarization—a result that is not surprising, considering that the reflectance of water at near normal incidence is only about 2%

across the wavelength band of interest. Water clouds can exhibit the rainbow peak as with water aerosols. The high albedo and multiple scattering of Earth water clouds tends to dilute any liquid polarization signature, and other clouds such as Earth's ice clouds and the sulfuric acid clouds of Venus can produce many different types of signatures depending on composition and particle size and shape.

Waviness has a similar effect to that of clouds, hindering the detection of a polarization signal from the ocean. Higher winds make the surface an irregular mass of swells, waves, and ripples, and increase the fraction of the surface covered by reflective (but primarily non-polarizing) sea foam.

The magnitude and polarization of exozodiacal light (exo-zodi) is another large unknown, because we have only limited measurements of zodiacal light in our own Solar System, and instrumentation is not yet sensitive enough to measure exo-zodi in mature exoplanet systems. Exo-zodi is expected to be polarized, so it will likely contribute an additional "noise" polarization peak which will compete with the water peak signature.

The Rayleigh effects could be mitigated by using only the longer wavelengths of the TPF-C band, taking advantage of the dependence of Rayleigh scattering on the inverse fourth power of wavelength. However, this would result in throwing away ½ to ¾ of the available flux in the detector range, requiring either a larger telescope or longer integration times, and it would do nothing to reduce the dilution of the polarization signal by other factors. Still, if multiple wavebands are available on TPF-C, as baselined, then comparing the results of different wavebands from an exoplanet observation, with the above in mind, may be useful. Shifting to a slightly longer waveband has also been suggested; the silicon bandgap limits silicon detector technology to not much longer than 1000 nm, however several new detector technologies have already been demonstrated which cover the remainder of the near infrared, in some cases out to 5 μm. We have investigated this idea in two NIR wavebands centered on 1.6 μm and 2.2 μm, which fall within atmospheric water vapor windows, and below the wavelength ranges where the unpolarized black body emission from Earth rises. Preliminary findings are that these longer wavelengths significantly reduce the polarized and total Rayleigh scattering, but have little effect on the detectability of oceans unless the aerosols are very thin by Earth standards, because aerosol scattering dominates for Earth-like atmospheres with clear-day visibility of 23 km.

The net effect of clouds, aerosols, absorption, atmospheric and oceanic Rayleigh scattering, waves, and exo-zodi may severely limit the percentage of ocean planets that would display a significant polarization signature, and may also generate a significant number of false positives on dry planets.

All of this suggests that polarization measurements by a TPF-C type telescope may not provide a positive detection of surface liquid water on exoplanets. On the other hand, the placement of the polarization peak in Figure 54 relative to the curves shown there may give a strong hint of what type of planetary surface and atmosphere is being observed, especially when used in combination with the shape of the radiometric light curve relative to the three cases in Figure 54, and the overall planet contrast ratio relative to the cases in Tables 6 and 8.

We have also suggested that polarization could be used to help determine whether an object which appears to be near a star is in fact a planet in orbit around the star, or a background object. If the object exhibits polarization perpendicular to the line between object and the star, then the object probably is a planet and the polarization is likely due to Rayleigh scattering in the planet's atmosphere, reflection from a liquid surface, or a combination of the two effects. This method has the advantage that it can be used to show probable association with a single observation. The presence of polarization as described above could also be used, along with multiple observations, to constrain the orbital inclination. These association and inclination techniques need not wait for TPF; they could be implemented immediately by ground-based observatories.

It is difficult to say from our study here whether or not it makes sense to add a polarizer to TPF. We have shown that multiple factors tend to dilute or shift a liquid polarization peak; if there are any water planets within range of TPF, we might expect that a large percentage would have the oceans obscured by some combination of atmospheric Rayleigh scattering, aerosols, absorption, clouds, or orbital exo-zodi. If included, a polarizer would likely be implemented in a filter wheel to allow insertion and removal, with perhaps three polarizers at 45° or 60° angles and an open spot included in the wheel. Any mechanism like a filter wheel can malfunction and cause loss of functionality, but if TPF has a filter wheel anyway to provide wavelength selection, then adding a few extra polarizing filters might not have a large impact on reliability.

7.4 Contributions

This work is novel in including a much more complete atmosphere in simulations of exoplanet light scattering, and also includes new ideas on using polarization to help determine planetary association, as well as a novel graphical method of showing different planetary polarization types (Figure 54). The following are what I would consider the useful contributions to the field from this work:

- Summarized previous work in the field;
- Showed variety and impact of multiple factors in seeking exo-oceans, including factors that obscure or even create false positives;
- Provided a new type of graph to compare polarization from different planet types, in which the x-axis represents orbital longitude, and the y-axis represents polarization fraction;
- Discussed how to use this graph, along with unpolarized light curves and overall planet contrast ratio, to constrain exoplanet surface and atmosphere characteristics;
- Suggested polarization could assist in showing association between a putative planet and the supposed planet star, in ground-based observatories as well as in a polarization-equipped space observatory such as a modified TPF.

7.5 Future Research

Humankind remains fascinated with the possibility of habitable worlds beyond Earth. The Terrestrial Planet Finder will continue to be an important thrust for NASA moving forward, with development work starting up within the next few years. Ground-based observatories are using larger baselines and ever-improving adaptive optics to image smaller planets closer to the parent star.

The model developed here could be expanded and improved as more data on other star systems becomes available. Future model development might include the following:

- Additional simulations of near infrared bands between 1 and 3 μ (Zugger et al. in process));
- More detailed and accurate cloud models;
- Models of exo-zodi polarization and effects;
- Collaboration with other researchers when more terrestrial exoplanet data is available.

The model could be used to help determine whether or not it makes sense to place a polarizer on TPF, and as terrestrial exoplanets are discovered, their light signatures can be compared against the model to assist in determining the possibility that these planets have an Earth-like environment.

Appendices

Appendix A: Milestones

Milestone	Date
NASA grant work underway:	1 August 2007
Comprehensive Examination:	20 December 2007
Presentation to Virtual Planetary Laboratory:	31 March 2008
End of original NASA grant funding:	30 September 2008
Lookup Table generator up and running:	3 October 2008
First Draft Thesis to advisor:	20 November 2008
Final Report to original sponsor:	1 December 2008
First cut code, BatchLUT/6SVlut/Oceans_v2 up and running end-to-end:	20 December 2008
Complete code, BatchLUT/6SVlut/Oceans_v2 up and running end-to-end:	1 March 2009
Committee Meeting	28 August 2009
ARL Thesis Charge Number awarded	September 2009
Working model bilut45/Oceans238:	April 2010
Submit paper to ApJ:	16 June 2010
Post on arXiv astro-ph:	17 June 2010
Working model bilut46/Oceans238:	02 July 2010
Comments back from ApJ:	18 July 2010
Response to ApJ:	20 Aug 2010
Acceptance by ApJ:	28 Aug 2010
Draft Thesis thru Results to CRP	13 October 2010
VPL Grant Expires:	31 October 2010
Published in ApJ:	10 November 2010
Draft Thesis Ch 6.3 – 7 to CRP	22 November 2010
Draft Thesis Appendix A-F to CRP	1 December 2010
Thesis to Committee	13 December 2010
Submit Draft for Format Review	15 December 2010
Thesis Defense:	5 January 2011
Activate Intent to Graduate	7 January 2011
Submit Final eTD	31 March 2011
Degree conferred:	15 May 2011

Appendix B: Scattering Theory From Maxwell's Equations

The following discussion is based on Shen and Kong (1995), Stutzman and Thiele (1981), Bohren and Huffman (1983), Neff (1981), Measures (1992), Kyle (1991), and Thomas and Duncan (1993).

B.1 Molecular and Particle Scattering

When an electromagnetic wave (radiation) interacts with a particle of matter, the wave's oscillating electric field causes the particle's electron cloud to oscillate in the same direction, the direction of the yellow arrow in Figure 62.

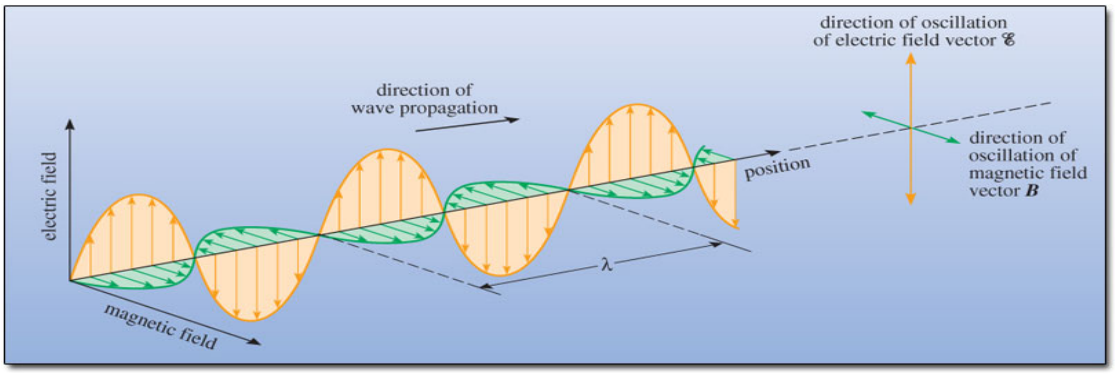

Figure 62: Diagram showing electromagnetic wave and electric field[33]

If the wavelength of the radiation is much larger than the particle (as is the case when light interacts with an atom or air molecule), and the particle can be approximated by a dielectric sphere, then the particle acts like an ideal dipole antenna, and has the scattering pattern shown in Figure 63. Molecular and small particle scattering is often referred to as Rayleigh scattering;

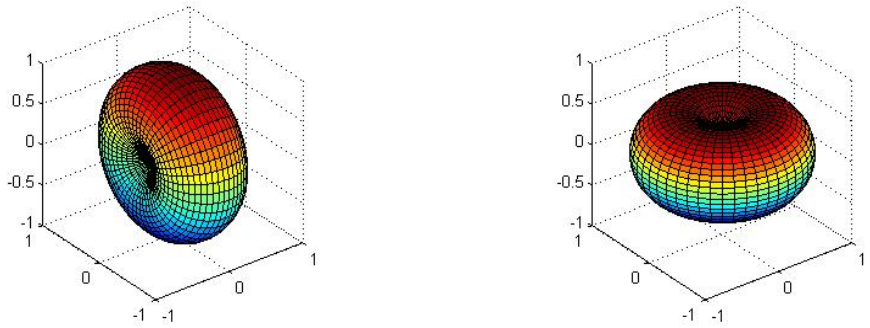

Figure 63: Dipole scattering pattern viewed in *xz* and *xy* planes (generated using MATLAB)

[33]From OpenLearn, http://openlearn.open.ac.uk, used by permission

this is the process that causes the blue sky, because of the λ^{-4} wavelength dependence of the scattering cross-section. For visible wavelengths (~ 400 to 700 nm), Rayleigh scattering theory is sufficient to explain scattering by atoms, molecules, and small aerosols. The more general Mie solution is needed to explain scattering by larger particles.

As the particle size and radiation wavelength become closer to the same dimension (either by decreasing the wavelength or increasing the particle size), the scattering pattern becomes asymmetrical; the forward scatter and backscatter lobes become narrower, the amplitude of the forward lobe increases relative to that of the backscatter lobe, and an increasing number of small backscatter lobes form, leading to the pattern known as the scattering phase function. Figure 64 shows the scattering phase function for a water aerosol in air with a (vacuum) wavelength one tenth the diameter of the aerosol droplets.

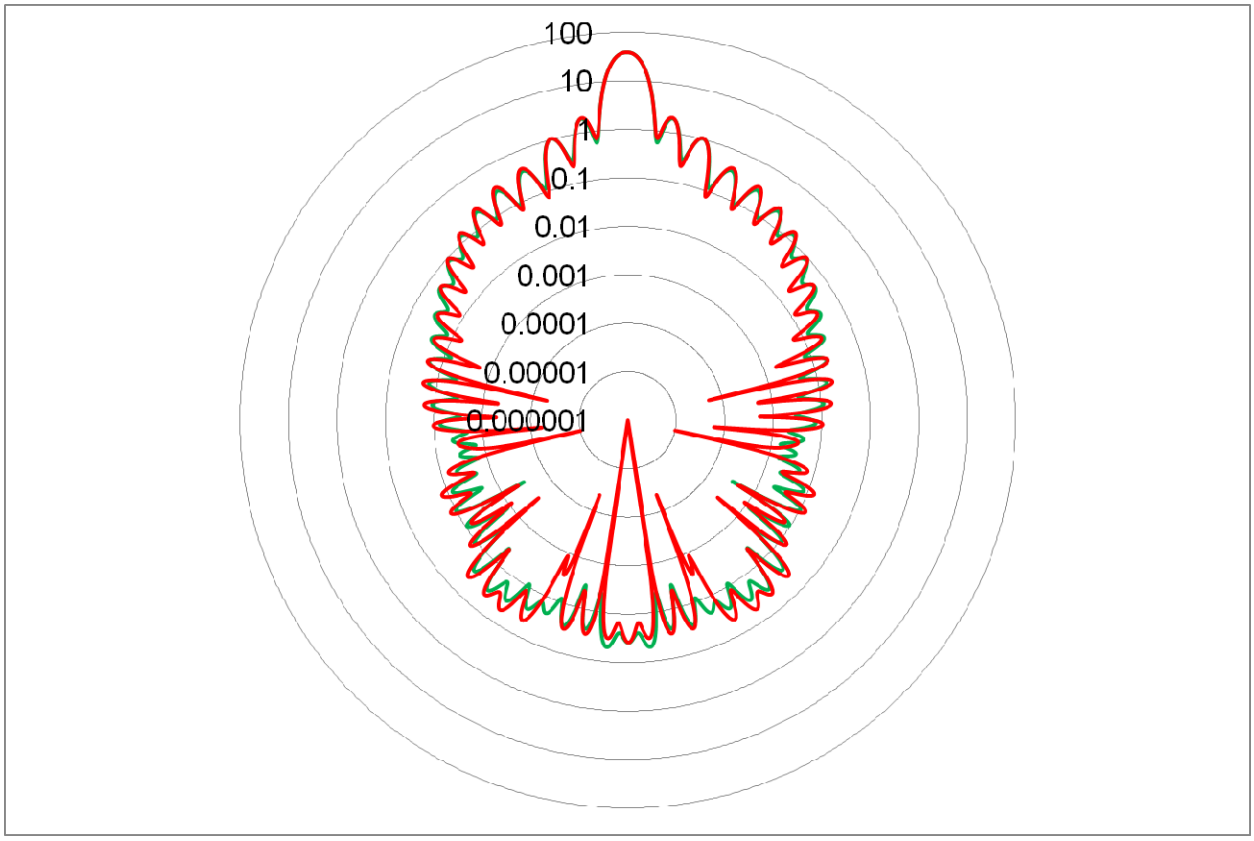

Figure 64: Logarithmic phase function for 0.5 µm wavelength light scattered by a 5% volume concentration of 5 µm water droplets in air; red = parallel polarization, green = perpendicular[34]

When the radiation wavelength is on the same order as the particle radius, then constructive and destructive interference produce a maximum variation in the scattering pattern. A non-rigorous thought experiment can explain why. Suppose the electromagnetic radiation impinges on a transparent particle (e.g. a raindrop), with an index of refraction different from that of the surrounding medium (such as air). A portion of the wave will be reflected back at both the front

[34]Plotted by the author based on data calculated by Mie code calculator provided by Pavel Zakharov at http://zakharov.zzl.org/datashow.php?runid=25TzVSae

surface (air to water interface) and back surface (water to air interface) of the droplet. The components reflected from the front and back surfaces can interfere constructively and destructively at the observer's location near the backscatter direction. Additionally, a smaller portion of the wave will be doubly reflected, that is, reflected back at the surface, and then internally reflected at the front surface. The doubly reflected wave is then traveling in the forward direction, along with the unreflected wave, resulting in regions of constructive and destructive interference. Whether the doubly reflected wave adds to or subtracts from the wave passing directly through the droplet will depend on the droplet diameter. If a half-wavelength or several half-wavelengths of the radiation approximately fit within the droplet, then doubly reflected radiation will interfere constructively (add) with the wave passing through the droplet, because the doubly reflected radiation will be delayed by a full cycle. On the other hand, if a quarter-wavelength or several quarter-wavelengths of the radiation approximately fit within the droplet, then doubly reflected radiation will interfere destructively with (subtract from) the wave passing directly through the droplet, because the doubly reflected radiation will be delayed by half a cycle. Similarly, radiation scattered backwards from the front and rear surfaces of the droplet will also interfere constructively or destructively depending on the droplet diameter.

Mie scattering theory rigorously explains the radiation/particle interaction for any size spherical, transparent particles; Rayleigh scattering represents a special case of Mie scattering for small particles. The following discussion derives the equations for Rayleigh scattering. For a detailed discussion of Mie scattering theory, see Mie (1908), Van de Hulst (1957), and Bohren and Huffman (1983). Three-dimensional plots of scattering phase function patterns are given in Bas (2002).

B.2 First Principles

Now let's look at Rayleigh scattering processes in more detail, starting with Maxwell's equations in differential form,

$$\nabla x\vec{E} = -\frac{\partial B}{\partial t} \tag{74}$$

$$\nabla x\vec{H} = \vec{J} + \frac{\partial \vec{D}}{\partial t} \tag{75}$$

$$\nabla \bullet \vec{B} = 0 \tag{76}$$

$$\nabla \bullet \vec{D} = \rho_v \tag{77}$$

which are known respectively as Faraday's law of induction, Ampere's law, and Gauss' magnetic and electric laws. The symbols used here are:

E = electric field strength (volts per meter)
D = electric flux density (coulombs per square meter)
H = magnetic field strength (amps per meter)
B = magnetic flux density (webers per square meter, or teslas)
J = electric current density (amps per square meter)

ρ_v = electric charge density (coulombs per square meter)

The first four quantities are related by the definitions of electric permittivity (ε) and magnetic permeability (μ) of materials,

$$\vec{D} = \varepsilon \vec{E} \tag{78}$$
$$\vec{B} = \mu \vec{H} \tag{79}$$

If we assume that all field vectors, all currents, and all charge densities are time-varying at a single frequency, ω, and eliminate D and B using Equations (78) and (79), we have Maxwell's equations for time-harmonic fields,

$$\nabla x \vec{E} = -j\omega\mu \vec{H} \tag{80}$$
$$\nabla x \vec{H} = j\omega\varepsilon \vec{E} + \vec{J} \tag{81}$$
$$\nabla \bullet \mu \vec{H} = 0 \tag{82}$$
$$\nabla \bullet \varepsilon \vec{E} = \rho_v \tag{83}$$

Equations (80) and (81) imply that in order for an electromagnetic wave to propagate in a medium, oscillating currents *J* must be excited somewhere in the medium. If these currents are known then E and H can be found. Two auxiliary functions, *A* and Φ, are usually introduced in order to solve these equations:

$$\vec{B} = \nabla x \vec{A} \tag{84}$$
$$\vec{E} = -j\omega \vec{A} - \nabla \Phi \tag{85}$$

where *A* is called the vector potential and Φ is called the scalar potential. These describe the potential field that will drive the oscillating currents. Note that Equation (84), the curl of *A*, is not sufficient to uniquely define *A*; however if we also define the divergence of *A*, then we will have described *A* to within a constant. The divergence of *A* is defined using the Lorentz condition,

$$\nabla \bullet \vec{A} + j\omega\varepsilon\phi = 0 \tag{86}$$

which is chosen based on relativity constraints. Substituting Equations (84) and (85) into (80), we have

$$\nabla x(\nabla xA) = j\omega\mu\varepsilon(-j\omega \vec{A} - \nabla \Phi) + \mu \vec{J} \tag{87}$$

Simplifying the right side and invoking the vector identify for the curl of a curl,

$$\begin{aligned} &\nabla x(\nabla x \vec{A}) = \nabla(\nabla \bullet \vec{A}) - \nabla^2 \vec{A} \\ &= j\omega\mu\varepsilon(-j\omega \vec{A} - \nabla \Phi) + \mu \vec{J} = \omega^2 \mu\varepsilon \vec{A} - j\omega\mu\varepsilon \nabla \Phi + \mu \vec{J} \end{aligned} \tag{88}$$

Using the Lorentz condition (Equation (86)) to replace the divergence of A yields

$$-j\omega\varepsilon\nabla\Phi - \nabla^2\vec{A} = \omega^2\mu\varepsilon\vec{A} - j\omega\mu\varepsilon\nabla\Phi + \mu\vec{J} \tag{89}$$

Simplifying yields the second order differential equation for A,

$$\nabla^2\vec{A} + \omega^2\mu\varepsilon\vec{A} = \mu\vec{J} \tag{90}$$

Similarly, combining Gauss' electric law (Equation (83)), the definition of Φ (Equation (85)), and the Lorentz condition (Equation (86)) we can arrive at the second order differential equation for Φ,

$$\nabla^2\Phi + \omega^2\mu\varepsilon\Phi = -\frac{\rho_v}{\varepsilon} \tag{91}$$

can be broken down into three scalar component equations, which, with the addition of Equation (91) are the four inhomogeneous Helmholz wave equations. The solution of these equations is beyond the scope of this appendix (see Harrington 1962), but we will need the results:

$$\vec{A}(r) = \frac{\mu}{4\pi}\iiint dV \frac{\vec{J}(\vec{r}')e^{-jk\left|\vec{r}-\vec{r}'\right|}}{\left|\vec{r}-\vec{r}'\right|} \tag{92}$$

$$\Phi(r) = \frac{1}{4\pi\varepsilon}\iiint dV' \frac{\rho_v(\vec{r}')e^{-jk\left|\vec{r}-\vec{r}'\right|}}{\left|\vec{r}-\vec{r}'\right|} \tag{93}$$

where k, the wavenumber, is given by

$$k = \omega\sqrt{\mu\varepsilon} \tag{94}$$

and r and r' are the vectors representing the positions of the potentials and the sources, respectively. The magnitude difference, $|r-r'|$, is then the distance between the observation point and the source point. The triple integrals extend over all points r' where the source is not zero. The point of the above development is that, if we know the sources in a volume, instead of having to solve Maxwell's equations, we can use Equations (92) and (93) to calculate A and Φ, then calculate the electric and the magnetic fields from the sources using the definitions of A and Φ (Equations (84) and (85)).

B.3 Rayleigh Scattering and the Ideal Dipole

To proceed further, we need to introduce the concept of the ideal dipole. An ideal dipole, also known as an infinitesimal antenna, is a piece of uniform amplitude current of vanishingly small length, that is, much shorter than the wavelength of the radiation in question, i.e., $\Delta z << \lambda$.

In a real dipole antenna the current must fall off to zero at the ends, because there is nowhere for oscillating current to go at the ends; however, if the real antenna meets the above size criterion, which is equivalent to the antenna being "electrically small," then the approximation works well.

For our purposes, we model the atoms, molecules, or suspended small aerosol particles in a medium as dipole antennas which are excited by a propagating electromagnetic wave. The incident wave sets the electron cloud of each particle oscillating relative to the less mobile positively charged nucleus (in the case of single atoms) or matrix. This oscillation is in response to, and generally in the same direction as, the applied electric field of the wave. The positive and negative charges move in opposite directions, slowing and reversing directions as they reach maximum separation. Since the velocity of the charges is constantly changing, they are always accelerating, thus emit electromagnetic radiation. This is the Rayleigh scattering process. Now we will calculate the field pattern produced by the dipole scatterer.

Suppose an ideal dipole of length Δz, cross-sectional area Δa, and uniform current amplitude is located at the center of our coordinate system, along the z axis. The current density $J(r')$ in amps per square meter (z-directed) is then simply the current I over the cross-sectional area Δa, and the dipole differential volume is equal to its length times its area. Also, the source is located at the origin, so that

$$\vec{J}(r') = \hat{z}\frac{I}{\Delta a} \tag{95}$$

$$dV' = \Delta a \Delta z \tag{96}$$

$$\vec{r}' = 0 \tag{97}$$

Substituting these values into the equation for A (Eq. 11a), where $\left|r - r'\right| = r$, the triple integral simplifies to $I\,\Delta z$ (z-directed), and A simplifies to

$$\vec{A} = \hat{z}\frac{\mu I \Delta z e^{-jk\vec{r}}}{4\pi r} \tag{98}$$

From the definition of A, Equation (84), we know that we need only take the curl of A to calculate the magnetic field. However, because of the geometry of the problem, this is best done in spherical coordinates. We will need the definition of the curl operator in spherical coordinates, and the conversion from the z unit vector to r and θ unit vectors:

$$\nabla x\vec{A} \equiv \hat{r}\frac{1}{r\sin\theta}\left[\frac{\partial}{\partial\theta}(A_\varphi \sin\theta) - \frac{\partial A_\theta}{\partial\varphi}\right] + \hat{\theta}\frac{1}{r}\left[\frac{1}{\sin\theta}\frac{\partial A_r}{\partial\varphi} - \frac{\partial}{\partial r}(rA_\varphi)\right] + \hat{\varphi}\frac{1}{r}\left[\frac{\partial}{\partial r}(rA_\theta) - \frac{\partial A_r}{\partial\theta}\right] \tag{99}$$

and

$$\hat{z} = \hat{r}\cos\theta - \hat{\theta}\sin\theta \tag{100}$$

Equations (98), (99), and (100) allow us to find the curl of *A*, which will give us the magnetic field from the dipole:

$$\vec{H} = \frac{1}{\mu}\vec{B} = \frac{1}{\mu}\nabla x\vec{A} = \hat{\varphi}\frac{jkI\Delta z e^{-jk\bar{r}}}{4\pi r}\left(1 + \frac{1}{jkr}\right)\sin\theta \tag{101}$$

so the magnetic field is directed around the dipole, in the *xy* plane, as required by the right hand rule. Now that we have the equation for the magnetic field, the equation for the electric field follows from Ampere's Law (Equation (81)):

$$\vec{E} = \frac{1}{j\omega\varepsilon}\nabla x\vec{H} = \eta \bullet \frac{jkI\Delta z e^{jk\bar{r}}}{4\pi r} \bullet \hat{r}\left[\frac{1}{jkr} + \frac{1}{(jkr)^2}\right]2\cos\theta + \hat{\theta}\left[1 + \frac{1}{jkr} + \frac{1}{(jkr)^2}\right]\sin\theta \tag{102}$$

where $\eta = (\mu/\in)^{1/2}$. Equations (101) and (102) can be converted into three scalar equations:

$$H_\varphi = \frac{jkI\Delta z e^{jkr}}{4\pi r}\left[1 + \frac{1}{jkr}\right]\sin\theta \tag{103}$$

$$E_r = \eta \bullet \frac{jkI\Delta z e^{-jkr}}{4\pi r} \bullet \left[\frac{1}{jkr} + \frac{1}{(jkr)^2}\right]2\cos\theta \tag{104}$$

$$E_\theta = \eta \bullet \frac{jkI\Delta z e^{-jkr}}{4\pi r} \bullet \left[\frac{1}{jkr} + \frac{1}{(jkr)^2}\right]\sin\theta \tag{105}$$

We now have a set of equations for the electric and magnetic fields from an ideal dipole; the dipole is our model for the scattering particles in the medium under consideration. The particles can be atoms, molecules, or larger particles, as long as they are much smaller than the wavelength of any incident electromagnetic wave we are considering. Now let's apply an incident wave and examine the scattering intensity.

B.4 Near Field

For simplicity, suppose we have a plane wave impinging on a single particle, and that the particle can be modeled by a dielectric sphere of radius r_0 and dielectric constant $\in$. To simplify the analysis, we set the origin of the spherical coordinates at the center of the sphere and let the incident plane wave propagate along the z-axis. Invoking the *z* unit vector conversion used above, the *E* field of the plane wave is then expressed in spherical coordinates as,

$$\vec{E} = E_0 \hat{z} e^{j\vec{k}\bullet\vec{r}} = E_0(\hat{r}\cos\theta - \hat{\theta}\sin\theta)e^{-j\vec{k}\bullet\vec{r}} \tag{106}$$

In order to look at the fields close to the sphere (the "near zone" or "near field"), it will help to modify Equations (103), (104), and (105) by multiplying the right side of each equation by $\eta(jkr)^2 / \eta(jkr)^2$. Examining the fields close to the dielectric sphere (on the inside and outside) allows us to set some boundary conditions and better define constants. Also, in practice *I* and Δz are not usually known, so we combine the multiplicative constants in the equations into one constant *C*, such that

$$C = \eta \bullet \frac{jkI\Delta z}{4\pi} \bullet \frac{1}{(jk)^2} \tag{107}$$

Equations (103), (104), and (105) can then be rewritten as

$$H_\varphi = \frac{C\sin\theta}{\eta r^3}\left[(jkr) + (jkr)^2\right]e^{-jkr} \tag{108}$$

$$E_r = \frac{2C\cos\theta}{r^3}\left[1 + jkr\right]e^{-jkr} \tag{109}$$

$$E_\theta = \frac{C\sin\theta}{r^3}\left[1 + (jkr) + (jkr)^2\right]e^{-jkr} \tag{110}$$

It now becomes clear why we modified the form of Equations (103), (104), and (105) to study the near field. For $kr << 1$, the bracketed expressions for the E field components both approach 1, so the scattered E field near the sphere simplifies to

$$\vec{E}_s = \hat{r}E_r + \hat{\theta}E_\theta = \frac{C}{r^3}(\hat{r}2\cos\theta + \hat{\theta}\sin\theta) \tag{111}$$

$$\vec{E}_s = \hat{r}E_r + \hat{\theta}E_\theta = \frac{C}{r^3}(\hat{r}2\cos\theta + \hat{\theta}\sin\theta) \tag{112}$$

Inside the sphere, an electric field is excited, parallel to the incident field, having the form

$$\overrightarrow{E_i} = C_1[\vec{r}\cos(\theta - \sin\theta)] \tag{113}$$

where C_1 is some constant. At the sphere surface ($r = r_0$) the inner and outer D fields ($\in E$) must be equal – note that the outer E field is the sum of the incident field E_i and the scattered field E_s. When *kr* <<1, the exponential is approximately unity. Setting the inner and outer r- directed terms equal to each other, and similarly the θ-directed terms, and canceling the cos θ and sin θ terms, we have two boundary conditions:

$$\varepsilon_0 E_0 + \varepsilon_0 \frac{C}{r_0^3} 2 = \varepsilon C_1 \tag{114}$$

$$-E_0 + \frac{2C}{r_0^3} = -C_1 \tag{115}$$

Solving these two equations for *C* gives

$$C = \left(\frac{\varepsilon - \varepsilon_0}{\varepsilon + 2\varepsilon_0}\right) r_0^3 E_0 \tag{116}$$

We can now replace the constant *C* in Equations (108), (109), and (110) to obtain the complete field solution,

$$H_\varphi = \frac{E_0}{\eta}\left(\frac{\varepsilon - \varepsilon_0}{\varepsilon + 2\varepsilon_0}\right)\frac{r_0^3}{r^3}\sin\theta\left[(jkr) + (jkr)^2\right]e^{-jkr} \tag{117}$$

$$E_r = 2E_0\left(\frac{\varepsilon - \varepsilon_0}{\varepsilon + 2\varepsilon_0}\right)\frac{r_0^3}{r^3}\cos\theta\left[1 + jkr\right]e^{-jkr} \tag{118}$$

$$E_\theta = E_0\left(\frac{\varepsilon - \varepsilon_0}{\varepsilon = 2\varepsilon_0}\right)\frac{r_0^3}{r^3}\sin\theta\left[1 + (jkr) + (jkr)^2\right]e^{-jkr} \tag{119}$$

B.5 Far Field

At large distances from the sphere where *kr* >>1, the $(jkr)^2$ terms will dominate. This is the "far zone" or "far field" condition. In the far field then, the r-directed component of the E field becomes insignificant, and the scattered field solution is

$$H_\varphi = \frac{E_0}{\eta}\left(\frac{\varepsilon - \varepsilon_0}{\varepsilon + 2\varepsilon_0}\right)\frac{r_0^3}{r^3}\sin\theta(jkr)^2 e^{-jkr} \tag{120}$$

$$E_\theta = -E_0\left(\frac{\varepsilon-\varepsilon_0}{\varepsilon+2\varepsilon_0}\right)\frac{r_0^3}{r^3}\sin\theta(jkr)^2 e^{-jkr} \tag{121}$$

which simplifies to

$$H_\varphi = -\frac{E_0}{\eta}\left(\frac{\varepsilon-\varepsilon_0}{\varepsilon+2\varepsilon_0}\right)\frac{k^2 r_0^3}{r}\sin\theta e^{-jkr} \tag{122}$$

$$E_\theta = -E_0\left(\frac{\varepsilon-\varepsilon_0}{\varepsilon+2\varepsilon_0}\right)\frac{k^2 r_0^3}{r}\sin\theta e^{-jkr} \tag{123}$$

The sin θ factor gives the Rayleigh scattering field pattern a torus or "donut" shaped pattern, with the z axis positioned vertically through the center. Two cross-sectional views of this pattern, in a plane through the *z*-axis (axis of the dipole), and in the plane perpendicular to the *z*-axis, were shown earlier in Figure 63 (the pattern is identical to the far field pattern from a dipole antenna).

B.6 Scattering Cross Section

The total power scattered by the dipole can be found by integrating the complex power density flowing outward from the dipole over a sphere *s* around the dipole. The complex power density flowing outward is given by the Poynting vector *S*, where

$$\vec{S} = \vec{E}x\vec{H} \tag{124}$$

For the time-harmonic case, which we are using, the time-averaged Poynting vector is given by

$$\left\langle \vec{S} \right\rangle = \frac{1}{2}\mathrm{Re}\left\{\vec{E}x\vec{H}^*\right\} \tag{125}$$

where the angle brackets indicate time averaging, the "Re" operator takes the real part of the argument, and the asterisk indicates complex conjugate. We have derived above the *E* and *H* fields around the dipole. We are interested in the scattering cross section at a distance from the dipole, so we use the simpler far field equations for *E* and *H* (Equations (122) and (123)), yielding,

$$\left\langle \vec{S} \right\rangle = \frac{E_0^2}{2\eta}\left(\frac{\varepsilon-\varepsilon_0}{\varepsilon+2\varepsilon_0}\right)^2 \frac{k^4 r_0^6}{r^2}\left(\sin^2\theta\right)\hat{r} \tag{126}$$

The scattering cross section σ of an object as a function of direction is defined as $4\pi r^2$ times the ratio of the scattered radiation intensity to the incident power density,

$$\sigma(\theta) = \frac{4\pi r^2 \left\langle \vec{S} \right\rangle \bullet \hat{r}}{{E_0}^2 / 2\eta} = 4\pi \left(\frac{\varepsilon - \varepsilon_0}{\varepsilon + 2\varepsilon_0} \right)^2 k^4 {r_0}^6 \sin^2 \theta \tag{127}$$

This is the function that is plotted as Figure 63 - the $\sin^2 \theta$ dependence produces a torus or "donut" shaped pattern.

To calculate the total scattered power P_S we return to Equation (126), and integrate the time-average power density over a sphere around the dipole,

$$P_s = \iint_s \left\langle \vec{S} \right\rangle \bullet d\vec{s} = \int_0^{\pi} \left[(\left\langle \vec{S} \right\rangle \bullet \hat{r}) 2\pi r^2 \sin\theta \right] d\theta \tag{128}$$

This reduces to

$$P_s = \frac{8\pi}{3} \left(\frac{\varepsilon - \varepsilon_0}{\varepsilon + 2\varepsilon_0} \right)^2 k^4 {r_0}^6 \left(\frac{{E_0}^2}{2\eta} \right) \tag{129}$$

We find the total scattering cross section σ_{total} from the total scattered power by taking the ratio of total scattered power P_S to the incident power density, ${E_0}^2 / (2\eta)$:

$$\sigma_{total} = \frac{P_s}{{E_0}^2 / 2\eta} = \frac{8\pi}{3} \left(\frac{\varepsilon - \varepsilon_0}{\varepsilon + 2\varepsilon_0} \right)^2 k^4 {r_0}^6 = \frac{8\pi}{3} \left(\frac{\varepsilon - \varepsilon_0}{\varepsilon + 2\varepsilon_0} \right)^2 \frac{\omega^4}{c^4} {r_0}^6 \tag{130}$$

The most important results from Equation (130) are that the scattered power is proportional to the fourth power of frequency and the sixth power of particle size. The strong wavelength dependence means that, for a given particle size, a wave in the deep violet (400 nm) is scattered a factor of $(7/4)^4 = 9.4$ times as strongly as a wave in the deep red (700 nm). Because sunlight contains more blue than violet, and our eyes are not very sensitive to violet light, the scattered skylight appears blue.

We have derived both the total scattering cross section and the scattering cross section as a function of direction for Rayleigh scattering, the special case where the wavelength of the incident radiation is much larger than the scattering particle. Using Equations (117), (118), and (119) without the small particle assumption leads to the more general Mie theory, leading in turn to the scattering phase function as in Figure 64. This development is found in Bohren and Huffman (1983) and Van de Hulst (1957). Such a development does assume spherical, transparent particles, but the results give good agreement for many non-spherical particles.

Appendix C: New IDL Code Developed for This Project

C.1 Summary and list of new routines

I developed a number of new IDL programs and subroutines for this project, which fall in to three categories: 1) the bilut routine, which calls 6SV with the proper parameters and places the 6SV outputs into lookup tables, 2) a simple routine which generates the table of angles to be used as inputs to 6SV; and 3) modifications to Darren William's Oceans program which allow it to use the 6SV lookup tables to calculate polarized planetary orbital light curves for planets with various types of surfaces and atmospheres. I also wrote a number of test programs to troubleshoot and verify the other routines during development, but I will not cover these in detail.

C.2 bilut Routine

The bilut routine allows the user to choose 6SV surface and atmosphere characteristics, angles to be modeled, etc., then performs thousands of calls to the modified 6SV and uses the results to populate a lookup table. The lookup table is then given a descriptive filename containing most of the parameters of the model for quick identification.

Example: LUT46_87r7_50-100_Ocean1_5mUS62Marit40km1AtmroKY.txt

LUT = identifier indicating that this is a lookup table
46 = version number of the bilut routine used to generate the LUT
87 = maximum zenith angle used (both solar/stellar and viewer zenith angles)
r7 = version of list of zenith angles used
50-100 = wavelength range, in this case 500 nm to 1000 nm
Ocean = surface type modeled
1_5m = wind speed, here 1.5 m/s
US62 = atmospheric absorption model, here US 1962 Standard Atmosphere
Marit = aerosol model used, in this case Maritime aerosols
40km = visibility input for aerosol model
1Atm = atmospheric pressure (parameterized in 6SV as altitude, in this case, sea level)
ro = vestigial parameter which no longer has any meaning
KY = plane parallel to spherical correction algorithm, in this case, Kasten & Young

Plane parallel approximation: 6SV uses the plane-parallel approximation of the atmosphere, so I added an option to bilut to allow the user to partially compensate for the difference between the plane parallel approximation and the spherical atmosphere reality using either the published Kasten and Young approximation algorithm or my own algorithm (see Appendix E).

C.3 Routine inputanggen

This routine generates a table of the three angles of interest - solar zenith angle, viewer zenith angle, and relative azimuth – which is stored as a text file in the /inputs subdirectory and used as an input to bilut. I experimented with many variations on how many zenith angles and azimuth angles were needed, and how they should be distributed (see Sensitivity Analysis).

C.4 Oceans Code Modifications and New Routines

The Oceans code performs 3D geometry calculations for light leaving a star, scattering from grid points on an Earth-sized planet orbiting a star at 1AU, and reaching an observer. The code sums the radiance reaching the observer over the illuminated portion of the planet. In order to work with 6SV, Oceans was modified to:

1. read in a specified lookup table (previously generated by bilut and 6SV) (read_lut),
2. find the rows in the lookup table with the angles most nearly matching the desired angles (find8rows and find2rows), and
3. perform a 3D interpolation from those closest matching rows (interp8frac).

The program was also modified to:

4. set different paths depending upon which computer it was run on (oceans_setup),
5. create 2D pixel maps for troubleshooting and verification,
6. perform Stokes parameter rotation to rotate the output to the scattering plane reference (see Appendix D),
7. at the user's option, compensate for plane-parallel versus spherical atmosphere using either a published algorithm or my own algorithm (see Appendix E).

Each of these routines and modifications is discussed briefly below.

read_lut routine: This routine allows Oceans to read in the lookup table (LUT) generated previously by the bilut routine and calls to 6SV. The LUT includes a separator, **, which tells read_lut where the header information ends and the table data begins. The routine strips off the header (the portion before the ** separator), counts the number of rows of data, and holds the LUT in memory as the variable "lutdata."

find8rows and find2rows routines: The modified Oceans code uses a new routine I wrote called find8rows, which finds the eight rows of the lookup table which surround the data point. These eight rows can be thought of as the eight vertices of a rectangular solid surrounding the data point. For an input data point with SZA1, VZA1, and RelAz1, the routine first finds SZAa, the closest SZA above SZA1, and SZAb, the closest SZA below SZA1. The routine then collects all the rows of the LUT which have SZAa and SZAb into two new submatrices. Next, the routine performs the same above/below search on the second column of each submatrix to find the closest VZAa and VZAb above and below VZA1. The lines of each submatrix with these values of VZA are then extracted and used to form two sub-submatrices from each submatrix. The process is repeated once more with the third column, RelAz, leading to eight

individual rows being selected as the cube vertices. Since these operations are somewhat repetitive, find8rows works by calling a lower level routine I wrote called find2rows, which finds the above/below values as just described. Find8rows works by using multiple calls to find2rows with different input matrices and other parameters.

There are a few pitfalls which the routine is designed to avoid:

1. In order for the interpolation (next step) to work, the eight vertices must be at "right angles." This means that the lookup table must be constructed so that a consistent set of zenith and relative azimuth angles is used.
2. If one of the angles in the data point is beyond the maximum or minimum values in the LUT, then the value of the angle for that data point is set equal to the maximum or minimum. This avoids an improper interpolation of a point which lies outside the cube.
3. If one of the angle values falls exactly on the LUT angle value (usually because of case 1 above), then that value of the angle is used as both the above and below value. Again, this avoids an improper interpolation.

Interpolation. The next step is to perform two separate linear 3D interpolations to determine the values of the reflective Stokes parameters, I, Q, and U, based on the distances from the data point to the eight vertices of the cube. The closer the data point is to each vertex, the more weight is given to the value of the flux at that vertex (values of *I*, *Q*, and *U* for that line of the LUT). The most elegant way to perform this interpolation is to use linear algebra[35]:

$$Ax = I \tag{131}$$

$$\mathrm{x} = \left[\mathrm{A}^{\mathrm{T}}\mathrm{A}\right]^{-1}\mathrm{A}^{\mathrm{T}}\mathrm{I} \tag{132}$$

$$\mathrm{I} = (\mathrm{x}_1 \bullet \mathrm{SZA1}) + (\mathrm{x}_2 \bullet \mathrm{VZA1}) + (\mathrm{x}_3 \bullet \mathrm{RelAz1}) + \mathrm{x}_4 \tag{133}$$

where *I* is the reflective Stokes parameter (*Q* and *U* are calculated separately using the same method), and *A* is the matrix of values in the LUT where column 1 is SZA, column 2 is VZA, column 3 is RelAz, and column 4 is all ones.

If the *A* matrix is invertible, this works well; however, if the matrix is singular or nearly so, then the result is either unusable or subject to a large computational error. Because of this problem, and the large number of times it occurred when running the interpolation program, I wrote a new routine which does 3D linear interpolation without matrix inversion.

interp8frac routine: this routine performs 3D linear interpolation using the eight vertices of the solid (as discussed above) and the desired point that falls within them. In cases where there is an exact match, the routine uses the exact match for both the "above" and "below" values. The values of each of the Stokes parameters, *I*, *Q*, and *U* for the point of interest are separately

[35] T. J. Kane, personal communication, May 2009

calculated as a weighted average of the eight values in the vertices, depending linearly on how close the point of interest is to each vertex in each dimension.

oceans_setup routine: This routine gathers all Oceans parameters to be modified, including orbital parameters, cloud fraction and albedo, lookup table file name, and computer system to be run on (which determines the directory path), and passes the chosen values to all subroutines using COMMON blocks. Revision information is also included.

pixel maps: as an aid in troubleshooting and verification, I added an optional feature to produce 2D maps of the planetary pixels at full phase (OL = 180°), quadrature (OL = 90°), and the Brewster angle (OL = 74°). These were particularly useful in verifying the Stokes rotation.

Stokes parameter rotation: 6SV reports Stokes parameters relative to a ground-referenced scattering plane, but we need the Stokes parameters relative to the scattering plane, so a routine was added to Oceans to rotate the LUT values to the scattering plane reference; this routine and the theory behind it are detailed in Appendix D.

Appendix D: Rotating Stokes Parameters to the Scattering Reference Plane

D.1 Introduction and Definition of Planes

The Stokes parameters (discussed in Section 2.2.7), a set of four parameters which describe the intensity and polarization of an electromagnetic wave, require a reference plane, or "zero angle," in order to be fully interpreted. Three commonly used reference planes are:

1) the scattering plane, which is the plane including both the incoming and outgoing rays;
2) the incoming/ground-normal plane, which is the plane that includes both the incoming ray and the normal to the surface; and
3) the outgoing/ground-normal plane.

The calculated Stokes parameters depend on the reference plane used in the calculation. The angle X (chi), the angle between the electric field polarization and the reference plane, is a natural parameter to use when verifying which reference planes are used by a model such as 6SV. The angle 2α is used to rotate the Stokes parameters between two reference planes, as described in section D.2. In section D.3 we determine which reference plane 6SV is using, and in section D.4 we derive a formula to calculate α to rotate the Stokes parameters from the 6SV reference plane back to the scattering plane.

D.2 Formula for Rotation of Stokes Parameters Q and U Using Rotation Angle α

The formula for modifying the Stokes parameters for rotation is given by a number of references; Hovenier and DeHaan (1985) is very specific about directions and signs:

"If we rotate the plane of reference through an angle, $\alpha \geq 0$ in the anti-clockwise direction, when looking in the direction of propagation, the new Stokes parameters are given by:"

and the reference then provides a 4 x 4 rotation matrix, which when multiplied times the original Stokes parameters, gives the new Stokes parameters. Using our notation, with the original Stokes parameters from 6SV being transformed to the Stokes parameters referenced to the scattering plane (SP), the result is:

$$Q_{SP} = Q_{6SV}\cos(2\alpha) + U_{6SV}\sin(2\alpha) \tag{134}$$

$$U_{SP} = -Q_{6SV}\sin(2\alpha) + U_{6SV}\cos(2\alpha) \tag{135}$$

where α is the angle of rotation. It now remains for us to find α as a function of the Solar Zenith Angle (SZA), Viewer Zenith Angle (VZA), and Relative Azimuth (RelAz). The alternate rotation, in the opposite direction, results in equations that differ only in the sign of the U_{6SV} and

Q_{6SV} terms (Schutgens et al. 2004)). We can check that this is also true in 6SV by entering two cases, with the following input angles, which differ only in that the values of the stellar azimuth angle and viewer azimuth angle are swapped, resulting in a sign change in the relative azimuth and in X. As expected, the result is of this swap is identical Stokes parameters except for the sign of U, as seen in Table 10.

Table 10: Verification of rotation in 6SV - sign change in relative azimuth causes sign change in U

Case	Stellar Zenith Angle	Stellar Azimuth Angle	Viewer Zenith Angle	Viewer Azimuth Angle	Relative Azimuth Angle	X
Inputs, + case	60	0	60	110	+110°	+35°
Inputs, - case	60	110	60	0	-110°	-35°
		I	**Q**	**U**		
Outputs, + case		0.03958	0.01224	-0.03344		
Outputs, - case		0.03958	0.01224	0.03344		

D.3 Determination of the Stokes Reference Plane Used by 6SV

In Kotchenova et al. (2006), the authors state:

"The Stokes parameters are specified in the coordinate system associated with the direction of propagation of incident light. To obtain their values with respect to the solar-viewer coordinate system, one should rotate them using the transformation matrix."

Since the direction of propagation is a simple vector, and we seek a reference plane, the above statement is ambiguous. We will need to determine experimentally what reference plane 6SV uses for the Stokes parameters. But first, why does 6SV rotate the Stokes parameters to another reference plane? The reason for rotating from the scattering plane to another reference plane is that, for multiple scattering, each order of scattering has a different scattering plane and therefore a different reference. In order to keep track of multiple scattering, the software transforms each output to a fixed reference plane. We now attempt to determine what that fixed plane is.

We will proceed on the hypothesis that 6SV uses one of the three commonly used reference planes listed above. When we have chosen the correct plane, and rotation based on this plane gives us the correct answers, then we will have confirmation that we understand the reference plane which 6SV uses and the rotation is correct. Referring to Figure 65, suppose we have a ray (blue) from a star incident to a surface at a zenith angle θ to the normal. For convenience, we use a rectangular coordinate system with the planet surface (green) in the x-y plane, the surface normal along the z-axis, and the incoming ray in the x-z plane. If the ray is spectrally reflected, then the outgoing ray (red, "to observer") has the same zenith angle θ to the normal, and the relative azimuth between the incoming and outgoing rays is 180°. Clearly, the two rays determine a plane, the scattering plane, which includes both rays and the surface normal, and is

identical to the x-z plane. The incoming/ground-normal plane (blue dashed lines) is determined by the incoming ray and the z-axis, and the outgoing/ground-normal plane (red dashed lines) is determined by the outgoing ray and the z-axis. Because both rays and the normal are all coplanar, the scattering plane, the incoming/ground-normal plane, and the outgoing ground-normal planes are all identical for this case. Stokes parameters based on any of these three reference planes will be identical.

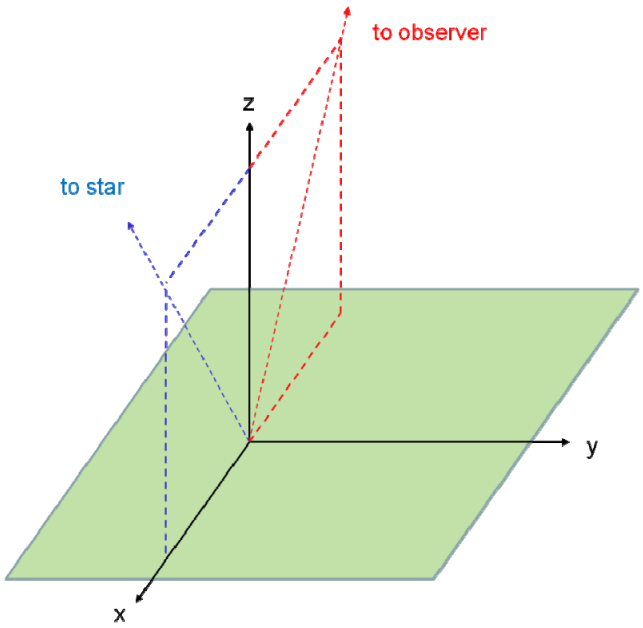

Figure 65: Scattering diagram for specular reflection case

Now suppose the outgoing ray is scattered in another direction, still at an angle θ to the normal, but now with a smaller relative azimuth. We can imagine the outgoing ray rotating around the point on the surface to approach the incoming ray as in Figure 66.

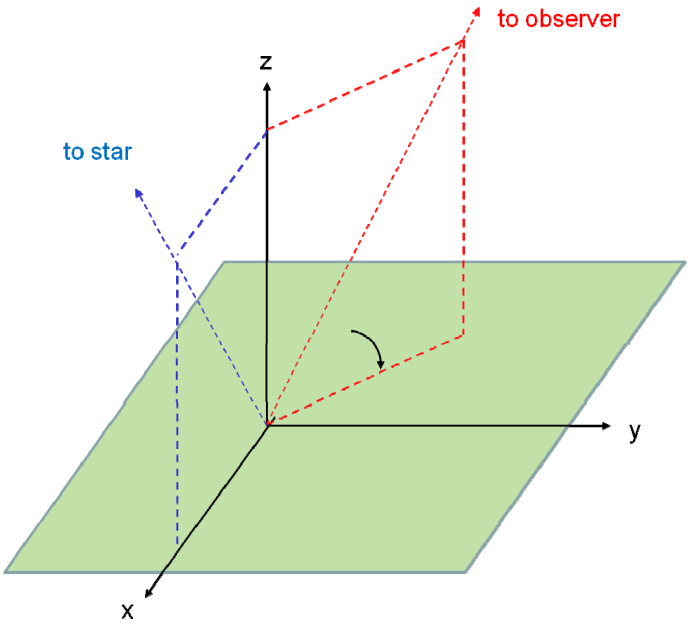

Figure 66: Scattering diagram for case with equal zenith angles and obtuse relative azimuth angle

We see that the scattering plane, which is defined by the incoming and outgoing rays, is no longer perpendicular to the surface; as the outgoing ray approaches the incoming ray (Figure 67) the scattering plane becomes more "tilted" to the ground, and its zenith angle approaches θ. However, both ground-normal planes, by definition, remain perpendicular to the surface throughout this rotation. So as the azimuthal direction of the outgoing ray varies from 180° (Figure 65) to ≈ 0° (Figure 68), the position of the incoming/ground-normal plane is held constant, and the orientation of the scattering plane varies from aligned with the z-axis to tilted at a zenith angle of θ. The third plane, the outgoing/ground-normal plane, rotates around the scattering point with the outgoing ray, while remaining perpendicular to the surface. Note that the scattering plane hits both the incoming/ground-normal plane and the outgoing/ground-normal plane at the same angle.

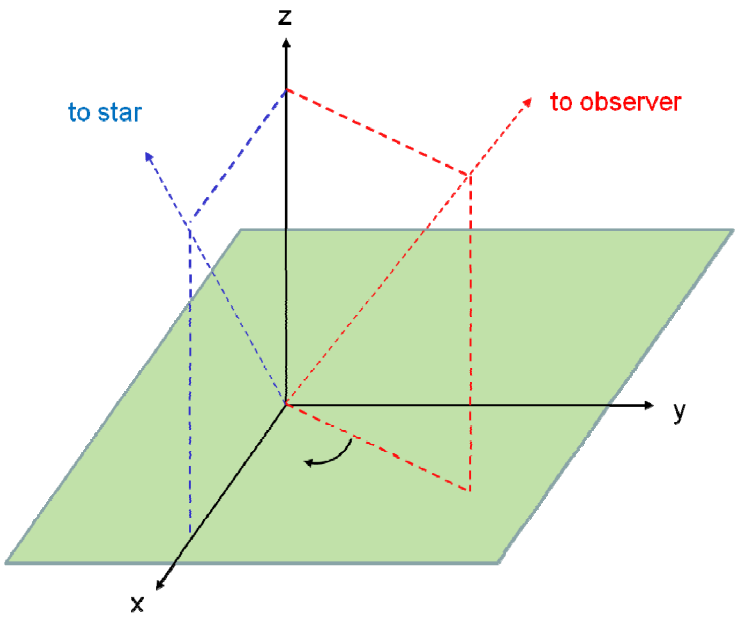

Figure 67: Scattering diagram for case of equal zenith angles and acute relative azimuth angle

As the relative azimuth approaches zero, and the outgoing ray approaches the incoming ray (Figure 68), the incoming/ground-normal and outgoing/ground normal planes are nearly identical (violet), and the scattering plane (orange) hits both ground-normal planes at right angles. (We consider the limit as the relative azimuth approaches zero because, if the "to star" and "to observer" rays are identical, they define a line, not a plane. Therefore, depending on the model, the answer at a relative azimuth of zero degrees with equal zenith angles may not be what we expect.) The differences in orientation between the three planes, and the resulting difference in calculated *X*, allow us to determine which reference plane is used by 6SV.

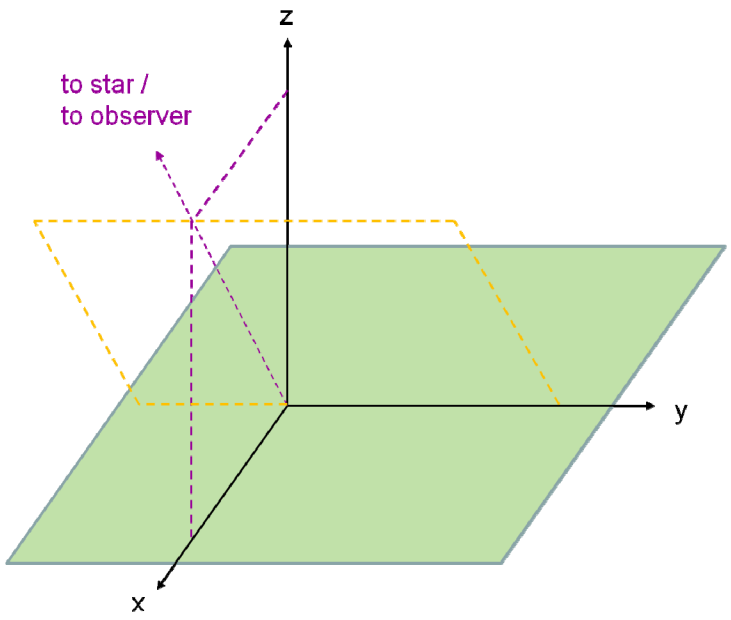

Figure 68: Scattering diagram for case with star and observer at same zenith angle and relative azimuth approaching zero

D.3.1 Expected Results from Different Reference Planes

Rayleigh scattering produces polarization because in free space, an electromagnetic wave cannot propagate in the direction of the electric field vector. For Rayleigh scattering, the angle of polarization X is always perpendicular to the scattering plane, because the parallel E-field is always the one that is reduced; therefore, in a coordinate system referenced to the scattering plane, X is always 90°. For a ground-normal coordinate system, the scattering plane is identical to the ground-normal plane in the specular reflection (Figure 65) case, so again $X = 90°$ for this case; however, for the Figure 68 case, the scattering plane (orange) is at a 90° angle to the ground-normal planes (violet), so $X = 0$. This difference can be used to determine if 6SV is using a ground-normal reference.

D.3.2 6SV Reference Plane Test Results

To test 6SV to determine if it is using a ground-normal or scattering plane reference, we set up a Rayleigh scattering atmosphere over a dark surface, with the zenith angles of the star (first column) and observer (second column) both set to 45°, and vary the relative azimuth (third column) from 0° to 180° as in our thought experiment above (except reverse order). The resulting outputs from 6SV are as follows:

SZA	VZA	RelAz						X
45.0	**45.0**	**0.0**	**0.17078**	**0.00505**	**0.00000**	**0.08792**	**0.08287**	**0.0**
45.0	45.0	10.0	0.16969	0.00608	0.00075	0.08788	0.08181	3.5
45.0	45.0	20.0	0.16649	0.00898	0.00223	0.08774	0.07875	7.0
45.0	45.0	30.0	0.16142	0.01326	0.00511	0.08734	0.07408	10.5
45.0	45.0	40.0	0.15484	0.01814	0.00978	0.08649	0.06835	14.2
45.0	45.0	50.0	0.14721	0.02269	0.01639	0.08495	0.06226	17.9
45.0	45.0	60.0	0.13904	0.02595	0.02472	0.08249	0.05655	21.8
45.0	45.0	70.0	0.13082	0.02703	0.03425	0.07893	0.05190	25.9
45.0	45.0	80.0	0.12303	0.02526	0.04420	0.07414	0.04888	30.1
45.0	**45.0**	**90.0**	**0.11602**	**0.02028**	**0.05358**	**0.06815**	**0.04787**	**34.6**
45.0	45.0	100.0	0.11007	0.01210	0.06133	0.06109	0.04898	39.4
45.0	45.0	110.0	0.10530	0.00112	0.06644	0.05321	0.05209	44.5
45.0	45.0	120.0	0.10172	-0.01193	0.06808	0.04490	0.05683	50.0
45.0	45.0	130.0	0.09924	-0.02601	0.06570	0.03662	0.06263	55.8
45.0	45.0	140.0	0.09767	-0.03990	0.05909	0.02889	0.06879	62.0
45.0	45.0	150.0	0.09679	-0.05236	0.04847	0.02222	0.07457	68.6
45.0	45.0	160.0	0.09636	-0.06221	0.03442	0.01708	0.07929	75.5
45.0	45.0	170.0	0.09619	-0.06853	0.01787	0.01383	0.08236	82.7
45.0	**45.0**	**180.0**	**0.09615**	**-0.07071**	**0.00000**	**0.01272**	**0.08343**	**90.0**

The first row of the output represents the Figure 68 case (zenith angles = 45° and relative azimuth ≈ 0°), and the last row represents the specular (Figure 65) case (zenith angles = 45° and relative azimuth = 180°). Since X (the rightmost column) varies from 0 to 90°, we see that 6SV does in fact use one of the ground-normal coordinate systems. So in our model, we need to rotate the 6SV outputs from a ground-normal reference plane to the scattering plane. If the above quote from Kotchenova et al. (2006) is correct, the reference plane used by 6SV is the incoming/ground-normal plane, so we will hypothesize that this is correct, derive a formula to perform the appropriate rotation, rotate some sample outputs from 6SV, and determine if we get the correct answer.

D.4 Derivation of Formula for Stokes Rotation Angle α

We now need a formula to calculate the rotation angle α that will be used to rotate the 6SV output back to the scattering plane. Tilstra et al. (2003) does a similar rotation to that needed for our case, except that the rotation performed is from the scattering plane to the outgoing/ground-normal plane.[36]

In the derivation used in Tilstra et al. (2003), α is found as follows:

1. the normals of each of the two planes, the "old" reference plane and "new" reference plane, are calculated using the cross product of the two vectors which define each plane;
2. the angle between the two normals (α) is calculated using their inner (dot) product;
3. α is converted into the angle between the planes, β, by adding it to or subtracting it from 90° and doubling the result;

[36] Tilstra (2003) provides equations in two different forms; the versions which include variables with the zero subscript refer to data from the SCIAMACHY (Scanning Imaging Absorption Spectrometer for Atmospheric CHartographY) satellite-borne spectrometer, so the first set applies here.

4. β is converted into *X* by choosing the correct sign and taking modulo 180°.

The usual 3D trig identities are used to calculate the scattering angle *SCA* in terms of the solar zenith angle *SZA*, Viewer Zenith Angle *VZA*, and Relative Azimuth *RelAz*:

$$\cos(SCA) = \cos(VZA)\cos(SZA) + \sin(VZA)\sin(SZA)\cos(RelAz) \tag{136}$$

Now using Tilstra et al. (2003) as a guide, we develop a new rotation formula for α, based on the knowledge that 6SV uses the incoming/ground-normal reference plane. As with Tilstra et al. (2003), we start with the outgoing scattered light vector *v* and the incoming sunlight vector *w*:

$$\vec{v} = (\cos\phi\sin\theta, \sin\phi\sin\theta, \cos\theta) \tag{137}$$

$$\vec{w} = (\cos\phi_i\sin\theta_i, \sin\phi_i\sin\theta_i, \cos\theta_i) \tag{138}$$

which are unit vectors using spherical coordinates converted to Cartesian coordinates. Continuing to follow Tilstra, we calculate the normal to the scattering plane as

$$\vec{n_s} = \vec{w}\times\vec{v} \tag{139}$$

which when expanded becomes:

$$\begin{aligned}\vec{n}_s = (&\sin\varphi_i\sin\theta_i\cos\theta - \sin\varphi\sin\theta\cos\theta_i,\\ &\cos\varphi\sin\theta\cos\theta_i - \cos\varphi_i\sin\theta_i\cos\theta,\\ &\cos\varphi_i\sin\theta_i\sin\varphi\sin\theta - \cos\varphi\sin\theta\sin\varphi_i\sin\theta_i)\end{aligned} \tag{140}$$

For the other plane, the outgoing/ground-normal plane, Tilstra (2003) defines the normal as

$$\vec{n_m} = \vec{v}\times\vec{e_z} \tag{141}$$

where e_z is the unit vector in the vertical (z) direction. The value of the normal, after normalization to a magnitude of 1, Tilstra calculates to be:

$$\vec{n_m} = (\sin\phi, -\cos\phi, 0). \tag{142}$$

We are using the incoming/ground-normal plane, and its normal is calculated using the w and e_z vectors:

$$\vec{n}_i = \vec{w}\times\vec{e}_z \tag{143}$$

This should be analogous to calculating n_m, which Tilstra finds as:

$$\vec{n}_m = \vec{v} \times \vec{e}_z = (\cos\varphi \sin\theta, \sin\varphi \sin\theta, \cos\theta) \times \vec{e}_z = \det \begin{bmatrix} i & j & k \\ \cos\varphi \sin\theta & \sin\varphi \sin\theta & \cos\theta \\ 0 & 0 & 1 \end{bmatrix} \quad (144)$$

$$= \hat{i} \sin\varphi \sin\theta - \hat{j} \cos\varphi \sin\theta$$

which can be normalized to

$$\vec{n}_m = (\sin\varphi, -\cos\varphi, 0) \quad (145)$$

which matches Tilstra. If we now calculate the normal to the incoming/ground-normal plane:

$$\vec{n}_i = \vec{w} \times \vec{e}_z = (\cos\varphi_i \sin\theta_i, \sin\varphi_i \sin\theta_i, \cos\theta_i) \times \vec{e}_z = \det \begin{bmatrix} i & j & k \\ \cos\varphi \sin\theta & \sin\varphi \sin\theta & \cos\theta \\ 0 & 0 & 1 \end{bmatrix} \quad (146)$$

we notice that *w* and *v* are identical except for the subscripts *i*, so clearly the normal is:

$$\vec{n}_i = (\sin\varphi_i, -\cos\varphi_i, 0) \quad (147)$$

We now calculate the angle between the normals of the two planes using the dot product (inner product):

$$\begin{aligned} &|\vec{n}_i||\vec{n}_s|\cos\alpha = \vec{n}_i \cdot \vec{n}_s = (\sin\varphi_i, -\cos\varphi_i, 0) \cdot \\ &(\sin\varphi_i \sin\theta_i \cos\theta - \sin\varphi \sin\theta \cos\theta_i, \\ &\cos\varphi \sin\theta \cos\theta_i - \cos\varphi_i \sin\theta_i \cos\theta, \\ &\cos\varphi_i \sin\theta_i \sin\varphi \sin\theta - \cos\varphi \sin\theta \sin\varphi_i \sin\theta_i) \end{aligned} \quad (148)$$

The dot product I calculated by hand, and the magnitudes of the vectors are:

$$|\vec{n}_i| = \sin^2\varphi_i + \cos^2\varphi_i = 1 \quad (149)$$

and, from Tilstra et al. (2003),

$$|\vec{n}_s| = \sin\Theta = \sin(SCA) \quad (150)$$

so the formula for α for rotation between the scattering plane and the incoming/ground reference plane is, using Tilstra's notation (left) and our notation (right),

$$\cos\alpha = \frac{\sin\theta_i \cos\theta - \sin\theta \cos\theta_i \cos(\varphi - \varphi_i)}{\sin\Theta} = \frac{\sin(SZA)\cos(VZA) - \sin(VZA)\cos(SZA)\cos(relAz)}{\sin(SCA)} \quad (151)$$

We now attempt to rotate the Stokes reference plane back to the scattering plane. For this testing, we use data generated by 6SV for a variety of solar and viewer zenith angles and relative azimuth angles. We use the new formula for alpha which calculates the angle between the scattering plane and the incoming/ground normal plane, and the formula for the scattering angle given above. The formula for alpha is dependent on which reference planes we are trying to rotate between. The scattering angle formula, on the other hand, is a consequence of 3D trigonometry. Planetary conditions are a constant surface reflectance of 0.01, with a sea-level Rayleigh scattering atmosphere and altitude correction. When the rotation produces a *Xss* of approximately 90° for all cases, then we have generated the correct rotation back to the scattering plane. (The total is not exactly 90° due to multiple Rayleigh scattering and dilution by the unpolarized surface.)

Checking this using a spreadsheet (Table 11), we find that the total of α and Xss is approximately 90° for all cases, so if we rotate the Stokes parameters from 6SV by +α we should obtain the answer rotated back to the scattering plane.

To do this in the 6SV/Oceans model, we rotate the Q and U parameters using the formula from above

$$Q_{SP} = Q_{6SV}\cos(2\alpha) + U_{6SV}\sin(2\alpha) \tag{152}$$

$$U_{SP} = -Q_{6SV}\sin(2\alpha) + U_{6SV}\cos(2\alpha) \tag{153}$$

The rotated parallel and perpendicular components are then calculated by the modified Oceans code as the sum and difference of the *I* and *Q* parameters.

We now check the rotation formula given in Tilstra et al. (2003) in Table 12:

$$\cos\alpha = -\frac{\sin\theta\cos\theta_i - \sin\theta_i\cos\theta\cos(\varphi-\varphi_i)}{\sin\Theta} = \frac{-\sin(VZA)\cos(SZA)+\sin(SZA)\cos(VZA)\cos(relAz)}{\sin(SCA)} \tag{154}$$

and find that, in the columns labeled Tilstra, the sum of *Xss* and alpha is not 90°. However, in the last three columns, labeled –Tilstra, we negate the formula for the cosine of alpha, and find that the resulting alpha does in fact total with *Xss* to 90°. So a simple negation of the formula given by Tilstra et al. (2003) gives the correct rotation alpha (α).

Table 11: Results of rotation using the derived formula.

SZA	VZA	RelAz	Stokes-I	Stokes-Q	Stokes-U	Xss	SCA Deg	alpha	Xss + alpha
15	0	180	0.11494	-0.00344	0	90.00	15.0	0.0	90.0
15	15	179.5	0.10499	-0.01337	0.00012	89.74	30.0	0.3	90.0
15	30	179.5	0.09043	-0.02623	0.00017	89.81	45.0	0.2	90.0
15	45	179.5	0.07455	-0.03762	0.0002	89.85	60.0	0.1	90.0
15	60	179.5	0.05974	-0.04265	0.00021	89.86	75.0	0.1	90.0
15	75	179.5	0.04383	-0.03544	0.00017	89.86	90.0	0.1	90.0
45	45	179.5	0.08152	-0.06165	0.0008	89.63	90.0	0.4	90.0
45	45	134.5	0.08347	-0.02796	0.05576	58.32	81.4	30.7	89.0
45	45	90	0.09812	0.0184	0.04744	34.40	60.0	54.7	89.1
45	45	45	0.12721	0.01886	0.01162	15.82	31.4	73.7	89.5
45	45	30	0.13572	0.01256	0.00473	10.32	21.1	79.3	89.6
45	45	15	0.14144	0.00739	0.00131	5.03	10.6	84.7	89.7
45	45	0.1	0.14346	0.00541	0.00001	0.05	0.1	90.0	90.0
45	45	0	0.14346	0.00541	0	0.00	0.0	90.0	90.0
60	45	125	0.1075	0.00511	0.08384	43.26	89.9	45.2	88.4
60	40	100	0.11583	0.04867	0.06458	26.50	73.4	62.9	89.4
80	70	90	0.17762	0.14043	0.04372	8.65	86.6	80.6	89.2
80	50	60	0.23282	0.11858	-0.04309	-9.99	60.7	102.1	92.2
80	40	120	0.20399	0.08425	0.12698	28.22	100.6	60.2	88.4
80	40	70	0.21822	0.13774	-0.0382	-7.75	69.5	99.0	91.2

Table 12: Results of using the Tilstra rotation and the negative of the Tilstra rotation.

SZA	VZA	RelAz	Stokes-I	Stokes-Q	Stokes-U	Xss	SCA Deg	Tilstra cos alpha	Tilstra alpha	Tilstra Xss + alpha	--Tilstra --cos alpha	--Tilstra alpha	--Tilstra Xss + alph
15	0	180	0.11494	-0.00344	0	90.00	15.0	-1.00	180.0	270.0	1.00	0.0	90.0
15	15	179.5	0.10499	-0.01337	0.00012	89.74	30.0	-1.00	179.7	269.5	1.00	0.3	90.0
15	30	179.5	0.09043	-0.02623	0.00017	89.81	45.0	-1.00	179.8	269.6	1.00	0.2	90.0
15	45	179.5	0.07455	-0.03762	0.0002	89.85	60.0	-1.00	179.9	269.7	1.00	0.1	90.0
15	60	179.5	0.05974	-0.04265	0.00021	89.86	75.0	-1.00	179.9	269.7	1.00	0.1	90.0
15	75	179.5	0.04383	-0.03544	0.00017	89.86	90.0	-1.00	179.9	269.7	1.00	0.1	90.0
45	45	179.5	0.08152	-0.06165	0.0008	89.63	90.0	-1.00	179.6	269.3	1.00	0.4	90.0
45	45	134.5	0.08347	-0.02796	0.05576	58.32	81.4	-0.86	149.3	207.6	0.86	30.7	89.0
45	45	90	0.09812	0.0184	0.04744	34.40	60.0	-0.58	125.3	159.7	0.58	54.7	89.1
45	45	45	0.12721	0.01886	0.01162	15.82	31.4	-0.28	106.3	122.1	0.28	73.7	89.5
45	45	30	0.13572	0.01256	0.00473	10.32	21.1	-0.19	100.7	111.0	0.19	79.3	89.6
45	45	15	0.14144	0.00739	0.00131	5.03	10.6	-0.09	95.3	100.3	0.09	84.7	89.7
45	45	0.1	0.14346	0.00541	0.00001	0.05	0.1	0.00	90.0	90.1	0.00	90.0	90.0
45	45	0	0.14346	0.00541	0	0.00	0.0	0.00	90.0	90.0	0.00	90.0	90.0
60	45	125	0.1075	0.00511	0.08384	43.26	89.9	-0.70	134.8	178.1	0.70	45.2	88.4
60	40	100	0.11583	0.04867	0.06458	26.50	73.4	-0.46	117.1	143.6	0.46	62.9	89.4
80	70	90	0.17762	0.14043	0.04372	8.65	86.6	-0.16	99.4	108.1	0.16	80.6	89.2
80	50	60	0.23282	0.11858	-0.04309	-9.99	60.7	0.21	77.9	67.9	-0.21	102.1	92.2
80	40	120	0.20399	0.08425	0.12698	28.22	100.6	-0.50	119.8	148.0	0.50	60.2	88.4
80	40	70	0.21822	0.13774	-0.0382	-7.75	69.5	0.16	81.0	73.3	-0.16	99.0	91.2

Appendix E: Compensating for the 6SV Plane-Parallel Atmosphere Approximation Using Altitude

E.1 Introduction

Without altitude compensation, the plane-parallel atmosphere approximation used by 6SV causes an increasing overestimation in the optical path length of the atmosphere starting around a solar zenith angle of roughly 80°. The IDL program I wrote to call 6SV and assemble a lookup table from its outputs (bilut__.pro) includes the algorithm 'altcomp,' which allows the user to partially convert the plane-parallel approximation used by 6SV to a spherical atmosphere. The user is given the choice of using an approximation I developed based on an exponential atmospheric pressure profile, or that developed empirically by Kasten and Young, based on Earth's atmospheric pressure profile. The choice is made by selecting one of the following values for the variable altcomp:

altcomp = 0; no altitude compensation, uses standard 6SV plane parallel approximation
altcomp = 1; use Kasten and Young approximation, based on Earth's atmosphere
altcomp = 2: use Zugger approximation.

When altcomp = 0, this issue is ignored, although testing showed that the effect is small for the total integrated signal from Earth-like and thinner atmospheres (see Section 6.3, Verification and Error Analysis). When altcomp = 1 or 2, one of two algorithms is used to partially compensate for the plane-parallel approximation. Compensation is performed by calculating an "effective altitude" for the surface which causes 6SV to calculate an optical path closer to the actual spherical optical path. Clearly, the method has limitations.

E.2 Kasten & Young Approximation

There have been a number of attempts to model the actual airmass experienced by sunlight entering Earth's atmosphere at large zenith angles; some of these are shown Figure 69 along with the simple plane-parallel approximation and the exact spherical calculation.[37] The best simple approximation is Kasten & Young (1989):

$$X = \frac{1}{\cos(ZA) + 0.50572(96.07995 - ZA)^{-1.6364}} \tag{155}$$

where X is airmass, and the zenith angle ZA is given in degrees. I then use the antilog of the ratio between the Kasten & Young airmass, and the airmass calculated using the plane parallel

[37] http://en.wikipedia.org/wiki/Airmass#Zenith_angle_and_altitude, posted by Jeff Conrad, used with permission of the author.

approximation, to calculate the effective altitude to be input to 6SV. These equations are implemented in the code provided at the end of this appendix.

A comparison of various approximations to the airmass in Earth's spherical atmosphere is shown in Figure 69. For additional information on the models depicted in the figure, see Hardie (1962), Rozenburg (1966) Young and Irvine (1967), and Kasten and Young (1989).

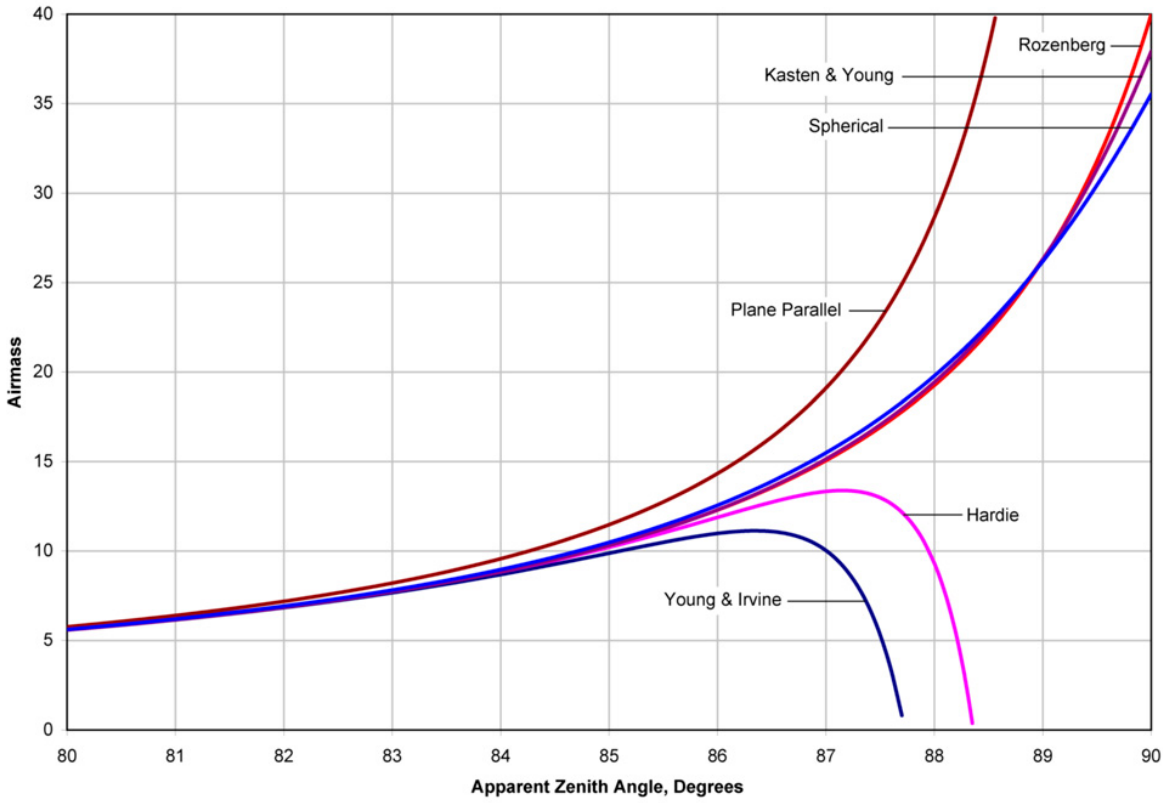

Figure 69: Comparison of various approximations to the airmass of Earth's spherical atmosphere with zenith angle

E.3 Exponential Approximation (my method)

The algorithm I developed calculates the length of the incoming optical path in the plane parallel approximation, which is h/cos(zenith angle), calculates the actual length of the optical path in a spherical atmosphere, then takes the ratio of these two results to determine what altitude in a plane-parallel atmosphere would be approximately equivalent to the actual spherical atmosphere. The actual path lengths of the incoming and outgoing rays are different, except when the zenith angles are identical, and unfortunately only one altitude can be entered into 6SV per calculation.

Therefore, the algorithm uses only the incoming ray. The effective altitude is then included in the parameters fed to 6SV to calculate the reflectance for a given combination of the three angles. The following section shows the derivation I used to achieve this solution.

In order to correct the plane-parallel approximation to the spherical reality, we start by assuming an exponential atmosphere. For the lookup table, we need to calculate the correction factor for both the Solar Zenith Angle (SZA) and the Viewer Zenith Angle (VZA), then multiply the correction factors together to obtain the overall correction factor. This overall correction factor is then used to calculate the equivalent altitude (or pressure) at which the surface should be located to compensate and return the correct amount of molecular absorption, Rayleigh scattering, and eventually, aerosol scattering. Note that this will result in some loss of accuracy in calculating the coupling between the atmosphere and the surface.

Therefore, for each combination of SZA and VZA (but independent of RelAz), there is a corresponding compensation used to calculate the LUT. This altitude appears in the input file to 6SV:

```
0.60  0.70  0.0    0.0    0.0    180.0  3    21   -90    0  0  6
0.60  0.70  2.8    0.0    2.8    180.0  3    21   -90    0  0  6
0.60  0.70  6.5    0.0    6.5    180.0  3    21   -90    0  0  6
0.60  0.70  10.2   0.0    10.2   180.0  3    21   -90    0  0  6
0.60  0.70  13.9   0.0    13.9   180.0  3    21   -90    0  0  6
0.60  0.70  17.6   0.0    17.6   180.0  3    21   -90    0  0  6
0.60  0.70  21.3   0.0    21.3   180.0  3    21   -90    0  0  6
0.60  0.70  25.1   0.0    25.1   180.0  3    21   -90    0  0  6
0.60  0.70  28.8   0.0    28.8   180.0  3    21   -90    0  0  6
0.60  0.70  32.5   0.0    32.5   180.0  3    21   -90    0  0  6
0.60  0.70  36.2   0.0    36.2   180.0  3    21   -90    0  0  6
0.60  0.70  39.9   0.0    39.9   180.0  3    21   -90    0  0  6
0.60  0.70  43.6   0.0    43.6   180.0  3    21   -90    0  0  6
0.60  0.70  47.3   0.0    47.3   180.0  3    21   -90    0  0  6
0.60  0.70  51.0   0.0    51.0   180.0  3    21   -90    0  0  6
0.60  0.70  53.1   0.0    53.1   180.0  3    21   -90    0  0  6
0.60  0.70  54.7   0.0    54.7   180.0  3    21   -90    0  0  6
0.60  0.70  58.5   0.0    58.5   180.0  3    21   -90    0  0  6
0.60  0.70  62.2   0.0    62.2   180.0  3    21   -90    0  0  6
0.60  0.70  65.9   0.0    65.9   180.0  3    21   -90    0  0  6
0.60  0.70  69.6   0.0    69.6   180.0  3    21   -90    0  0  6
0.60  0.70  73.3   0.0    73.3   180.0  3    21   -90    0  0  6
0.60  0.70  77.0   0.0    77.0   180.0  3    21   -90    0  0  6
0.60  0.70  80.7   0.0    80.7   180.0  3    21   -90    0  0  6
```

Here, where 90 km is given as the altitude, we would need to put in a different altitude for each combination of SZA and VZA. How to calculate this altitude? First we ask, given the radius of the planet r, the atmosphere height h, and the zenith angle ZA, what is the ratio between the actual (spherical) path length e to the plane-parallel calculated path f?

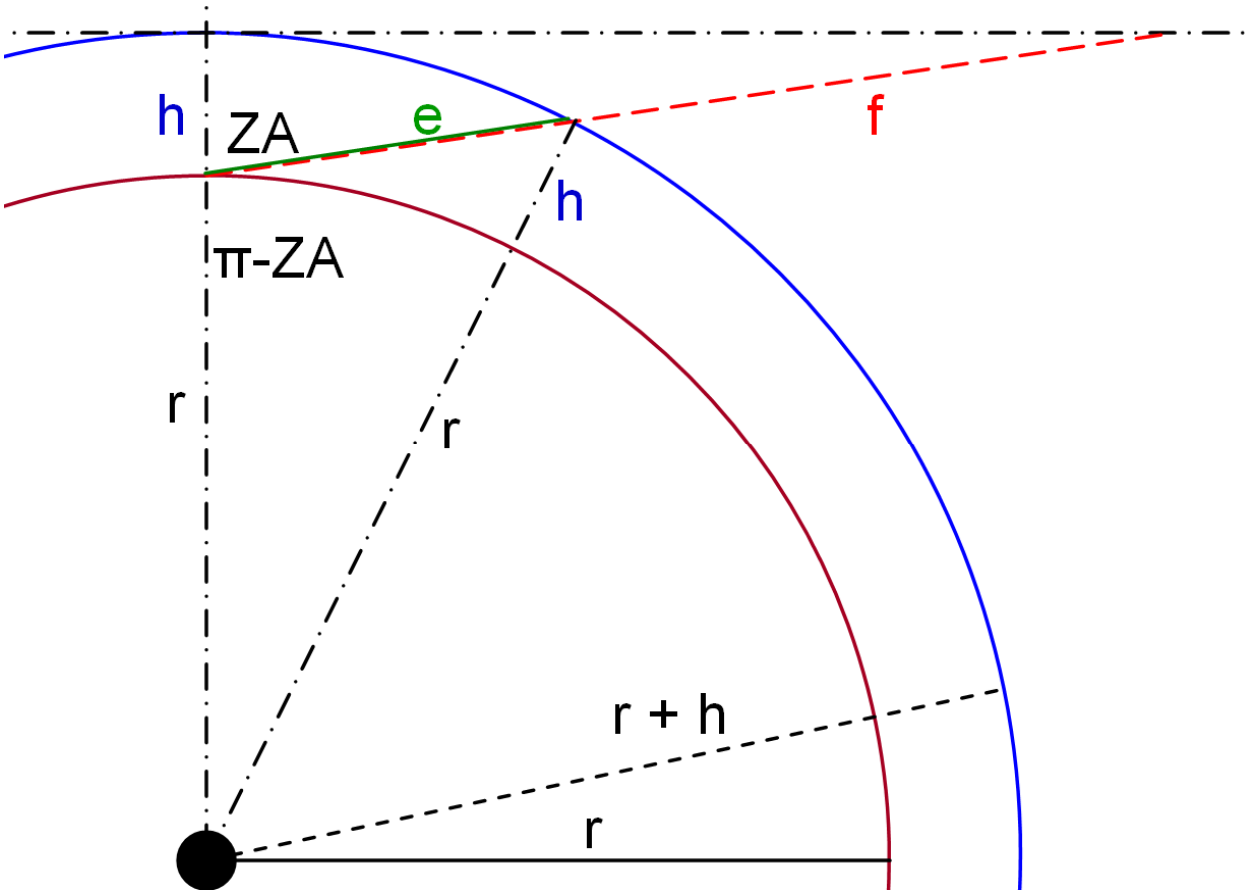

Figure 70: Geometry of the spherical atmosphere

Referring to Figure 70:

$$\cos(ZA) = adjacent / hypoteneuse = h / f \tag{156}$$

$$f = h / \cos(ZA) \tag{157}$$

Calculating *e* is more complicated. Remembering the generalized Pythagorean theorem,

$$a^2 = b^2 + c^2 - 2bc\cos(A) \tag{158}$$

we apply this first to the triangle formed by *e*, *r*, and $r + h$:

$$(r + h)^2 = e^2 + r^2 - 2er\cos(\pi - ZA) \tag{159}$$

$$0 = e^2 + r^2 - 2er\cos(\pi - ZA) - (r + h)^2 \tag{160}$$

$$0 = e^2 - 2er\cos(\pi - ZA) - r^2 - 2rh - h^2 + r^2 \tag{161}$$

$$0 = e^2 - 2er\cos(\pi - ZA) - 2rh - h^2 \tag{162}$$

Use quadratic formula to solve:

$$0 = ax^2 + bx + c \tag{163}$$

$$\begin{aligned} a &= 1 \\ b &= -2r\cos(\pi - ZA) \\ c &= -2rh - h^2 \\ e &= \left[-b +/- \left(b^2 - 4ac\right)^{1/2}\right]/2a \end{aligned} \tag{164}$$

(Note: the root with the subtraction is negative)

Now we measure the lengths of *r* and *h*, and the angle ZA, and use MATLAB to calculate the resultant lengths of e and f and their ratio. We then measure the lengths of *e* and *f* directly and compare the answers.

****
Program to check the planar-to-spherical path length against the diagram:

The angle of segment *e* to the normal is 81.4164

The angle of segment *f* to the normal is 81.5584

The measured length of segment e is 1.0720

The length of segment *e* calculated using the formula and r, h, and ZA is 1.1002

The measured length of segment *f* is 2.8610

The length of segment *f* calculated using the formula and r, h, and ZA is 2.8610

ratio of *e* to *f* using measurements from the diagram is 0.3747

ratio of *e* to *f* calculated using the formula is 0.3845
****

The 3% error in *e* and resultant similar error in *e/f* is due to the fact that, in the diagram, I was not able to draw *e* and *f* perfectly parallel.

Now that we have a formula to calculate the ratio between the spherical and planar path lengths, we need to compensate for the difference in path lengths by changing the altitude/pressure of the planetary surface depending on the zenith angles.

Pressure and altitude – for an isothermal atmosphere,

$$P(z) = P_o \exp[-mgz / kT] \tag{165}$$

which is usually simplified to

$$P(z) = P_o \exp[-z / h] \tag{166}$$

by choosing $h = -kT/mg$, and calling it the "scale height."

If h in the diagram above is actually the scale height, then e and f are also scale heights.

The optical path length is proportional to the integrated pressure; recalling that

$$\int_0^\infty e^{-ar} dr = \frac{1}{a} \tag{167}$$

and remembering that the optical path stretches between ground level and space, we find that the optical path is

$$d_{opt} = \int_0^\infty P_0 e^{-r/h} dr = P_0 h \tag{168}$$

Then the optical path in the plane parallel atmosphere is proportional to

$$d_{opt}^{pp} \propto P_0 f \tag{169}$$

and the optical path in the spherical atmosphere is proportional to

$$d_{opt}^{sph} \propto P_0 e \tag{170}$$

so the ratio between the optical path lengths is the same as that between the physical distances through the atmosphere:

$$\frac{d_{opt}^{sph}}{d_{opt}^{pp}} = \frac{e}{f} \tag{171}$$

So what altitude *A* should we use as the input to 6SV, in order to compensate for the plane parallel approximation in 6SV? From the above, we will need to reduce the base pressure by the fraction *e/f*,

$$\frac{P_a}{P_0} = \frac{e}{f} \tag{172}$$

Scale height remains the same regardless of starting point, so we need to find the point on the exponential curve where the pressure has dropped to e/f times the original pressure P_0. Returning to the exponential pressure formula, letting a = the desired altitude, we now have

$$\begin{aligned} P_a &= \frac{e}{f} P_0 = P_0 \exp(-a/h) \\ \frac{e}{f} &= \exp(-a/h) \\ \ln\left(\frac{e}{f}\right) &= -\frac{a}{h} \\ a &= -h \ln\left(\frac{e}{f}\right) \end{aligned} \tag{173}$$

Check: if we set $e/f = 1/2.718$, then we have $\ln(1/2.718) = -1$, and $a = h$.

Check2: If the scale height h is about 7 km (4.3 mi) as on Earth, and the desired ratio $e/f = 0.5$, then we have

$$a = -h \ln\left(\frac{e}{f}\right) = -7 \ln(0.5) = (-6.35)(-.693) = 4.9 km \tag{174}$$

which is in general agreement with the 5 to 5.5 km estimates used for Earth's scale height.

Check3: at normal incidence, $e = f$, so $e/f = 1$, and the altitude is

$$a = -h \ln\left(\frac{e}{f}\right) = -h \ln(1) = 0 km \tag{175}$$

so the measurement is not compensated.

Check4: with
R_e = 6378 km
h = 7 km
ZA = 80.7 degrees,
e/f = 0.98

$$a = -h \ln\left(\frac{e}{f}\right) = -7 \ln(0.98) = 0.14 \text{ km} \tag{176}$$

for ZA = 85 degrees, alt = 0.45 km
for ZA = 87 degrees, alt = 1.1 km

To summarize the solution, based on SZA, and *h*, the bilut routine calculates the incoming plane-parallel optical path f, and the spherical optical path e, for the incoming (SZA) path. Using the formula above, it then calculates the equivalent altitude for a plane parallel atmosphere, which is then used as an input to 6SV.

```
; ===========================================================================
; COMPENSATE FOR PLANE PARALLEL APPROXIMATION BY VARYING ALTITUDE WITH ZENITH
ANGLE

IF altcomp eq 1 or altcomp eq 2 THEN BEGIN
  print, ' '
  print, '--altitude compensation enabled--'
  print, ' '
  ;Set altitude column to all zeroes, and check size
  altcol = altcol * 0
  sizealtcol = size(altcol)
  rowsaltcol = sizealtcol(2)

     ; Divide input atmospheric height and planet radius by 100 to prevent
overflow
     h = double(hin)
     r = double(rin)
     pi = 3.14159;

     ; Calculate value of altitude to compensate for plane parallel
approximation
     FOR k = 0, rowsaltcol-1 DO BEGIN

        ;ZA = 81.5*pi/180
        ; First calculate e/f from SZA
        ZA = SZA(k)*pi/180

; Zugger approx: Use quadratic equation to solve for the spherical optical
path
        a = 1;
        b = double(-2*r*cos(pi - ZA));
        ;c = -2*r*h - h^2;
        c = double(-1*(2*r*h + h^2))

        e1 = double((-b + sqrt(b^2 - 4*a*c))/2*a)
        ;print, e1

        ; f is the plane-parallel model optical path
        f = h/cos(ZA)
```

```
        ; eOVERf is the ratio between the desired spherical optical path e
        ; and the plane-parallel model optical path f
        eOVERfSZA = double(e1/f)
        ; ------------------
   ; REV 36 REMOVED CODE: used geometric mean between incoming/outgoing paths

        eOVERf = eOVERfSZA


        ; KASTEN & YOUNG APPROXIMATION
        if altcomp eq 1 then begin
           eky = cos(ZA) + 0.50572*((96.07995 - SZA(k))^(-1.6364))  ;*pi/180
           if eky ne 0.0 then eky = 1/eky
           if eky eq 0.0 then begin
             eky = 1.0
             print, 'ERROR, ATTEMPT TO DIVIDE BY EKY = 0'
           end
           eOVERf = eky*cos(ZA)
        end


        altcol(k) =  hin*alog(eOVERf)
     END
     print,
'*****************************************************************************
**************************'
     print, 'ZA = ', ZA
     print, 'h = ', h
     print, 'r = ', r
     print, 'a = ', a
     print, 'b = ', b
     print, 'c = ', c
     print, 'discr = ', sqrt(b^2 - 4*a*c)
     print, 'e = ', e1
     print, 'f =', f
     print, 'e/f = ', eOVERf
     print, 'altitude = ', altcol(k-1)
END
```

Appendix F: Changes to 6SV Code

The 6SV software calculates the water-leaving radiance and directional reflectance using a number of subroutines which call each other. Figure 71 shows this process diagrammatically.

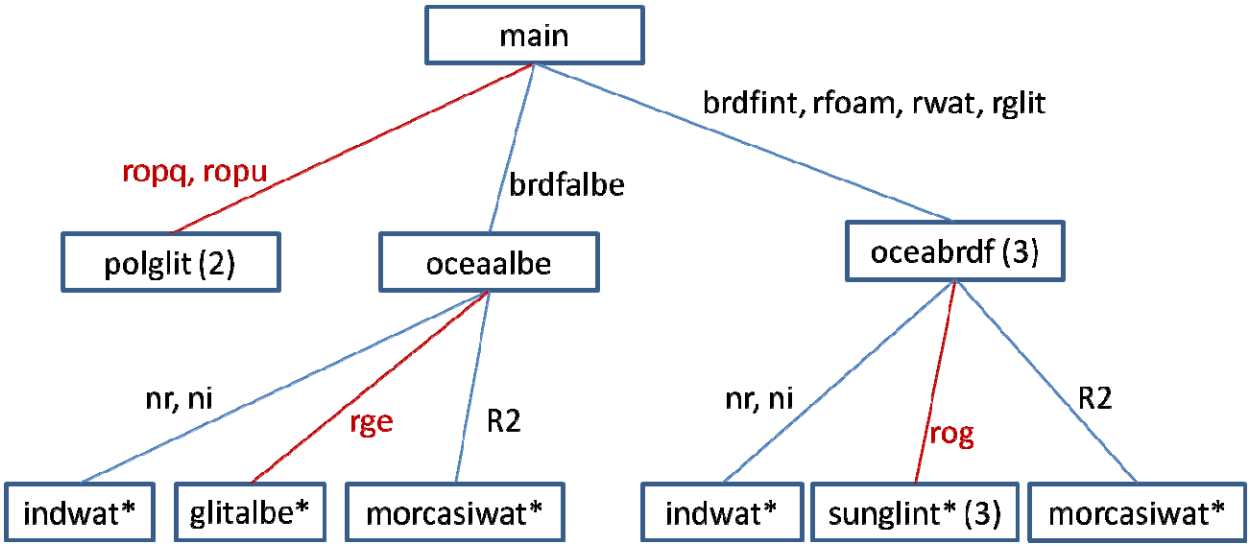

Figure 71: Diagram of the interplay between 6SV subroutines in calculating ocean-leaving radiance and directional reflectance

Key:

ropq, ropu = polarized reflective Stokes components
brdfalbe = spherical albedo of ocean
brdfint(j,k) = total reflectance of sea water
rfoam = foam coverage x foam reflectance
rwat = the reflectance of the water just above the surface
rglit = the reflectance of the sunglint
nr, ni = complex index of seawater
rog = reflectance of sunglint
R2 = reflectance of water below the surface
rge = spherical albedo of seawater
* = subroutines included within oceatools
(*x*) = called *x* times from subroutine above, not including loops

In Fortran, execution begins with the *main* routine, and it calls the other subroutines. In 6SV, there are about ninety individual subroutines listed separately with their own *.f files, and a number of other routines which are grouped together in a single *.f file, such as the six subroutines on the bottom row of Figure 71 which are all included in the Fortran source code file OCEATOOLS.f. Ocean reflectance consists of Fresnel reflection from the surface, reflection

from foam, and scattering from within the water. A brief description of the subroutines in Figure 71 follows.

morcasiwat = Morel Case I water – Morel classified waters into Case I, in which the optical properties are dominated by a combination of phytoplankton and their breakdown products (along with the intrinsic properties of water), as opposed to Case II waters, which are dominated by sediment and "yellow substance." Typically, the open ocean is Case I water; for our purposes, we set the pigment to zero in 6SV, so the reflectance properties are based on pure saltwater.

indwat = index of refraction of water, which calculates the index of refraction of water with the user-defined salt concentration, and calculates the reflection coefficients of saltwater to parallel and perpendicular polarizations. I used the salt concentration of the open ocean on Earth, 34.3 parts per thousand.

glitable – calculates the glitter spherical albedo, rge, that is, the non-directional reflectance of the ocean surface glitter.

sunglint - calculates total reflectance of the sea surface glint in the direction of interest, rog, equivalent to the Stokes reflectance parameter I.

polglit - calculates the polarized components of the reflectance of the sea surface glint in the direction of interest, ropq and ropu, equivalent to the Stokes reflectance parameters Q and U.

ocealbe – calculates the spherical albedo of the ocean.

oceabrdf – calculates the total ocean brdf including sunglint, whitecaps (sea foam), and pigment concentration.

To calculate the polarized and total glitter from the ocean surface, 6SV uses the *sunglint* and *polglit* subroutines, respectively. Therefore, in order to obtain the outputs needed for our model, I needed to modify both of these.

F.1 Modifications to the sunglint subroutine

The *sunglint* and POLGLIT routines were modified to use the reflectance equations derived in section 5.2.3.3. The 6SV subroutine *sunglint* calculates the unpolarized reflectance rog, equivalent to the Stokes-I reflectance parameter. The notation used by 6SV is as follows:

rog = apparent reflectance = π x BRDF

R1 = Fresnel reflectance = $\rho = R_{tot}$ (above)

mun = cosine of tilt angle = $\mu_n = \cos(\beta)$

sigma2 = $\sigma^2 = 0.003 + 5.12\times10^{-3}\ W$

tv = θ_v = viewer zenith angle

ts = θ_s = solar zenith angle

fi = relative azimuth

wspd = windspeed = W

The description of the subroutine inputs and outputs from 6SV follows:

```
      subroutine sunglint(wspd,nr,ni,azw,ts,tv,fi,rog)
C input parameters:   wspd=speed of the wind (in m/s)
C                     nr=index of refraction of the sea water
C                     ni=extinction coefficient of the sea water
c                     azw=azim. of the sun - azim. of the wind (in deg.)
C                     ts=solar zenith angle (in deg.)
C                     tv=view zenith angle (in deg.)
C                     fi=relative azimuth (sun-satellite)
C output parameters:  rog=reflectance of the sun glint.
```

The following modifications were made to subroutine *sunglint* in OCEATOOLS.f to calculate unpolarized reflectance Rog. Here, "CZ" indicates comments added to the code, and "CZ_remove" indicates lines of code commented out.

```
CZ Comment out existing calculation of reflectance
CZ_remove Rog=pi*R1*proba/4./cs/cv/(cos(tilt)**4)

CZ Calculate mu-n and the square and fourth powers
      mun = cos(tilt)
      if(sca.lt.1e-6)sca=1e-6
CZ      mun = abs((cs - cv)/2./cos(sca/2))
      if (abs(mun).lt.1e-6)mun = 1e-6
      mun2 = mun**2
      if (abs(mun2).lt.1e-8)mun2 = 1e-8
      mun4 = mun**4
      if (abs(mun4).lt.1e-10)mun4 = 1e-10
      if (abs(cv).lt.1e-6)cv = 1e-6

CZ Calculate sigma squared from wind speed using eqn from Cox & Munk 1954
      sigma2 = 0.003+0.0512*wspd

CZ Calculate reflectance Rog as Fresnel refl R1 x exponential probability
      Rog = (exp((mun2-1)/(sigma2*mun2)))*R1/4./mun4/sigma2
CZ change to work w/ main09, which multiplies by cv
      Rog = Rog/cv
```

F.2 Modifications to the POLGLIT.f subroutine

As with the *sunglint* routine, the POLGLIT routine was modified to use the reflectance equations derived in section 5.2.3.3.

```
CZ Following commented out
CZ_remove      sigmaC=0.003+0.00192*wspd
CZ_remove      sigmaU=0.00316*wspd
CZ_remove      C21=0.01-0.0086*wspd
CZ_remove      C03=0.04-0.033*wspd
CZ_remove      C40=0.40
CZ_remove      C22=0.12
CZ_remove      C04=0.23
CZ_remove      xe=(cos(phw)*zx+sin(phw)*zy)/sqrt(SigmaC)
CZ_remove      xn=(-sin(phw)*zx+cos(phw)*zy)/sqrt(SigmaU)
CZ_remove      xe2=xe*xe
CZ_remove      xn2=xn*xn
CZ_remove      coef=1-C21/2.*(xe2-1)*xn-C03/6.*(xn2-3)*xn
CZ_remove      coef=coef+c40/24.*(xe2*xe2-6*xe2+3)
CZ_remove      coef=coef+C04/24.*(xn2*xn2-6*xn2+3)
CZ_remove      coef=coef+C22/4.*(xe2-1)*(xn2-1)
CZ_remove      proba=coef/2./pi/sqrt(sigmaU)/sqrt(sigmaC)*exp(-(xe2+xn2)/2.)

CZ old calculation of factor which feeds into Q and U
CZ_remove        factor=pi*proba/4./cs/cv/(cos(tilt)**4)

      mun = cos(tilt)
      if(sca.lt.1e-6)sca=1e-6

CZ      mun = abs((cs - cv)/2./cos(sca/2))
      if (abs(mun).lt.1e-6)mun = 1e-6
      mun2 = mun**2
      if (abs(mun2).lt.1e-8)mun2 = 1e-8
      mun4 = mun**4
      if (abs(mun4).lt.1e-10)mun4 = 1e-10

      if (abs(cv).lt.1e-6)cv = 1e-6
CZ
      sigma2 = 0.003+0.0512*wspd
      factor = (exp((mun2-1)/(sigma2*mun2)))/4./mun4/sigma2/cv
```

The code then calculates the Stokes *Q* reflectance *ropq* and Stokes *U* reflectance *ropu* using *factor* and the rotation factors it calculates.

F.3 Modifications to main.f

The main subroutine of 6SV was modified to output the Stokes parameters, and to remove unneeded outputs. The code changes are shown below.

`main.f in /uranus/s0/mzugger/6SV/WEarth2/`

First, let's look at the lines of code I added to main.f to produce the LUT:

```
============================================================
```

```
------------------------------------------------------------
Added to header, lines 4 - 6
------------------------------------------------------------

CZ This version unpacked from 6SV lut .tar file sent by Eric V
CZ Updated to produce a polarized LUT
CZ March - April 2009

Added in Declarations, lines 307 - 308

CZ Variables added by Zugger
      real roI,roIparl,roIperp,Xchi,plumet1,phipos
      integer iout,ioutac,ioutcr

------------------------------------------------------------
Added at end of Declarations, lines 429 - 439
------------------------------------------------------------

CZ NO STATEMENTS EXCEPT DECLARATIONS BEFORE THIS POINT

CZ*****************************************
CZ Switches to turn outputs on and off
CZ*****************************************
CZ To suppress printout of initial conditions,set iout=0; to enable, iout=1
       iout=0
CZ To suppress calc and output of atmospheric correction, set ioutac=0
      ioutac=0
CZ To suppress output of complementary results, set ioutcr=0; enable ioutcr=1
      ioutcr=0

------------------------------------------------------------
Added to suppress first printout, lines 2305 - 2307, 2419 - 2420
------------------------------------------------------------

CZ Loop to write outputs; set iout=1 to write, 0 to suppress

      if(iout.eq.1)THEN

      endif
CZ End loop to write outputs

------------------------------------------------------------
Added to suppress second printout, lines 2580 - 2582, 2596
------------------------------------------------------------

CZ      ioutac=0
CZ To suppress atmospheric correction, ioutac=0; to enable, ioutac=1
      if (ioutac.eq.1) then

CZ End loop to suppress output of ac

------------------------------------------------------------
Added to test plumet, which seems to be calculated incorrectly in 6SV, lines
3037 - 3038, 3242 - 3244
------------------------------------------------------------

CZ TEST next line
```

```
        plumet1=plumet/seb

CZ check plumet
      write(iwr,3502)plumet1
 3502 format('plumet1 = ',f8.4)

------------------------------------------------------------
Added these comments to show what variables are used as outputs by 6SV, lines
3233 - 3237
   (write line is from unmodified main.f)
------------------------------------------------------------

CZ The next line prints out:
CZ rpfet = app. polarized reflectance
CZ plumet = app. polarized radiance
CZ xpol = direction of plane of polarization
CZ rpfet/refet = total polarization ratio
CZ
        write(iwr, 429 )rpfet,plumet,xpol,rpfet/refet

------------------------------------------------------------
Added to suppress output of "Complementary Results", lines 3275, 3320 - 3321
------------------------------------------------------------

      if (ioutcr.eq.1) then

      endif
CZ End loop to suppress complementary result output

------------------------------------------------------------
Added to suppress output of "atmospheric correction result", lines 3396, 3419
-  3420
------------------------------------------------------------

CZ Loop to disable printout of atmospheric correction result
         if (ioutcr.eq.1) then

      endif
CZ End loop to disable printout

------------------------------------------------------------

================================================================================
```

We also need another piece of information from the main.f code listing, which is that phi is calculated by subtracting the solar az from the viewer az:

```
        phi=phi0-phiv   (line 2262)
```

Since SAz = phi0 = 0, phi is always less than or equal to zero, which causes problems with my ReadLUT routine, so we use absolute value:

```
phipos = abs(phi)
```

Based on the outputs from 6SV, we find that:

```
rpfet = app. polarized reflectance
plumet = app. polarized radiance
xpol = direction of plane of polarization
rpfet/refet = total polarization ratio
```

From the above it appears that:

```
refet = Stokes-I
xpol = Xchi
Iparl = 1/2 x (I + Q) = 0.5*(refet+rqfet)
Iperp = 1/2 x (I - Q) = 0.5*(refet-rqfet)

phipos = abs(phi)
```

Returning to the code listing:

```
================================================================================

c        write(6,*) 'rogbrdf=',rogbrdf,' rodir=',brdfints(mu,1),
c    s            ' diff=',rogbrdf-brdfints(mu,1)
      endif

      endif
CZ End loop to disable printout

CZ ************************************
CZ  calculate scattering angle

      asolr = asol*3.14159/180
      avisr = avis*3.14159/180
      phipos=abs(phi)

CZ calculate scattering angle
      csca = cos(avisr)*cos(asolr) + sin(avisr)*sin(asolr)*cos(phirad)
      csca = min(csca,1.0)
      csca = max(csca,-1.0)
      sca = acos(csca)
      if (sca.eq.0.0) then
         sca = 1e-8
      endif
      scad = sca*180/3.14159
CZ      write(6,*)"scattering angle = ", scad


CZ The following lines added by Zugger to create LUT
CZ main08.f removed 0.5* to give real reflectances in LUT

        roIparl=(refet+rqfet)
        roIperp=(refet-rqfet)

       Xchi = 0
c      Xchi = 0.5*(atan(rufet/rqfet))*180/3.14159
c      if (Xchi.eq.nan) then
c        Xchi = 0.0
c      endif
```

```
CZ min function added 12 Nov 2009, rem Jul 2010
      Iparl = roIparl
      Iperp = roIperp

      open(11,file='/uranus/s0/mzugger/6SV/LUTtemp.txt',ACCESS='APPEND')

CZ main09 added cos factor back in

      refet = refet*cos(avisr)
      rqfet = rqfet*cos(avisr)
      rufet = rufet*cos(avisr)


      write(11,3504)asol,avis,phipos,refet,rqfet,rufet,Iparl,
     s Iperp,trmoy,scad

CZ Write above output to screen also for debug

      write(iwr,3504)asol,avis,phipos,refet,rqfet,rufet,Iparl,
     s Iperp,trmoy,scad

CZ Format changed 30 Oct 2009

 3504  FORMAT(f5.1,1x,f5.1,1x,f6.1,1x,f9.5,1x,f9.5,1x,f8.5,1x,f9.5,
     s 1x,f9.5,1x,f6.4,1x,f5.1)

CZ END Lines added by Zugger
      stop
```

Appendix G: Additional Verification and Error Analysis

G.1 Additional Verification of Oceans Code

G.1.1 Total Illuminated Area

The Oceans code uses the variable asurf0 for the area of each pixel. The area of the pixel is calculated for each pass through the loop using the number of latitude points *nlat*, the number of longitude points *nlon*, and the radius of the Earth, and also multiplying by the cosine of the latitude to include the fact that pixels nearer the poles are smaller:

(177)

Inserting a variable to sum all pixel areas, and reporting the value of this sum at full phase, Oceans reports a total illuminated area of 2.556 x 10^{14} m^2. Using the radius of the Earth to calculate the approximate total area, and dividing by two because half of the Earth is illuminated, we obtain:

$$A_{illum} = \frac{1}{2} 4\pi (r_{planet})^2 = 2\pi (6.378 \times 10^6)^2 = 2.556 \times 10^{14} \quad \text{m}^2 \tag{178}$$

which agrees to four digits with the value reported by the Oceans code.

G.1.2 Solar Constant

Oceans code also calculates the incoming solar radiation in W m^{-2}, often called the solar constant, and calls it f_{star}; when a print statement is used to obtain this value, Oceans reports f_{star} = 1360.5, which is very close to the canonical value of 1365 W m^{-2}. Oceans uses the following formula to calculate f_{star} using the Sun's output, the Earth-Sun distance, using the following formula:

$$f_{star} = \frac{l_{star}}{4\pi (d_{star})^2} = \frac{P_{Sun}}{4\pi (a_{1AU})^2} = \frac{3.826 \times 10^{26}}{4\pi (149.6 \times 10^9)^2} = 1361 \quad \text{W sr}^{-1} \tag{179}$$

G.1.3 Three-Dimensional Trigonometry

Here, we verify some of the 3D trigonometry used in the Oceans code.

Orbital Angles Converted to Scattering Angles. Our model defines the orbital parameters (along with the planetary surface and atmospheric parameters), which are listed below along with the name of the variable in Oceans:

- Position of the planet in the orbit (orbital longitude) orblon
- Inclination of the orbit to line of sight of the observer on Earth incl
- Obliquity (tilt) of the planet's axis oblq
- Direction the planet's axis tilts eqnx
- Latitude of the pixel being calculated lat
- Longitude of the pixel being calculated lon

In order to calculate scattering from the planet's surface, we need to convert these angles into a set of angles referred to the local surface of the planet. Now imagine that we are standing on the surface of the exoplanet, looking up at the sky, where we identify the apparent position of the parent star and the exoplanet observer on Earth. We can now picture the angles needed to perform the surface scattering calculation. These three angles[38] are listed below, along with the variable names used in Oceans:

- Angle of the parent star to the zenith (Stellar Zenith Angle) znstar
- Angle of the observer on Earth to the zenith (Viewer Zenith Angle, VZA) znerth
- Relative azimuth angle between the two (RelAz) azmthdif

Figure 18 (included earlier) shows these angles on a locally flat surface; however, to handle surface scattering, we need to consider non-Euclidian geometry, specifically spherical trigonometry, the study of triangles on a sphere.

Spherical Trigonometry Navigators have used spherical trigonometry for hundreds, perhaps thousands of years, to determine position in the ocean based on navigational fixes. The Williams Oceans model uses a number of equations from spherical trigonometry to perform the angle conversions described above, that is, to convert the available geometric information into the geometric parameters used to calculate the scattering for each pixel. These are described in the next section.

First, we need the Cosine Rule for spherical triangles:

[38] Note that, for a surface which has a directional component, such as a wavy ocean with directional waves, an additional parameter is needed. Rather than being able to use only the Relative Azimuth, in this case we need both the Stellar Azimuth (SAz) and the Viewer Azimuth (Vaz). We avoid this issue (which would massively increase the size of lookup tables and model run times) by using a direction-independent wave scattering model.

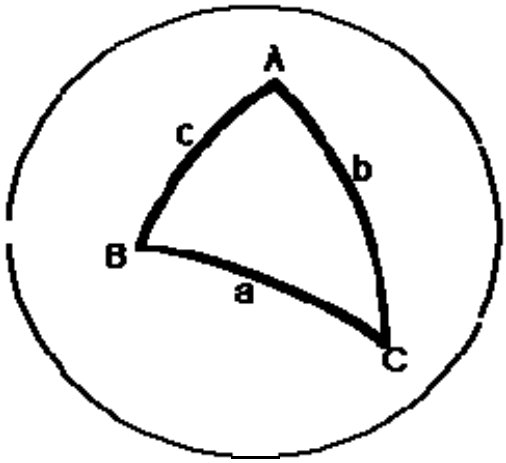

Figure 72: Spherical triangle showing naming convention for angles and segments

Given A, B, and C are the angles of a spherical triangle, and a, b, and c are the corresponding great circle segments, the Cosine Rule says that:

$$\cos(a) = \cos(b)\cos(c) + \sin(b)\sin(c)\cos(A) \tag{180}$$

or equivalently,

$$a = \arccos[\cos(b)\cos(c) + \sin(b)\sin(c)\cos(A)] \tag{181}$$

with both angles and arcs measured in radians. The rule is a generalization of the Pythagorean Theorem, which states that, on a flat surface, with a right triangle,

$$a^2 = b^2 + c^2 \tag{182}$$

where a is the hypotenuse, the segment which faces the right angle A. To generalize this theorem to any triangle on a flat surface, we add a term to allow A to have any value between zero and 180^o:

$$a^2 = b^2 + c^2 - 2bc\cos(A) \tag{183}$$

When the formula is further generalized to work on the surface of a sphere, the result is the Cosine Rule.

The Cosine Rule formula is mathematically accurate, but when an inverse cosine (arcos) is performed with an argument close to zero, it is computationally inaccurate if there are insufficient significant figures because of rounding – it is "ill-conditioned." In order to get around this problem, the Cosine Rule is sometimes replaced using haversine functions. The name haversine comes from the old navigator's term half-versed-sine, where the versed sine of an angle θ is 1 – cos(θ), so the half-versed-sine is simply ½ [1 – cos(θ)].

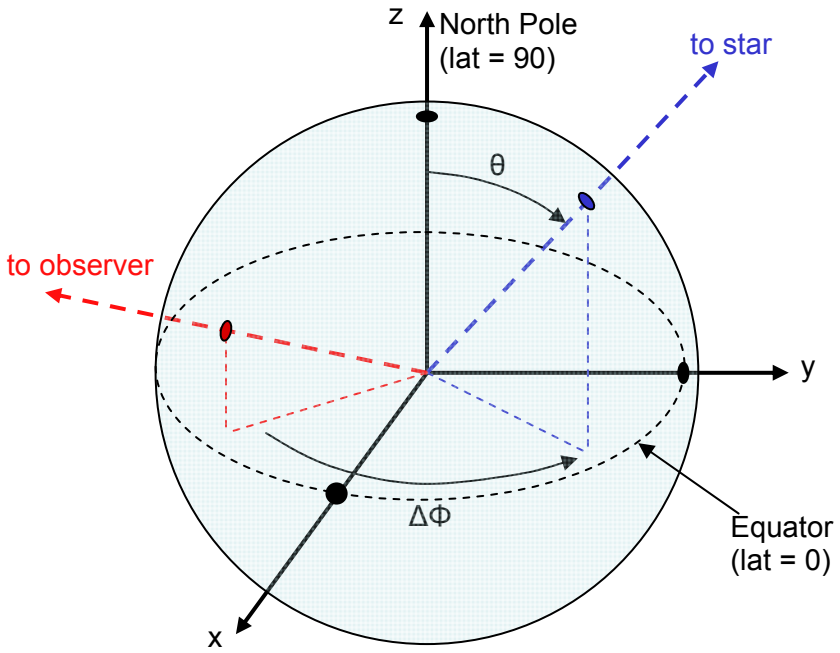

Figure 73: Coordinate system and definition of angles

Spherical Geometry in the Oceans Model. The following is based in part on conversations with Darren Williams during March 2009.

1) The angle between the star and the observer on Earth, with the planet under study at the apex of the angle, is called *str2erth* in the Oceans code. In Figure 73 it is the angle between the dashed lines labeled "to star" and "to observer." This angle is given by:

$$str2erth = \arccos(zstar) = \arccos[-\cos(orblon)\sin(incl)] + \varepsilon \qquad (184)$$

where *str2erth*, *orblon*, and *incl* are as defined above, and ε is a small number, such as 1 x 10^{-6}, added to avoid zero values which can cause singularities.

We can verify this equation by checking some special cases. For an inclination of zero, corresponding to an orbit in the plane of the sky, and perpendicular to our line of sight, the angle formed by the star, the planet, and the observer is always 90° by definition. Checking our formula,

$$str2erth = \arccos[-\cos(orblon)\sin(0)] = \arccos[0] = 90^{o} \qquad (185)$$

Now assume we are looking at the system edge-on, that is, the inclination is 90°. Then the sin term is one; now assume that the observer, star, and planet are arranged in a line. If the planet is in front of the star, that is, in transit, then the orbital longitude is zero, and the star-planet-observer angle is 180°. Using the equation, we have:

$$str2erth = \arccos[-\cos(0^o)\sin(90^o)] = \arccos[-1\times 1] = 180^o \quad (186)$$

which checks out. If the planet is behind the star, that is, in secondary transit, then the orbital longitude is 180^o and the star-planet-observer angle is zero. The equation gives us:

$$str2erth = \arccos[-\cos(180^o)\sin(90^o)] = \arccos[1\times 1] = 0^o \quad (187)$$

which again checks out.

2) Stellar latitude: for planets with more than one type of surface, we calculate the stellar latitude for each point on the orbit; that is, we calculate where the substellar point falls with respect to the planet's equator. This quantity, called *lats* by Oceans, is determined as follows:

$$lats = \arcsin[-\sin(oblq)\cos(orblon + eqnx)] \quad (188)$$

Suppose the inclination of the orbit is 90^o (edge-on), and the planet's axis points at the observer, that is, $orblon = 0^o$. Then, for an obliquity greater than zero but less than 90^o, the stellar latitude will be zero (over the equator) only at the equinox points, which will occur at maximum separation, or orbital longitudes of 90^o and 270^o. Let's see if the formula gives us the correct answer.

$$lats = \arcsin[-\sin(oblq)\cos(90^o + 180^o)] = \arcsin[0] = 0^o \quad (189)$$

The cosine of 90 + 180 or 90 + 270 is zero, so the formula works for both equinox points with an edge-on orbit.

3) Calculation of required angles
In any case, in order to calculate the required angles, we first need to determine the latitude and longitude of the star (*lats*, *lons*) and the observer on Earth (*lat0*, *lon0*). To do this, we will need a quantity that Oceans refers to as *deltheta* (although, since it is a relative azimuth, *delphi* would be more appropriate):

$$deltheta = \arccos\left[\frac{zstar - \sin(lats)\sin(lat0)}{\cos(lats)\cos(lat0)}\right] \quad (190)$$

The latitude of the star is constant for a planet with zero obliquity, but varies seasonally for nonzero obliquity:

$$lats = \arcsin\left[-\sin(oblq)\cos(orblon + eqnx)\right] \quad (191)$$

although we assume a homogeneous surface and zero obliquity in our model. (Theoretically, on a planet with a homogeneous surface, obliquity should not matter in our model.) The latitude of the observer is:

$$lat0 = dsklat(amatrix) \tag{192}$$

and the longitude of the observer is:

$$lon0 = (n4 \times 15^o) - 180^o \tag{193}$$

$$lons = lon0 + deltheta \tag{194}$$

$$str2erth = \arccos(zstar) = \arccos[-\cos(orblon)\cos(90 - incl)] = \arccos[-\cos(orblon)\sin(incl)] \tag{195}$$

Area of the surface pixel, given
rplnt = planet radius,
dlat = π/nlatres = fractional size of the latitude grid, and
dlon = 2π/nlonres = fractional size of the longitude grid:

$$asurf0 = \frac{\pi \times r_{planet}}{nlat} \times \frac{2\pi \times r_{planet}}{nlon} \cos(lat) = (rplnt)^2 (dlat)(dlon)\cos(lat) \tag{196}$$

The projected area of the surface element, as scaled by the cosine of the Stellar Zenith Angle:

$$asurf = asurf\,0 \bullet \cos(znstar) \tag{197}$$

Stellar Zenith Angle (SZA), znstar:

Starting with the haversine formula,

$$\text{haversin}(c) = \text{haversin}\ (a - b) + \sin(a)\ \sin(b)\ \text{haversin}(C) \tag{198}$$

and letting
c = znstar,
a = lat,
b = lats, and
C = longitude difference, we have

$$\sin^2\left(\frac{znstar}{2}\right) = \sin^2\left(\frac{lat - lats}{2}\right) + \sin(90 - lats)\sin(90 - lat)\sin^2\left(\frac{lon - lons}{2}\right) \tag{199}$$

$$\sin^2\left(\frac{znstar}{2}\right) = \sin^2\left(\frac{lat - lats}{2}\right) + \cos(lats)\cos(lat)\sin^2\left(\frac{lon - lons}{2}\right) \tag{200}$$

$$znstar = 2\arcsin\sqrt{\left[\sin^2\left(\frac{lat - lats}{2}\right) + \cos(lats)\cos(lat)\sin^2\left(\frac{lon - lons}{2}\right)\right]} \tag{201}$$

which matches the formula used in Oceans to determine *znstar*, also known as Stellar Zenith Angle.

Viewer Zenith Angle (VZA), znerth:

The derivation for *znerth* is similar to that for *znstar*, with latitude and longitude of the star (*lats* and *lons*) replaced by the latitude and longitude of the observer on Earth (*lat0* and *lon0*). The resulting formula is then:

$$znerth = 2\arcsin\sqrt{\left[\sin^2\left(\frac{lat-lat0}{2}\right)+\cos(lat0)\cos(lat)\sin^2\left(\frac{lon-lon0}{2}\right)\right]} \tag{202}$$

as used in Oceans.

Relative Azimuth (RelAz), azmthdif:

Starting with the Law of Cosines, we have

$$\cos(str2erth) = \sin(\theta_1)\sin(\theta_2)+\cos(\theta_1)\cos(\theta_2)\cos(\varphi_1-\varphi_2) \tag{203}$$

Converting the zenith angles to angles to the horizon by subtracting from 90°, and substituting the definition of str2erth and azmthdif for the difference in φ, we have

$$\begin{aligned}&\sin(90-znstar)\sin(90-znerth)+\cos(90-znstar)\cos(90-znerth)\cos(azmthdif)\\&=-\cos(orblon)\sin(incl)\end{aligned} \tag{204}$$

Solving for azmthdif,

$$\cos(azmthdif) = \frac{-\cos(orblon)\sin(incl)-\sin(90-znstar)\sin(90-znerth)}{\cos(90-znstar)\cos(90-znerth)} \tag{205}$$

we obtain the formula used in the Oceans code:

$$azmthdif = \arccos\left[\frac{-\cos(orblon)\sin(incl)-\cos(znstar)\cos(znerth)}{\sin(znstar)\sin(znerth)}\right] \tag{206}$$

which completes our verification of Oceans 3D trigonometry by analysis.

G.2 Additional Verification of 6SV Code: 6SV implementation of Fresnel equations

The Fresnel equations are used in two subroutines of 6SV: subroutine *sunglint* in OCEATOOLS.f, and POLGLIT.f. The *sunglint* subroutine calculates the unpolarized Stokes I parameter, while POLGLIT.f calculates the Q and U parameters; otherwise, the implementations are identical in the two subroutines, so we can verify both at the same time.

The following code is used to calculate the scattering angle:

```
       csca=-cos(xts*dtr)*cos(xtv*dtr)-sin(xts*dtr)
      s      *sin(xtv*dtr)*cos(phi*dtr)
         sca=acos(csca)
       alpha=(pi-sca)/2.0
```

The above matches Hansen Travis 1974, which gives the scattering angle as (using our notation):

$$\cos(SCA) = \cos(SZA)\cos(VZA) - \sin(SZA)\sin(VZA)\cos(RelAz) \tag{207}$$

Here, the rl and rr (parallel and perpendicular reflectance) parameters are used to calculate r1 and r2, which are the reflective Stokes I and Q parameters, and the rotation angle α is calculated from the scattering angle:

```
C Originally from Deuze et al cannot mak it work to be investigated
       rl=(sqrt(m*m-sin(alpha)*sin(alpha))-m*m*cos(alpha))/
      s         (sqrt(m*m-sin(alpha)*sin(alpha))+m*m*cos(alpha))
C
       rr=(cos(alpha)-sqrt(m*m-sin(alpha)*sin(alpha)))/
      s        (cos(alpha)+sqrt(m*m-sin(alpha)*sin(alpha)))
C
       r1=(rl*rl+rr*rr)/2.
       r2=(rl*rl-rr*rr)/2.
       r3=rl*rr
```

$$\cos(SCA) = -\cos(SZA)\cos(VZA) - \sin(SZA)\sin(VZA)\cos(relAz) \tag{208}$$

$$\alpha = \frac{\pi - SCA}{2} \tag{209}$$

$$r_l = \frac{\sqrt{m^2 - \sin^2\alpha} - m^2\cos\alpha}{\sqrt{m^2 - \sin^2\alpha} + m^2\cos\alpha} \tag{210}$$

$$r_r = \frac{\cos\alpha - \sqrt{m^2 - \sin^2\alpha}}{\cos\alpha + \sqrt{m^2 - \sin^2\alpha}} \tag{211}$$

$$r_2 = \frac{1}{2}\left[r_l^2 - r_r^2\right] = \frac{1}{2}\left\{\left[\frac{\sqrt{m^2 - \sin^2\alpha} - m^2\cos\alpha}{\sqrt{m^2 - \sin^2\alpha} + m^2\cos\alpha}\right]^2 - \left[\frac{\cos\alpha - \sqrt{m^2 - \sin^2\alpha}}{\cos\alpha + \sqrt{m^2 - \sin^2\alpha}}\right]^2\right\} \qquad (212)$$

Taking the formula for the Fresnel perpendicular, and dividing top and bottom by n_1, and remembering that $m = n_2/n_1$,

$$R_\perp = R_s = \left[\frac{\cos\theta_i - m\sqrt{1 - m^{-2}\sin^2\theta_i}}{\cos\theta_i + m\sqrt{1 - m^{-2}\sin^2\theta_i}}\right]^2 = \left[\frac{\cos\theta_i - \sqrt{m^2 - \sin^2\theta_i}}{\cos\theta_i + \sqrt{m^2 - \sin^2\theta_{ii}}}\right]^2 = r_r^2 \qquad (213)$$

Now taking Fresnel parallel formula, and again dividing through by n_1,

$$R_{//} = R_p = \left[\frac{\sqrt{1 - m^{-2}\sin^2\theta_i} - m\cos\theta_i}{\sqrt{1 - m^{-2}\sin^2\theta_i} + m\cos\theta_i}\right]^2 = \left[\frac{\sqrt{m^2 - \sin^2\theta_i} - m^2\cos\theta_i}{\sqrt{m^2 - \sin^2\theta_i} + m^2\cos\theta_i}\right]^2 = r_l^2 \qquad (214)$$

which verifies that r2 above is, in fact, the reflective Stokes parameter *Q*.

G.3 Additional Verification Using Independently Developed MATLAB Model

Dr. Karl Reichard recommended that I consider developing a simplified polarized planetary scattering code using MATLAB. This code would be developed directly from theory, and independently of both Oceans and 6SV, in order to provide independent verification of the results. Three separate MATLAB routines were developed, covering different portions of the task. These are:

1) A test routine to extract the Fresnel reflecting portions of the lookup table, where angle of incidence equals angle of reflectance, and relative azimuth is 180°;
2) MATLAB-Generated Lookup Table - a lookup table for an all-water planet with no atmosphere, generated in MATLAB using Fresnel's equations, and in the same format as the 6SV/Oceans generated code, so that it can be fed into the same modified Oceans code; this code was used for troubleshooting;
3) MATLAB Lightcurve simulating routine - a complete polarized lightcurve simulating code for a waveless all-water planet with a Rayleigh scattering atmosphere, using Fresnel's equations to simulate the air/water interface and the Rayleigh scattering equations, geometry, and judicious simplifications to create a complete but simplified model.

The MATLAB LUT, when fed into the modified Oceans code, produces a lightcurve which can be compared to the known result, and was used in troubleshooting the modified Oceans code. The MATLAB Lightcurve simulating routine produces complete lighcurves which can be compared against those independently generated by the full modified 6SV/modified Oceans simulation. This latter code is discussed below.

MATLAB Fresnel Model

I developed a simplified model of a wave-free water planet in a circular orbit with an edge-on orbital inclination (90^o) from the observer's point of view. Using geometry, Fresnel's law of reflection, the antenna pattern of a dipole (Rayleigh scattering particle), and some engineering approximations, I was able to generate polarized planetary light curves for the simplified cases of a water surface under a thin atmosphere, and a Rayleigh scattering atmosphere over a dark surface, which strongly resembled those from our more sophisticated model. The code in the simple model can be verified by inspection, and is independent of the more complex models, so the correspondence between these curves serves as verification of the results.

Given a point source, a spherical planet with a specularly reflecting surface (e.g. wave-free ocean), and a point receiver, at any position around the orbit, there is one point on the sphere where the light from the star strikes the planet and reflects to the receiver. For the simplified model, the reflection occurs only at the specular point, where the stellar zenith angle and the viewer zenith angle are equal, and the relative azimuth is 180°. The reflectances of the two polarizations, the parallel and the perpendicular, are then given by the Fresnel equations.

Adding Rayleigh Scattering to the MATLAB Model

We can add Rayleigh single scattering to this model by using the phase function for Rayleigh scattering. We can ignore multiple scattering to first order for an Earth-like atmosphere, because at 500 nm $\tau_R \approx 0.13$, which means that the fraction of light scattered at vertical incidence is

$$I / I_0 = \exp(-0.13) = 0.88 \tag{215}$$

or 12% scattering, and the magnitude of double scattering will be roughly

$$0.12 \; x \; 0.12 = 0.0144 \tag{216}$$

or about 1.4%, which we can ignore for the simplified model. For the outgoing flux, we will assume Rayleigh scattering is essentially a simple attenuation, and should not affect polarization for single-scattering.

We also need the illuminated fraction of the planet, which has an elevated cosine dependence on phase angle θ, period T, and angle offset φ:

$$\tfrac{1}{2} \; x \; [1 + \cos(2\pi(\theta - \varphi)/T]. \tag{217}$$

Running the MATLAB model for various proportions of Rayleigh scattering and water surface scattering, we obtain a number of curves which can be summarized as the positions of the polarization peaks in the various cases as shown in Table 13. We note that the end members, the top and bottom rows, match the results for the Ocean planet with a thin atmosphere, and the Rayleigh scattering atmosphere, respectively, and the rows between these grade between the two extremes.

Table 13: OL of Polarization Peaks as Calculated by MATLAB Model (second peak symmetric about 180°).

Water Surface Scat Fraction	Rayleigh Scat Fraction	First Peak, deg	Second Peak, deg
1	0	73.9	286.1
0.75	0.25	75.4	284.6
0.67	0.333	76.2	283.8
0.5	0.5	78.3	281.7
0.33	0.667	81.6	278.4
0.25	0.75	83.6	276.4
0	1	90	270

G.4 Verification of 6SV calm ocean planet results versus 2% reflecting spherical mirror

Among the planets modeled was an ocean planet with a thin atmosphere, light winds, and no clouds. To verify the that the ocean planet model was working properly, we calculated the total radiant intensity (W sr^{-1}) from this planet when fully illuminated (full phase), and compared this

result to the radiant intensity from a spherical mirror of the same size with a reflectance of 0.02 (2%), a verification method used previously by (McCullough 2006). The result for the 2% mirror is calculated using two different analytical methods below, which give nearly identical answers.

Conservation of Radiance and the Convex Mirror

By modeling a water planet as a convex mirror, and utilizing the principle of conservation of radiance, we can calculate the expected intensity from the planet.

Conservation of radiance: the radiance L in W m^2 sr^{-1} of the image of a surface (e.g. the Sun or a star) in a perfectly specular mirror is equal to the radiance of the original surface (Sun/star), independent of the shape of the mirror (Horn 1986).

Convex mirror irradiance to intensity: The intensity I from a perfect specular convex mirror with radius r, measured at a distance much greater than r, given an incident flux density of E (W m^{-2}) is, from Tousey (1957):

$$I = \frac{r^2}{4} E \quad \text{W sr}^{-1} \tag{218}$$

The reflectance of flat water over a dark substrate (or with a depth of kilometers) at vertical incidence is about 2%, so for a water Earth in full phase ($\alpha = 0$, OL = 180), we have

$$\begin{aligned} r_{planet} &= 6378 \times 10^3 \quad \text{m} \\ E &= 1365 \quad \text{W m}^{-2} \\ I &= \frac{(6.378 \times 10^6)^2}{4} 1365 \times 0.02 = 2.78 \times 10^{14} \quad \text{W sr}^{-1} \end{aligned} \tag{219}$$

Lens Maker's Equation and Solar Radiance

We can obtain the same answer using a similar analytical technique. Here we will use the radiance of the Sun and the lens maker's equation to calculate the brightness of a water planet in full phase.

Remembering that radiance L is defined for <u>projected</u> surface area, the radiance of the solar disk is given by:

$$L_{Sun}^{disk} = \frac{P/2}{\pi R^2 \times 2\pi} = \frac{3.85 \times 10^{26}/2}{\pi (6.96 \times 10^8)^2 \times 2\pi} = 2.01 \times 10^7 \quad \text{W sr}^{-1}\ \text{m}^2 \tag{220}$$

Suppose we now model the water Earth as a convex mirror, with the Sun acting as the object, and the reflection of the Sun in the water as the image. Then using the lens maker's equation

(Equation (221)), which works for mirrors as well, we define the object distance d_o as the distance from the surface of the Earth to the surface of the Sun. The image distance d_i is then the distance behind the mirror's/Earth's surface, and f for a convex mirror is half the radius, so

$$\frac{1}{d_0}+\frac{1}{d_i}=\frac{1}{f} \tag{221}$$

$$d_i=\frac{1}{\left(\frac{1}{f}-\frac{1}{d_0}\right)}=\frac{1}{\left(\frac{2}{r}-\frac{1}{1AU}\right)}=3.185\times10^{6}\quad \text{m} \tag{222}$$

which puts the image very close to f, as expected given the large Earth-Sun distance compared to the radius of Earth. Now recalling that the ratio of the image to object height equals the ratio of the image to object distance, we calculate the height of the Sun's image in the Earth "mirror" as

$$\frac{h_i}{h_o}=-\frac{d_i}{d_o}=-\frac{3.185\times10^{6}}{150\times10^{9}}=2.12\times10^{-5} \tag{223}$$

$$h_i=h_o\times2.12\times10^{-5}=6.96\times10^{8}\times2.12\times10^{-5}=14800\quad \text{m} \tag{224}$$

This is not the spot size of the Sun on the surface of the ocean, but the apparent size of the virtual image of the Sun which appears about half way to the center of the Earth. Now that we have the image and the radiance of the Sun, using the 2% reflectance of water at normal incidence we can calculate the radiance and radiant intensity of the Sun's reflection in the ocean at normal incidence:

$$L_i=\rho L_{Sun}=0.02L_{Sun}=0.02\times2.01\times10^{7}=4.02\times10^{5}\quad \text{W m}^{-2}\ \text{sr}^{-1} \tag{225}$$

$$I_i=L_i\times\pi h_i^{2}=4.02\times10^{5}\times\pi(14800)^{2}=2.77\times10^{14}\quad \text{W sr}^{-1} \tag{226}$$

which is almost an exact match to the earlier result using Tousey. The difference is that the convex mirror approximation assumes incident parallel flux, which in turn assumes a point source. The lens maker's method uses the diameter and distance of the Sun, which results in a non point source with an apparent size of about ½ degree as seen from Earth. The more accurate lens maker's method thus gives a slightly lower radiant intensity.

Comparison of Analytical and Model Results

Returning to Table 9, we find that the radiant intensity from the simulation is 1.06 to 1.25 times that of the planet replaced by a 2% reflecting spherical mirror. The simulations using the longer wavelength portions of the TPF waveband more closely match the mirror; this is due to the reduced scattering from within the water column for longer wavelengths.

G.5 Graphical depiction of glint spot on an ocean planet

Figure 74 shows the glint spot from a water planet with a thin atmosphere and light wind (equivalent to 1.5 m/s at 1 atm) at OL = 74°; Figure 74a shows the parallel component, which is diminished at and near the Brewster angle, and Figure 74b shows the perpendicular component. The color scales, which represent the amount of flux scattered to the observer from each pixel, are the same – the parallel component peak is reduced by a factor of 3 due to Brewster angle effects. The vertical extent of the violet region is approximately +/-43° latitude, and the horizontal extent is approximately 58° of longitude. Pixels are defined as the area lying between 2° lines of latitude and longitude, so pixels shrink (and flux per pixel decreases) toward the poles as the cosine of latitude. These pixel graphs were used to troubleshoot the Stokes rotation routine, and to confirm that it was working properly when the expected result of an approximately circular glint spot with higher reflectance in the perpendicular polarization was achieved.

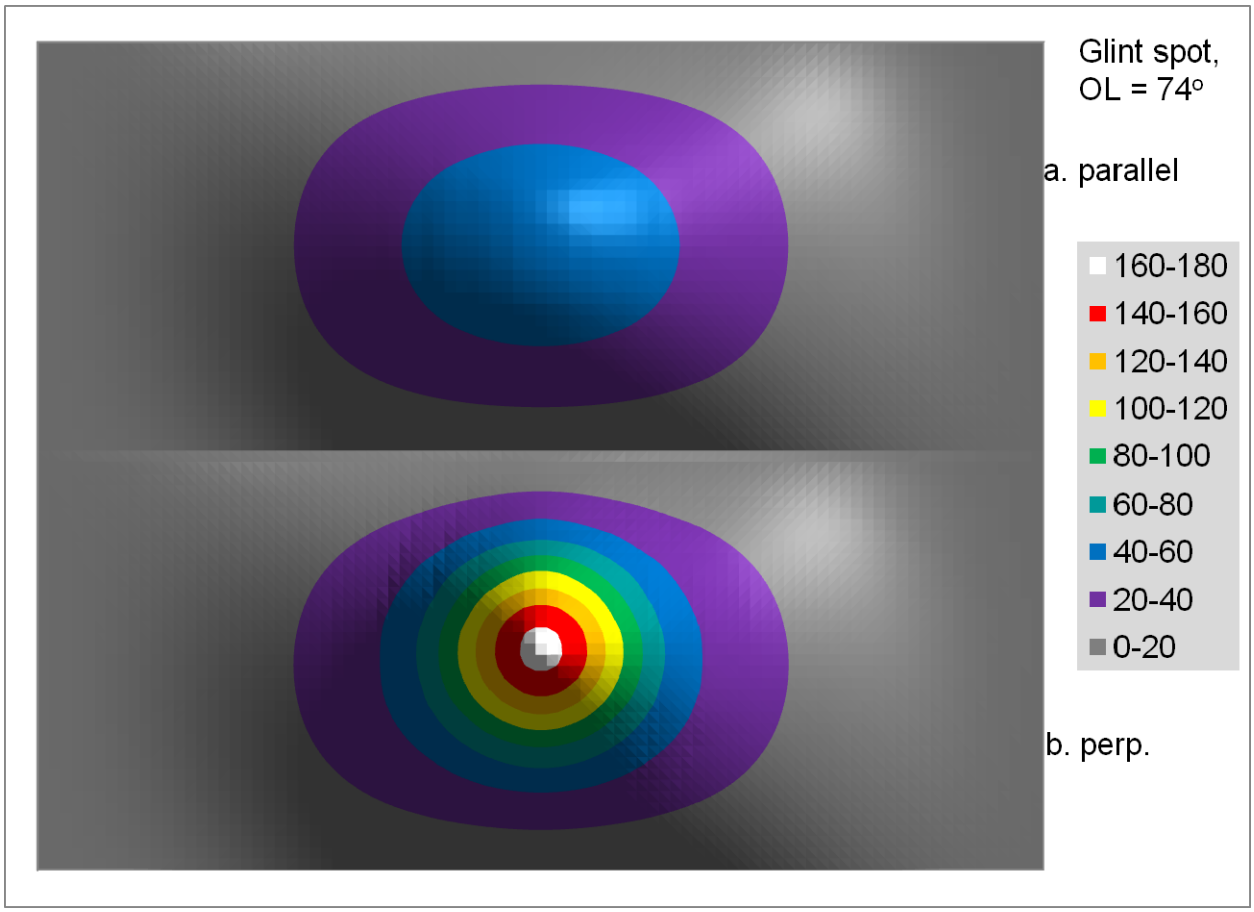

Figure 74: Relative flux per pixel, produced at and near the glint spot for a water planet, thin atmosphere, no clouds. Planet is located at OL = 74°. a) parallel polarization, b) perpendicular polarization, same scale

References

Acarreta, J., J. De Haan and P. Stammes (2004). "Cloud pressure retrieval using the O2-O2 absorption band at 477 nm." J. Geophys. Res **109**(D05204).

Bailey, J. (2007). "Rainbows, Polarization, and the Search for Habitable Planets." Astrobiology **7**(2): 320-332.

Barman, T. (2007). "Identification of Absorption Features in an Extrasolar Planet Atmosphere." The Astrophysical Journal **661**(2): L191-L194.

Bas, C. (2002). Investigation of Surf-Zone Plumes With a Two-Dimensional Bistatic Lidar and the Polarization Ratio Method. Electrical Engineering. University Park, PA, The Pennsylvania State University. **Doctor of Philosophy**.

Beichman, C. and T. Velusamy (1999). Sensitivity of the TPF interferometer for planet detection.

Berner, R. A., A. C. Lasaga and R. M. Garrels (1983). "The carbonate-silicate geochemical cycle and its effect on atmospheric carbon dioxide over the past 100 million years." American Journal of Science **283**(7): 641.

Bjoraker, G. L., H. P. Larson and V. G. Kunde (1986). "The abundance and distribution of water vapor in Jupiter's atmosphere." Astrophysical Journal **311**: 1058-1072.

Bohren, C. F. (1992). "On the absurdity and inadvisability of calling particles Mie scatterers." Optics & Photonics News **3**(2): 18-19.

Bohren, C. F. and E. E. Clothiaux (2006). Fundamentals of Atmospheric Radiation: An Introduction with 400 Problems. Germany, Wiley-VCH.

Bohren, C. F. and D. R. Huffman (1983). Absorption and Scattering of Light by Small Particles. New York, Wiley-Interscience.

Boltzmann, L. (1895). "On the Minimum Theorem in the Theory of Gases." Nature **52**(1340): 221.

Brack, A. (1993). "Liquid water and the origin of life." Origins of Life and Evolution of Biospheres **23**(1): 3-10.

Brewster, D. (1815). "On the Laws Which Regulate the Polarisation of Light by Reflexion from Transparent Bodies." Philosophical Transactions of the Royal Society of London **105**: 125-159.

Cash, W. (2006). "Detection of Earth-like planets around nearby stars using a petal-shaped occulter." Nature **442**(7098): 51-53.

Cash, W., C. Copi, S. Heap, N. J. Kasdin, S. Kilston, M. Kuchner, M. Levine, A. Lo, et al. (2007). "External Occulters for the Direct Study of Exoplanets." submitted to the ExoPlanet Task Force in Response to the NASA Call for White Papers, April **2**.

Chamberlain, J. W. and D. M. Hunten (1987). Theory of planetary atmospheres: an introduction to their physics and chemistry, Academic Press.

Chandrasekhar, S. and D. D. Elbert (1954). "The illumination and polarization of the sunlit sky on Rayleigh scattering." Transactions of the American Philosophical Society **44**: 643.

Clark, J. (2006). "The Atomic Hydrogen Emission Spectrum " Chemguide from http://www.chemguide.co.uk/atoms/properties/hspectrum.html.

Cockell, C. S., A. Léger, M. Fridlund, T. Herbst, L. Kaltenegger, O. Absil, C. Beichman, W. Benz, et al. (2009). "Darwin–A Mission to Detect, and Search for Life on, Extrasolar Planets." Astrobiology **9**(1): 1-22.

COESA (1962). US Standard Atmosphere. Washington, DC, US Government Printing Office.

Coulson, K. (1988). Polarization and Intensity of Light in the Atmosphere. Hampton, Virginia, A. Deepak Publishing.
Coulson, K. L., J. V. Dave and Z. Sekera (1960). "Tables Related to Radiation Emerging from a Planetary Atmosphere with Rayleigh Scattering." Univ. Calif. Press, Berkeley--LA.
Cowan, N. B., E. Agol, V. S. Meadows, T. Robinson, T. A. Livengood, D. Deming, C. M. Lisse, M. F. A'Hearn, et al. (2009). "Alien maps of an ocean-bearing world." The Astrophysical Journal **700**: 915-923.
Cox, C. and W. Munk (1954). "Measurement of the Roughness of the Sea Surface from Photographs of the Sun's Glitter." Journal of the Optical Society of America **44**(11): 838-850.
Cox, C. and W. Munk (1955). "SOME PROBLEMS IN OPTICAL OCEANOGRAPHY1." Journal of marine research **14**: 63-78.
Des Marais, D. J., M. O. Harwit, K. W. Jucks, J. F. Kasting, D. N. C. Lin, J. I. Lunine, J. Schneider, S. Seager, et al. (2002). "Remote Sensing of Planetary Properties and Biosignatures on Extrasolar Terrestrial Planets." Astrobiology **2**(2): 153-181.
Dollfus, A. (1957). "Étude des planètes par la polarisation de leur lumière." Supplements aux Annales d'Astrophysique **4**: 3-114.
Draine, B. T. and P. J. Flatau (1994). "Discrete-dipole approximation for scattering calculations." J. Opt. Soc. Am. A **11**(4): 1491–1499.
Einstein, A. (1905). "On a heuristic point of view concerning the production and transformation of light." Annalen der Physik **17**: 132-148.
Feldman, W. C., S. Maurice, A. B. Binder, B. L. Barraclough, R. C. Elphic and D. J. Lawrence (1998). "Fluxes of Fast and Epithermal Neutrons from Lunar Prospector: Evidence for Water Ice at the Lunar Poles." Science **281**(5382): 1496.
Ford, E. B., S. Seager and E. L. Turner (2001). "Characterization of extrasolar terrestrial planets from diurnal photometric variability." Nature **412**(6850): 885-887.
Girod, B., G. Greiner and H. Niemann (2000). Principles of 3D image analysis and synthesis, Springer Netherlands.
Goloub, P., J. L. Deuze, M. Herman and Y. Fouquart (1994). "Analysis of the POLDER polarization measurements performed over cloud covers." IEEE Transactions on Geoscience and Remote Sensing **32**(1).
Goody, R. M. and Y. L. Yung (1989). Atmospheric Radiation: Theoretical Basis, New York and Oxford: Oxford University Press.
Guyon, O. (2003). "Phase-induced amplitude apodization of telescope pupils for extrasolar terrestrial planet imaging." Journal reference: Astron. Astrophys **404**: 379.
Haltrin, V. (2002). Algorithm and code to calculate specular reflection of light from a wavy water surface. The 7th International Conference on Remote Sensing for Marine and Coastal Environments, Ann Arbor, MI, Veridian.
Hansen, J. E. and J. W. Hovenier (1974). "Interpretation of the Polarization of Venus." Journal of the Atmospheric Sciences **31**(4): 1137-1160.
Hansen, J. E. and L. D. Travis (1974). "Light scattering in planetary atmospheres." Space Science Reviews **16**(4): 527-610.
Hardie, R. H. (1962). Stars and Stellar Systems. Astronomical Techniques. W. A. Hiltner. Chicago, University of Chicago Press.
Harland, W. B. (1964). "Critical evidence for a great infra-Cambrian glaciation." International Journal of Earth Sciences **54**(1): 45-61.

Hart, M. H. (1978). "The evolution of the atmosphere of the Earth." Icarus **33**(1): 23-39.
Henry, G. W., G. W. Marcy, R. P. Butler and S. S. Vogt (2000). "A Transiting "51 Peg-like" Planet." The Astrophysical Journal **529**(1): L41-L44.
Hoffman, P. F. and D. P. Schrag (2002). "The snowball Earth hypothesis: testing the limits of global change." Terra Nova **14**(3): 129-155.
Horn, B. (1986). Robot vision, McGraw-Hill Higher Education.
Hovenier, J. W. and J. F. de Haan (1985). "Polarized Light in Planetary Atmospheres for Perpendicular Directions." Astronomy & Astrophysics **146**: 185-191.
Kalas, P., J. R. Graham, E. Chiang, M. P. Fitzgerald, M. Clampin, E. S. Kite, K. Stapelfeldt, C. Marois, et al. (2008). "Optical Images of an Exosolar Planet 25 Light-Years from Earth." Science **322**(5906): 1345-1348.
Kaltenegger, L. and M. Fridlund (2005). "The Darwin mission: Search for extra-solar planets." Advances in Space Research **36**(6): 1114-1122.
Kaltenegger, L., W. A. Traub and K. W. Jucks (2007). "Spectral evolution of an Earth-like planet." The Astrophysical Journal **658**(1): 598-616.
Kasten, F. and A. Young (1989). "Revised optical air mass tables and approximation formula." Applied Optics **28**(22): 4735-4738.
Kasting, J. (2009). Invited Talk: The Search for Life on Other Planets. Our Universe: From the Big Bang to Life. The Pennsylvania State University, February 28 2009.
Kasting, J. F., D. P. Whitmire and R. T. Reynolds (1993). "Habitable Zones around Main Sequence Stars." Icarus **101**(1): 108-128.
Kemp, J. and R. Wolstencroft (1971). "Circular polarization: Jupiter and other planets." Nature **232**: 165-168.
Kiang, N. Y., J. L. Siefert, Govindjee and R. E. Blankenship (2007). "Special Paper: Spectral Signatures of Photosynthesis. I. Review of Earth Organisms." Astrobiology **7**(1): 222-251.
Koepke, P. (1984). "Effective reflectance of oceanic whitecaps." Applied Optics **23**(11): 1816-1824.
Kotchenova, S. Y. and E. F. Vermote (2007). "Validation of a vector version of the 6S radiative transfer code for atmospheric correction of satellite data. Part II. Homogeneous Lambertian and anisotropic surfaces." Applied Optics **46**(20): 4455-4464.
Kotchenova, S. Y., E. F. Vermote, R. Matarrese and J. F. J. Klemm (2006). "Validation of a vector version of the 6S radiative transfer code for atmospheric correction of satellite data. Part I: Path radiance." Applied Optics **45**(26): 6762-6774.
Kuchner, M. J. and D. N. Spergel (2003). "Notch-filter masks: practical image masks for planet-finding coronagraphs." The Astrophysical Journal **594**(1): 617-626.
Kyle, T. (1991). Atmospheric Transmission, Emission, and Scattering, Pergamon Press.
Lafrenière, D., R. Jayawardhana and M. H. van Kerkwijk (2008). "Direct Imaging and Spectroscopy of a Planetary Mass Candidate Companion to a Young Solar Analog " Arxiv preprint arXiv:0809.1424.
Lawson, P. R., A. Ahmed, R. O. Gappinger, A. Ksendzov, O. P. Lay, S. R. Martin, R. D. Peters, D. P. Scharf, et al. (2006). "Terrestrial Planet Finder interferometer technology status and plans." Proceedings of SPIE **6268**.
Levine, M., S. Shaklan and J. Kasting (2006). Terrestrial Planet Finder Coronagraph, Science and Technology Development Team (STDT) Report, JPL Document D-34923.

Levoni, C., M. Cervino, R. Guzzi and F. Torricella (1997). "Atmospheric aerosol optical properties: a database of radiative characteristics for different components and classes." Applied Optics **36**(30): 8031-8041.
Liou, K. N. (2002). An Introduction to Atmospheric Radiation, Academic Press.
Lorentz, H. A. (1892). La théorie électromagnétique de Maxwell et son application aux corps mouvants, EJ Brill.
Lorenz, L. V. (1890). "On the reflection and refraction of light from a transparent sphere." Videnskaps Selskabets Skrifter **6**: 1-62.
Lorenz, R. (2003). "Planetary science. The glitter of distant seas." Science **302**(5644): 403-404.
Lovelock, J. E. (1972). "Gaia as seen through the atmosphere." Atmospheric Environment (1967) **6**(8): 579-580.
Lovelock, J. E. and L. Margulis (1974). "Atmospheric homeostasis by and for the biosphere: the Gaia hypothesis: Tellus, v. 26."
Lucas, P., J. Hough, J. Bailey, M. Tamura, E. Hirst and D. Harrison (2009). "Planetpol polarimetry of the exoplanet systems 55 Cnc and Boo." Monthly Notices of the Royal Astronomical Society **393**(1): 229-244.
Mallama, A. (2009). "Characterization of terrestrial exoplanets based on the phase curves and albedos of Mercury, Venus and Mars." Icarus **204**(1): 11-14.
Manalo-Smith, N., G. L. Smith, S. N. Tiwari and W. F. Staylor (1998). "Analytic forms of bidirectional reflectance functions for application to Earth radiation budget studies." Journal of Geophysical Research **103**(D16): 19733-19752.
Marcy, G., R. P. Butler, D. A. Fischer, S. S. Vogt, J. T. Wright, C. G. Tinney and H. R. A. Jones (2005). "Observed Properties of Exoplanets: Masses, Orbits, and Metallicities." Progress of Theoretical Physics Supplement **158**: 24-42.
Marois, C., B. Macintosh, T. Barman, B. Zuckerman, I. Song, J. Patience, D. Lafreniere and R. Doyon (2008). "Direct Imaging of Multiple Planets Orbiting the Star HR 8799." Science **322**(5906): 1348-1352.
Maxwell, J. C. (1865). "A dynamical theory of the electromagnetic field." Philosophical Transactions of the Royal Society of London **155**: 459-512.
Maxwell, J. C. (1867). "On the Dynamical Theory of Gases." Philosophical Transactions of the Royal Society of London **157**: 49-88.
Maxwell, J. C. (1873). "Clerk Maxwell's Kinetic Theory of Gases'." Nature **8**(84): 122–123.
Mayor, M. and D. Queloz (1995). "A Jupiter-sized companion to a Solar-type star." Nature **378**: 355-359.
McClatchey, R. A., R. W. Fenn, J. E. A. Selby, F. E. Volz and J. S. Garing (1972). Optical properties of the atmosphere, 3rd edition, Air Force Cambridge Research Labs, Hanscom AFB.
McCullough, P. R. (2006). "Models of Polarized Light from Oceans and Atmospheres of Earth-like Extrasolar Planets." arXiv:astro-ph/0610518.
Meadows, V. S. and D. Crisp (1996). "Ground-based near-infrared observations of the Venus nightside: The thermal structure and water abundance near the surface." Journal of Geophysical Research-Planets **101**(E2): 4595-4622.
Measures, R. (1992). Laser Remote Sensing, Krieger Publishing Company.
Mie, G. (1908). "Contribution on optical properties of turbid solutions, with special reference to colloidal metallic solutions." Annalen der Physik **25**: 337-445.

Mishchenko, M. I., J. W. Hovenier and L. D. Travis (2000). "Light Scattering by Nonspherical Particles."
Monahan, E. and I. Muircheartaigh (1980). "Optimal power-law description of oceanic whitecap coverage dependence on wind speed." Journal of Physical Oceanography **10**(12): 2094-2099.
Mumma, M. J., G. L. Villaneuva, R. E. Novak, T. Hewagama, B. P. Bonev, M. A. DiSanti, A. M. Mandell and M. D. Smith (2009). "Strong Release of Methane on Mars in Northern Summer 2003." Science: 1165243v1165241.
Neff, H. (1981). Basic Electromagnetic Fields. New York, Harper & Row.
Oakley, P. and W. Cash (2009). "Construction of an Earth Model: Analysis of Exoplanet Light Curves and Mapping Earth at 10 parsecs with the New Worlds Observer." The Astrophysical Journal **700**: 1428-1439.
Ollivier, M., J. M. Le Duigou, D. Mourard, O. Absil, F. Cassaing, E. Herwats, L. Escarrat, B. Chazelas, et al. (2006). "PEGASE: a DARWIN/TPF pathfinder." Proceedings of the International Astronomical Union. Direct Imaging of Exoplanets: Science and Techniques **200**: 241-245.
Ottaviani, M., K. Stamnes, J. Koskulics, H. Eide, S. R. Long, W. Su and W. Wiscombe (2008). "Light Reflection from Water Waves: Suitable Setup for a Polarimetric Investigation under Controlled Laboratory Conditions." Journal of Atmospheric and Oceanic Technology **25**(5): 715-728.
Pavlov, A. A., J. F. Kasting, L. L. Brown, K. A. Rages and R. Freedman (2000). "Greenhouse warming by CH 4 in the atmosphere of early Earth." Journal of Geophysical Research **105**(11): 981–911.
Perryman, M. (2000). "Extra-solar planets." Reports on Progress in Physics **63**: 1209.
Petty, G. W. (2006). A First Course in Atmospheric Radiation. Madison, WI, Sundog Publishing.
Purcell, E. M. and C. R. Pennypacker (1973). "Scattering and Absorption of Light by Nonspherical Dielectric Grains." The Astrophysical Journal **186**: 705.
Rayleigh, L. (1871). "On the scattering of light by small particles." Philosophical Magazine **41**: 447-451.
Raymond, S. N., A. M. Mandell and S. Sigurdsson (2006). "Exotic Earths: forming habitable worlds with giant planet migration." Science (New York, NY) **313**(5792): 1413.
Rozenburg, G. V. (1966). Twilight: A Study in Atmospheric Optics. New York, Plenum Press.
Russell, H. N. (1916). "The stellar magnitudes of the sun, moon and planets." Astrophysical Journal **43**: 103–129.
Sagan, C. and J. B. Pollack (1967). "Anistropic Nonconservative Scattering and the Clouds of Venus." Journal of Geophysical Research **72**: 469-477.
Sagan, C., W. R. Thompson, R. Carlson, D. Gurnett and C. Hord (1993). "A search for life from the Galileo spacecraft." Nature **365**: 715.
Schutgens, N., L. Tilstra, P. Stammes and F. Bréon (2004). "On the relationship between Stokes parameters Q and U of atmospheric ultraviolet/visible/near-infrared radiation." J. Geophys. Res **109**.
Seidelmann, K. P., Ed. (1992). Explanatory Supplement to the Astronomical Almanac. Mill Valley, California, University Science Books
Selsis, F., J. F. Kasting, B. Levrard, J. Paillet, I. Ribas and X. Delfosse (2007). "Habitable planets around the star Gliese 581?" A&A **476**: 1373-1387.

Shapley, H., Ed. (1953). Climatic Change: Evidence, Causes, and Effects, Harvard University Press, Cambridge.
Shen, L. and J. Kong (1995). Applied Electromagnetism, PWS Publishing Company.
Slade, M. A., B. J. Butler and D. O. Muhleman (1992). "Mercury Radar Imaging: Evidence for Polar Ice." Science **258**(5082): 635-640.
Smith, B. and R. Terrile (1984). "A circumstellar disk around Beta Pictoris." Science **226**(1421): 316.
Sobolev, V. V. (1975). "Light scattering in planetary atmospheres." (Translation of Rasseianie sveta v atmosferakh planet, Moscow, Izdatel'stvo Nauka, 1972.) Oxford and New York, Pergamon Press (International Series of Monographs in Natural Philosophy) **76**: 263.
Sparks, W., J. Hough, T. Germer, F. Chen, S. DasSarma, P. DasSarma, F. Robb, N. Manset, et al. (2009). "Detection of circular polarization in light scattered from photosynthetic microbes." Proceedings of the National Academy of Sciences **106**(19): 7816.
Squyres, S. W., R. E. Arvidson, J. F. Bell, J. Bruckner, N. A. Cabrol, W. Calvin, M. H. Carr, P. R. Christensen, et al. (2004). The Opportunity Rover's Athena Science Investigation at Meridiani Planum, Mars, American Association for the Advancement of Science. **306:** 1698-1703.
Stam, D. (2008). "Spectropolarimetric signatures of Earth-like extrasolar planets." Astronomy and Astrophysics **482**(3): 989-1007.
Stokes, G. G. (1852). "On the Change of Refrangibility of Light." Philosophical Transactions of the Royal Society of London **142**(463-562): 1.
Sumner, D. Y., J. L. Kirschvink and B. N. Runnegar (1987). "Soft-sediment paleomagnetic fold tests of late Precambrian glaciogenic sediments." Eos **68**: 1251.
Takano, Y. and K. Liou (1989). "Solar radiative transfer in cirrus clouds. Part I: Single-scattering and optical properties of hexagonal ice crystals." Journal of the Atmospheric Sciences **46**(1): 3.
Takano, Y. and K. Liou (1995). "Radiative Transfer in Cirrus Clouds. Part III: Light Scattering by Irregular Ice Crystals." Journal of the Atmospheric Sciences **52**(7): 818.
Takashima, T. and K. Masuda (1985). "Degree of radiance and polarization of the upwelling radiation from an atmosphere-ocean system." Applied Optics **24**(15): 2423-2429.
Thiele, W. and W. Stutzman (1981). Antenna Theory and Design. New York, J. Wiley.
Thomas, M. and D. Duncan (1993). Atmospheric Transmission. The Infrared & Electro-Optical Systems Handbook. G. Zissis.
Tilstra, L. G., N. A. J. Schutgens and P. Stammes (2003). Analytical Calculation of Stokes Parameters Q and U of Atmospheric Radiation. De Bilt, The Netherlands, Koninklijk Nederlands Meteorologisch Instituut (KNMI).
Tinetti, G., V. S. Meadows, D. Crisp, W. Fong, E. Fishbein, M. Turnbull and J. P. Bibring (2006). "Detectability of planetary characteristics in disk-averaged spectra. I: The Earth model." Astrobiology **6**(1): 34–47.
Tinetti, G., V. S. Meadows, D. Crisp, N. Y. Kiang, B. H. Kahn, E. Bosc, E. Fishbein, T. Velusamy, et al. (2006). "Detectability of Planetary Characteristics in Disk-Averaged Spectra II: Synthetic Spectra and Light-Curves of Earth." Astrobiology **6**(6): 881-900.
Toon, O., C. P. McKay, T. P. Ackerman and K. Santhanam (1989). "Rapid calculation of radiative heating rates and photodissociation rates in inhomogeneous multiple scattering atmospheres." Journal of Geophysical Research **94**(D13).
Tousey, R. (1957). "Optical problems of the satellite." J. Opt. Soc. Am **47**: 261-267.

Traub, W. A., M. Levine, S. Shaklan, J. Kasting, J. R. Angel, M. E. Brown, R. A. Brown, C. Burrows, et al. (2006). TPF-C: status and recent progress (Invited Paper). Proceedings of SPIE.

Udalski, A., B. Paczynski, K. Zebrun, M. Szymanski, M. Kubiak, I. Soszynski, O. Szewczyk, L. Wyrzykowski, et al. (2002). "The Optical Gravitational Lensing Experiment. Search for Planetary and Low-Luminosity Object Transits in the Galactic Disk. Results of 2001 Campaign." Acta Astronomica **52**(1): 1-38.

Unwin, S. (2009). Analysing architecture, Routledge.

Van de Hulst, H. (1957). Light Scattering by Small Particles. New York, John Wiley & Sons.

Vermote, E. and S. Kotchenova (2008). "Atmospheric correction for the monitoring of land surfaces." Journal of Geophysical Research-Atmospheres **113**: 12.

Vermote, E. F., D. Tanré, J. L. Deuzé, M. Herman, J. J. Morcrette and S. Y. Kotchenova. (2006). "Second Simulation of a Satellite Signal in the Solar Spectrum-Vector (6SV)." from 6s. ltdri. org/6S_code2_thiner_stuff/6S_Manual_Part_1. pdf.

Voigt, W. (1889). "Ueber die Beziehung zwischen den beiden Elasticitätsconstanten isotroper Körper." Annalen der Physik **274**(12): 573-587.

Walker, J. C. G., P. B. Hays and J. F. Kasting (1981). "A Negative Feedback Mechanism for the Long-Term Stabilization of Earth's Surface Temperatures." J. Geophys. Res **86** 9776-9782.

Williams, D. M. and E. Gaidos (2008). "Detecting the Glint of Starlight on the Oceans of Distant Planets." Icarus **195**(2): 927-937.

Wolszczan, A. and D. A. Frail (1992). "A planetary system around the millisecond pulsar PSR 1257+ 12." Nature **355**(6356): 145-147.

Young, A. and W. M. Irvine (1967). "Multicolor photoelectric photometry of the brighter planets. I. Program and procedure." Astronomical Journal **72**: 945-950.

Yung, Y. L. (1976). "A numerical method for calculating the mean intensity in an inhomogeneous Rayleigh scattering atmosphere." Journal of Quantitative Spectroscopy and Radiative Transfer **16**: 755-761.

Zeisse, C. R. (1995). "Radiance of the ocean horizon." Journal of the Optical Society of America **12**(9): 2022-2030.

Zugger, M., J. Kasting, D. Williams, T. Kane and C. Philbrick (2010). "Light Scattering from Exoplanet Oceans and Atmospheres." The Astrophysical Journal **723**: 1168.

Zugger, M., J. Kasting, D. Williams, T. Kane and C. Philbrick (in process). "Searching for Earths in the Near Infrared."

VITA

Michael E. Zugger – Senior Research Engineer, Penn State Applied Research Laboratory

EXPERIENCE

Senior Electro-Optic Research Engineer, Penn State Applied Research Lab

o Model scattering by extrasolar planets under NASA Astrobiology grants.
o Design, prototype, test, and document optical and electro-optic (E/O) systems including an instrument for studying human color vision.
o Systems engineer for proposal and Phase A efforts for JANUS XRFM satellite instrument.

Lead Electrical Engineer, Swift Satellite X-ray Space Telescope, PSU Astronomy

o Design, build, and test the electronics for a laboratory prototype x-ray CCD camera.
o Lead the design, construction, I&T of flight electronics for the Swift x-ray telescope.
o Design, test, and repair of ground-based astronomical instrumentation for optical and infrared camera systems (ET, PIRIS, JCAM). Won $1.3 million NASA grant for x-ray detectors.

Graduate Researcher, Communications & Space Sciences Lab, Penn State

o Design, build, and calibrate a visible-wavelength transmissometer (M.S. Thesis Topic).
o Set up and operate the tropospheric lidar systems locally and at remote sites.

Analog/Fiber Optics Design Engineer, Laser Precision Corp, Utica NY

o Design F/O test equipment: optical time-domain reflectometers (OTDRs), power meters.
o R&D: optical masking OTDR, optical return loss measurement, improved dyn. range OTDR.
o EMI/EMC design and test, including military MIL-STD-461 and European CE.

Research Engineer, Grumman Newport News, Newport News VA

o Led company's internal fiber optics R&D program – F/O sensor evaluation, design, budgets.
o Bearing vibration test, acoustic testing, shaft alignment, fatigue test sub drivetrain component.
o Represented company on committee writing fiber optic mil specs & standards for Navy subs.

EDUCATION

- **Ph.D. EE Candidate, Penn State University, GPA 3.8.** Concentrations: electro-optics, space systems, and remote sensing.
- **MSEE, Penn State University. GPA 3.9.** Concentrations: electromagnetics, electronic design, communications & signal processing, control systems.
- **BSEE, University of Rochester.** Concentrations: circuit design, communications; informal geology/biology minor.

SELECTED PUBLICATIONS

- "Light scattering from exoplanet oceans and atmospheres," *The Astrophysical Journal,* 723(2) 1168-11-79, 2010 (1st author)
- "The JANUS X-ray Flash Monitor," A. Falcone et al., *Proceedings of SPIE,* 7435, 2009
- "Optical scattering properties of phytoplankton: Measurements and comparison of various species at scattering angles 1^o - 170^o," *Limnol. Oceanogr*, *53*(1), 381-386, 2008 (1st author).
- "Development of a Spectrum Generator," *OSA Frontiers in Optics*, 2006 (1st author)
- "The X-ray Telescope for the SWIFT Gamma-Ray Burst Mission," A. Wells et al., AIP Conf. Proc. 727, p642, 2004
- "Results from upgrades to the radial velocity instrument, Extrasolar Tracker, at the Kitt Peak Nat. Obs. 2.1m," *Proc. SPIE,* 5492, 445-451, Ground-based Instr. for Astronomy, 2004
- "Laboratory X-ray CCD Camera Electronics - a test bed for the Swift X-ray Telescope," J. Hill et al., *Proc. SPIE,* vol. 4140, pp87-98, 2000 (2nd author)